THE UNIVERSITY *of* EDINBURGH

Neutron Scattering Studies of Hydrogenated Molecular Materials

Katherine Lauren Brown

Doctor of Philosophy
The University of Edinburgh
April 2021

Best advice I got when I entered academia:
"We are all smart.
Distinguish yourself by being kind."

ANNE GALLOWAY

Abstract

This thesis employs three neutron scattering techniques; neutron diffraction, inelastic neutron scattering, and quasielastic neutron scattering; to probe the properties of hydrogenous systems. These results are complemented by other techniques in order to provide useful information on the three systems to be studied. These systems are chosen for their relevance to industrial situations and the key influence of hydrogen bonding upon their properties. Neutron scattering has a key advantage over X-ray scattering, in that the cross-section of hydrogen is much larger for neutron scattering, allowing for hydrogenous systems and hydrogen bonding phenomena to be directly probed. Neutrons are also better suited to inelastic scattering measurements, as their lower energy allows for energy transfer between the probe and the sample to be measured with higher resolution.

The first family of systems studied in this thesis are the methylammonium lead halide ($MAPbX_3$) compounds, where X = Cl or Br. This family of compounds is of interest due to their high performance as solar panel materials, and relative ease of manufacture. The studies carried out use inelastic neutron scattering, quasielastic neutron scattering, and Raman spectroscopy to probe the molecular excitations in these compounds as a function of temperature. It is found that there is a step change in the molecular dynamics in these compounds as they transition out of the orthorhombic phase, with the short-lived tetragonal phase acting as a region of transitional dynamics. In the case of $MAPbBr_3$ this change in molecular dynamics is corroborated with a change in photovoltaic properties at these temperatures.

Secondly, the phase diagram with pressure of NH_4F is studied using neutron diffraction and computational studies. NH_4F is analogous to ice in structure at ambient pressure, and the known phases of NH_4F are all analogous to those observed in ice. As gas inclusion compounds are easily formed with ice, this makes NH_4F a candidate gas storage material. An apparent tetragonal distortion

is observed in the cubic phase of NH_4F, commencing at approximately 6 GPa and increasing with pressure. However, as this distortion is not reproduced in computational studies, further experiments are carried out to establish that this effect is instead due to deviatoric stress. The tetragonal distortions reported in the literature at high pressures and low temperatures are therefore inferred to also be due to strain effects.

Finally, the mixing behaviour of CH_4 in H_2O with pressure is investigated using quasielastic neutron scattering. This system is relevant to natural gas extraction processes. Selective deuteration is used to isolate the dynamics of the H_2O molecules. It is found, at pressures below mixing, the diffusion coefficient of the water is reduced, whereas above the mixing pressure it is in agreement with that of pure water. This disparity is explained through the increase in viscosity of the water due to the presence of bubbles before mixing, and the reduced proportion of bubbles as the mixing pressure is approached.

Lay Summary

Hydrogen is the lightest and most common element in the universe. On Earth it is normally found as a constituent in molecules or compounds as gaseous hydrogen is too light to be constrained by Earth's gravity. Hydrogen also participates in a unique type of bonding, referred to as simply "hydrogen bonding". This has wide-reaching consequences for many different materials containing hydrogen, and affects many different fields within science. Due to the commonness of hydrogen-containing materials, it remains an important area of research.

The small size of hydrogen atoms creates some difficulty in measuring their position or motion in materials. However, this is not a problem in neutron scattering because neutrons interact directly with the atomic nucleus, and the strength of this interaction is not dependent on the position of the element in the periodic table. In the case of materials containing hydrogen atoms, this means that they can be measured by scattering neutrons from them. Neutron scattering techniques are able to measure numerous material properties and are a commonly used for studying materials containing light elements. This thesis studies three very different materials, with the common thread being the importance of hydrogen to their properties. For all of these materials neutron scattering techniques are the primary method employed in their study.

First, the rotation of a molecule contained in the structure of the methylammonium lead halides is studied. This family of materials have promising photovoltaic properties for use in solar panels but are unlikely to ever be used in commercial products. An understanding of the molecular dynamics in the methylammonium lead halides is important for the further development of other photovoltaic materials. The results show that as the materials are warmed there is a rapid change in the molecular dynamics at a particular temperature. A reduction of molecular motion is observed at the same point as a reduction in photovoltaic properties.

Second, changes to the structure of ammonium fluoride as pressure is increased are characterised. Ammonium fluoride has a structure similar to that of ice at normal conditions and, as ice can take on many structures as temperature and pressure is changed, it is of interest to see if ammonium fluoride has similar properties. No new structures in ammonium fluoride are found in the investigations presented in this thesis. However, the high pressures applied result in distortions which have previously been interpreted as structural changes.

Third, the mixing between water and methane with pressure is studied. Methane is hydrophobic, meaning that it resists mixing with water. However, previous studies have observed that upon applying a specific pressure methane and water mix easily. Here, the dynamics of the water molecules are measured to investigate whether there is a change as to their motion during this mixing process. It is found that the presence of the methane bubbles initially causes the water to move more slowly, then, when the bubbles are dissolved, the water behaves as though it were pure water once more.

Declaration

I declare that this thesis was composed by myself, that the work contained herein is my own except where explicitly stated otherwise in the text, and that this work has not been submitted for any other degree or professional qualification except as specified.

Parts of this work have been published in [27][166].

(*Katherine Lauren Brown, April 2021*)

Acknowledgements

This thesis only came together due to the combined efforts of a large number of people, all of whom I owe great thanks.

Foremost, I must offer gratitude to my supervision team. Firstly to Dr. John Loveday, who introduced me into the world of high pressure physics and was a reassuring voice when I was unsure about the next direction for a project. This thesis would not exist without your optimism and support. My second supervisor, Prof. Paul Attfield, was always ready to dispense sage advice in all matters scientific and personal, and has been a constant throughout my studies. And lastly to Dr. Chris Stock, who taught me inelastic and quasielastic scattering techniques, and assisted me in getting my work published.

The experimental work in this thesis was carried out both at Edinburgh and at international neutron scattering facilities, and has thus had many contributors. At Edinburgh, I must specifically thank Bernhard Massani for his tutelage in diamond anvil cell techniques, assistance in methane clathrate growth, and help running neutron scattering experiments. Dr. Manila Songvilay contributed to the chapter 6 by aiding with sample growth and the running of experiments. For the experiments carried out at ISIS I would like to thank Dr. Victoria García Sakai, Dr. Stuart Parker, Dr. David Voneshen and Dr. Craig Bull, as well as the other members of the experimental teams. Zainab Sharif was of great assistance by providing the deuterated samples used for and helping to run the experiment at ISIS in chapter 7. Key contributors to chapter 8 were Dr. Stefan Klotz, Dr. Ciprian Pruteanu and Dr. Jean-Marc Zanotti, without whom the experiment would not have taken place. I must also thank all members of the team at the SNS who ran the experiment on SNAP presented in chapter 7 for me. The theoretical work included in chapter 7 was carried out with the support of Lewis Conway and Dr. Andreas Hermann: thank you for tutoring me in the basics of DFT.

For their unwavering support in difficult times, and for enabling my off-the-wall outreach idea, I must thank the CM-CDT team: Dr. Chris Hooley, Dr. Julie Massey and Debra Thompson. Dr. Paul Clegg, Prof. Catherine Heymans and the University of Edinburgh Student Counselling Service also provided invaluable pastoral support at various points throughout my PhD. I would also be remiss

to not mention the support I received from my parents, Angela and David, who allowed me to press-gang them into being test-readers, and the rest of my family. However, possibly the most important support I've had comes from my friends and peers: Christian, Michael, Liam, Sarah, Hannah, James, Sophie, Eoin, Emily, Rosie, David, Iain, Gavin, Mylo, and everyone else in the group chat. You are all hilarious, wonderful people, who sometimes even gave me scientific advice, and my time at the University of Edinburgh would not have been the same without you.

Contents

List of Figures

List of Tables

Chapter 1

Introduction

Current estimates say that 75% of baryonic matter in the universe comprises of hydrogen atoms [179]. As such, hydrogen contributes hugely to the world we see around us. The most common isotope of hydrogen is the only atom on the periodic table to not contain neutrons: formed from a single proton and electron, it is the lightest element in the universe. Most of the hydrogen on Earth is within other compounds, as gaseous hydrogen is too light to be constrained by the Earth's gravitational field. Understanding the bonding behaviour of hydrogen is key to the study of many materials, including those important for biology and geology [64].

The low atomic number of the hydrogen atom makes its position difficult to measure using x-ray scattering techniques, which are commonly used to study the structure of materials. In order to obtain this information in hydrogenous materials, one must instead use neutron scattering. Whereas in x-ray scattering the x-rays scatter from the electrons in a system, neutrons scatter from the nuclei of the atoms. This results in the fact that, though hydrogen has the smallest visibility to x-rays, it has one of the largest for neutron scattering. Neutron scattering was first observed in 1936 shortly after the discovery of the neutron. However, it was not developed as a technique until the Manhattan project: the first neutron diffraction studies of gypsum and rocksalt were conducted in 1944 [120]. The techniques within neutron scattering have since been used to characterise many materials, including crystalline, amorphous and liquid samples, with hydrogenous materials counted amongst those studied.

This thesis consists of studies on three different systems using a variety of neutron

scattering techniques. Firstly, I present results about the dynamical behaviour of two methylammonium lead halides. Following this, I show data which expands ammonium fluoride's high pressure phase diagram. Finally, I describe the methane-water mixing dynamics at pressure. Despite their differences, the properties studied in these systems rely upon hydrogen bonding, illustrating the broad usefulness of understanding the physics behind this phenomena. The following sections in this chapter describe why these materials were chosen for study, and the aims for this thesis.

1.1 The Methylammonium Lead Halides

At the end of 2018, renewable energy provided an estimated 26% of the world's electricity, yet the world is still not on track to meet international climate and sustainable development goals [150]. In the last 10 years photovoltaic technologies have become the largest renewable power technology in terms of investment [122]. Silicon solar panels - the most commonly used on the market - are limited to a theoretical maximum efficiency of ∼29%, with the highest efficiency performance recorded so far of 26.7% [5], and as such there has been a large amount of interest in alternate solar panel materials. An example is organic-inorganic hybrid materials, which currently reach efficiencies of ∼22% in thin-film solar panels [79, 99] and are attractive because of their ease to manufacture.

Organic-inorganic hybrid materials are materials whose crystal structure incorporates both organic molecules and inorganic atom species. A well known example are the methylammonium lead halides, which are the material family of focus in this thesis. These materials adopt a perovskite structure, with the methylammonium (MA, CH_3NH_3) cation constrained within a cage consisting of halide and lead atoms, and a formula of $MAPbX_3$ with X as either bromine (Br), chlorine (Cl) or iodine (I). These hybrid materials are very similar in structure to the inorganic caesium lead halide family ($CsPbX_3$), but have been found to surpass them in performance as a photovoltaic material [193]. This then raises the question: what is it about the presence of the molecular species that causes the hybrid organic-inorganic material to be a better solar cell candidate material than the purely inorganic analogue?

A great deal of effort has been put into researching the methylammonium lead halides, with some studies focussing on the implementation of these materials into

solar panel devices and others aiming to understand the fundamental properties of the materials. In both cases, the choice of halide ion and molecular cation have proved to make a difference to various material properties, including the band gap [188], the material stability [28] and the phase diagram [8, 138]. The most efficient solar panel devices developed so far have exploited the effect of the halide ion on the material properties, using a mixture of halide ions in the compound to carefully tune the band gap [99, 130].

These materials exhibit a clear coupling between the inorganic and organic components. The MA molecule is constrained within the cage of inorganic molecules, and in turn is able to influence the surrounding inorganic atoms through van der Waals interactions and hydrogen bonding. As temperature is lowered, all of the members of the $MAPbX_3$ family exhibit multiple phase transitions: from a cubic state at room temperature in which the molecules are expected to tumble freely, through one or two tetragonal phases, and finally reaching a orthorhombic phase at low temperature in which the molecule is expected to have significantly fewer degrees of freedom [8, 138, 183, 184]. These phase transitions give the opportunity to further probe the relationship between the organic and inorganic components of the system through studying the properties of the material as these structural changes occur.

In this thesis, both methylammonium lead bromide ($MAPbBr_3$) and methylammonium lead chloride ($MAPbCl_3$) are studied using inelastic and quasielastic neutron scattering. These results provide information on the motion of the MA cation as temperature is reduced and the systems undergo phase transitions. In both compounds, the molecular dynamics begins to increase at the transition out of the low-temperature orthorhombic phase, continuing to grow throughout the short-lived tetragonal phase that is present in both compounds. A maximum in the molecular dynamics is reached upon transitioning out of this short-lived phase: in the case of $MAPbBr_3$ the system takes on another tetragonal structure, for $MAPbCl_3$ it is a cubic phase. Additionally, in $MAPbBr_3$ a second higher energy excitation appears in the short-lived tetragonal phase and persists to high temperatures, whereas no additional excitations appear in $MAPbCl_3$ upon transitioning out of the low temperature phase.

1.2 Ammonium Fluoride

Ice is a ubiquitous material in nature, both on Earth and further afield: it is a key constituent of many bodies within the solar system (including Neptune, Uranus, Titan, and Europa [72, 168]). As ice is so common, many studies have investigated its properties with the aim of better understanding more complex phenomena in which water plays a role. The phase diagram of ice has been intensely studied and to date 18 different crystal structures of ice have been reported [152]. The richness of the water phase diagram comes about due to the fact that its properties are governed by hydrogen bonding, rather than covalent or ionic bonding.

As in ice, hydrogen bonding strongly influences the structure of the ammonium halides. The ammonium halides are ionic compounds comprising of an NH_4^+ and a X^- ion, where X is fluorine (F), chlorine (Cl), bromine (Br) or iodine (I). The members of this family with smaller halide ions, such as F and Cl, have stronger hydrogen bonds due to the shorter bond lengths and higher electronegativity of the halide. As such the hydrogen bonding is more important in understanding their structures. In the case of a larger halide ion, the Coulomb forces due to the ionic nature of the system begin to dominate [135, 136].

Ammonium fluoride, NH_4F, has recently become of interest as its room temperature ambient pressure structure is analogous to ice Ic, the ambient pressure, low temperature, structure of ice [3, 100, 137, 180]. As such, the question arises as to whether the phase diagram of NH_4F is as rich as the phase diagram of ice with the application of temperature and pressure. If this is the case, this would make NH_4F an excellent candidate system for the study of hydrogen bonding and to inform better understanding of the behaviours of hydrogen bonded systems such as ice.

At present, the phase diagram of NH_4F has been predominantly studied by x-ray diffraction and Raman studies [3, 17, 31, 71, 100, 126, 137, 180, 194]. Neutron diffraction studies have been carried out on the three ambient temperature phases of NH_4F below 3 GPa [3, 71, 100]. However, no higher pressure neutron diffraction results exist in the literature to validate the observations made in x-ray diffraction studies and thus key details regarding the hydrogen positions at these pressures are missing. The four phases currently identified in NH_4F are all analogous to phases seen in ice [3, 31, 71, 100], though Raman scattering results suggest the existence of high pressure phases that have not

yet been observed by x-ray diffraction [17, 194]. This thesis presents neutron diffraction data that investigates the NH_4F phase diagram. These results will be supported by additional density functional theory (DFT) investigations and Raman spectroscopy. No new phases of NH_4F are identified beyond the four known phases. Rather, the signals previously identified as being indicative of a new phase are identified as being a result of deviatoric stress.

1.3 Methane-Water Mixing

Approximately 70% of the Earth's surface is covered in water, and it is the only planet in the solar system to have liquid water on its surface. However, many other planets and moons are thought to have liquid water deep beneath the surface: in particular both Titan and Europa are predicted to have large liquid water seas beneath the icy exterior. Titan has also been observed to have liquid and gaseous methane on its surface, suggesting a methane cycle similar to the water cycle on Earth [168]. Methane, water, and ammonia, and structures comprised of a combination of these, are often referred to as "planetary ices" due to their abundance on icy planets and moons. Many studies have been carried out studying the solid structures formed by these molecular species, in order to better understand the structure of planets [19, 43, 113]. Studies into the liquid states of these planetary ices are less common and almost exclusively focused upon the liquid behaviour of individual species rather than mixtures [4, 171]. In both the solid and the liquid phases of planetary ices, hydrogen bonding is the dominant interaction, and as such an understanding of the liquid mixtures can reveal information about the mechanisms for the formation of the solid compounds.

At pressures and temperatures relevant to the surface of the Earth, including at the seafloor, methane is in a gaseous state. As such, the interaction between gaseous methane and liquid water is relevant to understanding chemical processes on Earth, including the transport and use of natural gas for fuel. The theory describing the mixing behaviour of gases with liquids was first formulated by Henry in 1803. Henry's law states: "At a constant temperature, the amount of a given gas that dissolves in a given type and volume of liquid is directly proportional to the partial pressure of that gas in equilibrium with that liquid." [78]. From this, we would expect methane gas to mix with water more easily as pressure is increased. However, this is not the case: methane gas does

not mix with water until a pressure exceeding 1.5 GPa is reached, at which point mixing suddenly occurs [140, 141].

The mechanism behind this anomalous mixing behaviour is unclear. Methane is considered the simplest example of a hydrophobic molecule, meaning that the methane creates a void in which hydrogen bonds cannot form. To minimise the energy cost of these voids, this results in the clustering of the hydrophobic molecules, as is seen in the separation of oil and water. Though clustering is not observable in solid methane-water compounds, measurements show that the hydrophobic interaction is present within these, requiring high pressures of approximately 20 GPa to overcome and reach a strongly interacting state [153]. However, the mechanism for this hydrophobicity is little understood and depends on many energetic considerations, suggesting that there is some intrinsic change in the methane-water system at 1.5 GPa which causes the mixed state to become energetically favourable [140, 141].

Current studies of this methane-water mixing have previously been carried out using photomicrographs and Raman spectroscopy to identify methane rich and poor regions [140], and a more recent study has characterised the liquid structure of this system using neutron diffraction and simulations [141]. However, this provides little information regarding the dynamical behaviour of the molecules during mixing. In this thesis, experiments are carried out using quasielastic neutron scattering to characterise the rotation and diffusion of the water molecules before and after mixing. These results are much lower than those of pure water before mixing, and are in agreement after mixing. This difference can be explained by a large viscosity change across the mixing transition, which is expected due to the volume occupied by the bubbles in the mixture. The viscosity before mixing is slightly underestimated when only considering Brownian motion, so we also appeal to hydrogen bonding and hydrophobic interactions to justify this.

1.4 Thesis Outline

This chapter has provided a brief introduction for the techniques and systems to be studied in this thesis. Chapter 2 gives a broader context for this, describing the theory behind our understanding of material structures and the types of excitations that are observed. Chapter 3 builds on this foundation to expand the

background and motivations behind the selection of the three sets of materials for study, and explains the links between them.

Chapters 4 and 5 provide details about the experimental techniques used. Firstly, chapter 4 introduces the neutron scattering techniques to be used throughout this thesis: diffraction; inelastic scattering; and quasielastic scattering. Raman spectroscopy is explained as a complimentary technique. A brief introduction to the use of density functional theory for calculating structures is also given. Secondly, chapter 5 introduces the high pressure techniques used for the study of ammonium fluoride (chapter 7) and methane-water mixtures (chapter 8) .

The first of the results chapters, chapter 6, focuses on the studies of the dynamics of the molecule in methylammonium lead bromide ($MAPbBr_3$) and methylammonium lead chloride ($MAPbCl_3$). The behaviour of the molecular motions in $MAPbBr_3$ is characterised using inelastic neutron scattering, Raman spectroscopy, and quasielastic neutron scattering. In the study of $MAPbCl_3$ different quasielastic scattering instruments were used to carry out a broader study of the rotational and diffusional motions than was discussed for $MAPbBr_3$.

Chapter 7 presents the high-pressure study carried out on ammonium fluoride (NH_4F) to investigate its phase diagram. The key results for this chapter are derived from high-pressure neutron diffraction studies. Raman spectroscopy and density functional theory results are presented complementary to these.

The last of the results chapters, chapter 8, details the quasielastic neutron scattering study carried out on high-pressure methane and water mixing (CH_4-H_2O). This characterises the diffusional behaviour of the water molecules as pressure is increased.

Finally, chapter 9 presents a short summary of all the results found in this thesis, and makes some concluding remarks.

Chapter 2

The Structure and Excitations of Materials

Many of a material's properties find an origin in the arrangement of its atomic constituents, making the study of the structure of materials key to their understanding. The most fundamental example of this is the difference between the solid, liquid and gaseous phases of the same element. Under changing temperature and pressure conditions, multiple solid and liquid phases are achievable. In this thesis, the focus of the studies carried out is often on the excitations and dynamical properties of a material, but nonetheless this requires an understanding of the material's structure in order to fully contextualise. As such, this chapter begins with a discussion of how the structures of solids and liquids are defined. The key excitations studied in this thesis will then be explained. As the focus of this thesis is molecular systems, intramolecular excitations will be explored and how these are relevant to solid crystalline materials. Following this, the concept of diffusion will be explained, linking into the prior discussion of fluid structures. The existence of molecular diffusion in crystals will also be discussed.

2.1 Crystallography

A crystal is a specific type of solid, which is defined by its ordered repeating structure of atoms. This results in a long-range ordering, as any two points can

be linked by knowing the repeating structure of atoms. Mathematically, it is expressed as a convolution as follows:

$$Crystal\ structure = Lattice \otimes Basis, \tag{2.1}$$

where the basis is a structural unit of atoms which is regularly repeated and the lattice describes the overall shape, size and symmetry of this structural unit [36, 89, 160, 161, 187]. In order to fully describe the structure of a material both need to be fully defined, with the aim being to describe them in the simplest way possible.

The lattice mathematically describes the repeating symmetry in the crystal, describing the relation between any two points by translation vectors. For a 3D crystal, three primitive translation vectors are defined. The description of the translation vectors as primitive simply means that they are in their simplest form. Together the primitive translation vectors form a primitive unit cell, which is defined as containing only one lattice point. Because of this, the position of any point **T** on a 3-dimensional lattice can be described as a sum of the primitive translation vectors **a**, **b** and **c** [36, 89, 160, 161]:

$$\boldsymbol{T} = n_a\boldsymbol{a} + n_b\boldsymbol{b} + n_c\boldsymbol{c}, \tag{2.2}$$

where n_x are integers. It should be noted that it is sometimes convenient to not use the primitive unit cell, and instead describe the system with a larger unit cell. In particular, for some molecular species, larger unit cells are used in order to make the relative orientations of the molecules clearer. A special case of a primitive unit cell is a Wigner-Seitz cell, which describes the volume in space that is closer to one lattice point than any other.

An example of a generalised unit cell with sides of length a, b, c and angles α, β, γ is shown in Fig. 2.1. From these side lengths and angles the symmetry of the unit cell may be described. Seven key different crystal systems are defined from the symmetries of the unit cell. Table 2.1 shows these and the related symmetry requirements.

In the discussion thus far of crystal structures, we have simply been confined to a geometric description with no inclusion of how the atoms make up the material. This information is described by the basis. The different possible

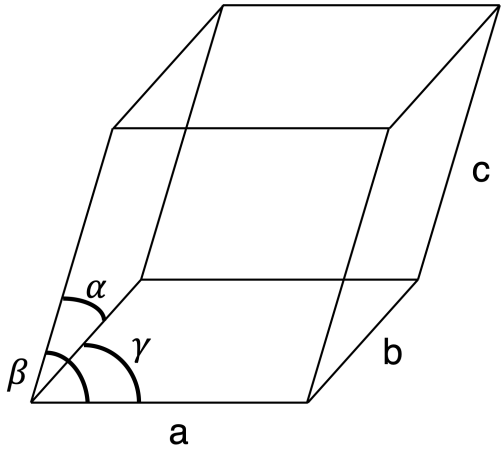

Figure 2.1 *A generalised unit cell, with sides a, b, c, and angles α, β, γ labelled.*

Table 2.1 *The seven different crystal systems, with restrictions on the dimensions and angles for each.*

Crystal system	Unit cell dimensions	Unit cell angles (°)
triclinic	$a \neq b \neq c$	$\alpha \neq \beta \neq \gamma \neq 90$
monoclinic	$a \neq b \neq c$	$\alpha = \gamma = 90$
orthorhombic	$a \neq b \neq c$	$\alpha = \beta = \gamma = 90$
tetragonal	$a = b$	$\alpha = \beta = \gamma = 90$
trigonal	$a = b = c$	$\alpha = \beta = \gamma \neq 90$
hexagonal	$a = b$	$\alpha = \beta = 90$, $\gamma = 120$
cubic	$a = b = c$	$\alpha = \beta = \gamma = 90$

positions of atoms within the unit cell result in the usefulness of further symmetry descriptions. Importantly, if the atoms are only positioned at the corners of the unit cell, it is referred to as a primitive cell and otherwise it is a centred cell. These two possibilities for each of the seven crystal systems result in fourteen Bravias lattices [89, 160, 161]. Further considerations of rotational and translational symmetry within the unit cell when the atoms are included result in a total of 230 space groups. The space group provides a full description of the symmetries within a crystal, and is the key information needed to describe a crystal structure.

As a crystal is mathematically described as an infinitely large structure of well defined symmetry, the identification of a single point within a crystal is not a useful exercise. However, the ability to talk about the positions of individual atoms within a unit cell and how they relate to neighbouring cells is useful. This is done by using Miller indices. Any plane within a crystal may be described by specifying three lattice points which it intercepts. The Miller indices are found by choosing an origin and defining the points on the **a**, **b** and **c** axes the plane intersects. The values h, k and l are the reciprocal values of these intercepts, and are chosen to be integers in their simplest form. The resulting Miller index is written as (h, k, l). Different notation is used to describe the plane normal to this, $[h, k, l]$, or a group of Miller planes that are equivalent due to symmetries in the system, $\{h, k, l\}$ [89, 160, 161].

2.1.1 Stress and Strain

In some conditions the crystalline lattice of a sample may become distorted. In high pressure systems, the application of force to cause the increase in pressure can be the cause of such a distortion. The force that is acting upon the sample is referred to as the stress and the strain is the deformation of the sample due to the stress. There are three primary types of stress: compressive, tensile and shear [36, 89]. Compressive and tensile stresses cause deformation in the direction of the applied force, whereas for shear stress this is not necessarily the case.

Distortions of crystalline lattice due to strain manifest in the data collected. As such it is necessary to quantify the stresses present in a system. In the region where a material's response scales linearly with an applied uniaxial force, Hooke's Law can be used. This relates the stress $\boldsymbol{\sigma}_i$ and strain $\boldsymbol{\varepsilon}_j$ through a matrix of

constants characteristic of the material:

$$\boldsymbol{\sigma}_i = \boldsymbol{C}_{ij}\boldsymbol{\varepsilon}_j. \tag{2.3}$$

The matrix $\boldsymbol{C}_{ij}$ describes the stiffness of the material, which in turn decrees the speed of sound in the material [20, 89, 159]. The inverse of $\boldsymbol{C}_{ij}$ is the elastic compliance matrix $\boldsymbol{S}_{ij}$, which is sometimes used to simplify equations. Note that in equation 2.3 the stress and strain are expressed as vectors when in reality they are matrices: this simplification is possible due to the symmetry of the matrices.

The Cauchy stress matrix is a generalised version of the stress used equation 2.3, which describes the stresses applied along all three axes:

$$\boldsymbol{\sigma} = \begin{bmatrix} \sigma_x & \tau_{xy} & \tau_{xz} \\ \tau_{xy} & \sigma_y & \tau_{yz} \\ \tau_{xz} & \tau_{yz} & \sigma_z \end{bmatrix}. \tag{2.4}$$

Here, the diagonal terms describe the compressive or tensile stresses (depending on their sign), and the off-diagonal terms describe the shear stresses [20, 36, 89]. The case where $\sigma_x \neq \sigma_y \neq \sigma_z$ is referred to as deviatoric stress. In the case of no shear stresses being applied, the stress tensor for deviatoric stress can be expressed as:

$$\boldsymbol{\sigma} = \begin{bmatrix} \sigma_P & 0 & 0 \\ 0 & \sigma_P & 0 \\ 0 & 0 & \sigma_P \end{bmatrix} + \boldsymbol{D}_{ij} = \boldsymbol{\sigma}_P + \boldsymbol{D}_{ij}, \tag{2.5}$$

where $\boldsymbol{\sigma}_P$ describes the principal stresses and $\boldsymbol{D}_{ij}$ is a matrix containing the deviatoric contribution (which may include off-diagonal terms) [159]. The principal stress acts only to change the volume of the material, whereas the deviatoric contribution acts to change its shape.

In the case of a stress being applied along a single axis of the sample $\sigma_x = \sigma_y \neq \sigma_z$ the uniaxial stress component $t = \sigma_z - \sigma_x$ is used to compare the stresses parallel and perpendicular to the applied force. The pressure dependence of t depends on the ratio between the applied shear stress and the strain response, which is referred to as the shear modulus G [159]. This is similar to the bulk modulus K, which describes the change in volume of the sample due to a uniform compression.

2.2 The Structure of Fluids

A fluid differs greatly from a crystal, because by definition the components in the fluid state are disordered. The term "fluid" encompasses both liquids and gases, which are distinguished by the fact that liquids have a definite volume while gases do not. The atoms or molecules in a gas can thus be separated by a large distance. The atoms or molecules within a liquid do not have significantly larger separations compared to those seen in crystals, but are still free to move around. It should be noted that glasses have a structure very similar to that of a liquid, but the atoms or molecules are fixed in position.

Despite the disordered structure, the intra-molecular interactions are the same throughout the fluid. In the more closely-packed case of liquids this results in molecular ordering over small length scales, due to a preferred alignment of the molecules. These correlations weaken as distance increases.

The structure of a fluid can be easily understood by choosing an origin particle in the fluid, then counting the number of particles at a distance r from this point. The equation for the average number of particles in a spherical shell of radius $r \to r + dr$ is:

$$n(r)dr = 4\pi r^2 \rho_0 g(r) dr, \tag{2.6}$$

where ρ_0 is the average number density and $g(r)$ is the pair distribution function [36, 58, 160]. Figure 2.2 gives a simple visualisation of $n(r)$. Integrating $n(r)dr$ gives the co-ordination number of the fluid, that is the number of neighbours a particle has within a set radius. One finds that simple liquids have well defined nearest neighbours, next-nearest neighbours and so forth. The radius enclosing all of the nearest neighbour particles is the first co-ordination shell.

This expression of the structure of a fluid through co-ordination shells means that the average environment of any point in the fluid is the same as that of any other point. In addition, it requires that fluids are spatially homogeneous and rotationally isotropic. This means that fluids have the highest possible symmetry - larger than that of any crystal [36, 58].

The pair distribution function $g(r)$ describes the probability of finding a particle at a distance r from a given origin, and can be extracted from diffraction data. Both crystals and fluids have a pair distribution function, which can be used

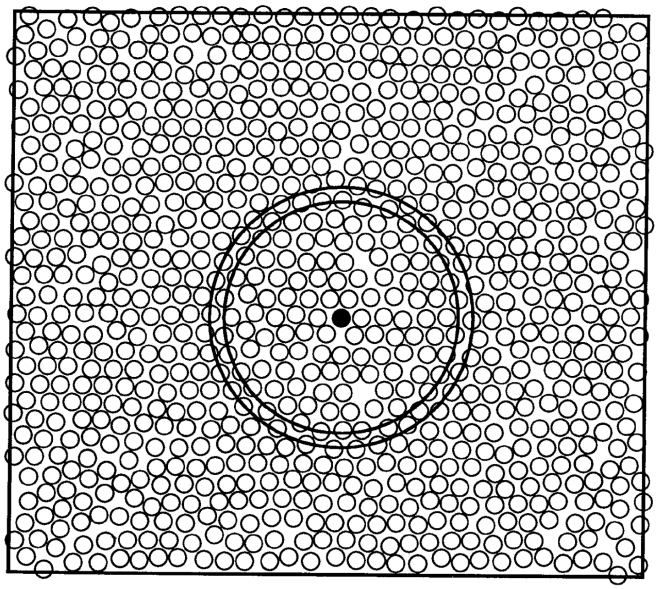

Figure 2.2 *Diagram showing the structure of a hard sphere liquid in 2D. The coloured circle is taken as the origin, and the number of atoms within a radius $r \rightarrow r + dr$ is counted. These radii are illustrated as the larger concentric circles. Figure adapted from reference [36].*

model the structure of the system from experiment. However, for the fluid the pair distribution function is significantly broadened due to the disorder and they are subject to different symmetry requirements.

2.3 Excitations

Having established the structural properties of materials relevant to the studies in this thesis, the associated excitations shall now be discussed. The key excitations to be discussed are: phonons and vibrational modes; and rotation and diffusion. These have been separated into two categories due to the differing nature of these motions. Phonons and vibrational modes are co-operative motions, in which multiple atoms move in tandem. Rotation and diffusion (as they are used in this thesis) are self motions, in which individual atoms and molecules are not coupled to their neighbours and are driven by their internal kinetic energy, though they still interact with their surroundings as they move. It is also possible for rotation and diffusion to be co-operative motions, with the species undergoing translational motion co-operatively. These different co-operative and self excitations require different approaches in measurement, which shall be discussed in chapter 4.

2.3.1 Phonons and Vibrational Modes

The most common type of crystalline excitation is the phonon, which is a vibration of the crystalline lattice. Phonons will not be studied in any detail in this thesis, however it is useful to understand them, as these concepts can be extended to other molecular excitations.

The classical approach to derive phonons is to consider an array of atoms, and characterise the interactions between them as springs. The displacement of an atom from its equilibrium position then causes a force to act on the neighbouring atoms according to Hooke's Law. Solving the equations of motion for this, one finds that the displacement of atoms has the form of a wave equation, giving a frequency and wavevector. In the quantum case, one considers the array of atoms as coupled quantum oscillators. This requires a quantisation of the frequency, and leads to the conclusion that only discrete phonon modes can be observed in a crystal [89, 160]. The number of phonon modes observed is dependent on the number of different types of atom in the system. Different types of phonons are caused dependent on whether the atoms move in phase (acoustic modes) or out of phase (optical modes), with the latter typically being higher energy [89, 160].

Similarly, the motion of atoms within a molecule can also be modelled by considering the bonds between atoms to be acting as springs. These are referred to as the vibrational modes of the molecule, or vibrons. The key difference between phonons and vibrons is that phonons are much longer range.

In general, if one neglects interactions with neighbours, a molecule existing in 3D space has $3N$ excitations, where N is the number of atoms in the molecule. Translational motion accounts for three of these excitations, and the others are linked to vibrational modes and rotation of the molecule. Figure 2.3 shows an example of the three vibron modes observed in a triatomic molecule such as H_2O, HF_2^+ or CO_2. These three key types of mode; symmetric and asymmetric stretching, and bending; are characteristic of all molecules with three or more atoms.

As in the case of phonons, these vibron modes are quantised with the energy of the excitation depending on the mass and potential of the atoms involved, i.e. the strength of interaction between the two species. For some molecules, the potential in which an atom rests is not parabolic and thus the oscillations are anharmonic.

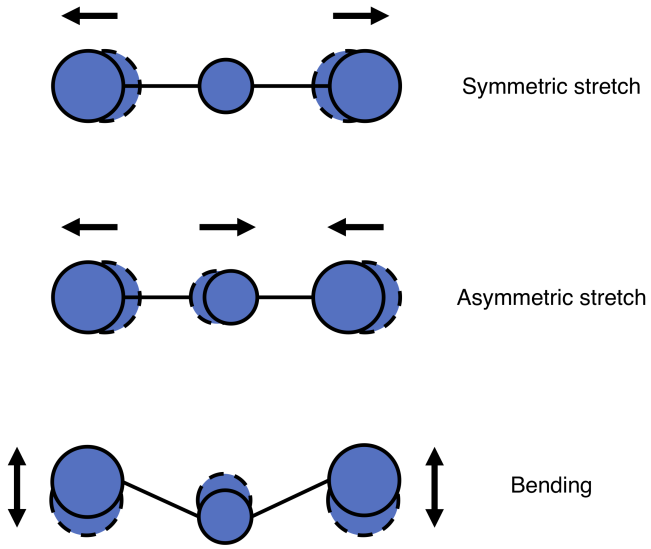

Figure 2.3 *Diagram showing the vibron modes that occur in a triatomic molecule: here a linear molecule, such as HF_2^+, is shown for simplicity.*

2.3.2 Rotation and Diffusion

In this section, diffusion and rotation will be described. Compared to phonons and vibrons, as discussed above in section 2.3.1, diffusion and rotation are not necessarily a collective motion. Rather, they can be either a collective or self motion depending on the phenomena involved. A single diffusion event is simply when an atom or molecule hops from one position to another. For a heavy species this will be a thermally activated motion, whereas for lighter species (hydrogen, for example) this can be due to quantum tunnelling. A collective diffusion excitation is when there are co-operative spacial and temporal density variations, so the diffusion of one particle affects that of its neighbours. For reasons that will be elucidated in chapter 4, this thesis is not concerned with collective diffusion.

Self-diffusion is simply the random walk of a particle within the medium. The random walk predicts that the root mean square distance travelled by a particle after N steps is $\sqrt{\langle l^2 \rangle} = \sqrt{N}$. We thus characterise the diffusion in a medium by the mean square distance travelled, and the time it takes for each step τ. The Einstein-Smoluchowski relation for the diffusion coefficient is true for both microscopic and macroscopic diffusion, and is a central coefficient of interest in

this thesis:

$$D_T = \frac{\langle l^2 \rangle}{6\tau}. \tag{2.7}$$

The subscript T here is used to denote this as translational motion [47, 58].

This coefficient of diffusion can also be used to describe the viscosity of a medium containing a larger species. This description is referred to as the Stokes-Einstein law:

$$D_T = \frac{kT}{C_S \pi a \eta}, \tag{2.8}$$

where a is the radius of the larger species, η is the viscosity of the medium, and C_S is a constant that depends on the choice of model. For example, in the original Stokes' equations $C_S = 6$, but was modified by Sutherland to be $C_S = 4$ for the case where the diffusing particle has the same radius as that of the particles in the medium [47, 58, 94].

The viscosity, or viscous stress, is defined as the rate of change of deformation of the fluid over time. Microscopically, this can be considered to be due to the relative velocities of the fluid particles. Viscosity is small for small velocity gradients, in which the particles may flow more unimpeded, and is hence inversely proportional to the coefficient of diffusion. The case of a suspension, in which a large radius species such as droplets or particles are placed into a medium, is of relevance to this thesis. The presence of the larger species acts to impede the motion and increase the viscosity of the medium. This comes from considerations of the Brownian motion of both of the species and the available volume to each. The viscosity of the medium can be calculated using the following equation derived by Batchelor [14]:

$$\frac{\eta_0}{\eta_s} = 1 + \alpha\phi + 6.2\phi^2. \tag{2.9}$$

Here ϕ is the volume fraction of the larger species, η_0 is the viscosity of the pure medium, and η_s is the viscosity of the medium in the mixture. The choice of parameter α is dependent on the nature of the larger species: in the case where hard spheres are placed into a medium $\alpha = 5/2$; in the case where the larger species is a gas bubble $\alpha = 1$ [125]. When the larger species makes up less than 1% of the mixture, one only need use the first order term to approximate the viscosity change.

The Arrhenius equation was formulated to describe the temperature dependence of reaction rates. It has been found to be true for both the diffusion coefficient

and the time for each step τ. For the diffusion coefficient one can thus write:

$$D_T = D_0 \mathrm{e}^{-E_a/k_B T}. \tag{2.10}$$

This requires the inclusion of an activation energy E_a for the diffusion event, which describes the energy barrier to be overcome to allow for the species to hop between positions. The term D_0 describes the diffusion coefficient that would be observed at infinite temperature, when the species would always have the thermal energy required to diffuse [58, 77]. When pressure is considered, this Arrhenius equation becomes:

$$D_T = D_0 \mathrm{e}^{-(E_a + PV_a)/k_B T}, \tag{2.11}$$

where the term V_a is the activation volume for diffusion, i.e. the minimal volume that must be available to the molecule for diffusion to occur.

The diffusion coefficient is important in the expression of Fick's Second Law, which describes the spacial and temporal dependance of the concentration φ:

$$D_T \nabla^2 \varphi(\boldsymbol{r}, t) = \frac{\partial}{\partial t} \varphi(\boldsymbol{r}, t). \tag{2.12}$$

Fick's Law will not be explicitly employed in this thesis, however it is worth noting because it explicitly considers continuous motion of the particles. In the case of strong interaction strength between the diffusing species, deviations from Fick's Law are observed though the definition of the diffusion coefficient still holds [77]. This results in jump diffusion behaviour, in which there is a second characteristic time wherein the diffusing species rests in place for a time between two diffusion events. These rest times follow a distribution rather than having a fixed value. Jump diffusion shall be discussed further in chapter 4.

The rotation of molecules is very similar to diffusion. Like diffusion, it is the motion of a species through a medium, and can occur through either thermal activation or tunnelling depending on the size of the atoms involved. However, a different coefficient of diffusion must be defined in the case of rotation, as in this case no mean square distance travelled can be defined. Instead, the coefficient of diffusion for rotation is simply defined in terms of the time τ_R taken for a complete rotation of the species [58, 77], as follows:

$$D_R = \frac{1}{2\tau_R}. \tag{2.13}$$

Analogously to jump diffusion, rotational motion can also be limited due to strong interactions of the molecule with its neighbours. In the case of strong interactions that render the molecule almost fixed in its orientation, the attempted rotational motions away from the fixed position are understood as librational modes.

Chapter 3

Background

The theme of this thesis is that all of the materials studied are molecular, or it is the molecules within them that are the point of interest. In this chapter the background for each of the materials to be studied will be given, with discussion of the techniques used to follow in chapter 4. First, the inorganic organic hybrid perovskites will be described, in which the molecule is confined within an inorganic structure of lead and halide ions. Following this, the known high pressure phase diagram of ammonium fluoride, another material with organic and inorganic components, will be presented. Finally, methane-water mixtures will be discussed: again this is to be studied at high pressures, but differs from the previous two systems in that it is purely molecular.

Hydrogenated molecular materials, like those studied in this thesis, pose different questions compared to non-hydrogenated materials. This is because the properties of these materials are strongly influenced by their hydrogen bonds. Hydrogen bonding is much weaker than covalent, ionic or metallic bonding, yet nonetheless it forms a key energetic consideration and has a strong influence in the structure of molecular materials. A prime example of this is the many high pressure and temperature forms of ice [4, 152]. As such, before the individual materials can be discussed, a full definition of hydrogen bonding must first be given. To contextualise this, a description of covalent, ionic and metallic bonding will be given first, as these will also have relevance within this thesis.

Covalent bonding is generally understood to be the strongest form of bonding. Here two atoms share electrons, resulting in a build-up of electron density between the atoms. As such, these bonds are highly directional, which contrasts with

metallic bonding, in which the shared electrons form a delocalised sea. In order to be bound together by the electron sea, metallic systems require a larger number of atoms than the two required for covalent bonding [161]. Like metallic bonding, ionic bonding is non-directional and is characterised by the Coulombic attraction between a positive and a negative charge. Thus ionic bonding can bond pairs of atoms as well as larger crystal structures [161].

Hydrogen bonding is a type of polar interaction, so like ionic bonding it is governed by the Coulomb force. In the case of hydrogen bonding, the positive and negative charges come about as the result of the hydrogen atom covalently bonding to a strongly electronegative element, such as fluorine, oxygen or nitrogen [161, 187]. This results in a slight positive charge on the hydrogen ion, which can then be bonded to a negative charge. As the existence of a hydrogen bond requires a covalent bond and a directional transfer of charge, hydrogen bonds are also directional. It should be noted that these polar behaviours do occur in systems which do not contain hydrogen, and even in non-polar molecules where temporary dipoles can form. These weak intermolecular non-bonded interactions are often referred to as van der Waals interactions, and are typically much weaker than hydrogen bonds.

It is found that hydrogen bonds come in a variety of strengths. The weakest form of hydrogen bonding is only distinguishable from van der Waals interactions by its directionality. The strongest hydrogen bonds typically form for oxygen-oxygen distances of between $\sim$2.4 and 2.55 Å [187]. These strong hydrogen bonds are typically the most symmetric, with the hydrogen atom being almost directly between the oxygen donor and acceptor. Longer, weaker hydrogen bonds are more asymmetric, with the hydrogen resting closer to the donating atom. A trend in the oxygen-oxygen distances joined by hydrogen bonds is also observed. When the hydrogen bond forms, if the unbonded oxygen-oxygen distance is greater than 2.55 Å the distance between them increases upon bonding, and the inverse is true for distances less than 2.55 Å [187]. Weaker hydrogen bonds may form what are known as bifurcated bonds, in which the hydrogen atom is simultaneously bonded to two acceptors. These bifurcated bonds can allow complex structures to form, and have been observed in solid hydrate systems [9, 69, 177].

It should be noted in this discussion we are considering hydrogen as a single proton. Deuterium, one proton and a neutron, does still form hydrogen bonds, but not in exact analogue to hydrogen. In general, deuteration does not change the distance between the donating and accepting atoms, but does cause

lengthening of short hydrogen bonds and increased asymmetry [4, 187].

3.1 The Methylammonium Lead Halides

The key phenomena exploited in solar cells is the photovoltaic effect, which is the generation of voltage and current in response to exposure to light. Solar cells are graded by their photovoltaic efficiency, defined as the percentage of the light incident upon them that is converted into electricity. The incident light excites electrons and holes in the photovoltaic material, which are then separated and act as the charge carriers in the material. As such, the band gap of any photovoltaic material must be comparable to the wavelength of visible light. The recombination time for the electrons and holes must also be large enough to allow for the charge to flow across the cell. The simplest solar cell design is a photovoltaic material attached to two electrodes, though more complicated cell designs have been developed [83, 154].

The methylammonium lead halides ($MAPbX_3$, with the halide as iodine, bromine or chlorine) have recently attracted a lot of interest due to their performance as photovoltaic materials. The first study on these materials was carried out in 1987 by Poglitsch and Weber, which characterised the structure of these materials with x-ray diffraction [138]. However, much of the research into the photovoltaic properties of these materials has been more recent: in particular there was much interest in $MAPbX_3$ after all-solid-state solar cell device architectures were developed in 2012 [44, 79]. The current highest efficiency reached for $MAPbX_3$ in one of these all-solid-state devices is $\sim$22%, using a $MAPbI_{3-x}Br_x$ thin film [79, 99]. This is comparable to the current highest efficiency of silicon solar cells, 26.7% [5]. Here, the focus will be solely on the single halide compounds.

All three of the materials in the $MAPbX_3$ family share the same high temperature cubic phase, however there are subtle differences between their phase diagrams as temperature is lowered. Figure 3.1 illustrates these differences. Notably: methylammoium lead bromide ($MAPbBr_3$) has an additional tetragonal phase [73, 138, 173]; and methylammonium lead chloride ($MAPbCl_3$) differs in its low temperature structure [41, 138]. The structure of the second tetragonal phase of $MAPbBr_3$ between 150 and 155K has been found to be more complex than the structure originally initially suggested from powder diffraction. Single crystal x-ray diffraction results obtained by Guo *et al* have shown that this phase is in

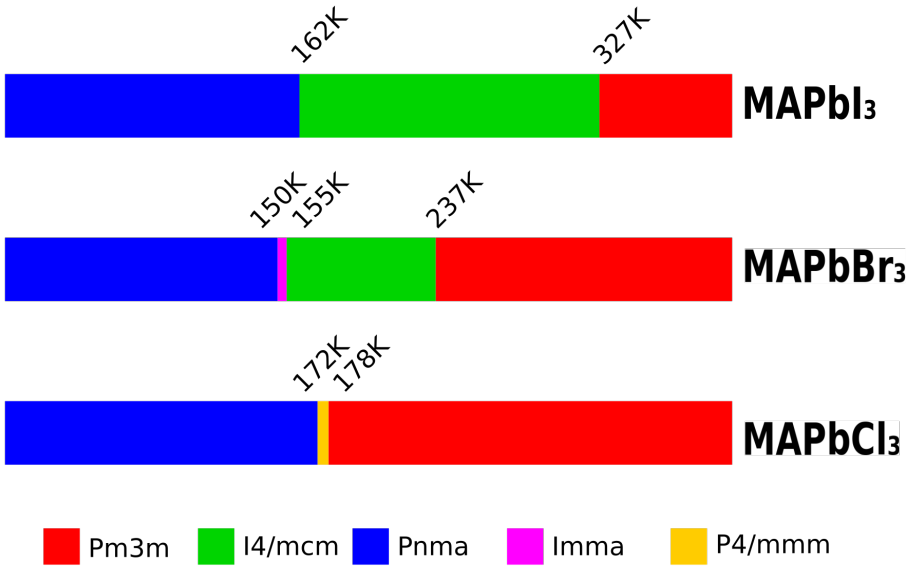

Figure 3.1 *The phase diagrams of the $MAPbX_3$ family with temperature [8, 41, 73, 84, 86, 119, 138, 174, 183, 184]. For the incommensurate phase of $MAPbBr_3$ the average structure is reported. Melting temperatures are neglected because the $MAPbX_3$ materials thermally decompose before melting occurs [28].*

fact incommensurate, with a modulation along the c axis [73]. Interestingly, single crystal x-ray diffraction experiments also identify the tetragonal phase of $MAPbCl_3$ to be modulated, but it does not have an incommensurate structure [86]. In this thesis phase II of $MAPbCl_3$ and phase III of $MAPbBr_3$ are often referred to as a "short-lived" tetragonal phase, as they are both only stable for less than 6 K. In their 1987 paper, Poglitsch and Weber identified the low temperature structure of $MAPbCl_3$ as having two possible orientations of the MA cation, as opposed to the single orientation enforced in $MAPbBr_3$ and $MAPbI_3$ [138], though their x-ray results did not show this clearly. Since then, neutron diffraction studies have supported this conclusion, finding the low temperature phase is best fitted by a symmetry group which allows for two cation orientations [41]. Figure 3.2 shows the low temperature orthorhomic phases of $MAPbBr_3$ and $MAPbCl_3$ as viewed along the **b** axis, illustrating the different cation orientations available in the two compounds.Finally, it is relevant for the following discussion of photovoltaic properties that methlyammonium lead iodide ($MAPbI_3$) is in the tetragonal phase at room temperature, while the other two are in the cubic phase.

The behaviour of all of these materials as temperature is decreased is characterised

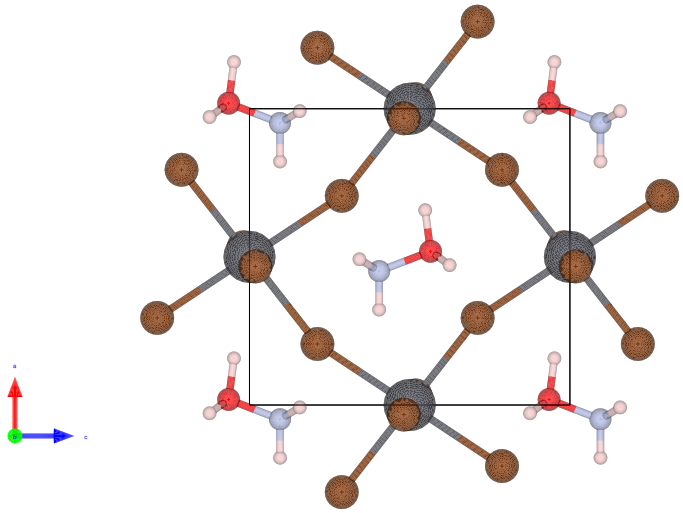

(a) *$MAPbBr_3$ phase IV [174]*

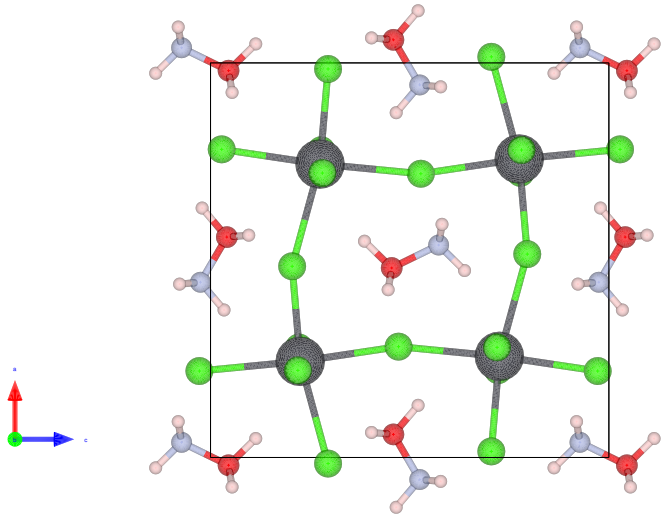

(b) *$MAPbCl_3$ phase III [41]*

Figure 3.2 *Diagrams showing the low-temperature othorhombic phases of $MAPbBr_3$ and $MAPbCl_3$, viewed along the* **b** *axis in order to best see the shape of the inorganic cage and the orientation of the MA cation.*

by a gradual locking-in of the MA cations. In the high temperature cubic phase the structure is that of an undistorted perovskite, with perfect octahedral configuration of the inorganic PbX_3. Then, as temperature is decreased, these octahedra rotate and tilt, in order to reduce the space between them [8, 41, 87, 119, 138, 174]. As such, in the high temperature phase the molecular cation is understood to be orientationally disordered in the cages, then as the cages collapse the available alignments of the molecule are reduced [111, 118, 149, 183]. In the lowest temperature phase, the molecules are suggested to align in a preferred orientation along the [110] crystalline direction [174, 184].

The positive charge on the MA cation is not equally distributed, rather it is associated with the NH_3 group. As such, it has been suggested that the preferred orientation of the cation (in particular in the low temperature phases of $MAPbI_3$ and $MAPbBr_3$) may result in domains in which all of the NH_3^+ groups align. This could result in a ferroelectric effect, in which there is a spontaneous electrical polarisation of the sample. Simulations have predicted the existence of such charged domains [103, 182], however experiments have found that the overall bulk material is not ferroelectric [147]. As a requirement of ferrelectricity is that the material has inversion symmetry, this implies that the $MAPbX_3$ compounds are centrosymmetric, though this may be broken locally resulting in the domains observed in calculations.

While the structural transitions in the $MAPbX_3$ family can be understood from the displacive motion of the octahedra, the presence of the molecule cannot be overlooked. The molecule forms hydrogen bonds with the lattice around it, both in the high temperature disordered and low temperature ordered phases [88, 101, 102, 190]. This means that the octahedra and molecules are coupled, and as such it is necessary to consider both to fully predict and euclidate the phase transitions of these materials.

In the above discussion, the molecule has been assumed to be stationary and fixed in position. However, multiple studies have shown that the molecule is tumbling within the cages. In particular, the molecular dynamics in $MAPbI_3$ have been probed using NMR, inelastic neutron scattering, quasielastic neutron scattering and DFT. The literature on $MAPbBr_3$ and $MAPbCl_3$ in this area is significantly more sparse. Studies have shown that the molecular cation in $MAPbI_3$ tumbles more unimpeded in the high temperature phase, and is slowed to 'glassy' dynamics at low temperatures [26, 53, 63, 103, 106]. At low temperatures the primary contribution is from the hopping of the hydrogen atoms between their

positions on the CH_3 group and on the NH_3^+ group [103, 106]. The full-body motion of the molecule activates at higher temperatures and is found not to be a smooth rotation on a sphere. Quasielastic neutron scattering results show that the molecule jumps between preferred orientations, with the time between jump on the order of tens of picoseconds [103]. The NMR spectra of $MAPbI_3$ near the cubic to tetragonal phase transition shows a different relaxational time for the two components of the molecule, the CH_3 and NH_3^+ groups, which the authors associate with an larger hydrogen bonding between the NH_3^+ and inorganic framework than between the CH_3 and framework [8]. Indeed, the hydrogen bonds between the molecule and the surrounding structure remain of great import when considering the molecular tumbling. The motion of the molecules does impact the surrounding structure on a short timescale, even at low temperatures: the hydrogen bonds between the molecule and inorganic octahedra cause the lighter halide atoms to move and distort the octahedral structure [26].

The presence of the molecule is key to the photovoltaic properties of these materials. The increased carrier lifetimes seen in the $MAPbX_3$ compounds compared to their inorganic analogue $CsPbBr_3$ have been associated with the motion of the molecules. Electron-phonon coupling in materials serves to reduce the carrier mobilities, by reducing the average path length through scattering of carriers from lattice vibrations. Many studies have been carried out to characterise the phonon spectrum of the $MAPbX_3$ compounds, to which the molecules do contribute [165, 173, 188]. However, theoretical calculations and photoluminescence measurements have concluded that the motion of the molecules acts to protect the charge carriers, lengthening the amount of time it takes for recombination to occur [39, 124, 193]. This occurs because the molecule is able to reorient to screen the electron-phonon coupling, resulting in an effective repulsion between the electron and hole charge carriers. The anomalously large spin-orbit effects observed in the $MAPbX_3$ family are also linked to the high photovoltaic performance of these compounds [62, 128]. This large spin-orbit effect acts to reduce the carrier masses, thus increasing their mobility. The spin-orbit effects have been linked to breaking of inversion symmetry within the crystal, but not explicitly with the behaviour of the molecule. This links with the previously discussed ferroelectricity and presence of domains in the sample. The band gaps of these materials are found to be linked to the structural distortions of the crystal structure [38, 48, 66, 144, 188] which is dependent on the hydrogen bonds formed between the cation and inorganic surroundings.

While the $MAPbX_3$ family has been heavily studied, these studies have been primarily focussed on $MAPbI_3$, leaving gaps in the literature for $MAPbCl_3$ and $MAPbBr_3$. The changes in phase diagram across this family implies that the physics underlying the key photovoltaic properties may also be changing. The increased photovoltaic efficiency in $MAPbX_3$ compounds where multiple halide ions are present makes the full understanding of each of the individual halide compounds important. The studies in this thesis aim to fill this gap for the molecular reorientations studied by QENS techniques.

3.2 Ammonium Fluoride

When one discusses hydrogen-bond dominated systems, the conversation would not be complete without the inclusion of water. As one of the most common substances on the surface of the Earth, and as a key component of numerous planetary bodies, H_2O has been studied from many angles throughout the history of science [152]. However, though it is extremely common, its phase diagram under pressure and temperature conditions is still not yet fully understood. There are currently 18 reported crystal structures of ice, as well as multiple amorphous forms and gas inclusion clathrate hydrate structures [4, 29, 113, 152].

The structures of ice are dominated by the hydrogen bonding between the molecules. Each water molecule is capable of participating in four hydrogen bonds simultaneously, donating two and accepting two, leading to a tetrahedral geometry around the oxygen atom. Any given nearest neighbour oxygen pair is then linked by a single hydrogen bond. These are the so-called "ice rules" which apply to all of the molecular water phases. This simple geometry gives rise to a wide range of interesting phenomena: the rich phase diagram of water, the ability to empty clathrate hydrates of the guest species to produce new metastable structures of ice, and the effects of other species on the phase transitions and ordering of the solid ices [4, 152].

In this thesis, we are aiming to characterise the structure of NH_4F because of its analogous structure to ice Ih in its ambient temperature and pressure phase. However, this is not the reason why NH_4F was historically originally studied. The ammonium halides, NH_4X with X = Cl, Br, I and F, were originally of interest due to their recorded polymorphism in the group, with the Cl, Br and I compounds being more commonly studied [13, 25, 105, 167]. In the inorganic analogues of

NH_4X, potassium and sodium halide (KX and NaX), the crystal structure for all of the halides is the same due to the cubic symmetry of the positive ion, with all of them adopting a NaCl structure [13]. Conversely, in the ammonium halides different structures are found: the orientation of the tetragonal ammonium ion is able to vary, meaning that multiple cubic structures are possible. In particular, both NaCl and CsCl-like structures are seen in the Cl, Br and I compounds [13, 24, 105, 167]. In NaCl the positive ion has six halide nearest neighbours, whereas in CsCl the positive ion has eight halide nearest neighbours [24].

By applying pressure and varying the temperature, it is possible to find a NaCl-like structure (sometimes referred to as the α phase), and three CsCl-like structures (known as the β, γ and δ phases) in ammonium chloride, bromide and iodide. The phase diagrams have often been drawn together, showing how the transition routes between these four cubic phases is common to the three compounds [135, 167]. This also illustrates the analogy between chemical and mechanical pressure. However, the combined phase diagram has since been discredited for numerous reasons. Firstly, an additional fifth phase (CsCl-like in nature) was discovered in NH_4Br which, from the combined phase diagram, would be expected in NH_4Cl but is not observed there[136]. Secondly, the combined phase diagram does not correctly describe the nature of the ordering in the analogous phases of the different compounds [136]. Additionally, a fifth phase has been since discovered in NH_4I above 9 GPa at room temperature [81] and a recent study on NH_4Br also identified a sixth phase at pressures above 57.8 GPa, neither of which have been reported in any of the other ammonium halides [82].

Ammonium fluoride is not NaCl-like or CsCl-like in its ambient phase. Instead it adopts a hexagonal zinc-blende structure which is not seen in the phase diagrams of the other ammonium halides [3, 100, 137, 180]. The phase diagram of NH_4F under pressure was first studied much later than those of the other ammonium halides, with four phases identified from measurement of volume changes [97, 135]. This phase diagram is shown in Figure 3.3 with details given in Table 3.1. Figure 3.4 then informs in more detail on the structures, with two views of NH_4F phase II presented, as this is a larger more complex structure. The structure of the room temperature phases I, II and III have been measured with both x-ray and neutron diffraction [3, 17, 71, 100, 126, 137, 180], and the high temperature phase IV identified through x-ray diffraction only [31]. This difference in the structures of the ambient temperature and pressure phases is ascribed to an increase in hydrogen bonding in ammonium fluoride compared to the other ammonium

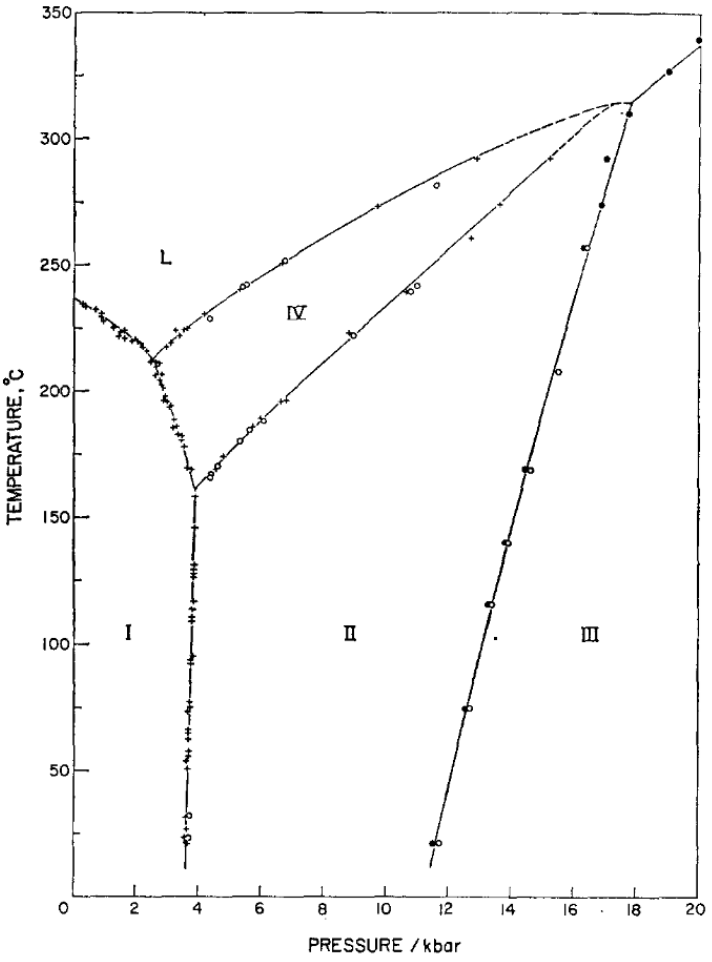

Figure 3.3 *The phase diagram of NH_4F up to* 2 GPa *and* 350 °C *(*623 K*) from Kuriakose et al [97].*

halides. This is evidenced by the low N-H stretching frequency and high H-N-H bending frequency in IR scattering [137]; the high activation energy for molecular reorientation calculated from NMR results [52]; a large value of the librational modes in Raman scattering and inelastic neutron scattering [2, 70]; and more recently the hydrogen bonds were directly observed through neutron Compton scattering [12]. However, one theoretical study was able to reproduce the structure of phase I of NH_4F without invoking hydrogen bonding, and only including electrostatic, van der Waals and repulsive interactions [146].

As has been previously mentioned, the phase I of NH_4F has a zinc-blende structure and is analogous to ice Ih, with a disordered hydrogen bond network [3, 100, 137, 180]. This phase is shown in figure 3.4a, though the hydrogen disorder is neglected in the diagram for clarity. Phase II adopts a rhombohedral structure that is analogous to ice IV, a metastable form of ice, again with a disordered

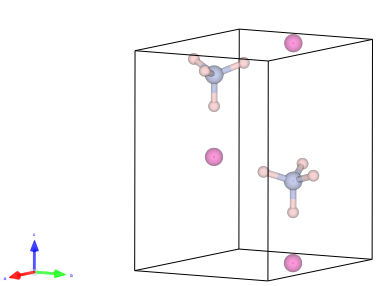

(a) *NH_4F phase I [100]*

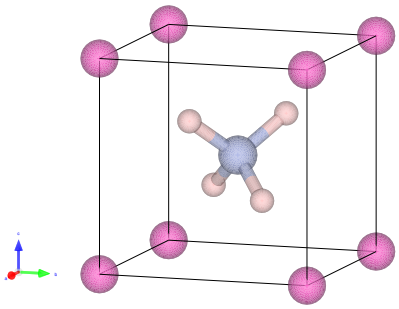

(b) *NH_4F phase III [17]*

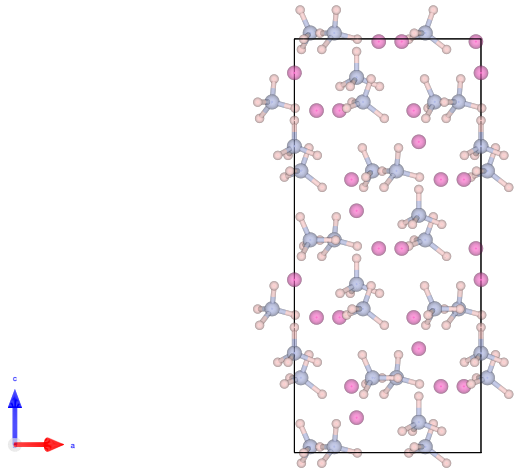

(c) *NH_4F phase II along* **b** *axis [100]*

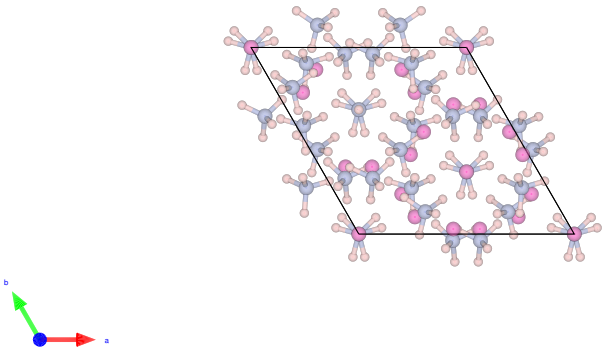

(d) *NH_4F phase II along* **c** *axis [100]*

Figure 3.4 *Diagrams showing the room temperature phases of NH_4F.*

Table 3.1 *Structural information from literature for the known NH_4F phases.*

Phase	Space Group	NH_4F Units	Lattice Parameter (Å)	Measurement Conditions	Reference
I	$P6_3mc$	2	$a = 4.436$ $c = 7.158$	0 GPa, 300 K	[100]
II	R3c	24	$a = 8.508$ $c = 16.337$	0.469 GPa, 300 K	[100]
III	$P\bar{4}3m$	1	$a = 3.350$	0 GPa (from EoS), 292 K	[17]
IV	$Fm\bar{3}m$	4	$a = 5.770$	0.4 GPa, 450 K	[31]

hydrogen bond network [100, 126]. This is shown in figures 3.4c and 3.4d, again with the hydrogen disorder not plotted. Lawson *et al* compare the two phases by considering the tetrahedra formed by the fluorine ions: in phase I these tetrahedra are all aligned, whereas in phase II there are two types of tetrahedra, one with a three-fold symmetry and the other noncentrosymmetric [100]. These multiple types of tetrahedra in phase II allow for a significantly improved packing along the c-axis in phase II compared to phase I.

Phases III and IV of ammonium fluoride are both structures that are seen in the other ammonium halides. The high temperature phase IV is an NaCl structure, can be considered as an ice Ic analogue, and is expected to be hydrogen disordered [31]. Interestingly, this phase is reported to be more plastic in ammonium fluoride than in any of the other ammonium halides. The high pressure phase III of NH_4F has a CsCl-like structure. This phase has been reported as both hydrogen ordered [71] and disordered [17], which would make it either an ice VII or ice VIII analogue respectively. The hydrogen ordered structure of this phase is shown in figure 3.4b. The most complete equation of state for phase III was established by Bellin *et al*, identifying it as being Murnaghan third order with $V_0 = 37.595\,\text{Å}^3$, $K_0 = 33.9\,\text{GPa}$ and $K' = 4.1\,\text{GPa}$ [17].

Additional to the four commonly accepted phases of ammonium fluoride, others have been observed through various methods. A Raman study carried out by Zou *et al* reports two additional phases at room temperature as pressure increased [194], with one transition from phase III into a new phase V reported at 1.5 GPa and a second transition to a new phase VI at 14.3 GPa. This result was then used in other Raman and theoretical studies [151, 191], however these new phases are expected to appear in regions that have been investigated through neutron and x-ray diffraction studies but have not been observed. Nabar *et al* identified three new phases through the heating of recovered samples of phase II and phase

III [126]. These new phases were studied through x-ray diffraction: two of these phases were identified as CsCl-like cubic, though the hydrogen positions could not be identified; and the third had a complicated structure that could not be solved from the diffraction pattern. Finally, a recent x-ray and Raman study by Bellin *et al*, which was able to probe higher pressures than any of the previous studies, reported a low-temperature tetragonal phase above 10 GPa [17]. In addition to this, their room temperature Raman results showed changes at approximately 10 GPa and 25 GPa, with a possible third change at 6 GPa, however their x-ray diffraction results at these pressures did not show any changes.

This thesis aims to resolve some of these contradictory observations regarding the structure of NH_4F, by completing neutron diffraction experiments at higher pressures than have previously been probed.

3.3 Methane-Water Mixing

Experiments on the behaviour of gases have been carried out since the 17th century, with Boyle's Law relating the relationship between pressure and volume of a gas published in 1662 [23]. The links between pressure and volume, and volume and temperature of a gas, and the mixing behaviour of gases were then expanded upon in the early 19th century [68, 78]. In this thesis we aim to study the behaviour of methane gas as it is pressurised with liquid water, and the two begin to mix together.

William Henry was the first to produce a general theory for the mixing of liquids with gases in 1803. The law, as stated in his original paper, is as follows:

> "...that water takes up, of gas condensed by one, two, or more additional atmospheres, a quantity which, ordinarily compressed, would be equal to twice, thrice, etc. the volume absorbed under the common pressure of the atmosphere." [78]

This has since been expanded to apply to any liquid, not just water, and to account for the effects of temperature. In the modern understanding, the general statement of Henry's original conclusion remains true: that the mixing behaviour of gases goes linearly with the pressure of the gas upon the surface of the liquid. The constant of proportionality linking the pressure with the mixing is called

Henry's constant.

It is of relevance to this thesis to note that in his original paper Henry follows his declaration of his law with the following statement:

> "By frequent repetition of the experiments, I obtained results differing a little from the general principle above stated; but, for all practical purposes, I apprehend, the law has been announced with sufficient accuracy." [78]

Henry attributes these deviations in his data from the general law to problems with his experimental setup. Henry's law is still commonly used in chemical processing and environmental sciences, with Henry's constant calculated for more than a thousand compounds mixing with pure water [115]. However, a recent study has suggested that the mixing of methane with water does not follow Henry's Law [140].

Ignoring intra-molecular interactions, the mixing of gases and liquids can be understood simply by considering the boundary between the two phases. A gas molecule that hits the boundary may be absorbed into the liquid phase, or it may deflect away again back into the gas. As pressure is increased the number of gas molecules at the boundary increases, and thus more of the gaseous species will enter into the liquid.

Thermodynamically, there are multiple contributions to be considered in mixing processes. The entropy and enthalpy of the system influence the mixing of the species: in particular entropy strongly opposes the mixing of uncharged species in water at low temperatures [50, 158]. In the case of methane, the intra-molecular interactions also become relevant, complicating this picture of gas mixing. Methane is the smallest example of a hydrophobic molecule, meaning that it excludes a volume so hydrogen bonds cannot occur and the water network doesn't form through this space [37]. Studies on the dynamics of water molecules surrounding a hydrophobic species have found that the reorientation speed decreases, suggesting that their motion is impeded by the volume excluded by the hydrophobic molecule [9, 177]. From a thermodynamic perspective, the mixing of hydrophobic species in water is enthalpically favourable, but, like the solution of uncharged species in water, is opposed by a loss of entropy at low temperatures [9, 54, 185]. Structurally, the changes in the water network due to the addition of a hydrophobic species are more unclear: traditionally a so-called

"iceberg model" was used to describe the formation of a water structure with more or stronger hydrogen bonds thought to form around the hydrophobic molecule. However more recent theoretical studies have questioned its existence [9, 185].

Pure water is suggested to have at least two liquid structures: a low density and a high density form, which by association implies the existence of multiple glassy phases of ice [4, 42, 110, 170]. The molecules in the liquid phase of water are constantly re-ordering, hydrogen bonds breaking and reforming. This is evidenced by the fact that the H_2O molecules in liquid are found to have an average of 3.3 hydrogen bonds at any given time, as opposed to the expected 4 in a crystalline solid [162]. The motion of the water molecules can be probed experimentally using multiple techniques; here, the focus will be on results from neutron scattering, as this is the key technique in this thesis.

Most of the early dynamical studies of water were interested in the changes in dynamics due to changing temperature, including the supercooling of water to below its freezing temperature [4]. Two characteristic times have been identified in the dynamics of liquid water from quasielastic neutron scattering; one linked to the rotational dynamics, and the other to the translational diffusion of the molecules [22, 109, 145, 175]; whereas solid water only exhibits a single rotational excitation [21]. Results from low temperature studies have confirmed that the rotation of the molecule is best understood as a jump of the hydrogen atoms between the tetrahedrally co-ordinated bond sites, i.e. the breaking and reformation of hydrogen bonds [175]. The temperature dependence of the translational diffusion has been studied at low pressures, and have found that it is strongly temperature dependent even when there are no changes in structure, and is instead linked to the viscosity of the liquid [94]. A higher pressure study has been carried out on the dynamics of liquid water, which reported that this jump rotation does not vary as pressure is increased, but the translational diffusion strongly decreases [22].

Studies of mixing salts into water, with the salt as a polar solvent, have yielded some interesting results regarding the mixing behaviour of water. The addition of salts has been seen to not influence the rotational dynamics of water molecules within the bulk, only the behaviour of those water molecules within the first solvation shell of the salt [131]. Additionally, the tetrahedrality of the water molecule averaged across the system was observed to be reduced upon the addition of a salt, in the same way that it is affected by the application of pressure or increase of temperature [129]. These results are interpreted to support the

notion that there are at least two structural types of water, with the bulk of the liquid having one structure, and the water molecules surrounding the solvent adopting a different one.

Similar to water, the quasielastic neutron scattering results on pure methane are also understood through two characteristic times, one for the rotation and the other for the diffusion of the molecules [49]. However, in the case where the methane molecule is incorporated into the solid water structure to form a clathrate hydrate, wherein the methane molecules are surrounded by cages formed by the water network, these results change. Studies on a sample of seafloor methane clathrate reveal that the translational diffusion is completely hindered, but three different types of rotation were seen, with the methane molecules behaving as almost-free rotors [76]. However, a high pressure result on a different crystal structure of methane clathrate reports that above approximately 20 GPa the methane molecules become strongly interacting with the water network and their rotation becomes coupled [153]. As such, this was identified as the pressure at which the hydrophobic nature of the methane molecule was overcome. Translational diffusion within a solid methane clathrate sample was found to be possible if two different methane clathrate structures coexisted, in which case the motion was best fitted by a jump diffusion model, meaning that the methane molecules did not travel continuously along the boundary between the structures [148].

Few studies have been carried out on the mixing of methane and water at pressure. Price *et al* studied the region of temperature between 150 °C and 350 °C, with pressures up to approximately 0.2 GPa, and found the expected linear mixing behaviour in this region [139]. This was later expanded up to 3.2 GPa at 100 °C by Pruteanu *et al*, who used Raman spectroscopy and photomicroscopy to find that the mixing behaviour deviated from linear at approximately 1.5 GPa [140]. More recent neutron diffraction investigations by Pruteanu *et al* have established that a hydrogen bonded network exists at all pressures throughout the mixing transition [141]. Instead, evidence is presented showing that the dipole moment of the methane molecules increases with pressure, showing that the electronic interactions have a strong influence on the miscibility. However, diffraction experiments alone do not provide a full picture of the system. Other properties must also be studied to allow for a complete comparison between the liquid and individual species. As such, this thesis will present results as to the dynamical properties of the liquid mixture as pressure is increased.

Chapter 4

Scattering and Other Techniques

This chapter will discuss the experimental techniques used in this thesis, primarily focussing on neutron scattering techniques. In addition to neutron scattering, Raman spectroscopy is also used as an experimental technique in chapters 6 and 7. This technique shares some fundamental physics with neutron scattering, as it comprises of the scattering of laser light from the sample. Finally, the background for the density functional theory (DFT) calculations described in chapter 7 are explained.

Due to the principle of wave-particle duality, the scattering of light, neutrons and electrons is understood from the same perspective of fundamental wave mechanics. In the below description of scattering, neutrons shall be used as the example, but the discussion holds for all of the other examples given.

By treating the incident neutrons as waves, we can consider them as a plane wave which is scattered spherically upon interaction with an obstacle. If there are multiple centres from which to scatter, the spherically scattered waves will interfere with one another to produce interference patterns. The interference observed depends on the relative phases of the scattered waves. In the case where all of the scattered waves are have a fixed phase relationship, this is referred to as coherent scattering. This provides information regarding the structure and any co-operative dynamics of the scattering samples. When the resulting scattered waves have no constant phase relationship this is called incoherent scattering, and provides information as to the self-dynamics of the scattering centres.

The scattering triangle, shown in Fig. 4.1, describes the momentum and direction

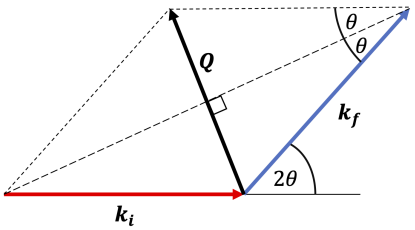

Figure 4.1 *The fundamental scattering triangle used in all scattering experiments (neutron, x-ray, electron, etc.).*

changes during a scattering event. The incident neutron has a momentum $\mathbf{k}_i$, then after scattering has momentum $\mathbf{k}_f$, where $\mathbf{Q}$ is the vector that connects the two, and the angle between the two momenta is defined to be 2θ. If $|\mathbf{k}_f|$ is fixed to be equal to $|\mathbf{k}_i|$ there is no momentum transfer between the neutron and the sample: this is called elastic scattering and reveals information about the structure of the sample. It should be noted that incoherent elastic scattering is isotropic, so only coherent scattering is useful. This is discussed further in section 4.1. In the case of $|\mathbf{k}_f|$ different to $|\mathbf{k}_i|$, there is a momentum transfer between the probe and the sample, which can be associated with the excitations within the sample. This is called inelastic scattering, and is discussed in sections 4.2 and 4.3. Here both incoherent and coherent inelastic scattering may provide useful information. It should be noted that inelastic scattering of neutrons is easier to measure than that of photons, as the finite mass of the neutrons results in a momentum change that is easier to detect.

The strength of the interaction between the probe and the scatterer is called the scattering length, and this decrees the probability that the probe will scatter from a scattering centre of this type. For the case of x-rays and light, the probe scatters from the electron cloud surrounding the atom. As such, the scattering length is proportional to the square of the number of electrons. Neutrons interact both through the weak and the electromagnetic force. The interactions through the electromagnetic force allow for the magnetic properties of the sample to be probed, but do not affect the scattering length. Therefore the weak force interactions decree the scattering length, which means that the degree to which neutrons scatter from different elements is more complicated and allows for isotopes of the same element to be distinguished. Importantly, it means that the coherent and incoherent scattering lengths of the same element may be vastly different. Figure 4.2 shows the coherent neutron scattering lengths of the elements, with the isotope variance shown for four cases. The sign of the

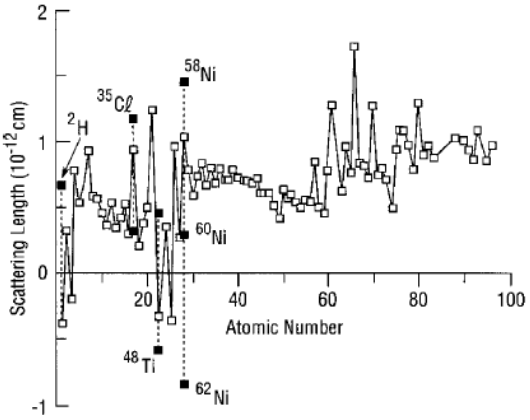

Figure 4.2 *The coherent neutron scattering lengths of the elements, with the isotope variance of scattering length shown for hydrogen, chlorine, titanium and nickel. Adapted from reference [157].*

scattering length indicates whether the incident and outgoing waves are in or (180°) out of phase [160]. Additionally, there is an imaginary component to the scattering length which originates from the probability for the neutron to be absorbed into the nucleus, but this is normally small.

In scattering experiments, it is only possible to analyse the data if the assumption can be made that the neutron only interacted with the sample once as it passed through. However, for samples with large scattering lengths the incident neutron may scatter twice or more as it passes through the sample. It is thus important to design the experiment such that multiple scattering events are reduced to an acceptably low level. This is commonly done by using thin samples, the large surface area of which exposes it to a large amount of incident beam, but the low thickness means that the incident neutrons pass through the sample in a short amount of time.

4.1 Diffraction

The key mathematical object that summarises a scattering experiment is the differential cross section, which expresses the number of incident particles that are then scattered to a certain direction (in spherical polar co-ordinates). The scattering lengths are measured in barns (b). For a elastic scattering experiment, where there is no energy transfer between the probe and the sample, this is

described mathematically as:

$$\frac{d\sigma}{d\Omega} = \frac{R(2\theta, \phi)}{N\Phi\Delta\Omega}, \tag{4.1}$$

where Ω is the solid angle, R is the number of neutrons measured at a given angle (in 2θ and ϕ), Φ is the incident flux, and N is the number of scattering units of interest (for instance atoms or molecules) [160]. This form for the differential cross section is the most basic, in that it assumes the incident neutrons are scattered isotropically from the sample, and thus the angle at which the final neutrons are measured do not contain any structural information about the sample. Equation is 4.1 therefore only appropriate to describe the elastic scattering from a single atom, or the incoherent elastic scattering from an array of atoms.

In an ordered array of atoms, each individual atom scatters isotropically but the overall observed signal is not isotropic and contains structural information about the sample. This is because the isotropically scattered neutrons from each atom interfere and only when the interference is constructive is a signal measured. Crystal structures, as were described in section 2.1, are highly repetitive structures with defined planes. As such, neutrons scattering elastically from crystalline planes follow the same rules as for light scattering between parallel planes. This is described by Bragg's Law:

$$n\lambda = 2d \sin\theta, \tag{4.2}$$

where λ is the wavelength, θ is the scattering angle, d is the distance between the planes, and n is an integer. When crystalline Miller planes are considered, d can be written as $d(hkl)$, thus showing intuitively how the scattering angle relates directly to the distance between different crystalline planes. A scattering signal is only observed in the case when $\mathbf{Q}$ is perpendicular to the Miller planes. Returning to the scattering triangle, the magnitude of the scattering vector $\mathbf{Q}$ for of first-order diffraction ($n = 1$) can now be written as follows:

$$Q = 2k \sin\theta = \frac{4\pi}{\lambda} \sin\theta = \frac{2\pi}{d(hkl)}, \tag{4.3}$$

where k is the magnitude of the neutron's momentum.

As the Bragg condition for a crystal requires $\mathbf{Q}$ to be perpendicular to the crystalline planes, this means that the measured signal is not a direct

measurement of the crystalline or real-space lattice. Instead, $\mathbf{Q}$ measures what is referred to as the reciprocal lattice. The distance between points in real space were described in section 2.1 by the translation vectors $\mathbf{a}$, $\mathbf{b}$ and $\mathbf{c}$. The reciprocal lattice vectors are constructed from these as follows:

$$\mathbf{a}^* = \frac{2\pi(\mathbf{b}\times\mathbf{c})}{\mathbf{a}\cdot(\mathbf{b}\times\mathbf{c})}; \qquad \mathbf{b}^* = \frac{2\pi(\mathbf{c}\times\mathbf{a})}{\mathbf{a}\cdot(\mathbf{b}\times\mathbf{c})}; \qquad \mathbf{c}^* = \frac{2\pi(\mathbf{a}\times\mathbf{b})}{\mathbf{a}\cdot(\mathbf{b}\times\mathbf{c})}. \tag{4.4}$$

The important property of the reciprocal space vectors is that $\mathbf{a}^*\cdot\mathbf{a} = 2\pi$ (and similar for $\mathbf{b}$ and $\mathbf{c}$). As we require $Q = 2\pi/d(hkl)$, the Bragg condition for $\mathbf{Q}$ can be written in terms of the reciprocal space vectors.

$$\mathbf{Q}(hkl) = h\mathbf{a}^* + k\mathbf{b}^* + l\mathbf{c}^*. \tag{4.5}$$

A simple consequence of this is that things that appear large in real space are small in reciprocal space and vice versa.

To translate directly between reciprocal and real space, one must use a Fourier transform. As such, by measuring the change in momentum and direction of the neutrons during the scattering event, one can Fourier transform the extracted data to give information about the real space behaviour of the sample. The structure factor $F(hkl)$ is the Fourier transform of the crystal structure, sampled at a single point in reciprocal space:

$$F(hkl) = \sum_n b_n \mathrm{e}^{i\mathbf{Q}(hkl)\cdot\mathbf{r}_n}, \tag{4.6}$$

where for the n^{th} nuclei b_n is the scattering cross section and $\mathbf{r}_n$ is the position. In an experiment, it is the intensity of the scattered beam for a Miller index (hkl) that is measured, which is proportional to the square of the structure factor: $I \propto |F(hkl)|^2$. As it is $|F(hkl)|^2$ that is measured, no phase information can be obtained from the data. This means that some prior knowledge about the sample being studied is necessary in order to analyse the data [160].

In the case of single crystals, each Miller index results in a discrete $\mathbf{Q}(hkl)$ position with associated $F(hkl)$. In the case of polycrystalline or powder samples the orientations of different crystallites differ. This means that the same (hkl) position will result in a different values of 2θ at which the Bragg condition is satisfied. As a result the diffraction patterns observed for powder samples are equivalent to that of a 2θ averaged single crystal experiment. This can make analysis more complex for powder samples due to the reduction of spatial

information and in some cases the merging of peaks with different intensities.

The fitting of powder diffraction data is often carried out through a Rietveld refinement. This requires knowledge of a possible structure, from which an expected diffraction pattern is calculated. The expected peak positions and intensities come from the input unit cell, but also required for the model are an expected peak shape, instrumental parameters and background signal. The calculated diffraction pattern is compared to the measured data. Parameters are then selected within the model, which are refined against the data using a least squares calculation. By iteratively converging these parameters the model reaches a 'refined' structure which is understood to be comparable to the true structure within a margin of error [123].

4.1.1 Characterising Strain

The presence of strain, as discussed in section 2.1.1, within a system manifests in the diffraction pattern. The case where the strains are small and localised is referred to as micro-strain and is typically not large enough to manifest in peak shifts. Instead this appears as the broadening of peaks. The alternate case of large strains across the crystal causes the peaks to appear to shift dependent on the angular position of the detectors. This is the situation of interest to this thesis.

The lattice strain $\varepsilon(hkl)$ compares the d-spacings of the compressed and uncompressed samples [159]. The measured lattice strain $\varepsilon_m(hkl)$ is expressed in terms of the d-spacings $d(hkl)$ as:

$$\begin{aligned}\varepsilon_m(hkl) &= \frac{d_0(hkl) - d_m(hkl)}{d_0(hkl)} \\ &= \varepsilon_P(hkl) - \left(\frac{d_P(hkl)}{d_0(hkl)}\right)\varepsilon_D(hkl).\end{aligned} \tag{4.7}$$

Here subscript 0 signifies the uncompressed state and m the measured state. As in section 2.1.1 subscript P refers to the principal stress, and D is used to signify the deviatoric contribution. The deviatoric contribution to the lattice strain is found to have the following angular dependence:

$$\varepsilon_D(hkl) = (1 - 3\cos^2\psi)Q(hkl) \tag{4.8}$$

where ψ is the angle between the load axis and the diffracting plane normal and $Q(hkl)$ is a unitless factor containing the elastic properties of the sample. Note that here $Q(hkl)$ is not the same as as the scattering vector used in the scattering triangle, though they share a notation. The exact form of the factor $Q(hkl)$ for a cubic system is [159]:

$$Q(hkl) = \frac{t}{3}(S_{11} - S_{12} - 3S\Gamma(hkl)), \tag{4.9}$$

with $S = S_{11} - S_{12} - S_{44}/2$, $\Gamma(hkl) = (h^2k^2 + k^2l^2 + l^2h^2)/(h^2 + k^2 + l^2)$ and S_{ij} and t as defined in section 2.1.1.

Thus, in measurements of the d-spacing of a crystal, the presence of deviatoric stress causes the measured result to have an angular dependence of:

$$d_m(hkl) = d_P(hkl)[1 + (1 - 3\cos^2\psi)Q(hkl)]. \tag{4.10}$$

By plotting the measured peak position against $(1 - 3\cos^2\psi)$ and fitting with a straight line the d-spacing in the case of no deviatoric stress and the factor $Q(hkl)$ can be calculated. Combining equations 4.10 and 4.9 it is clear that by finding $Q(hkl)$ for different peaks in the diffraction pattern, the material properties S and t may be extracted.

4.2 Inelastic Neutron Scattering

Inelastic scattering is characterised by an energy transfer between the scattered neutron and the sample, leading to a change in magnitude of the momentum of the neutron. This means that we must now create an extension to the methodology used in elastic scattering. The scattering triangle is now modified to have $\mathbf{k}_i$ and $\mathbf{k}_f$ with different magnitudes, which in turn changes $\mathbf{Q}$. The differential cross section is also extended to include energy dependence, resulting in a partial differential cross section $d^2\sigma/d\Omega dE$. This is related to the differential cross section used in elastic scattering as follows:

$$\frac{d\sigma}{d\Omega} = \int_0^\infty \frac{d^2\sigma}{d\Omega dE} dE. \tag{4.11}$$

The partial differential cross section relies on the same phenomena as the differential cross section, so it is not necessary to extend scattering theory beyond

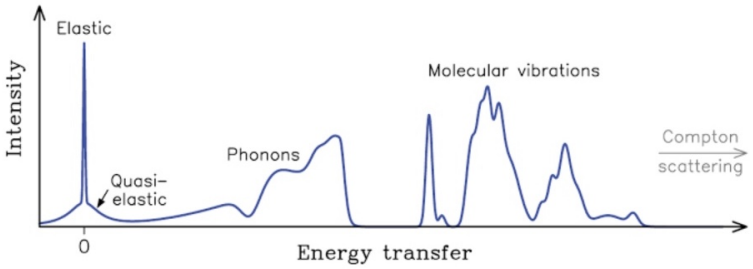

Figure 4.3 *A hypothetical plot of where different dynamical properties can be measured as energy transfer is increased, adapted from reference [160]. This plot considers the dynamics to be averaged across* **Q** *space. For more information on the* **Q** *and E dependance of different dynamics, see Shirane et al. Fig. 1.4 [157].*

this.

The momentum transfer seen in inelastic scattering is as a result of the excitation of energetic modes within the sample. An incoming neutron is able to excite a crystalline, intermolecular, rotational, diffusional or magnetic excitation. As with elastic scattering, inelastic scattering measures phenomena in reciprocal space. This means that the same principle of length inversion between reciprocal and real space also applies here. Thus localised phenomena such as intermolecular modes appear are long-range in reciprocal space, and the inverse is true for phonons. By measuring the momentum transfer and the position of the scattered neutron it is possible to characterise the excitations within a system.

Inelastic scattering can be split into coherent and incoherent contributions, both of which give separate information about a system. Coherent inelastic scattering gives information on collective excitation modes, such as phonons and magnons, whereas incoherent scattering contains information about self-dynamics such as diffusion.

The different information that can be obtained for different energy transfers in inelastic neutron scattering is shown in Fig. 4.3. The diagram does not include excitations such as magnons, which appear in the same energy range as phonons, but have different **Q** dependence, allowing them to be distinguished. Fig. 4.3 also illustrates the importance of designing an appropriate experiment for the dynamics you wish to study, as neutron scattering instruments are designed not to cover the entire dynamic range, but specific sections of it. Section 4.3 discusses the low energy transfer quasielastic measurements that can be carried out.

4.3 Quasielastic Neutron Scattering

Quasielastic neutron scattering, or QENS, is a measurement technique that is used to give information on slow dynamics such as diffusion and molecular reorientation [51]. This technique is commonly used in the study of liquids, porous materials, and molecular crystals. The name "quasielastic" comes from the fact that it is the neutrons with very small energy transfer to the sample that are measured: this can clearly be seen in Fig. 4.3.

As was discussed in chapter 2, diffusion and rotation can be either co-operative or self motions. In QENS, these can both be measured by utilising the differing properties of coherent and incoherent scattering. Co-operative excitations are seen in coherent scattering, and self motions are seen in incoherent scattering. As hydrogen as a very large incoherent cross section, this facilitates easy isolation of the self-diffusion and rotation of hydrogen atoms: a fact that will be utilised in this thesis. The neutron incoherent cross section of H is 80.3 barns, which is an order of magnitude larger than all of the other light elements, with only isotopes in period 6 and below of the periodic table having comparable or larger cross-sections [157].

The data collected in a QENS experiment is a high resolution measurement of the energy and $|\mathbf{Q}| = Q$ dependence of the elastic line. In these results, there are two components that make up the resulting data. The elastic line itself is, in theory, a delta function. However, the finite resolution of the instrument renders this as a Gaussian or Ikeda-Carpender function. In practise, to realise this one convolves a delta function with the desired amplitude with a measured resolution signal of the instrument. The dynamical component is superimposed upon this as a broader, less intense contribution, which has the form of a Lorentzian [15]. Fig. 4.4 illustrates this for $MAPbBr_3$, with the quasielastic component shown as a solid line, and the instrumental resolution shown as a dotted line.

The final form of the equation used to fit data containing a single excitation is thus:

$$S(Q,E) = I_{el}(Q)\delta(E) + I_{dyn}(Q)\frac{\Gamma(Q)}{E^2 + \Gamma(Q)^2} \tag{4.12}$$

where Γ is the linewidth of the dynamical component, and I_{el} and I_{dyn} are the relative amplitudes of the elastic and dynamic components. This function $S(Q,E)$ is convolved with the resolution function in order to correctly reproduce

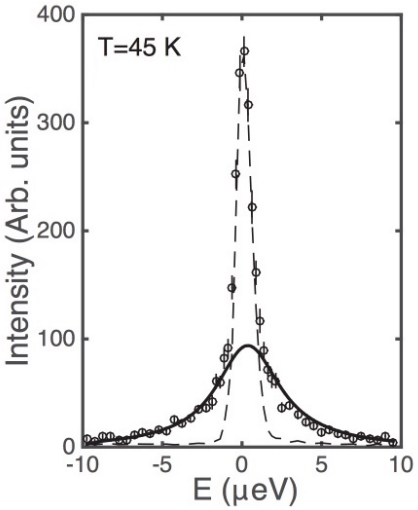

Figure 4.4 *QENS results obtained on $MAPbBr_3$ in reference [173]. The data is shown as circular points, the elastic contribution is shown as a broken line, and the quasielastic contribution is shown as a solid line.*

the data.

The linewidth $\Gamma(Q)$ is linked to the diffusion coefficient measured, and the properties of the diffusion. In the case of free rotation, the diffusion coefficient D_R does not have any spacial dependence (see equation 2.13). This means that the linewidth for a rotational excitation (now denoted Γ_R) does not have any Q dependence, and one finds that $\Gamma_R = \hbar D_R$. Conversely, as the Einstein-Smoluchowski diffusion coefficient D_T does depend on the mean square distance travelled (see equation 2.7), the linewidth does also. One finds that the linewidth for continuous translational diffusion (now denoted $\Gamma_T(Q)$) has a Q dependence such that $\Gamma_T(Q) = \hbar D_T Q^2$.

However, as discussed above in section 2.3.2, high interaction strengths between the diffusing species and the medium result in jump diffusion behaviour. This jump diffusion manifests differently in the Q dependence of the linewidth $\Gamma_T(Q)$. Table 4.1 lists the three most common models used to describe the linewidth for different jump diffusion types. All of these reduce to continual translational diffusion $\Gamma_T(Q) \sim \hbar D_T Q^2$ at low Q.

In general, the resolution of QENS instruments usually limits measurements of the diffusion coefficient D and the jump rates τ^{-1} to be larger than 10^{-7} $\mathrm{cm^2 s^{-1}}$ and 10^8 $\mathrm{s^{-1}}$ respectively [77]. However, modern high resolution instruments are now able to probe faster motions, including hydrogen tunnelling.

Table 4.1 *Different jump diffusion models that can be used to describe the Q dependence of the linewidth in QENS.*

Model name	Case described	Form
Singwi-Sjölander	Alternation between rotational and translational motion	$\Gamma_T(Q) = \dfrac{\hbar D_T Q^2}{1 + D_T Q^2 \tau}$
Chudley-Elliott	Jumps on a lattice	$\Gamma_T(Q) = \dfrac{\hbar}{\tau}\left(1 - \dfrac{\sin(Ql)}{Ql}\right)$
Hall-Ross	Jump diffusion in a restricted volume	$\Gamma_T(Q) = \dfrac{\hbar}{\tau}\left(1 - \mathrm{e}^{-D_T Q^2 \tau}\right)$

Table 4.2 *Different models that can be used to describe the Q dependence of the EISF in QENS. Here r is the radius of rotation, J_n is a cylindrical Bessel function of the n^{th} kind, and j_n is a spherical Bessel functions of the n^{th} kind.*

Case described	Model $f(Qr)$
Rotation on a 2D circle	$[J_0(Qr)]^2$
Rotation on a spherical surface	$[j_0(Qr)]^2$
Rotation in a spherical volume	$\left[\dfrac{3j_1(Qr)}{Qr}\right]^2$
Jumps between 2 sites on a circle	$\frac{1}{2}[1 + j_0(2Qr)]$
Jumps between 3 sites on a circle	$\frac{1}{3}[1 + 2j_0(\sqrt{3}Qr)]$
Jumps between 4 sites on a circle	$\frac{1}{4}[1 + j_0(2Qr) + 2j_0(\sqrt{8}Qr)]$
Jumps between 6 sites on a circle	$\frac{1}{6}[1 + j_0(2Qr) + 2j_0(\sqrt{3}Qr)]$

From the fit to the measured QENS data, one can extract a Q dependent parameter called the elastic incoherent structure factor (EISF):

$$I_{EISF}(Q) = \frac{S_{el}(Q)}{S_{el}(Q) + S_{dyn}(Q)} \tag{4.13}$$

where $S_{el}(Q)$ and $S_{dyn}(Q)$ are the areas beneath the elastic peak and dynamical component respectively [51]. The value $S_{el}(Q)$ is proportional to the differential cross section shown in equation 4.1. The EISF is found to decrease with Q, as the contribution from quasielastic scattering increases. From this, the Q dependance of the EISF can be fitted to extract information about the nature of the dynamical motions.

Table 4.2 shows several of the different models (here denoted $f(Qr)$) used to fit the EISF. The models describe the type of motion being carried out by the dynamic species and the radius in which this is occurring. In the case of rotations, this accessible space is the radius of rotation, whereas for translational diffusion

this is the radius of the sphere in which the species can diffuse.

In fitting the EISF, we must also consider that not all of the members of the dynamic species are participating in the same type of dynamics. The EISF is therefore fitted to the following equation:

$$A(Q) = p + (1 - p)f(Qr), \tag{4.14}$$

where p is the proportion of active rotators and $f(Qr)$ is one of the models described above [67]. This thus allows us to fully characterise the dynamical behaviour of the rotators within the sample.

4.4 Raman Spectroscopy

Raman spectroscopy relies upon the inelastic scattering of laser light from a sample. It differs from inelastic neutron scattering in the regard that only positions close to the Brillouin zone centre in crystalline materials may be probed. This is because the photons used are high energy and massless, so only very small momentum transfers may be achieved.

In Raman spectroscopy, there is a transfer of energy between the photon and the sample due to the excitation of a dynamical mode in the sample. The high energy of the laser light in Raman scattering means that the excitations observed range between optical phonons at low energy transfers and inter-molecular modes, including rotations, at high energy transfers. It should be noted that in Raman spectroscopy the excitation immediately de-excites and as such, it is possible to excite into "virtual states". This means that the Raman spectra observed is dependent on the energy of the incident photon.

Figure 4.5 shows the three types of interaction between the photon and excitation that are observed in Raman spectroscopy. Rayleigh scattering is where the photon excites the excitation, and a photon of the same energy is then emitted when it de-excites. In Stokes scattering the emitted photon is of a lower energy than that of the incident photon, and in Anti-Stokes scattering the emitted photon is of a higher energy. The energy levels of each excitation in a molecule are discrete and characteristic of the bond being excited. As such, a molecule may be fingerprinted by measuring the Raman spectrum.

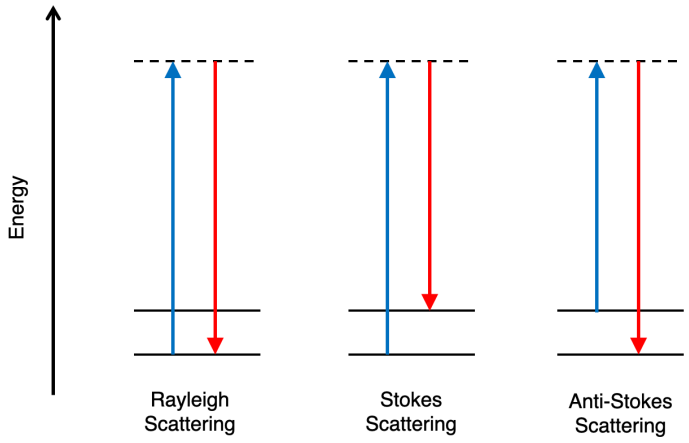

Figure 4.5 *The types of interaction between an incoming photon and an excitation associated with Raman spectroscopy.*

Fluorescence is a phenomenon that competes with Raman scattering, but is equally useful. In this case, the photon excites the excitation but is not immediately re-emitted. This means that only discrete energy levels may be accessed and thus the fluorescence spectra observed is dependent on the energy of the incident photon. Again, this technique may be used to identify the sample. It is possible to observe fluorescence and Raman spectroscopy simultaneously in a single measurement, but care must be taken to distinguish the two.

4.5 Calculating Structures: Density Functional Theory

Density Functional Theory (DFT) describes the computational technique of solving the Schrödinger equation for all of the electrons in a system, and thus inferring the properties of the system. In reality, to do this efficiently, a number of approximations must be made in order to solve this many-body problem.

The first of these approximations is to carry out the calculations using the electron density, rather than the wavefunctions. Hohenberg and Kohn proved that no two applied potentials can result in the same electron density [80]. As the solutions for the electron density are unique, they can be used in computations rather than the wavefunction. In a system with N electrons the electron density is N dimensional and the electron wavelengths have $3N$ dimensions. As such, treating the electron density results in a more efficient use of computation time.

The second approximation is Kohn-Sham theory, where a solution to the Schrödinger equation that only considers the non-interacting component of the electrons' kinetic energy is used [93]. The energy functional in this theory is as follows:

$$E[n] = T_S + E_{ne}[n] + E_{ee}[n] + E_{xc}[n]. \tag{4.15}$$

Here, the only term that does not depend on the electron density is the non-interacting component of the kinetic energy T_S. These calculations are all carried out at absolute zero in temperature, so the kinetic energy depends only on the potential. Note that the nuclei are considered to be stationary and thus have no kinetic energy. The terms $E_{ne}[n]$ and $E_{ee}[n]$ describe the Coulomb interaction between the neutrons and electrons, and electrons respectively. The final term $E_{xc}[n]$ is the exchange-correlation functional. This term contains the component of the kinetic energy not accounted for by T_S and any correlation contributions to the electron dynamics. The exchange-correlation function is unknown, and different DFT methods use different approximations.

The simplest approximations for the exchange-correlation function are based off the value of the electron density only. This works well for materials where the electronic density varies slowly with position, such as metals. However, for molecular systems like those considered in this thesis it is necessary to use an approximation that also considers the gradient of the electron density.

In this thesis, DFT is applied in order to find the crystal structure of a system at high pressure. Here, the energy of an atomic arrangement is calculated and then the atoms are re-positioned until an energetic minima is found. To compare the stability of structures at a given pressure the enthalpy is calculated:

$$H = U + PV \tag{4.16}$$

where U is the internal energy per formula unit, P is the pressure and V is the volume per formula unit. The structure with the smallest enthalpy is the most stable.

Chapter 5

High Pressure Techniques

High pressures are of interest to science because they provide insight on how materials and interactions change under extreme conditions. The application of high pressures gives the ability to alter and tune material properties, and to create new compounds which cannot be formed at ambient conditions [57, 112]. These extreme conditions are relevant for understanding the structure of planetary bodies and the formation of the solar system, as well as for use in industrial processes [56, 72, 168].

This chapter focusses on techniques used to create high mechanical pressures upon samples, which will be employed for the studies described in chapters 7 and 8. This differs from chemical pressure, where an element is substituted for another heavier element of the same group. Chemical pressure can be analogous to mechanical pressure. Application of chemical pressure has been proposed as a route to reaching higher pressures on samples of interest [7, 192]. In the $MAPbX_3$ compounds the substitution of the atom on the halide site and the application of mechanical pressure can both be used to tune the band gap [84]. Chemical pressure is not a key point of study in this thesis, so from this point forwards any discussion of high pressure will only concern mechanical pressure unless explicitly specified.

In particular, this thesis will employ only static compression techniques. These are techniques in which the material is held at high pressure conditions for an extended period of time. This differs from dynamic compression techniques wherein a sudden impulse (usually from a high powered laser) is exerted upon the sample. The resultant shockwave passes through the material and induce extreme

condition states on picosecond timescales [57]. Dynamic compression is able to reach higher pressures and temperatures than static compression. However, the short timescales make it impossible to study the states produced using neutron scattering techniques.

Even in static compression, pressure gradients are often still present in the sample. These non-homogenous stresses are referred to as non-hydrostatic conditions, and occur when there is shear stress as well as normal stress. These are problematic because only hydrostatic pressure is a thermodynamic parameter and is much easier to compare with theory [91]. The even distribution of pressure is improved by the inclusion of a pressure transmitting medium surrounding the sample. At lower pressures these are often fluids, as fluids cannot support shear stress. However at higher pressures where fluids solidify, powders of materials known to be uniformly compressible can be used. For example, solid helium is an acceptable pressure transmitting medium up to 40 GPa [91].

5.1 Equations of State and Pressure Markers

An important question in high pressure techniques is how the pressure can be correctly extracted from the measurement. Pressure is defined as the force per unit area acting on the sample. As such, in setups with a well known sample area and applied force, pressure is simple to calculate. This is referred to as a primary pressure scale. However, in many cases the force, or even the area of the sample, are not simple to determine. Thus, a second measurement must be taken in order to determine the pressure: a secondary pressure scale. Often, the equation of state of a material is employed in order to extract the pressure.

The equation of state of a material phase is a thermodynamic equation relating the thermodynamic properties of the material to the pressure and temperature. In high pressure physics, the term "equation of state" is commonly used to describe the function relating the sample volume, pressure and temperature of a sample. This means that for materials with a known equation of state, the pressure might be inferred by measuring the unit cell volume and temperature of the sample.

Materials with a well-established equation of state are used as pressure markers: they are placed alongside the sample in measurements and used to determine the pressure. The choice of pressure marker is determined by the technique and the

sample to be studied. In general, the requirements for a pressure marker are: to have no phase transitions in the pressure (and temperature) region to be studied; to not have a signal that overlaps significantly with that of the sample; and to have a strong signal in the relevant measurement technique. Equations of state must be determined by studies of multiple thermodynamic parameters in order for them to be considered reliable. As such there are a number of commonly used pressure markers that have well known equations of state. Common pressure markers in neutron diffraction are lead (Pb) and sodium chloride (NaCl), as they have simple structures and large neutron cross-sections [163, 169]. In Raman scattering, the fluorescence of ruby is used as it is highly Raman active and moves linearly with pressure below 80 GPa [16, 116]. The pressure dependence of the Raman edge of the diamond in a diamond anvil cell (DAC) can also be used as a pressure marker [16].

5.2 Diamond Anvil Cells

Diamond anvil cells (DACs) are one of the most common tools in static high pressure science when it comes to measurements on small sample sizes. Depending on the size and geometry of the diamonds, they are capable of reaching pressures exceeding 1 TPa [55]. They have the key advantage of diamonds being transparent in the wavelength range between ultraviolet and x-rays [112], and thus are appropriate for measurements involving lasers, optical light and x-rays. They are often used in experiments where only a small sample volume is necessary.

The construction of a Merill-Bassett DAC, like those used for the Raman experiments in this thesis, is shown in Fig. 5.1. It is made up of two opposed diamonds, with flattened tips referred to as culets that face each other. Hardened tungsten carbide seats mounted onto backing plates hold the diamonds in place. The cell is closed by bringing these backing plates together using screws. The sample is placed between the two culets, with a metal gasket (typically steel, tungsten or rhenium) used to enclose the sample and prevent the diamonds from touching. Diamonds touching often results in breakages due to the brittle nature of diamond.

For X-ray scattering and Raman spectroscopy experiments the culet diameter varies from tens to hundreds of microns, whereas for neutron scattering the culets can be up to several millimetres in size. The samples do not occupy the space

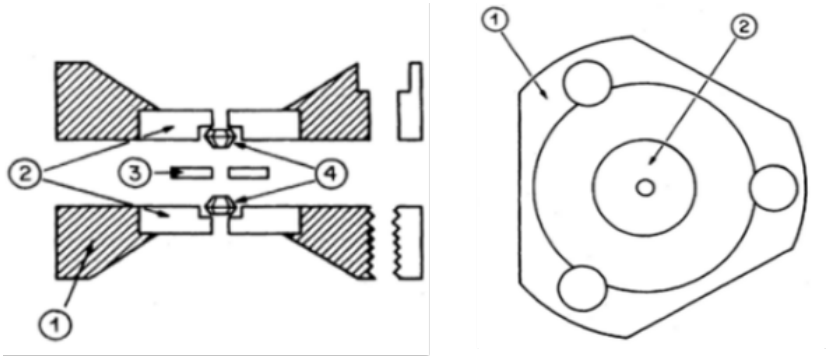

Figure 5.1 *A diagram of a Merrill-Bassett diamond anvil cell adapted from reference [85]. On the left is a side view and on the right is a top-down view. Here ① are the backing plates; ② are the seats of the anvils; ③ is the gasket; and the ④ shows the diamonds.*

of the whole culet, typically having a diameter one third that of the culet. The starting depth of the sample is decreed by the thickness of the gasket. In practise, this is usually one tenth of the diameter of the culets. For a flat culet, the rule-of-thumb maximum operating pressure that can be achieved without damaging the diamonds (in GPa) is

$$P = \frac{10}{d}, \tag{5.1}$$

where d is the culet diameter in mm [112]. So, for example, a flat 400 µm culet would allow for a sample volume of $\sim 2 \times 10^{-3}\,\mathrm{mm}^3$, and a maximum pressure of 25 GPa.

However, it is possible to reach higher pressures by changing the geometry of the culet. The most common example of this are bevelled anvils, in which the angle of the side of the diamonds is reduced near the tip, giving a reduced culet size. In the case of neutron scattering where large culets are required, the sides of the diamonds are machined to be conical in shape and to have more support from the seat. More complex geometries can also be achieved by etching the diamonds. These geometries better distribute the stresses in the diamond so higher pressures can be reached. This results in a much higher maximum pressure than equation 5.1 would imply for the culet size [117].

Though heating experiments in DACs are not carried out in this thesis, they are routinely carried out in high pressure science. Most commonly laser heating and resistive heating techniques are used, and can successfully reach temperatures of thousands of kelvin without reducing the pressure performance of the DAC [112].

5.3 The Paris-Edinburgh Press

There are multiple large-volume presses used for reaching high pressures, but the most commonly used is the Paris-Edinburgh (PE) press. The PE press is used for sample volumes up to $\sim$100 mm^3, though in order to reach the maximal pressure achievable on this setup ($\sim$28 GPa) a smaller volume of $\sim$30 mm^3 is required [30, 74, 90]. PE presses have become ubiquitous in high pressure neutron scattering experiments, in particular for diffraction and quasielastic scattering, where large sample sizes are necessary. They are also used in other high pressure measurements that require a larger sample size.

Figure 5.2 shows a diagram of the PE press. It is constructed from two opposing anvils, between which a sample prepared inside a gasket is placed. Typically a hydraulic press is used to apply a load to one anvil, thus inducing pressure on the sample.

The key feature which allows the PE press to reach higher pressures than other large volume presses is the toroidal gasket geometry, which encloses a spherical sample space. For reaching the highest pressures attainable with this setup, double toroidal gasket geometries are used, requiring a smaller sample volume. The anvils are commonly constructed from tungsten carbide (WC), zirconia-toughened alumina (ZTA), or sintered diamond (SD). Of the three, SD is able to

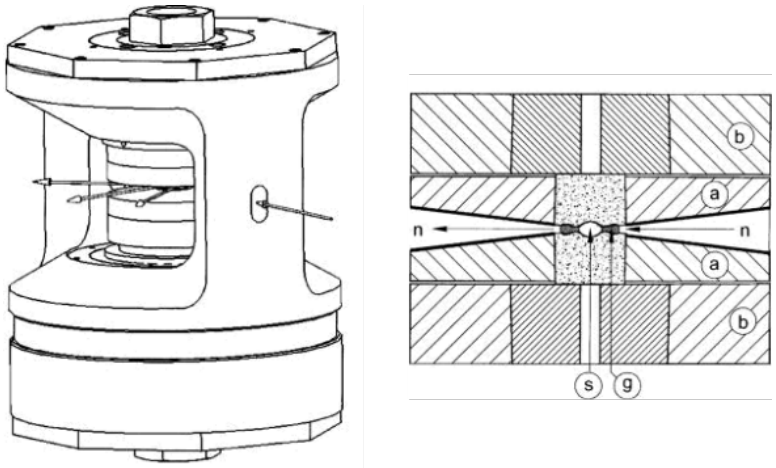

Figure 5.2 *A diagram of the VX Paris-Edinburgh press, adapted from reference [92]. On the left the whole PE press assembly is shown, with the arrows indicating the direction of the neutrons. On the right is a cross-section of the anvils and sample space. Here* 𝔞 *is the anvils;* 𝔟 *is the backing seats of the anvils;* 𝔤 *is the gasket;* 𝔰 *is the sample; and the* n *shows the direction of the neutrons.*

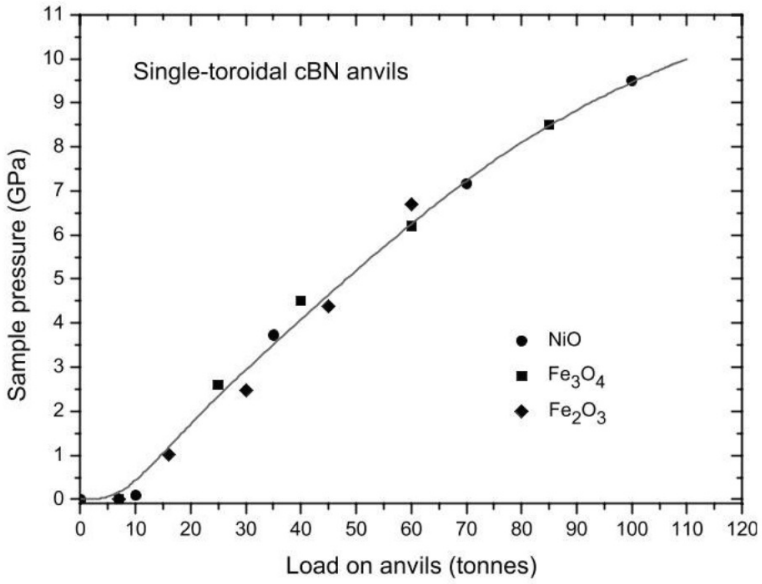

Figure 5.3 *A graph showing the loading curve for the Paris-Edinburgh press with single toroidal anvils taken from Ref. [92].*

reach the highest pressures, with WC and ZTA limited to ∼10 GPa and ∼7 GPa respectively [30]. However, ZTA anvils are the most transparent to neutrons of the three, meaning that the data collected with these anvils has the best signal-to-background ratio [30].

The hole in the backing seats upon which the anvils sit is often used for additional probes. In particular, temperature sensors and small heaters can be used to heat and monitor the temperature of the anvils. Low temperatures are achieved by using liquid nitrogen to cool either the entire PE press, or using a more directed flow to cool only the sample and anvils, and using the heaters on the anvils to fine-tune the temperature. As with DACs, the act of heating or cooling the cell does affect the pressure performance. The anvils are the most common point of failure, and the strength of the anvil materials does vary with temperature, meaning that the maximum pressure that can be probed is reduced upon heating or cooling. Additionally, cooling the PE press can cause the fluid in the hydraulic press used to apply pressure to freeze, making pressure changes at low temperature difficult.

It is possible to link the load applied onto the anvils to the pressure generated. Samples with a known equation of state have been measured and their pressure plotted against the load, which results in a curve as shown in figure 5.3. This assumes a perfectly packed sample, with no voids, and fully hydrostatic compression.

Chapter 6

The Dynamical Behaviour of $MAPbBr_3$ and $MAPbCl_3$

In chapter 3, the methylammonium lead halides were introduced as photovoltaic materials, with a great deal of interest in the field regarding the compound $MAPbI_3$. The photovoltaic properties of these compounds are understood to be linked to the presence of the molecular species, and thus understanding the behaviour of the molecule gives insight into the overall properties of the material. The goal of this chapter is to study the phase transitions in $MAPbBr_3$ and $MAPbCl_3$.

First the coupling between the motion of the molecule and the crystal structure changes in $MAPbBr_3$ is described. This will be done through high resolution quasielastic neutron scattering and simultaneous Raman and inelastic neutron scattering measurements. This is complimented with an in-depth quasielastic neutron scattering study of the molecular dynamics of the cation in $MAPbCl_3$. This is of interest because $MAPbCl_3$ has been reported to have two orientations of the cation in the low temperature phase, whereas $MAPbBr_3$ and $MAPbI_3$ have a single fixed orientation.

6.1 Experimental Setup

This section comprises of a total of five different experiments on the two samples of interest. Three different neutron scattering instruments are used, the function

of each is described in this section. For all of the experiments carried out in this chapter, the vanadium calibration and background subtraction of data was carried out in Mantid [6], using pre-written scripts. The neutron scattering signal from vanadium is almost entirely incoherent and thus gives a good representation of the detector performance, and is thus used to normalise the measured signal from the sample of interest. The analysis for all of these experiments was carried out using specially-written scripts in MATLAB. Sample growth and identification techniques are also detailed.

6.1.1 Low-Energy Neutron Spectroscopy Instrument: IRIS

The instrument IRIS, at the ISIS facility in Oxford, was used for experiments on both $MAPbBr_3$ and $MAPbCl_3$. IRIS is a time-of-flight inverted-geometry spectrometer, which means that the incoming neutrons are not energy-selected, rather the energy selection is carried out after scattering from the sample. The geometry of IRIS is nearly backscattering, and is close enough to be approximated as such. This results in the instrument resolution being maintained at high energies, leading to an increased energy resolution at all energies compared to chopper spectrometers [33, 121], but does give limitations as to the energies that can be selected. A diagram of IRIS can be seen in figure 6.1. The moderator, which tunes the energy of the incident neutrons, used for IRIS is hydrogen, cooled to 25 K, and there are two choppers used to limit the wavelengths incident on the sample and remove frame overlap. Frame overlap is a problem at the ISIS facility because it is a pulsed neutron source. If frame overlap is not filtered out then the slowest neutrons from one pulse will overlap with the fastest neutrons from the next pulse, which causes spurious results in the timing measurements used to calculate the energy of the final scattered neutrons.

On IRIS pyrolytic graphite and mica analysers are used for energy analysis, giving incident energies and resolutions as shown in table 6.1. The mica analysers have a reduced angular coverage compared to the pyrolytic graphite, as can be seen from the position of the diffraction detector in figure 6.1. Additionally the pyrolytic graphite analysers are more recently updated to provide an increased count rate [32]. For this reason, it is the pyrolytic graphite analysers that are used in all subsequent analysis.

For the study of $MAPbBr_3$, the PG 002 analysers were used, and diffraction patterns were collected simultaneously to the quasielastic scattering data collection.

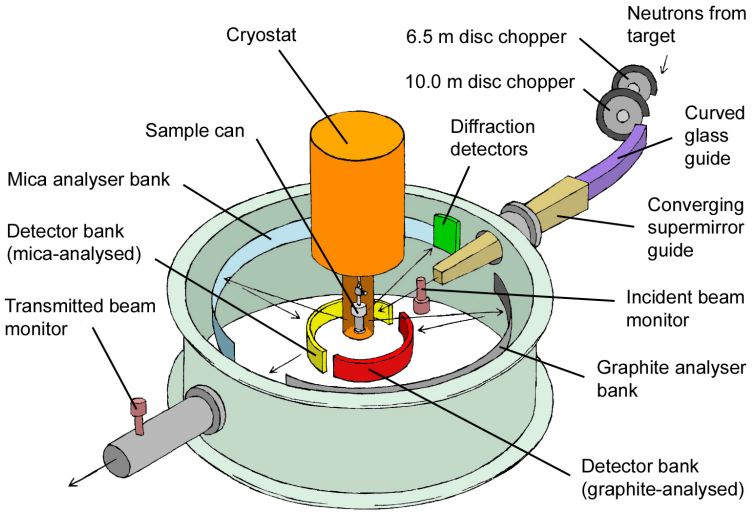

Figure 6.1 *A schematic of the instrument IRIS at ISIS with all components of the instrument labelled. Note that the energy analysing is carried out on the neutrons that are scattered from the sample.*

Table 6.1 *The incident energies, energy resolutions and maximum Q values available on IRIS [33]. Two available pyrolytic graphite (PG) reflections and three mica reflections are listed.*

	PG 002	PG 004	Mica 002	Mica 004	Mica 006
Analysing energy (meV)	1.84	7.38	0.207	0.826	1.86
Resolution (μeV)	17.5	54.5	1.0	4.5	11.0
Maximum Q (Å)	1.85	3.70	0.62	1.24	1.87

In the study of $MAPbCl_3$ both the PG 002 and PG 004 filters are used (incident energies 1.84 meV and 7.38 meV respectively). This means that a larger Q-range may be probed, though the larger $|Q|$ values will have a lower resolution. For the setup associated with the PG 002 analysers the dynamic range for quasielastic scattering was $\pm$ 0.5 meV and the d-spacing range for the diffraction was 3 to 3.7 Å.

A key component of quasielastic scattering is to both correctly subtract background and to use the optimal resolution. In this experiment an empty can background subtraction was carried out from a measurement performed at room temperature, and resolution was measured from the base temperature response of the $MAPbBr_3$ sample, which was found to be 23.8 µeV from a Gaussian fit (full-width at half-maximum). This resolution is larger than that expected for the PG 002 analysers as shown in table 6.1, which is likely linked to the fact that in reality a Gaussian fit is not sufficient for this and instead an Ikeda-Carpenter function should be used [33]. The Ikeda-Carpenter function depends on the decay rates of the neutrons, the moderator temperature and the neutron wavelength. A fit to the Ikeda-Carpenter function from the resolution data from this experiment was too complex, but it can be assumed that the resulting width for this would be closer to the predicted value of 17.5 µeV. As it is the raw resolution data that is used in the fits presented in this chapter, the calculated resolution width does not have any effect on the results.

The experiments on IRIS presented in this chapter were carried out by the author, Dr. Chris Stock, and Dr. Victoria García Sakai.

6.1.2 High-Energy Neutron Spectroscopy Instrument and Simultaneous Raman Spectroscopy Setup: MAPS

The high energy inelastic neutron scattering measurements on $MAPbBr_3$ were measured on the instrument MAPS, at the ISIS facility in Oxford. MAPS is a chopper spectrometer with an array of position sensitive detectors. The incident energies available on MAPS span from 15 meV to 2000 meV, and the energy resolution varies with incident energy. This instrument was designed as a vehicle for the study of magnetic excitations, so is thus optimised to provide a large range of $\mathbf{Q}$ and good resolution at high energies [133].

In order to have high energy incident neutrons, MAPS is aligned with an ambient

Table 6.2 *The Fermi chopper frequencies and associated neutron energies used for the $MAPbBr_3$ study on MAPS [133].*

Chopper frequency (Hz)	100	400	600
Neutron incident energy (meV)	60	250	650
Energy resolution (meV)	2	6	16
Approximate energy transfer (meV)	5 - 50	40 - 240	50 - 550

temperature moderator, and the incident energy is then tuned using choppers. There are two choppers on MAPS: one is a T_0 chopper that rotates at the same frequency as the source pulses, to remove frame overlap; and a second Fermi chopper that selects the incident energy. There are two Fermi choppers available for use, the S chopper and the A chopper. The A chopper has higher resolution than the S chopper, while the S chopper has larger flux. For these experiments the A chopper is used, with the exact settings listed in table 6.2.

In this particular experiment, there was reduced flux incident on the sample due to problems with the guide. However, as the excitation of interest in this sample was linked to the hydrogen motions, and hydrogen has a very large cross section, this problem was combatted by simply using extended counting times. The counting times were also tuned depending on the incident energy, with larger amounts of counts collected for the 400 Hz setting shown in table 6.2, as this setting captured the central area of the spectrum with greatest clarity.

Simultaneous to the collected neutron spectroscopy results, Raman spectroscopy was carried out on a sample thermally coupled to the sample used for neutron spectroscopy. This sample was placed underneath a sapphire window and both samples were connected to the inside of a specially made hollow sample stick. A modified Renishaw InVia spectrometer with wavelength 785 nm was mounted on top of the sample space, such that the laser beam could travel down the sample stick and down into the cryostat in which both samples were held. Two gratings of 1200 lines per mm and 1800 lines per mm were used, which provided measurements of different spectral ranges, giving a total range of 20 to 3200 cm^{-1} (2.5 to 396.8 meV). This allows for direct comparisons between the neutron and Raman results over much of the neutron energy range measured. It should be noted that at a wave number above 1700 cm^{-1} (210 meV) the intensity of the laser decreases, so the relative intensity for the collected spectra above this wavenumber is also reduced.

The experiment carried out on MAPS presented in this chapter were conducted

Table 6.3 *The incident energies, energy resolutions and maximum Q values for the running mode used to study $MAPbCl_3$ on LET.*

Incident Energy (meV)	Energy Resolution (μeV)	Maximum Q ($\mathring{A}^{-1}$)
17.80	750	5.40
6.50	170	3.25
3.34	76	2.30
2.03	38	1.82

by the author, Irene Robles García, Dr. Chris Stock and Dr. Stuart Parker.

6.1.3 Low-Energy Neutron Spectroscopy Instrument: LET

In the study on $MAPbCl_3$, the instrument LET is used to provide quasielastic results to compliment those collected on IRIS. LET is a low energy chopper spectrometer at ISIS, similar in design to the instrument MAPS as described in section 6.1.2. However, there are a number of key differences that separate the two instruments. As LET is part of Target Station 2 at ISIS, it only receives a lower frequency neutron pulse, compared to IRIS and MAPS in Target Station 1. However, Target Station 2 is more efficient than the older Target Station 1, so despite the lower flux it is able to utilise more neutrons from each individual pulse [18].

In order to select the incident energy of the neutrons, LET utilises five choppers (two of which are double-disk choppers). These allow the neutron pulse to be carefully shaped to the desired energies. From each pulse, the choppers are able to select multiple energies which are each incident on the sample at a different time. This allows for multiple measurements with different incident energies to be carried out simultaneously. The exact combination of energies that may be used must be carefully chosen to ensure that there is no frame overlap. LET uses a combination solid methane and liquid hydrogen moderator, and has access to neutrons of energies 0.5 meV to 30 meV. The setting used in the experiment on $MAPbCl_3$ is shown in table 6.3, chosen as it provides both a good amount of flux and resolution. Note that LET provides lower resolution than IRIS, but has greater range and flexibility in incident energy (see table 6.1).

The other defining feature of LET is its detectors: it employs 4 m tall position sensitive ^{3}He detectors positioned 3.5 m away from the sample. This gives

access to angles between $-40°$ and $140°$ in the horizonal plane, and $\pm 30°$ in the vertical plane. This gives a much larger accessible region out of plane from a single measurement than any of the other available spectrometers at the ISIS facility, and thus allows for extensive single crystal studies. However, to allow for comparison between this and the IRIS data collected on $MAPbCl_3$ the single-crystal result collected have been powder-averaged.

The experiment using MAPS was carried out by the author, Dr. Chris Stock, Dr. Manila Songvilay and Dr. David Voneshen.

6.1.4 Sample Growth and Identification

$MAPbBr_3$

A powder sample of $MAPbBr_3$ was prepared by the reaction of stoichiometric amounts of lead acetate and methylamine hydrobromide in hydrobromic acid, then evaporating away the excess acid to leave an orange coloured precipitate. This precipitate was washed with diethyl ether to remove any residual acid in the sample, and the sample was left in a dry environment to dry. However, it was found that the $MAPbBr_3$ powder grown did contain some residual acid and thus reacted with aluminium. As such, during neutron experiments the sample was wrapped in niobium foil to protect this residual acid from reacting with the outer aluminium sample holders. Care was taken to always store the sample in a dry atmosphere to prevent water absorption or possible degradation. A total of 35 g of sample was prepared in several batches by Dr. Chris Stock for use in these experiments. This sample was identified as $MAPbBr_3$ primarily by visual inspection, as the sample is a characteristic bright orange in colour.

Later, neutron diffraction data were collected on IRIS, and though only a small range of d-spacings (3 to 3.7 Å) may be observed, they did provide further evidence that the solution-synthesised sample was indeed $MAPbBr_3$. This limited range in d spacing is due to the constraints imposed by the quasielastic scattering results collected simultaneous to the diffraction results. $MAPbBr_3$ experiences three structural phase transitions between the cubic room temperature phase (phase I) and the orthorhombic phase at base temperature (phase IV), with phase II being tetragonal and phase III being identified as incommensurate and tetragonal, but in this thesis will often be referred to as the short-lived tetragonal

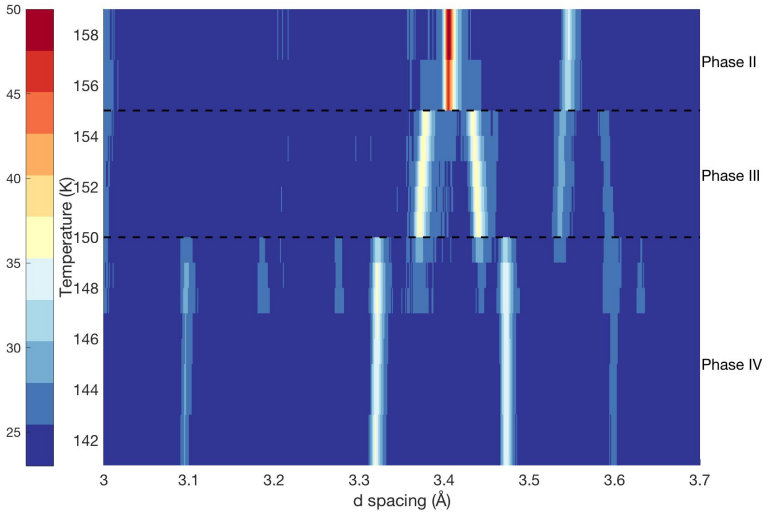

Figure 6.2 *The diffraction data obtained on IRIS for $MAPbBr_3$, showing the phase transitions II to III at* 155 K *and III to IV at* 150 K.

phase [119, 132, 138, 174]. The diffraction data obtained on IRIS, shown in figure 6.2, can be used to confirm the presence of two phase transitions: the first at 150 K (IV to III), the second at 155 K (III to II). Some coexistence can be seen between the phases, most noticeably just below 150 K around 3.4 Å and 3.5 Å. It should be noted that the extra lines seen only between 147 and 150 K not associated with phase II are present at lower temperatures, but counting times were not long enough to discern them clearly in the false colour image shown in figure 6.2. The range of **Q** space available on IRIS is not large enough to substantiate a structural refinement to allow a comparison to the space groups found by Poglitsch and Weber [138]. These measurements confirm the structural transitions and the presence of an intermediate phase between the orthorhombic and tetragonal phases in these solution-synthesised samples.

In these experiments, 13.16 g of sample was used in the MAPS experiment, and 11.29 g was used on the IRIS experiments. As such, the thermal history of the sample for the experiments carried out does differ, though care was taken to ensure that phase transitions were always approached slowly and carefully.

$MAPbCl_3$

The method for growth of $MAPbCl_3$ is very similar to that of $MAPbBr_3$ as described above: stoichiometric amounts of lead acetate and methylamine

hydrochloride are reacted in in hydrochloric acid, then the excess acid is evaporated away. In this case, the resulting precipitate is white or very pale yellow in colour. For this sample, care was taken to further develop this method to maximise yield and remove as much excess acid as possible, while taking a reasonable amount of time per growth. This was done by optimising the proportion of hydrochloric acid to reactants and controlling the speed of reaction by tuning the temperature and stirring speed. The optimised yield method produced between 2.5 and 3 g per growth. Furthermore, after being washed with diethyl ether, the resulting precipitate is dried overnight in an over at 40 °C, before being stored in a glovebox environment until experimentation. In order to verify the purity of the growths throughout the method optimisation, room temperature X-ray powder diffraction patterns from $2\theta = 5$ to 70° were taken using a Bruker D2 phaser with 30 kV X-rays, then compared to results collected by Chi et al [41]. This confirmed there were no impurity phases in the sample, such as $PbCl_3$. This sample growth was conducted by the author and Dr. Manila Songvilay, with some assistance from Dr. Chris Stock.

As with $MAPbBr_3$, the diffraction detectors on IRIS were used to verify the phase transitions in the $MAPbCl_3$ powder sample. In this case, in addition to the 3 to 3.7 Å d-range measurements carried out for all temperatures, a wider diffraction pattern was taken for d-range 1 to 7.4 Å for selected temperatures; 90 K, 150 K, 175 K, 200 K and 300 K; and a diffraction pattern of 1 to 6.4 Å for temperatures between 170 K and 180 K with 1 K steps. Due to detector overlap problems, a comprehensive diffraction pattern cannot be fully formed from this data and no fitting can be carried out, however the splitting behaviour of a number of peaks can be examined. Figure 6.3 shows selected regions of the resultant diffraction pattern, illustrating the two phase transitions at 173 K and 178 K. $MAPbCl_3$ experiences two phase transitions as temperature is lowered: from cubic (phase I) to short-lived tetragonal (phase II) then to orthorhombic (phase III) [41, 104]. As with the powder X-rays collected on this sample, peak identifications are based off previous results collected by Chi et al [41]. The peak at 5.65 Å in the cubic phase is the [001] peak, which splits as the temperature is lowered and the system transitions to tetragonal then to orthorhombic. Similarly, the peak at 2.8 Å is the [400] peak, which then splits into the [400], [040] and [004] peaks as the unit cell symmetry changes. Finally, the peak at 3.2 Å is the [222] peak, which shows a splitting in the tetragonal phase.

A total of 35 g of sample was generated for use in experimentation, with 11.67 g of

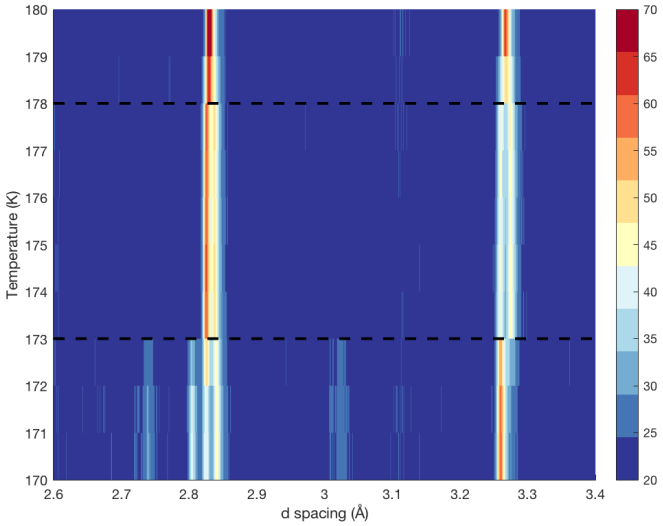

(a) *Data collected with d-spacing 2.6 to* 3.4 Å.

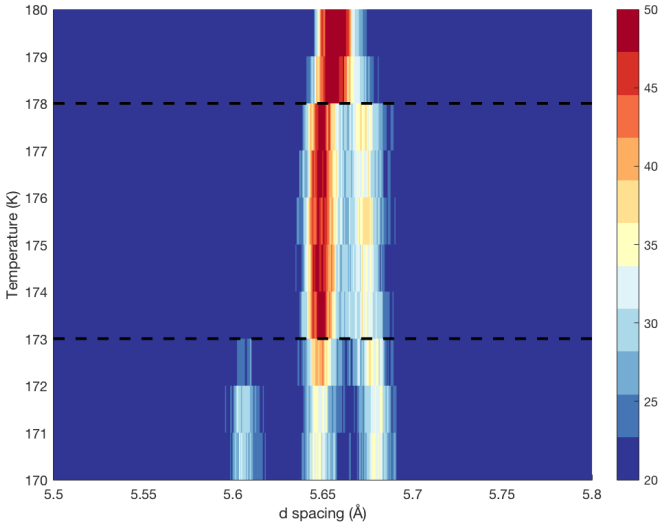

(b) *Data collected with d-spacing 5.5 to* 5.8 Å.

Figure 6.3 *The diffraction data obtained on IRIS for* $MAPbCl_3$*, showing the phase transitions I to II at* 173 K *and II to III at* 178 K*. Range of d-spacing values are chosen to select regions where there are no additional signals due to detector overlap.*

this being used for the experiment on IRIS. This sample was enclosed in a niobium foil envelope before being placed into the aluminium sample holder. The sample used for experimentation on LET was a 0.5 g single crystal grown via solution synthesis by Dr Gao Xu. The single crystal was mounted on the aluminium sample holder using aluminium wire after being loosely wrapped in quartz wool. Care was taken to heat and cool the single crystal slowly, as it is susceptible to breakage upon sudden temperature change.

6.2 $MAPbBr_3$ Results

6.2.1 Quasielastic Neutron Scattering Results

This section presents the analysis of the QENS results collected on $MAPbBr_3$ using IRIS with incident energy $E_i = 1.84\,\text{meV}$. Two example spectra are shown in figure 6.4, taken at 100 K and 200 K. The solid red curve is a fit to the sum of the elastic and dynamical components. There are two dynamical components identified in this data: one is shown in pink and the other, which appears at temperatures above 150 K, is shown in green. The dynamical contribution shown in pink shall henceforth be referred to as the "broader" β contribution, as it has a larger full-width at half-maximum than the green "narrower" α dynamical contribution at all temperatures and $|Q|$. Though the α component was not present at all temperatures, it is still appropriate to fit a model of two dynamical contributions to all the data. As such, the equation used for fitting this data is:

$$S(Q,E) = I_{el}(Q)\delta(E) + I_\alpha(Q)\frac{\Gamma_\alpha(Q)}{E^2 + (\Gamma_\alpha(Q))^2} + I_\beta(Q)\frac{\Gamma_\beta(Q)}{E^2 + (\Gamma_\beta(Q))^2}, \quad (6.1)$$

where this function is then convolved with the resolution data before the data is fit as detailed in section 4.3.

The full-width at half-maximum $\Gamma(Q)$ of both components were found not to vary strongly with $|Q|$, which suggests that the measured dynamic behaviour is not diffusive, which shall later be confirmed through fits to the EISF. Plots of how the two linewidths Γ_α and Γ_β averaged across the entire measured $|Q|$ range changes with temperature are shown in figure 6.5. The β dynamical component increases with temperature, indicative of shortening lifetimes, until the temperature exceeds $\sim$160 K where it levels out somewhat. The steepest

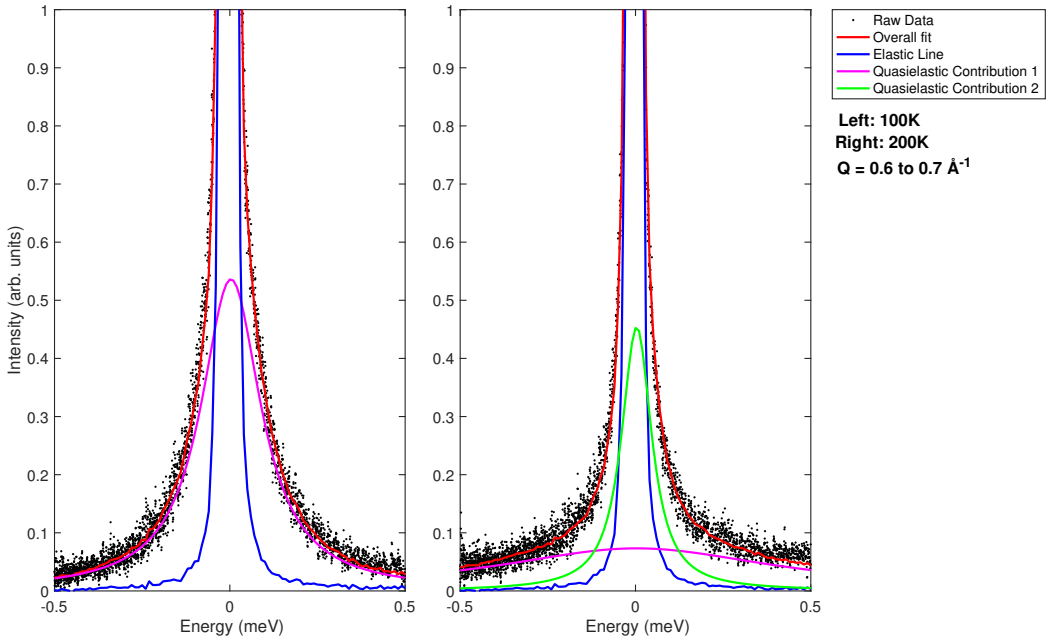

Figure 6.4 *Examples of the spectra obtained on IRIS at* $|Q| = 1.6\,\text{Å}^{-1}$*: left* 100 K*, right* 200 K*. The black circles show the data points, the red line shows the total fit, the blue shows the resolution delta function, and the pink and green show the dynamical contributions.*

increase in linewidth for the β contribution appears to be after the 150 K phase transition to the short-lived tetragonal phase. In the case of the α dynamical component, below the 150 K phase transition the linewidth is very small: below $\sim$140 K it cannot be distinguished from the elastic line as is it has a linewidth smaller than the resolution of the instrument. Above the 150 K phase transition to the short-lived tetragonal phase III and through into phase IV the linewidth of the α contribution increases; indeed by 200 K the linewidth has increased dramatically. Two separate experiments are plotted in different colours as the exact temperature of the phase transition is expected to be dependent on the thermal history [184].

The extracted average linewidth is equal to the diffusion coefficient multiplied by a constant, and thus is expected to have an Arrhenius dependance on temperature, the form of which can be seen in equation 2.10. As such the activation energy of the dynamical component may be extracted. Graphs showing the linewidth against $1000/T$ for both dynamical contributions are shown in figure 6.6. For the β contribution, two regions are apparent. Below the 150 K transition an activation energy of $E_a = 275 \pm 6$ K is extracted. Above 160 K there are significantly fewer

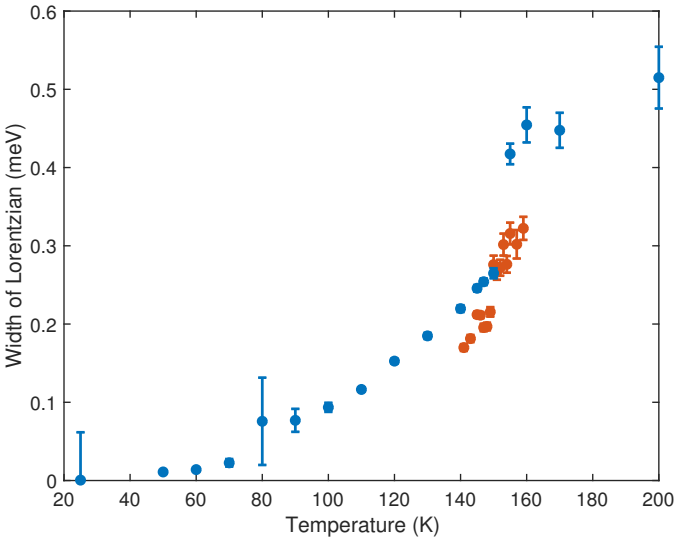

(a) *β dynamical component.*

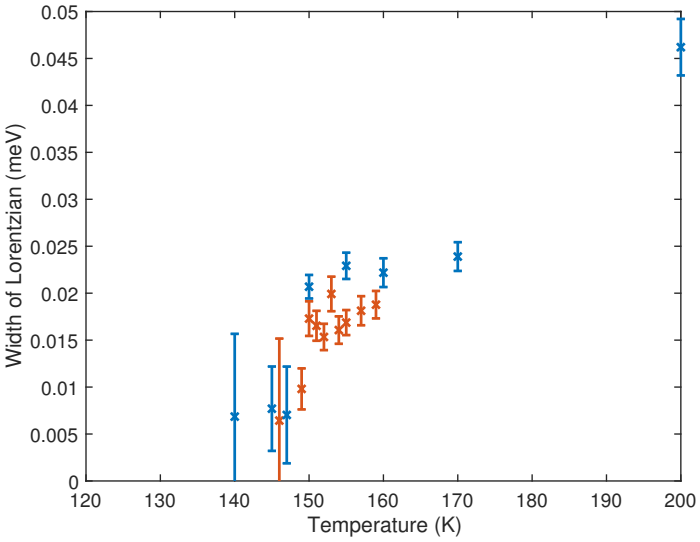

(b) *α dynamical component.*

Figure 6.5 *The variation in full-width at half maximum of the two $|Q|$ averaged fitted quasielastic components with temperature, labelled as β and α. In 6.4 the β contribution (present at all T) was shown in pink, and the α (present at high T) was shown in green. Blue and red data points label results from two separate experiments.*

data points, and therefore the activation energy has a much larger uncertainty, with the final result being $E_a = 113 \pm 110\,\mathrm{K}$. Despite the difficulties in extracting the activation energy for the β contribution, it is clear that there is a reduction in activation energy in phase II. The activation energy for the α dynamical contribution is also impacted by the reduced range of data in the region above the 150 K phase transition to the short-lived tetragonal phase . The resultant activation energy extracted for the α dynamical component is $E_a = 642 \pm 63\,\mathrm{K}$ which is much larger than expected for a dynamical process at this temperature. However this result is strongly skewed by the single data point at 200 K, so while it is possible to assert that the narrow dynamical contribution has a larger activation energy than that of the broader β component the exact values for activation energies cannot be directly compared.

From the fits to the raw data, the elastic incoherent structure factor (EISF) can be extracted, with the form of this detailed in section 4.3. In the calculations of the EISF presented here the intensity of the elastic peak $S_{el}(Q)$ is taken as the area underneath the resolution convolved delta function component of the fit, and the sum $S_{el}(Q)+S_{qe}(Q)$ is taken as the total of the area underneath the delta function component and the relevant dynamical contribution. The measured $I_{EISF}(Q)$ is fitted to a function $A(Q)$ dependent on the proportion of active rotators and radius of rotation, as was discussed in section 4.3. The radius of rotation shall be constrained to be between 0.85 Å, the approximate radius of the hydrogen atoms around the nitrogen atom, and 2.8 Å, the lattice spacing of the low temperature orthorhombic phase.

Plots of the $I_{EISF}(Q)$ extracted from the data at 200 K for both dynamical components are shown in figure 6.7. Multiple models to describe the molecular rotation have been tested and are shown in the figure. The expected models to be appropriate based upon previous studies are the three, four and eight site jump models [40, 104, 149, 183]. The forms of these models are shown in table 4.2. However, from the results obtained for both dynamical components in this experiment, it is clear that that the Q-range constrained by kinematics of the experiment is not sufficient to justify the choice of one model above another. Instead, the simplest model of a rotation on a spherical surface was used for this analysis, plotted in yellow in figure 6.7.

Figure 6.8a shows how the proportion of rotators for the β dynamical contribution changes across the phases. Here, the proportion of rotators increases from low temperature up to a 50% contribution above $\sim$100 K. At the 150 K transition to

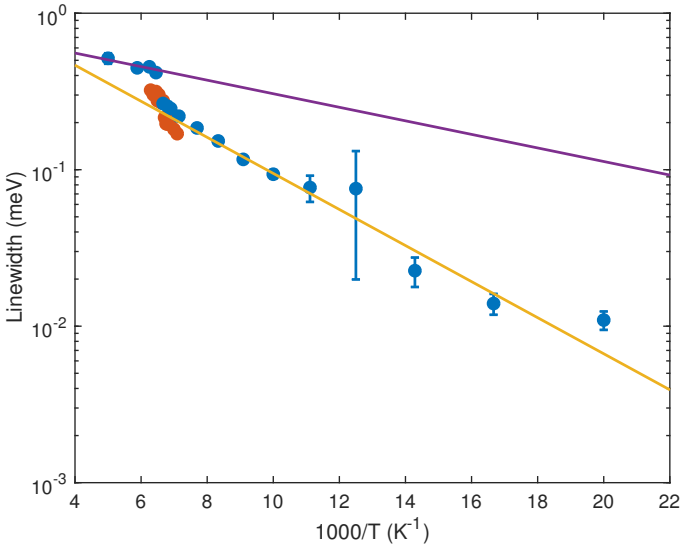

(a) *β dynamical component.*

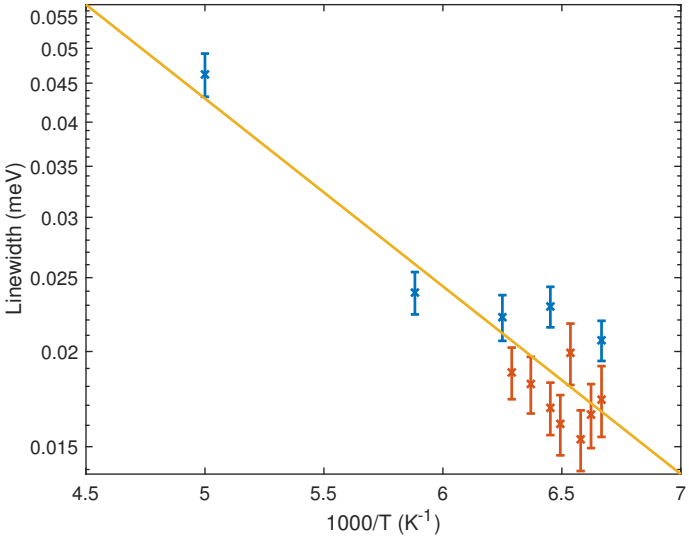

(b) *α dynamical component.*

Figure 6.6 *The Arrhenius fits to the quasielastic linewidths, labelled as β and α. Blue and red data points label results from two separate experiments, with fits shown as straight lines.*

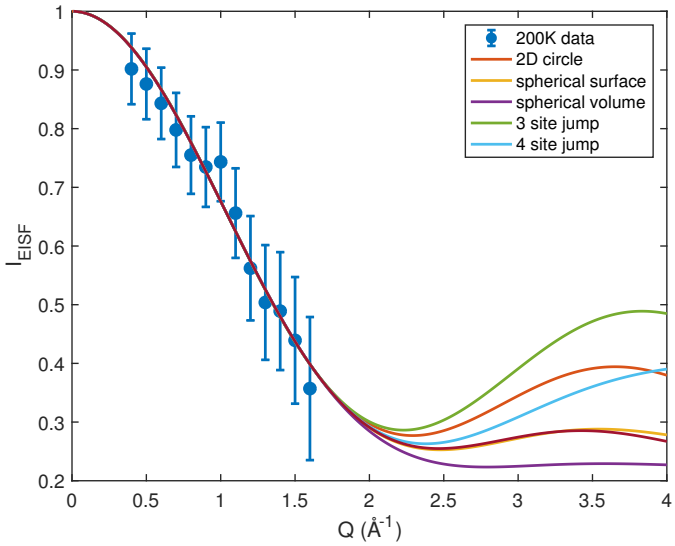

(a) *β dynamical component.*

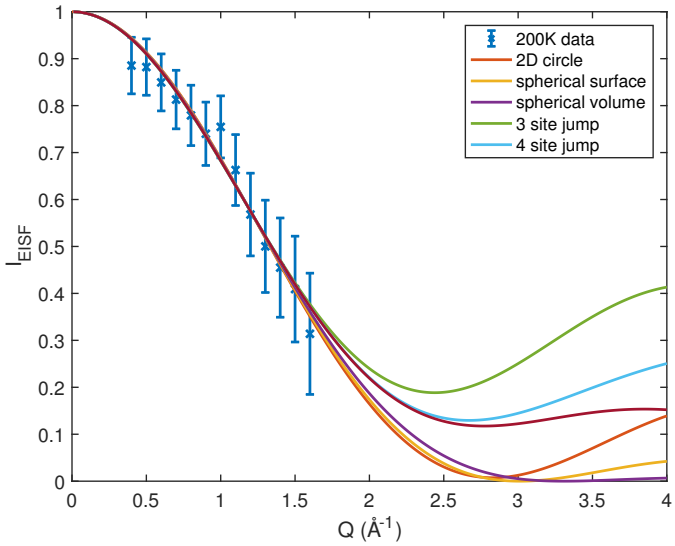

(b) *α dynamical component.*

Figure 6.7 *Comparison of the models that can be fitted to the EISF at* 200 K *for both dynamical components, labelled as β and α.*

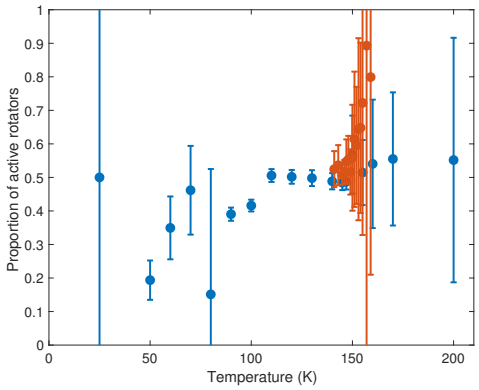

(a) *β dynamical component: change in proportion of active rotators.*

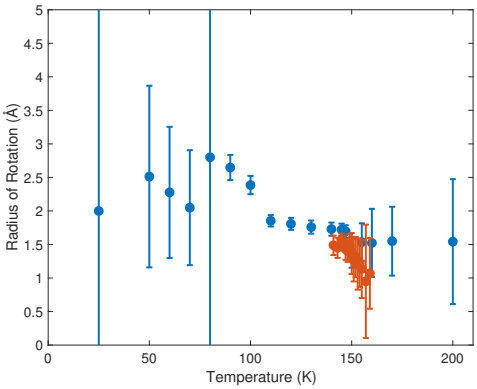

(b) *β dynamical component: change in radius of rotation*

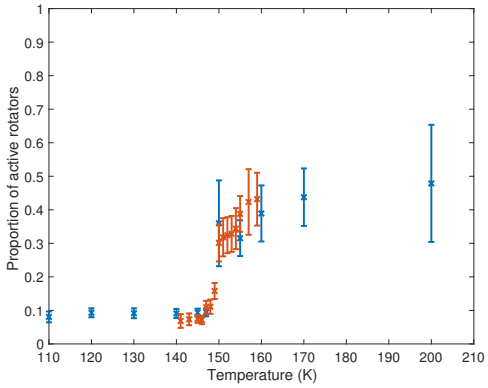

(c) *α dynamical component: change in proportion of active rotators.*

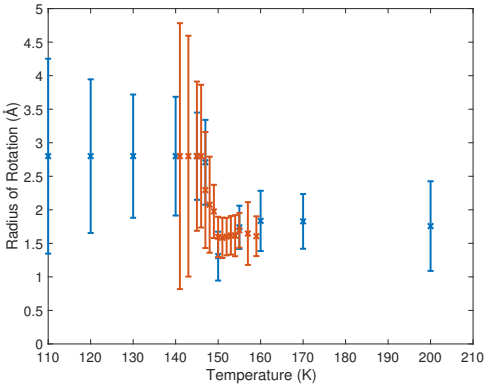

(d) *α dynamical component: change in radius of rotation*

Figure 6.8 *The extracted proportion of active rotators and radius of rotation vs temperature for the two dynamical components, labelled as β and α. Red and blue points signify the two different experiments.*

the short-lived tetragonal phase there is an increase in the active rotators, which is particularly pronounced for the experiment shown in red. However, the final proportion of active rotators reached in phase II is not significantly increased, with the value at 200 K being 55%. The variation in the radius of rotation for the β dynamical component is plotted in figure 6.8b. Below 100 K this value is not stable, but appears to be a larger radius motion. Above 100 K the radius extracted is 1.8 Å, decreasing slightly across the short lived tetragonal phase II to a value of 1.55 Å. The C−N distance in this compound is 1.457 Å [173], so the rotation here appears to be a whole-body motion of the molecule.

The proportion of active rotations for the α dynamical contribution is shown in figure 6.8c. Below 150 K the proportion of rotators is less than 10%, with the value increasing dramatically to 30% at 150 K, reaching a final value of nearly 50% at 200 K. This increase in rotators is a lot more pronounced for the α component than the β, suggesting that the 150 K phase transition to the short-lived tetragonal phase is a key transitory point for this dynamical contribution. The variation in the radius of rotation for the α dynamical component is plotted in figure 6.8d. The values shown here are not well fitted below 150 K, with the extracted values reflecting the maximum radius imposed by the fitting procedure. Above the 150 K phase transition the radius of rotation is 1.8 Å. This is the same radius as was extracted for the β dynamical component below 150 K, and is therefore also identified as a whole-body motion of the molecule.

From these results it is clear that the 150 K transition to the short-lived tetragonal phase III acts as an activation point for the molecular dynamics, in particular the second narrower α dynamical contribution that appears in this temperature region. In the case of the broader β excitation, the linewidth varies most strongly in this short-lived tetragonal phase III, suggesting it could act as a transitory phase for the dynamical motion between phase IV and phase II.

6.2.2 High Energy Inelastic Neutron Scattering and Raman Spectroscopy Results

Previous studies have already characterised the Raman spectra for members of the $MAPbX_3$ family, and the neutron spectra for $MAPbI_3$ [53, 73, 104, 114, 134, 189]. While previous inelastic neutron scattering measurements on $MAPbBr_3$ focussed at low energies below ∼75 meV to characterise the soft modes [173],

here simultaneous neutron and Raman spectroscopy results for energies between 5 and 550 meV (40 to 4400 cm^{-1}) are shown. These higher energies allow the internal molecular vibrations and their response to the structural transitions to be probed.

Typical momentum and energy data sets for $E_i = 650$ meV obtained from MAPS are displayed in figure 6.9 at 5, 151, and 240 K. At small momentum transfers well defined modes are observed. This is particularly prominent in panel (a) (5 K) where a series of sharp excitations are observed below $\sim 8\,\text{Å}^{-1}$ and the intensity grows with increasing momentum transfer as expected for phonon modes or lattice excitations. At higher momentum transfers, these excitations broaden in energy and even appear to disperse at high energies. Given the large momentum transfers, in particular in comparison to Raman spectroscopy which is a strictly $|Q| = 0$ probe, it is inferred that this region is crossing over to the deep inelastic region where the impulse approximation applies and hydrogen recoil effects become important.

Hydrogen recoil is particularly prominent in neutron scattering due to the fact that the neutron mass is of the same order as that of the hydrogen nucleus, meaning that when the H nucleus is struck at high energies, it behaves as if it is free. In the extreme limit of large energy and momentum transfers the energy position of the hydrogen recoil scales as Q^2 with the maximum energy transfer occurring when 2θ =90°. In this data, hydrogen recoil effects appear as a broadening of the signal in the energy at larger momentum transfers, and scattering angle 2θ and this is illustrated in Figs. 6.9 (plotted as a function of $|Q|$) and 6.10 (plotted as a function of 2θ) with an incident energy of E_i =650 meV.

In analysing the INS data and comparing it with Raman spectroscopy, a balance between minimising contamination from recoil effects and obtaining enough statistics for a meaningful spectra had to be established. The data is therefore integrated in 2θ in the range of 0° to 20°, which was found not to result in broadening of the inelastic response while providing enough statistics. The region of integration is shown in figure 6.10.

Figure 6.11 show the Raman and integrated neutron spectroscopy data collected at base temperature (5 K in the orthorhombic phase). The peak positions from the Raman data agree well with that found in previous studies, particularly that of Leguy *et al*, at base temperature, and as such their assignments of the Raman modes are used [73, 104, 114, 127, 134, 189]. Table 6.4 shows the energy ranges

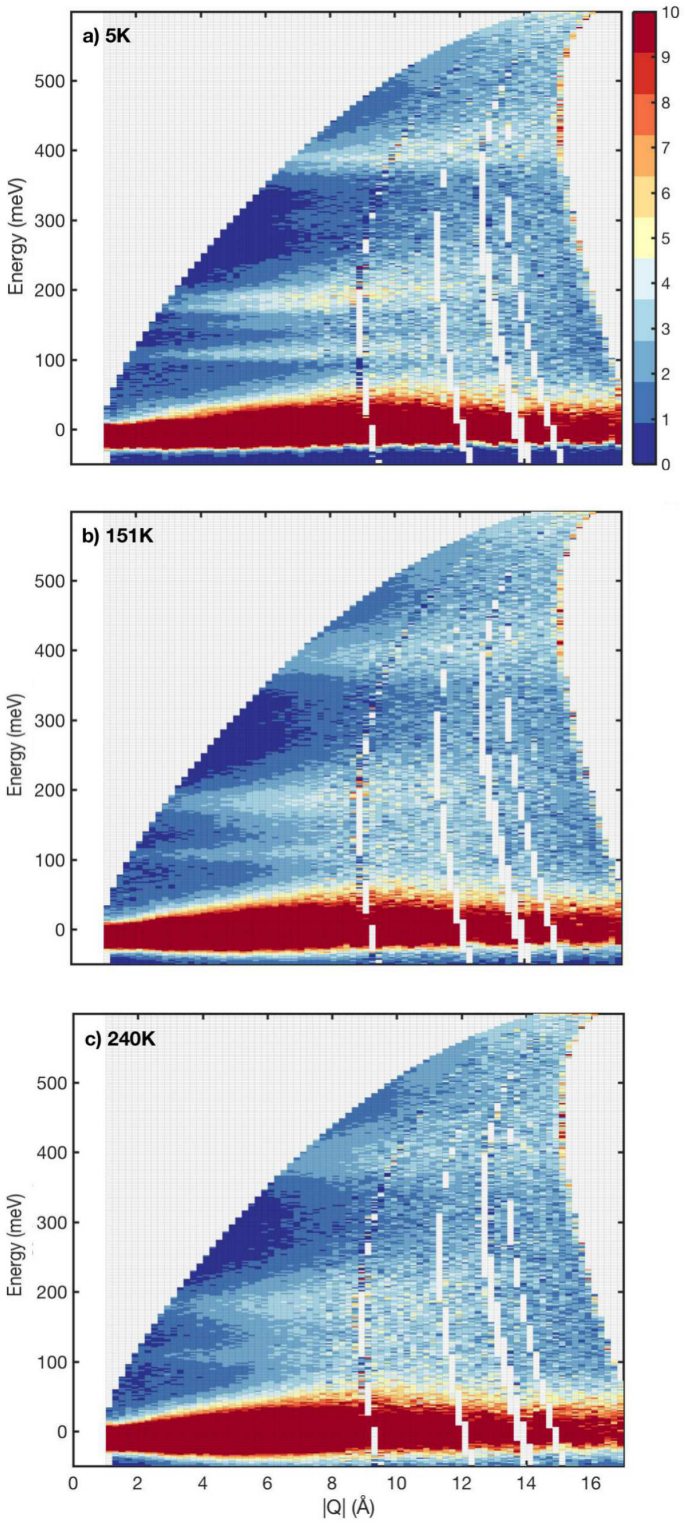

Figure 6.9 *Slices taken from the* 650 meV *data at the three temperatures discussed in this thesis, showing the* $|Q|$ *dependence of the intensities measured.*

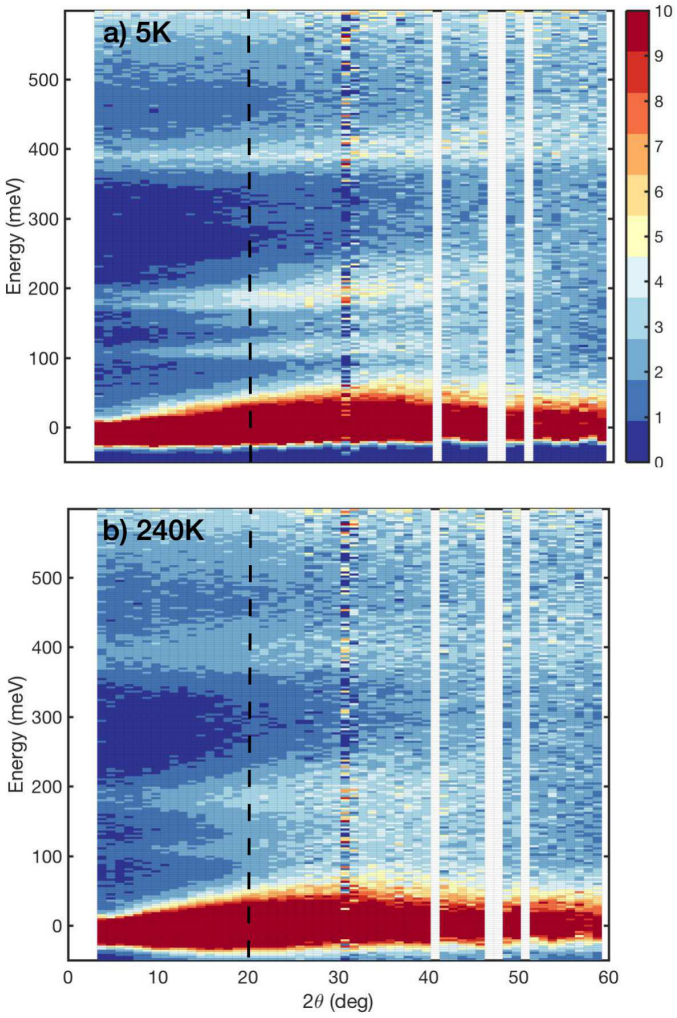

Figure 6.10 *Slices taken from the* 650 meV *data at base and high temperature, showing the* 2θ *dependence of the intensities measured. The dashed black lines show the cutoff at* 20° *which was used to remove hydrogen recoil effects.*

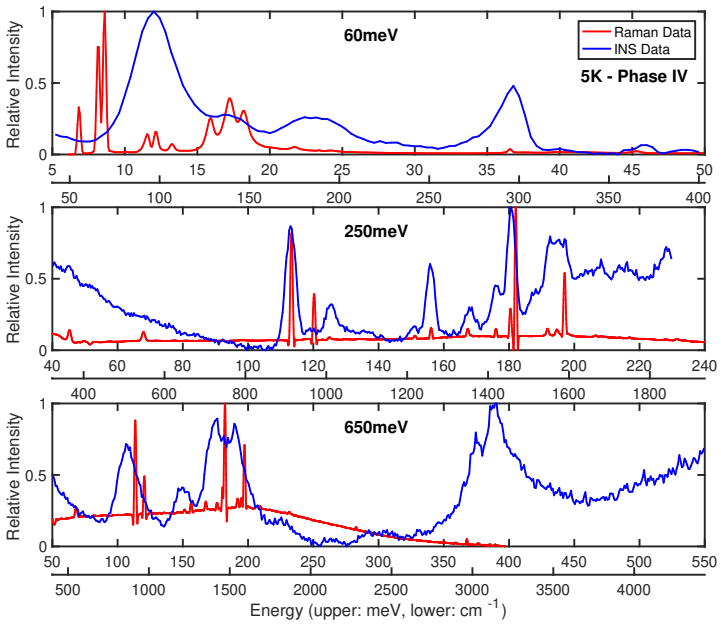

Figure 6.11 *The results from MAPS at 60, 250 and* 650 meV *in the orthorhombic phase at base temperature (*5.3 K*). Raman data is shown in red; inelastic neutron scattering data in blue.*

in which different excitations are observed in this data.

The peak positions in energy from Raman and neutron spectroscopy at high energies (E_i = 250 and 650 meV) show good agreement, with the neutron spectroscopy data being broader in comparison as a result of instrumental resolution. These higher energy modes are linked to intramolecular motions. Such motions are internal to the molecule and therefore do not disperse strongly with momentum. These modes show good agreement between neutron and Raman techniques.

However, there is a clear difference between the neutron spectroscopy and Raman spectra in the low energy area, a regime dominated by modes linked to the rotation of the $PbBr_3$ octahedra, and the lurching of the MA molecule [104, 127]. Such low-energy modes are highly dispersive throughout the Brillouin zone and, while Raman probes the modes at $|Q| = 0$, the neutron spectra performs a momentum averaging $\tilde{S}(Q,E) = \frac{1}{4\pi}\int S(\mathbf{Q},\mathbf{E})\mathbf{d\Omega}$ due to the powder nature of the sample. With lattice vibrations that vary considerably with momentum, a larger difference is therefore expected between Raman and neutron spectroscopy.

Results at temperatures above the transition from an orthorhombic phase are shown in figures 6.12 and 6.13 for 151 K and 240 K respectively. When comparing this to the data taken at base temperature, a large broadening in energy of

Table 6.4 *The energy ranges different excitations in the $MAPbBr_3$ crystal, as reported in reference [104] and observed in my experiment.*

Energy (meV)	Energy (cm^{-1})	Excitation
< 7.4	< 60	Phonons due to octahedral distortions
7.4 - 8.7	60 - 70	"Nodding donkey" around N
8.7 - 17.4	70 - 140	Phonon-like full-body lurching of molecule
17.4 - 19.8	140 - 160	"Nodding donkey" around C
		Attempted roll around C–N
36 - 41	290 - 330	C–N torsion
120 - 154	970 - 1240	C–N bending and stretching
167 - 181	1350 - 1460	CH_3 breathing
181 - 197	1460 - 1590	NH_3 breathing
350 - 372	2820 - 3000	C–H stretching
376 - 394	3030 - 3180	N–H stretching

all excitations is observed in the neutron response. This is in agreement with previous INS and Raman spectra [53, 104].

As temperature is increased the peak positions remain in agreement between neutron and Raman data, however the temperature dependence of the linewidths is different. The INS and Raman results show a difference with the neutron response broadening more noticably with increased temperature than the Raman spectra over a comparable energy range. This is illustrated in table 6.5 which displays the temperature variation of the full width at half maximum for the peak at 113 meV (915 cm^{-1}). This peak was chosen due to its clear separation from other peaks at all temperatures, and has been identified to be linked to the rocking motions of the MA cation [104, 127]. Both neutron and Raman peaks at low temperature are resolution limited. The peak measured with neutrons broadens to ∼10 meV while the Raman peak broadens only to ∼3 meV.

One reason for this increased broadening in the neutron response could be multiple phonon scattering which effectively folds in scattering from larger scattering angles resulting from the large neutron cross section of hydrogen. The possibility of such an effect is investigated in figure 6.14 where the momentum dependence of the neutron response over the range of 175-200 meV is plotted as a function of Q^2. This energy range has been chosen due to the presence of a well defined peak in the 650 meV data at all temperatures probed. However, all other peaks were observed to show a similar temperature dependence in the limit $Q \to 0$ to the one shown here. Normally one would expect the y-intercept in

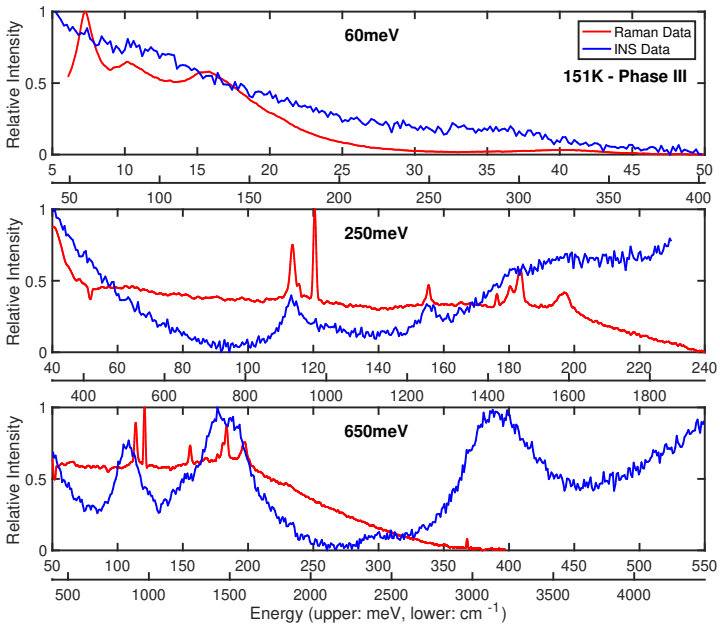

Figure 6.12 *The results from MAPS at 60, 250 and* 650 meV *in the incommensurate/tetragonal phase (*151 K*).*

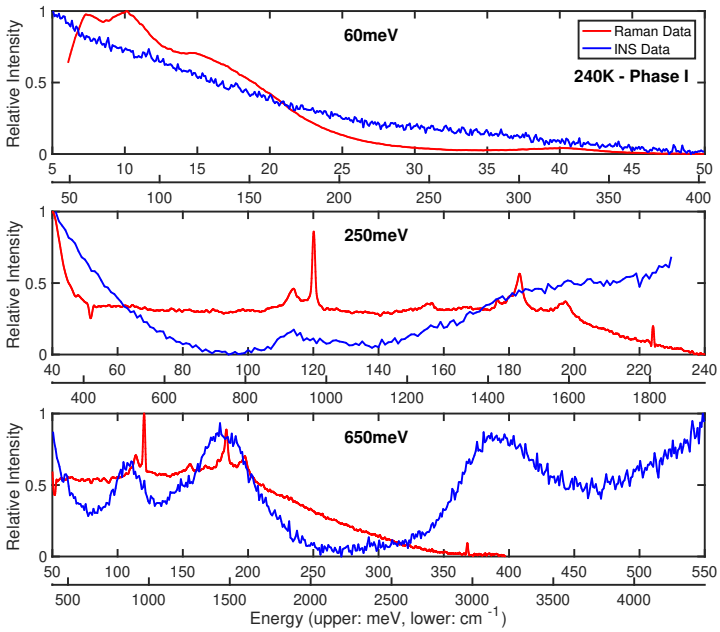

Figure 6.13 *The results from MAPS at 60, 250 and* 650 meV *in the cubic phase (*240 K*).*

Table 6.5 *Comparison of the FWHM of the* 113 meV *peak in the Raman and INS $MAPbBr_3$ data at three different temperatures.*

	FWHM of 113 meV peak (meV)		
Temperature	5.3 K	151 K	240 K
Neutron	5.122 ± 0.151	8.253 ± 0.968	10.176 ± 2.872
Raman	1.057 ± 0.019	2.474 ± 0.040	2.710 ± 0.090

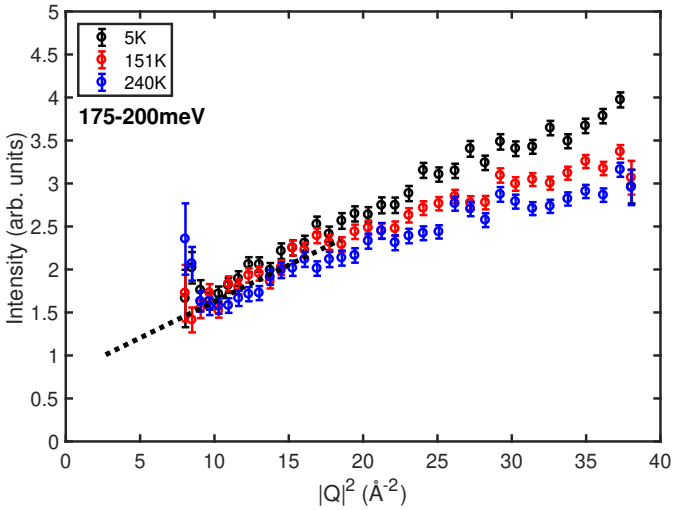

Figure 6.14 *Data collected at* 650 meV*, integrated over an energy range of 175 to* 200 meV *and plotted against $|Q|^2$. A dotted line is plotted as a guide to the eye.*

all cases to be zero, however here no explicit background subtraction has been carried out, leading to the non-zero value extrapolated here.

An increase in multiple phonon scattering would manifest as differing y-intercepts at each temperature. The data is in good agreement at low momentum transfers indicating no observable enhancement or change of multiple phonon scattering with increased temperature. Thus multiple phonon scattering effects are ruled out as the origin of this broadening and it must be a real result. This shall be discussed further in section 6.4.

6.3 $MAPbCl_3$ Quasielastic Neutron Scattering Results

This section concerns the two QENS data sets were collected on $MAPbCl_3$: one on a powder sample, which is studied using IRIS; and the other using a single crystal sample, which is studied using LET. Despite the difference in sample choice, it is possible to compare the two data sets directly. The LET data was powder averaged during processing in Mantid [6] in order to allow for direct comparison between the LET and IRIS data. The aim of analysing the single crystal data as a powder is that a model can be selected that satisfies all of the available data sets. This model can then be applied in future studies to investigate the directional dependance of the QENS signal within a single crystal. However, the LET single crystal data does not extend equally in all three dimensions of Q-space due to the configuration of the detectors and sample, and as such the high $|Q|$ powder averaged results are not truly analogous to powder data.

This section will present analysis from the IRIS and LET experiments side-by-side. However, as the IRIS data are much more complete than the LET in terms of temperature range covered, this will be the primary example given when discussing choice of fits.

Example spectra for the $E_i = 1.84\,\text{meV}$ (IRIS), $6.50\,\text{meV}$ (LET) and $7.38\,\text{meV}$ (IRIS) results are shown in 6.15, at temperatures in the orthorhombic and cubic phases. Each example exhibits two dynamical contributions in the high temperature phase, with all but the $E_i = 1.84\,\text{meV}$ data also exhibiting two excitations in the low temperature phase. All of the data is fit to the following model, which is the same as that used for $MAPbBr_3$ in section 6.2.1:

$$S(Q,E) = I_{el}(Q)\delta(E) + I_1(Q)\frac{\Gamma_1(Q)}{E^2 + (\Gamma_1(Q))^2} + I_2(Q)\frac{\Gamma_2(Q)}{E^2 + (\Gamma_2(Q))^2}, \quad (6.2)$$

where this function is then convolved with the resolution data before the data is fit as detailed in section 4.3. Here the components are currently labelled as simply "1" and "2" as it is not yet known whether all data sets capture the same molecular motions. As will become apparent, the dynamical contributions differ dependent on the incident energy employed, so care must be taken to distinguish between them.

The above fitting method described does not include the $17.80\,\text{meV}$ data set

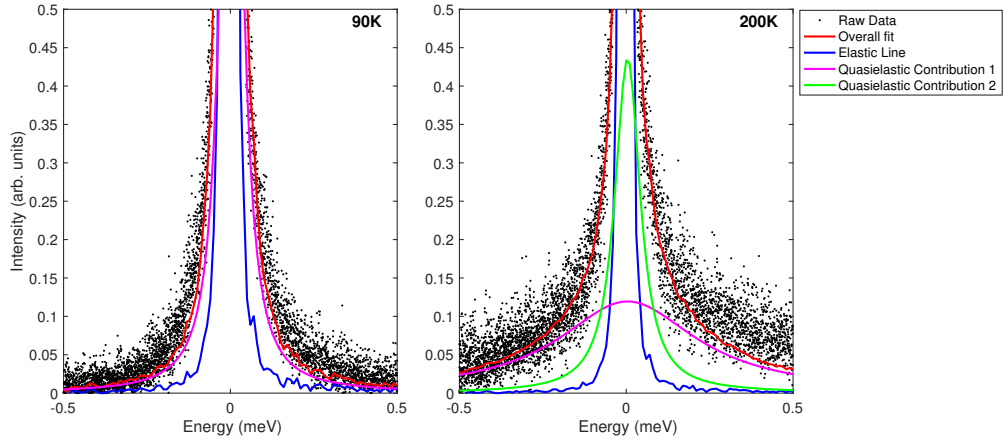

(a) $E_i = 1.84\,\text{meV}$

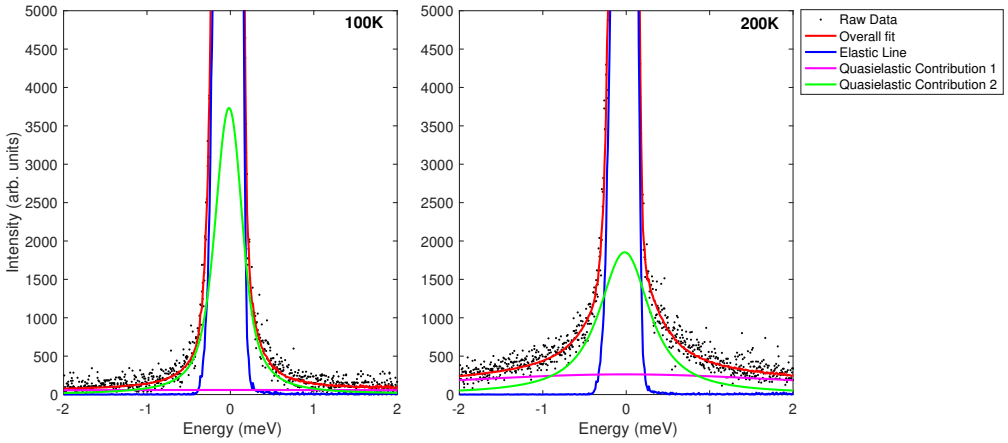

(b) $E_i = 6.50\,\text{meV}$

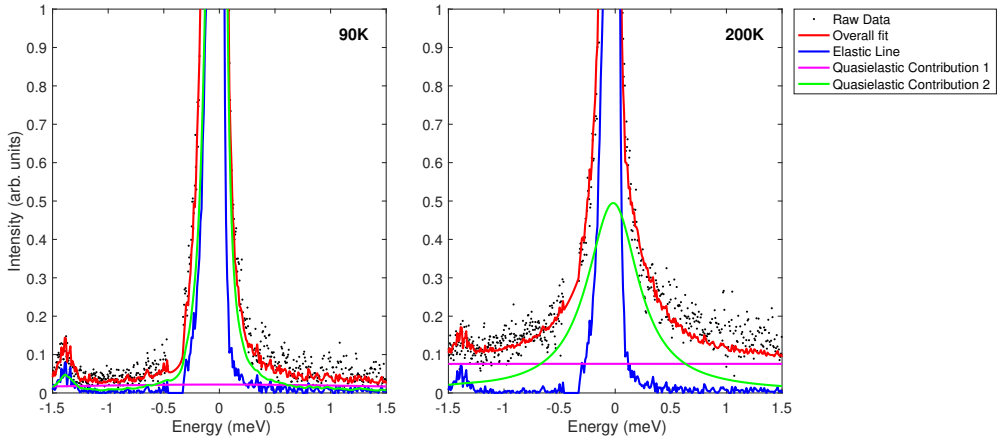

(c) $E_i = 7.38\,\text{meV}$

Figure 6.15 *Examples of the spectra obtained using incident energies* $1.84\,\text{meV}$, $6.50\,\text{meV}$ *and* $7.38\,\text{meV}$ *in the range* $0.9\,\text{Å}^{-1} \leq |Q| \leq 1.0\,\text{Å}^{-1}$. *The black circles show the data points, the red line shows the total fit, the dark blue shows the elastic line, and the magenta, light blue and green lines show the dynamical contributions.*

Table 6.6 *Assignment of the dynamical contributions observed in QENS data dependent on the incident energy E_i used.*

Motion Identifier	Average Linewidth of Dynamical Contribution	E_i of data set	Contribution
α	$\lvert\Gamma(Q)\rvert < 0.1\,\text{meV}$	1.84 meV	Narrower Contribution
		2.03 meV	Narrower Contribution
β	$0.1 < \lvert\Gamma(Q)\rvert < 0.5\,\text{meV}$	1.84 meV	Broader Contribution
		3.34 meV	Narrower Contribution
		6.50 meV	Narrower Contribution
		7.38 meV	Narrower Contribution
γ	$0.5 < \lvert\Gamma(Q)\rvert < 2.5\,\text{meV}$	2.03 meV	Broader Contribution
		3.34 meV	Broader Contribution
δ	$\lvert\Gamma(Q)\rvert > 2.5\,\text{meV}$	6.50 meV	Broader Contribution
		7.38 meV	Broader Contribution

collected on LET. This data set is found to be inappropriate for use in QENS analysis. The low counts and reduced resolution for this incident energy mean that for some temperatures and Q values the elastic line is indistinguishable from the inelastic contribution. Additionally, Bragg peaks at larger Q mean that any benefits from the increased Q range are lost. As such, this data set has been discarded and will not be included in subsequent discussion.

The full-width at half-maximums $\Gamma(Q)$ of all the dynamical contributions observed appear not to vary strongly with $|Q|$, and thus their average can be taken in order to compare them. A $|Q|$ independent linewidth is associated with rotational motion of the molecule. Plots of the full-width at half-maximum Γ_n for all of the dynamical components observed are shown in figure 6.16. Four different regions are identified into which the dynamical contributions from individual data sets may be sorted, and it is therefore postulated that depending on the incident energy used different molecular motions may be observed. Table 6.6 shows the assignment of the dynamical contributions from each data set into four different molecular motions, labelled α, β, γ and δ.

The molecular motions with the narrowest linewidth, α and β both show a clear step change at the 172 K phase transition into the short-lived tetragonal phase. On the contrary, both γ and δ appear to be temperature independent, with γ apparently decreasing in full-width at half-maximum with temperature. This shows that it is the longer-lifetime dynamics that are more sensitive to the change in structure at the 172 K transition.

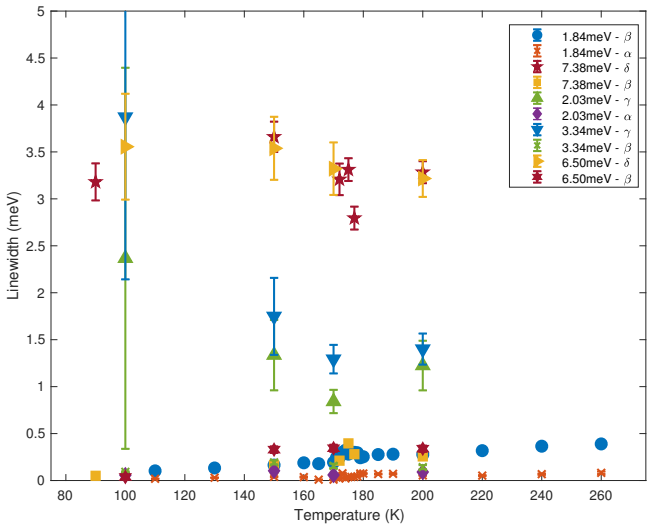

(a)

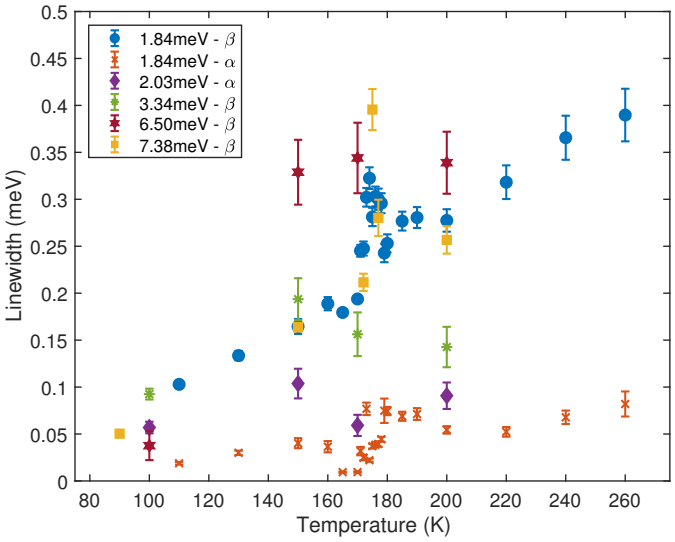

(b)

Figure 6.16 *The variation in full-width at half maximum Γ_n of the $|Q|$ averaged fitted quasielastic components with temperature, labelled by the incident energy. The second plot shows a closer view of the smaller full-width at half maximum region. The legends use the identifiers for each contribution as shown in Table 6.6.*

It is desirable to more closely examine the temperature dependence of these molecular dynamics. However, as the γ motion is only represented by four data points, further analysis will not be carried out on this, as the temperature range covered here is insufficient to draw full conclusions. In addition, the 2.03 meV and 3.34 meV contributions to the α and β motions respectively do not well fit the temperature trends observed, suggesting that they are not well fitted by the model chosen to describe the linewidths. These incident energies will therefore not be used in the analysis going forwards.

The average linewidth for these molecular motions is equal to the diffusion coefficient multiplied by a constant, and thus is expected to have an Arrhenius dependance on temperature. Graphs showing the linewidth against $1000/T$ for the α and β dynamical contributions are shown in figure 6.17. As the δ molecular motion appears to be temperature independent no attempt is made to fit an Arrhenius relation to this data. Both the α and β motions appear to have two different regions of behaviour, which are separated by the short-lived tetragonal phase (between 172 K and 178 K). For the α contribution, at temperatures above 178 K the Arrhenius relation appears flat, so no attempt is made to extract the activation energy from this. Below 172 K the α contribution has an activation energy of $E_a = 277 \pm 63$ K. The β contribution also shows a reduced gradient above 178 K, but here two activation energies may be extracted. Below the short-lived tetragonal phase the extracted activation energy for the β component is $E_a = 248 \pm 10$ K, and above 178 K one finds $E_a = 123 \pm 60$ K.

The elastic incoherent structure factor (EISF) is calculated from the area under the elastic and quasielastic components to the fits to the raw data, with each dynamical contribution treated separately. Figure 6.18 shows the EISF extracted for each of the dynamical components of the 1.84 meV, 6.50 meV and 7.38 meV data at 200 K. As in the treatment of the $MAPbBr_3$ data presented in section 6.2.1, multiple models to describe the molecular motion have been tested. In the case of the 1.84 meV data, there is not sufficient $|Q|$ range to distinguish between the models. However, for the 6.50 meV and 7.38 meV data there is a greater coverage in $|Q|$, from which it can be observed that the data is better fitted to a model with a larger number of jumps or rotation on a sphere. As it cannot be ascertained from this exactly which model is preferable, the model of a rotation on a spherical surface was used for analysis of all three molecular motions (α, β and δ).

The proportion of active rotators for the α component is shown in figure 6.19a.

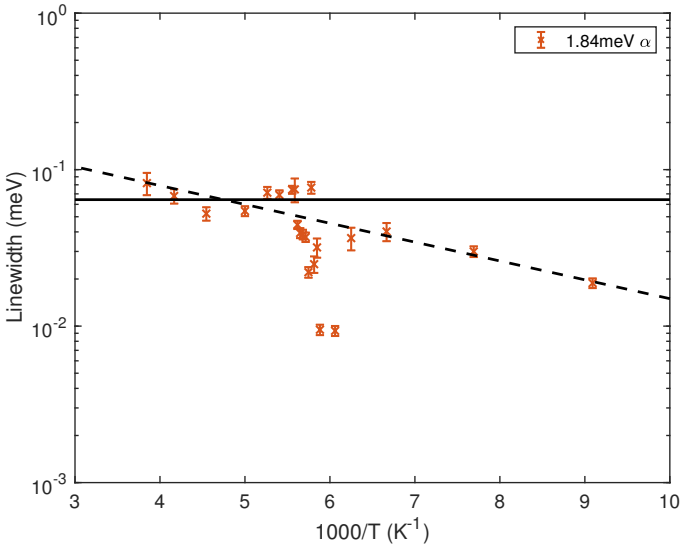

(a) *α molecular motion.*

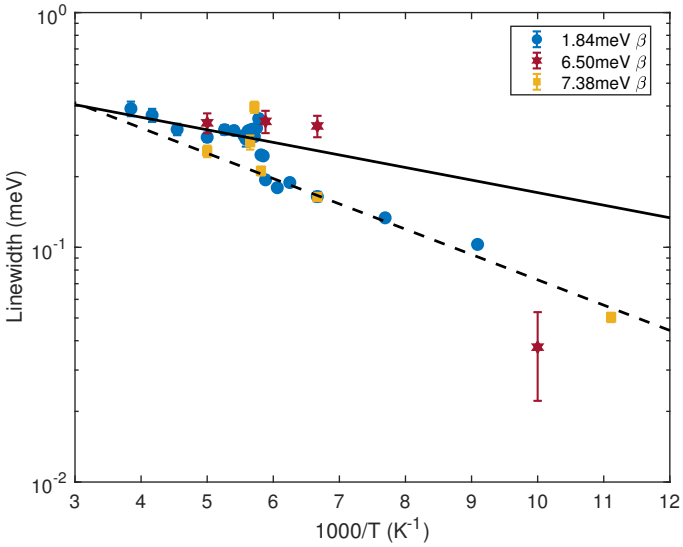

(b) *β molecular motion.*

Figure 6.17 *The Arrhenius fits to the quasielastic linewidths of two of the dynamical contributions measured: the α dynamical contribution (*1.84 meV *data), and the β dynamical contribution (*1.84 meV, 6.50 meV *and* 7.38 meV *data),*

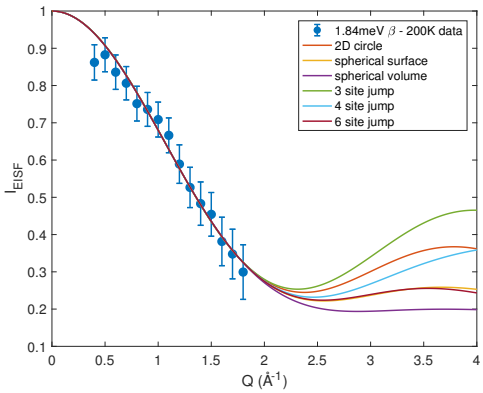

(a) 1.84 meV β *contribution.*

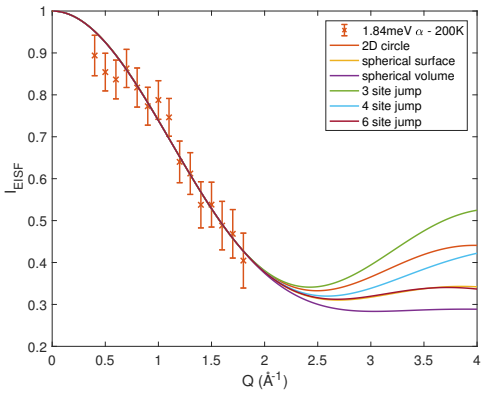

(b) 1.84 meV α *contribution.*

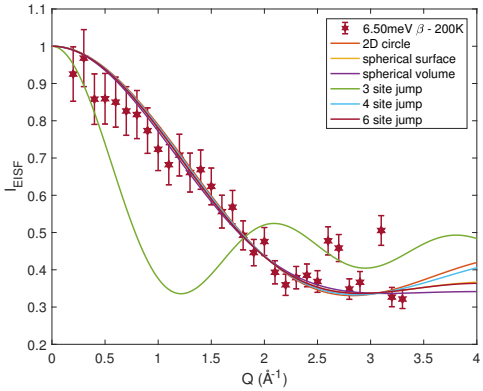

(c) 6.50 meV β *contribution.*

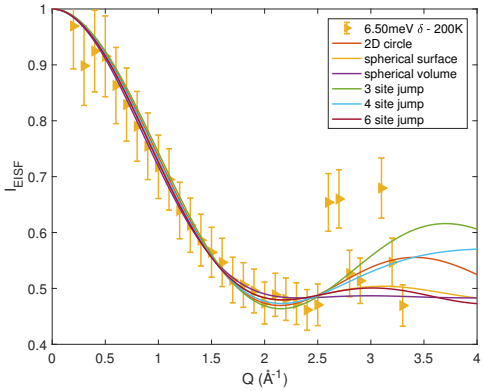

(d) 6.50 meV δ *contribution.*

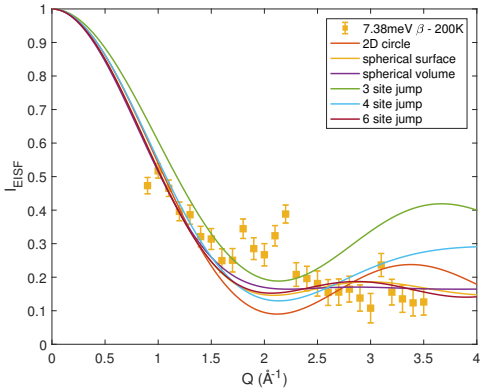

(e) 7.38 meV β *contribution.*

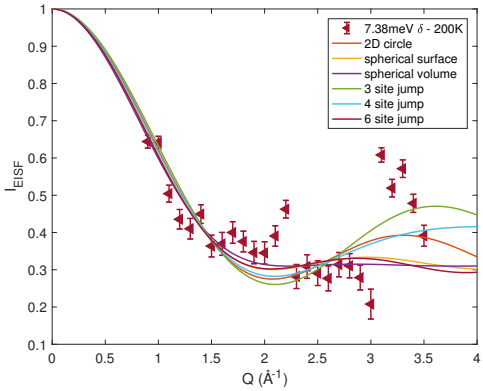

(f) 7.38 meV δ *contribution.*

Figure 6.18 *Comparison of the models that can be fitted to the EISF at* 200 K *for the dynamical components observed in the in the* 1.84 meV, 6.50 meV *and* 7.38 meV *data. Items on the left hand side (6.18a, 6.18c and 6.18e) all pertain to the* β *dynamical contribution. 6.18d and 6.18f both pertain to the* δ *dynamical contribution.*

This shows an increase in proportion of active rotators from 30% to 55% at the transition to the short-lived tetragonal phase (172 K). However, the proportion of active rotators appears to re-normalise again above 240 K, suggesting the increase in rotators for this motion is exaggerated by this fit. Figure 6.19b shows the radius of rotation for the α motion. Here, there is an increase in the radius of rotation on the approach to the short-lived tetragonal phase, which then reduces again after the phase transition. The value for the radius of rotation found between 172 K and 220 K is 1.5 Å, which is comparable to the C−N distance of the molecule, identifying it as a whole-body molecular motion.

In the case of the β component, a reliable fit to the EISF of the 1.84 meV data was not possible below 172 K, however results were successfully extracted from the 6.50 meV and 7.38 meV at all temperatures. The difficulty in fitting the 1.84 meV data is likely due to the low contribution of this signal in comparison to the elastic line at low temperatures. In figure 6.19c, the proportion of active rotators appears to not be strongly temperature dependent, though the data sets are not well in agreement. However, there appears to be an increase in proportion of rotators of order 20% between the 172 K and 178 K phase transitions. The radius of rotation for the β component shown in figure 6.19d appears invariable with temperature. Again, there is variation in the extracted radius of rotation between the data sets, however the value is comparable in magnitude to that of the α motion and is again identified as a whole-body motion of the molecule.

Finally, in the case of the δ component, figure 6.19e illustrates a smooth increase in proportion of rotators with temperature, going from 25% at 100 K to 70% at 200 K. This strong increase is perhaps unexpected based off the temperature independence of the average linewidth. This implies that this excitation is not best understood when averaged across $|Q|$. Figure 6.19f shows the temperature dependence of the radius of rotation of the δ motion. The two data sets presented here do not well agree on the response of the radius of rotation to the phase transition at 172 K. However, a change in radius of rotation from 1 Å to 2 Å, as shown by the 7.38 meV data, seems unlikely. Therefore it is concluded that while the short-lived tetragonal phase may have an influence on the radius of rotation, this effect cannot be quantified from this data. This δ motion appears to have a smaller radius of rotation than the α and β rotations, meaning that this may be linked to the rotation of the hydrogen atoms around the C−N axis.

These results found four different molecular motion in the QENS data obtained on $MAPbCl_3$, each with a different energy scale. From these results it is apparent

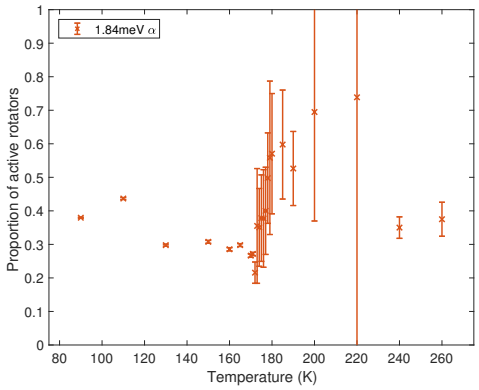

(a) *Proportion of active rotators extracted from α dynamical contribution.*

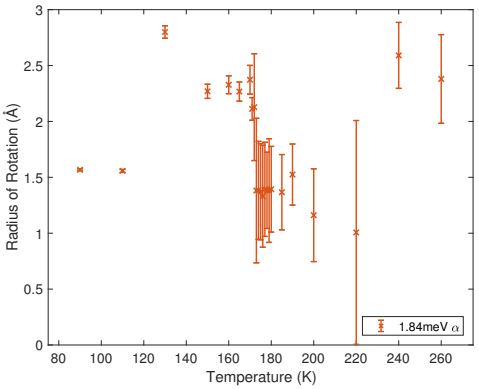

(b) *Radius of rotation extracted from α dynamical contribution.*

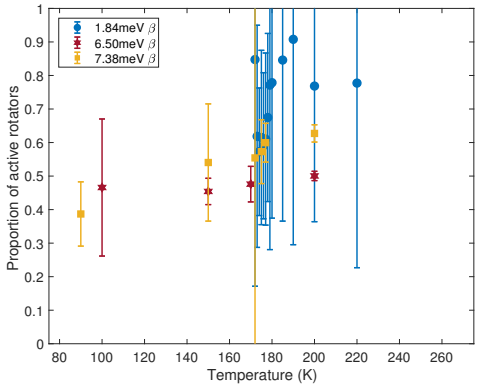

(c) *Proportion of active rotators extracted from the β dynamical contribution.*

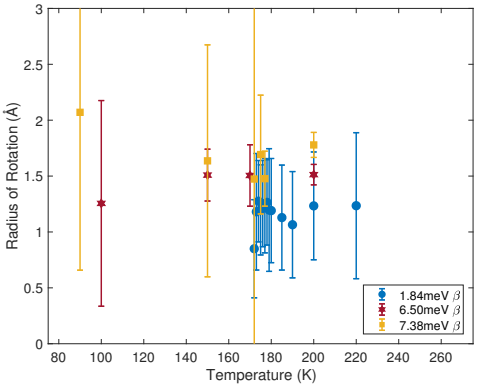

(d) *Radius of rotation extracted from the β dynamical contribution.*

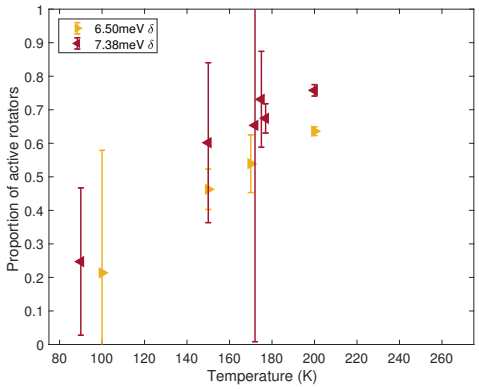

(e) *Proportion of active rotators extracted from the δ dynamical contribution.*

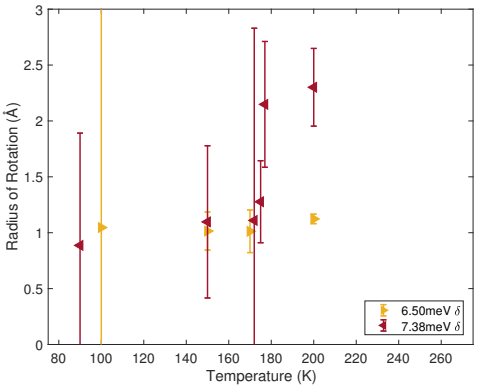

(f) *Radius of rotation extracted from the δ dynamical contribution.*

Figure 6.19 *The extracted proportion of active rotators and radius of rotation from the EISF fits to the* 1.84 meV, 6.50 meV *and* 7.38 meV *data, with three different dynamical contributions (α, β and γ) identified in the data.*

that the 172 K transition to the short-lived tetragonal phase II has an influence on the molecular dynamics, which manifests differently depending on the molecular motion in question.

6.4 Discussion

In this chapter so far three studies have been presented: two examining $MAPbBr_3$, and one focussing on $MAPbCl_3$. In this section the implications from these results will be discussed.

Firstly the results from the QENS experiments on $MAPbBr_3$ and $MAPbCl_3$ shall be summarised. The study of $MAPbBr_3$ identified two dynamical components of the molecule, the broader of which only enters the timescale measurable on the equipment at a higher temperature. In this compound the narrower dynamical component, referred to as α, appears at approximately 150 K, simultaneous to the transition to the short-lived tetragonal phase III. The broader dynamical component, referred to as β, also responds to the short-lived tetragonal phase, showing a large increase in quasielastic linewidth in this temperature range. In $MAPbCl_3$, by using multiple incident energy probes four dynamical dynamical contributions were measured. The two lower energy of these are identified as being the same molecular motions as observed in $MAPbBr_3$. Interestingly, the α molecular motion that is associated with the short-lived tetragonal phase in $MAPbBr_3$ is here observed to be onset at at 100 K, 70 K below the tetragonal phase in $MAPbCl_3$. The two high energy dynamical contributions in $MAPbCl_3$ appear mostly independent of temperature, whereas the two lower energy once again exhibit an increase in quasielastic linewidth associated with the short-lived tetragonal phase.

When the proportion of active rotators are extracted from the EISF, both $MAPbBr_3$ and $MAPbCl_3$ show an increase upon the transition out of the orthorhombic phase. This is most pronounced for the narrower dynamical α contribution in $MAPbBr_3$, with a similar, albeit less dramatic response, seen for the α contribution in $MAPbCl_3$. These rotations have a radius around 1.5 Å, which is reflective of a whole body molecular rotation. The broader β dynamical contribution in $MAPbBr_3$ and its equivalent in $MAPbCl_3$ both show increases in proportion of rotators upon transitioning to the short-lived tetragonal phase. In this case the effect is slightly greater in $MAPbCl_3$, though they are comparable

within error. These rotations once again have a radius of rotation of 1.5 Å, with a larger radius extracted for $MAPbBr_3$.

The fits to the EISF for the higher energy δ excitation in $MAPbCl_3$ showed a linear increase in active rotators for this motion. This δ component has a smaller radius of rotation than the α and β motions, suggesting it is a signature of the hydrogen ions rotating around the molecular axis. That this component is less sensitive to the phase transitions in the compound is reflective of the greater freedom of the hydrogen ions to move compared to the molecule as a whole, despite their participation in bonding.

In both $MAPbBr_3$ and $MAPbCl_3$ the orthorhombic phase is the one in which the molecular motions are most arrested. It is interesting that in both compounds the change in molecular dynamics is not a step change but rather occurs through a short-lived intermediate tetragonal phase. This suggests that the changing molecular dynamics could be the origin of these intermediate short-lived tetragonal phases. It is interesting that the molecular activity shows a gradual increase across the short-lived tetragonal phase, rather than step changes between phases, especially as the transitions are first order. However, in $MAPbBr_3$ and $MAPbI_3$ symmetry breaking domains have been observed to survive past the phase transition between the cubic and tetragonal phases [46, 61], meaning that some phase coexistence is possible. It could also be the case that the molecular motions in the short-lived tetragonal phase are more temperature sensitive than those in the other phases, by having an activation energy similar to the temperature at which the short-lived tetragonal phase is observed.

A separate analysis of the E_i =1.83 meV $MAPbCl_3$ data presented in this chapter has been published by Songvilay *et al* [166]. In their paper a single Lorentzian fit was used, as opposed to the two Lorentzians used here. As such, there are key differences between that work and this. In particular, this thesis has argued that the presence of multiple dynamical components is key to fully understanding the impact of the molecule on the phase transition at 171 K in $MAPbCl_3$. The conclusions presented by Songvilay *et al* state that the hydrogen bonding between the molecule and inorganic framework has no influence on the phase transitions of the system, and that the molecular and and framework dynamics are decoupled. They evidence this by comparing the disappearance of inelastic modes at 100 K to the apparent lack of change in quasielastic contribution at this temperature. However, the work presented in this chapter sees a key change in the quasielastic signal at 100 K: namely, the appearance of the narrow α quasielastic contribution.

Indeed, high quality fits to the quasielastic signal in $MAPbCl_3$ are difficult at temperatures below 100 K, due to the small size of the signal when compared to the instrumental resolution. The simultaneous appearance of these dynamical components in the timescale probed in this experiment and disappearance of the low energy inelastic modes implies that the amount of disorder in the system is linked to the activity of the molecule and the hydrogen bonding.

Previous QENS studies of $MAPbI_3$ have observed two dynamical components. Leguy *et al* focussed on the tetragonal and cubic phases, but nonetheless observed both rotations 20 K below the tetragonal to orthorhombic transition [103]. In contrary, Li *et al* only identified the motion of the H atoms around the C-N axis as persisting in the low temperature orthorhombic phase [106]. Support for full-body cation motion in the low temperature phase of $MAPbI_3$ comes from INS [53], and dielectric measurements and calorimetry where significant motion of the MA cations was observed down to 70 K [63]. It should be noted that the tetragonal phase in $MAPbI_3$ has a much larger stability range than that of the short-lived tetragonal phases which are identified as being regions of changing dynamics in this work.

While all previous studies of the dynamics of the $MAPbX_3$ compounds have identified two components, a comparison of the timescales extracted from experiment compiled by Gallop *et al* shows an interesting disparity [65]. The timescales of the two dynamical components extracted from experiment range from 0.1 to 3.1 ps for the "faster" contribution and from 1.2 to 108 ps for the "slower" excitation. This large range of dynamical timescales is evidence for the observations made on $MAPbCl_3$ in this chapter: namely that there are multiple energy scales of molecular dynamics which can be probed by tuning the experimental parameters.

The Arrhenius results extracted for the low temperature othorhombic phase whole-body molecular dynamical component in $MAPbBr_3$ and $MAPbCl_3$ are shown in table 6.7. The key results that may be compared are that of the β dynamical component. In the orthorhombic phase the activation energy for this motion is smaller in $MAPbCl_3$, and above the short-lived tetragonal phase the two activation energies are within error, with the value extracted for $MAPbBr_3$ being the slightly smaller.

Literature values for the activation energies of molecular dynamical components from Arrhenius fits are also shown in table 6.7. The result from Swainson *et al*

Table 6.7 *Results for activation energies found in these studies and literature values are compared. The activation energies are extracted from Arrhenius fits to the quasielastic diffusion coefficient ($MAPbCl_3$, this study) or linewidth (all others shown).*

	This study		**Literature value**		
	E_a (K)	Temperature Range (K)	E_a (K)	Temperature Range (K)	Reference
$MAPbCl_3$	277 ± 63	α $90 - 170$	243 ± 15	$30 - 160, 180 - 260$	[166]
	248 ± 10	β $90 - 170$			
	123 ± 60	β $170 - 260$			
$MAPbBr_3$	275 ± 6	β $50 - 145$	323 ± 20	$\sim 50 - 150$	[173]
	113 ± 110	β $150 - 200$			

for $MAPbBr_3$ is very different from what is observed here. Their results used a single Lorentzian fit, and as the α contribution in $MAPbBr_3$ is not present at this temperature this is expected to sufficiently describe the data. However, the instrument used by Leguy *et al* differed in incident energy from the one in this study, and therefore they are likely probing a different excitation to that observed here. Songvilay *et al*'s reported activation energy for $MAPbCl_3$ compares well to the one found in this study. This is reassuring as their analysis was carried out on the 1.83 meV data set presented in this chapter. However, this study has shown that the importance of considering multiple dynamical contributions in describing the methylammonium lead halides. Additionally, Songvilay *et al* are averaging two regions which one would expect to have differing activation energies, due to the different local environments of the molecule in each. No literature results for $MAPbI_3$ are shown, as no activation energy for the full-body rotation in the low temperature orthorhombic phase was found from a thorough literature search.

Hydrogen bonding is promoted when it is between two strongly electronegative atoms. Halogens have high electronegativity: fluorine has the largest of the elements in the periodic table, with the electronegativity decreasing down the group. Thus $MAPbCl_3$ would be expected to have stronger hydrogen bonding than $MAPbBr_3$. However, it has also been suggested that the smaller cage size in $MAPbCl_3$ means that there is a reduced energy barrier to rotation, as the N–H···X bond length is required to change less during molecular rotation [65]. The competition of these two energy barriers to dynamical activation perhaps explains why the activation energies for the β molecular motions are comparable in $MAPbBr_3$ and $MAPbCl_3$. The significant decrease of activation energy in $MAPbCl_3$ in the cubic phase suggests an associated decrease in hydrogen bonding.

It can be posited that the larger size of the inorganic cages in the cubic phase result in length scales less favourable for hydrogen bonding, allowing for increased molecular activity.

The importance of hydrogen bonding in these compounds has been previously studied both computationally and experimentally (see references [88, 101, 102, 190]). In particular, Yin *et al* report a drop in hydrogen bond strength as temperature is increased and the phase transitions occur, exactly in line with what is reported here [190]. In opposition to the conclusion that there is increased hydrogen bonding as the halide ion decreases in size, Svane *et al* suggest from their calculations that all of the $MAPbX_3$ compounds have the same hydrogen bond strength [172]. However, their results describe the behaviour at 317 K, where the hydrogen bonding is expected to be reduced due to increased cage size and thermal effects. As such, the low values for hydrogen bonding calculated by Svane *et al* are in agreement with the reduced values for activation energy found as temperature increased in these compounds.

The study of $MAPbCl_3$ was initiated to investigate the claim that the MA cation has two preferred orientations in the low temperature orthorhombic phase, as opposed to the single preferred orientation seen in $MAPbBr_3$ and $MAPbI_3$ [86, 138]. This study found two dynamical components related to the whole-body motion of the molecule (the α and β components). Both components were present above the short-lived tetragonal phase in $MAPbBr_3$ and $MAPbCl_3$, however, in the low-temperature orthorhombic phase the α component was only present in $MAPbCl_3$. This suggests that the molecule in the orthorhombic phase of $MAPbCl_3$ has an additional degree of freedom, in agreement with the suggestion that the molecule has two available orientations rather than one.

Now the spectroscopic study of the internal molecular motions of $MAPbBr_3$ obtained using a combination of the inelastic neutron scattering and Raman spectroscopy on MAPS shall be discussed. The energy locations and the temperature dependence of the Raman data presented are generally in agreement with previous studies [53, 73, 104, 114, 134, 189]. At low energies below $\sim$50 meV, Raman and neutron spectroscopy are in agreement with both showing a significant temporal broadening of the excitations upon heating from the orthorhombic phase. This broadening was previously linked to the onset of fast molecular relaxational dynamics [173]. This is corroborated by the QENS data on $MAPbBr_3$ discussed above. However, Raman and neutron spectroscopy show differences at higher energies with neutron spectroscopy measuring broadened

linewidths of internal molecular motions.

There are several possible reasons why this difference between neutron and Raman techniques might be observed. Firstly, Raman spectra are strictly at $|Q| = 0$, whereas inelastic neutron scattering integrates and averages over all $|Q|$ as discussed above owing to kinematics and powder averaging. This means that an effect at other positions in momentum, for example the zone boundary, could cause the momentum averaged energy width to be increased more than what is measured at a single wavevector like with Raman spectroscopy at $\mathbf{Q} = \mathbf{0}$. Studies have suggested that the electronic bandstructure may indicate a preferential coupling between lattice and electronic degrees of freedom at non zero $|Q|$ [26, 124]. As such it is expected that there might be a coupling of internal modes at regions away from the zone centre. However, the high energy internal molecular excitations observed in INS are highly localised in real space and therefore are expected to show no momentum dependence. Momentum averaging is thus ruled out as the cause of the broadening of neutron spectroscopy data.

Secondly, there is the possibility Raman techniques preferentially measure molecules close to the surface (see for example surface enhanced spectroscopy discussed in reference [39]), whereas inelastic neutron scattering considers the bulk system. However, while surface over bulk differences have been suggested in the organic-inorganic perovskites (for example the effect of dimensionality discussed in reference [143]), this latter possibility is unlikely in this case given that surface-enhanced Raman spectroscopy in molecular systems and liquids has typically resulted in a broadening of linewidths or intensity enhancement at the surface. Here, the reverse is true with the Raman measurements being more well defined in energy than the bulk neutron scattering technique. The agreement between neutron and Raman at lower energies also does not suggest a near surface versus bulk difference for neutron and Raman spectra noted here.

Thirdly, the inelastic neutron spectra are dominated by hydrogen cross section, whereas Raman is more sensitive to heavier elements, meaning that neutron scattering disproportionately samples the motions on the hydrogen sites. If this were the reason for the broadening, it would indicate a distribution of local environments experienced by the hydrogen ions, resulting in a corresponding spread in energy scales for the molecular motions involving them. The suggestion that the molecular cation in the system is experiencing a range of different local environments is supported in other experimental studies: ARPES studies of

$MAPbBr_3$ find both centrosymmetric and non-centrosymmetric domains which persist throughout the low temperature phase [128]. The full-body molecular motions present at all temperatures as observed from the QENS study presented in this chapter further corroborate the existence of multiple hydrogen local environments existing in the crystal at any given moment. It is therefore concluded that this is the reason for the observed difference in broadening between the INS and Raman results at high temperatures.

In combination, the INS and QENS results presented lead to the key conclusion that there is a large increase in disorder and molecular activity as temperature is increased. It is clear that some, but not all, of this motion is associated with the phase transitions in the material. The reduced molecular dynamics in the low temperature phases result in less distortion of the inorganic framework as the hydrogen bonds reorient. In the measurements presented in this thesis, these molecular dynamics persist down to the lowest temperatures measured, though they are significantly lessened at this point. Other studies have also observed such low-temperature molecular dynamics. In particular, in their computational results on $MAPbI_3$ Druzbiki *et al* identified molecular cation motion down to liquid helium temperatures [53]. The term "glassy disorder" was coined by to describe the strongly arrested molecular motions in the low temperature phase [63]. The persistent cation disorder throughout the phase diagram has lead to the $MAPbX_3$ family being labelled as plastic crystals [60]. It is a result of this disorder that, despite ferroelectric domains being predicted computationally [103, 182], experimental observations have ruled that the overall compound is not ferroelectric [147].

As it is the photovoltaic properties of these materials that make them of interest to study, the link between the molecular dynamics and the electronic properties must be discussed. The key contributions to the edges of the band structure in $MAPbI_3$ come from the hybridisation of the $5p$ orbitals of iodine and $6s$ orbitals of lead for the valence band, and the empty $6p$ orbitals of lead for the conduction band [59, 79]. While the MA cation does not contribute directly to the band structure, studies have identified a coupling between the cation rotation to the quasiparticle band gap of the system through hydrogen bonding between the cation and inorganic cages. This then influences the band gap of the system, with the states near the top of the valence band stabilised by the octahedral tilting in the low temperature phase [66, 101, 102]. The results presented in this thesis support this concept of valence band stabilisation, with the molecular dynamics

observed to slow in the low temperature phase, resulting in less distortion of the inorganic framework. They do also suggest that even in the orthorhombic phase the band gap could be sensitive to changes in the cation dynamics.

Therefore, the observed difference in the dynamics of the system between low and high temperature structural phases implies that there will be a linked change in the electronic and photovoltaic properties. Photoluminescence spectra results for $MAPbBr_3$ show that there is a change in the energy of the maximum photoluminescence intensity at the 150 K transition out of the low-temperature orthorhombic phase [188], in agreement with the observation made here that the molecular dynamics begin to change at this temperature. However, it is important to note that the change in photoluminescence observed at 150 K is not large. There are no such results published for $MAPbCl_3$, so a comparison cannot be made for this compound.

It has also been found that the cation dynamics in $MAPbBr_3$ provide screening which protects the energetic carriers [193]. This implies that, from the results presented here, the assumption can be made that the low temperature phase has least carrier protection and thus the carriers are less long-lived.

6.5 Summary

This chapter has presented three studies of the photovoltaic materials $MAPbBr_3$ and $MAPbCl_3$ to investigate the dynamics of the molecular cation as temperature is varied. $MAPbBr_3$ was studied using QENS and INS techniques, and a QENS study of $MAPbCl_3$ was carried out using multiple instruments.

The results from the QENS studies revealed that it is the short-lived tetragonal phase of both $MAPbCl_3$ and $MAPbBr_3$ that act as bridges between the different molecular dynamics in the low temperature orthorhombic and high temperature phases. From a comparison of Raman and high energy inelastic neutron scattering data collected on $MAPbBr_3$, the significance of the local environment around the hydrogen sites is implicated.

An important result from these studies is the increase in molecular disorder as temperature is increased, and how this relates to the hydrogen bonding between the molecular cation and the inorganic framework, particularly in the low temperature phases. This interplay between molecular dynamics and

structural phase transitions is a key piece of information for understanding the properties of these materials. From the previous literature, the molecular behaviour is implicated as being linked with other material properties, and as such the temperature dependence of this is important to better understand the photovoltaic performance of these compounds.

Future work to build on these results should include single crystal analysis of the QENS and INS spectra. In the orthorhombic and tetragonal phases the potential experienced by the molecule is directionally dependent, and as such the molecular motions are also expected to vary with the crystal direction.

Chapter 7

The Phase Diagram of NH_4F

This chapter concerns the results collected on the ice analogue NH_4F, and differs from the other results chapters in this thesis through choice of techniques. Here we are more concerned about the structure of the material than the dynamics and excitations present. The high-pressure phase diagram of NH_4F has so far only been studied up to 3 GPa with neutron diffraction, whereas x-ray diffraction and Raman studies have reached pressures of 30 GPa. In this chapter we present high pressure neutron diffraction data up to 21 GPa, alongside DFT simulation and Raman results, with the aim of creating a more complete phase diagram of NH_4F and resolving contradictions seen between previous studies, as detailed in chapter 3.

7.1 Experimental Setup

Two high pressure neutron diffraction experiments will be presented in this chapter, each of which was carried out with a different experimental setup. In both of these experiments it was necessary to deuterate the sample in order to remove the incoherent scattering signal due to hydrogen, which would have made the diffraction data difficult to interpret. The processing for both of these experiments was carried out using Mantid [6], and the analysis used the GSAS II software [178]. This section also presents the setup used for the Raman experiments and the parameters used in the DFT simulations.

7.1.1 Raman Experiments

Raman experiments were carried out using a Horiba LabRAM 300, which employs a HeNe 633 nm laser for measurement. Data was collected between $-100\,\mathrm{cm}^{-1}$ and $4000\,\mathrm{cm}^{-1}$ to obtain a full spectrum, with long count times used to reduce the background signal. To apply pressure a Merrill-Bassett diamond anvil cell was used, with culet sizes of 400 µm and 600 µm, with gasket holes of diameter 200 µm. Rhenium gaskets were used in all cases, and ruby powder was used as the pressure calibrant. For all experiments measurements were only taken on compression as it is not known if there are any hysteresis effects in NH_4F.

The NH_4F samples were loaded in a glovebag under an inert Ar atmosphere. As it was not possible to use a microscope in this loading, a slush was created using acetone, NH_4F and NaCl (with a 3:1 ratio between the NH_4F and NaCl), which was then pipetted into the cell. The cell was then allowed to sit for a while for the acetone to evaporate before it was closed. NaCl is incorporated in the loading due to the strong tendency for NH_4F powder grains to clump together into a mass, which makes it difficult to create a well packed sample in small gasket hole without the use of a microscope. The NaCl acts to disperse the NH_4F powder grains, and as it has no Raman active modes does not interfere with the measurements taken. NaCl can diffuse into an ice lattice and disrupt the structure, however no studies have been carried out to establish whether this is also energetically possible in NH_4F under pressure. The ND_4F samples were loaded in a glovebox under inert atmosphere. In this case it was possible to use a microscope and therefore a pure powder of ND_4F was loaded.

All Raman experiments were carried out by the author. The deuterated sample was prepared by Zainab Sharif.

7.1.2 High Pressure Neutron Diffractometer: PEARL

The diffractometer PEARL, at the ISIS facility in Oxford, UK, was used for the collection of neutron diffraction data of ND_4F. This diffractometer was specifically designed in order to be optimised for high pressure studies, and as such the layout of this instrument is tailored to the geometry of the Paris-Edinburgh press (see section 5.3). There are two sets of detector banks: the longitudinal and transverse banks, which each cover a different range of 2θ. Figure 7.1 shows a diagram of

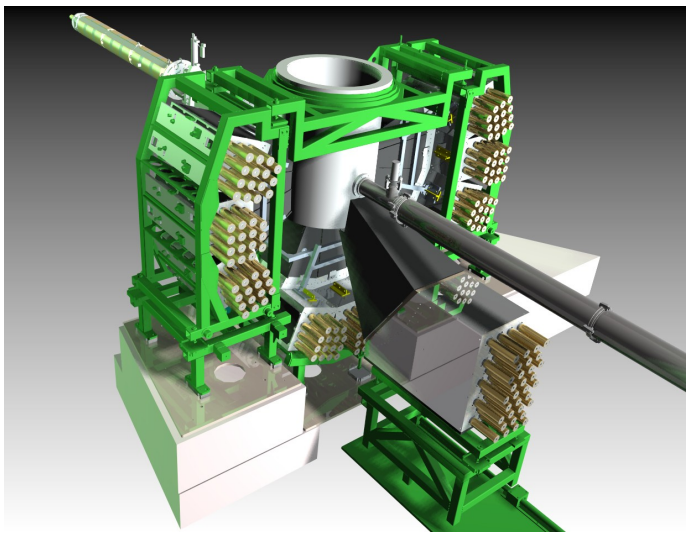

Figure 7.1 *A schematic of the instrument PEARL at ISIS. Here the neutrons arrive from the moderator from the top left of the image. The can in the centre is the space in which the Paris-Edinburgh press is held. Figure adapted from reference [30].*

the detector positions relative to the beam and Paris-Edinburgh press.

PEARL faces onto a methane moderator, which operates at 110K and provides neutrons of wavelength of 0.4 to 5.8 Å. It should be noted that, unlike the other instruments at ISIS described in this thesis (see sections 6.1.1, 6.1.2 and 6.1.3), PEARL does not employ a chopper to reduce the wavelength range incident on the sample. For the transverse detectors, which cover a 2θ range of $81.2° \leq 2\theta \leq 98.8°$, this incident wavelength range results in an available d-spacing range of 0.4 to 4.1 Å with an average resolution of $\Delta d/d \sim 0.64$ [30]. The longitudinal detectors, at $20.0° \leq 2\theta \leq 60.0°$ and $100.0° \leq 2\theta \leq 160.0°$, have a much larger maximum available d-spacing of 12.5 Å, but this has a much worse resolution and background, as for these the incident and scattered beams pass through the gasket material [30]. For the experiment carried out on ND_4F using PEARL the longitudinal detectors were not used, as the d-spacings provided from the transverse detectors were deemed sufficient to solve the structure.

The maximum pressure obtainable on PEARL is dependant on the choice of anvils in the Paris-Edinburgh press (the exact function of the Paris Edinburgh press is described in section 5.3). For the experiment described in this chapter, sintered diamond single toroidal (SDST) anvils were used, which are expected to allow pressures of 20 GPa to be reached in the sample [30]. The hydraulic load on the press was applied using pentane, for which the pressure increases can be automated for loads less than 10 GPa, after which the pressure was applied

manually. The ND_4F sample was loaded into the gasket in an inert atmosphere, along with fluorinert to ensure that the pressure was evenly applied across the sample. No pressure calibrant was used in this experiment, instead the equation of state for ND_4F reported by Bellin *et al* [17] was used.

As part of this experiment it was desired that the low temperature part of the phase diagram should be measured, and as such the Paris-Edinburgh press was suspended in a nitrogen cryostat. This allowed for the temperature to be controlled by partially immersing the Paris-Edinburgh press in liquid nitrogen and then using heaters on the anvils to tune the exact temperature as required. The minimum temperature accessible using this method is 110 K when using a pentane pressure medium to apply load onto the press (as in this experiment). The maximum temperature that can be achieved by the heater used in this experiment is 500 K, but here it was only employed to control the rate of warming from 110 K to room temperature.

A measurement of the full sample environment was carried out with no sample present to act as a background subtraction. This, and the full vanadium calibration, was carried out in Mantid [6].

The PEARL experiment on ND_4F was carried out by the author, Zainab Sharif, Dr. John Loveday and Dr. Craig Bull. The deuterated sample was prepared by Zainab Sharif.

7.1.3 Density Functional Theory Simulations

DFT calculations on NH_4F were carried out using the CASTEP code. These were used to optimise the geometry of NH_4F unit cells as pressure was increased. The geometry optimisations were performed with plane wave cut-offs of 1000 eV and a Monkhorst-Pack k-point grid with spacings of no more than 2π x 0.04 $\mathring{A}^{-1}$. Exchange-correlation effects were described within the generalised gradient approximation (GGA) using the Perdew-Burke-Ernzerhof (PBE) functional and ultra-soft pseudo-potentials as generated 'on-the-fly' by CASTEP.

The CASTEP simulations discussed in this chapter were carried out by the author and Lewis Conway, with supervision from Dr. Andreas Hermann. In particular, the author computed the enthalpy of different NH_4F structures with pressure, and Lewis Conway investigated candidate NF_4F structures and extracted the

elastic constants. Stress-strain calculations were carried out using ARCHER and all other calculations were run on the University of Edinburgh School of Physics and Astronomy cluster.

7.1.4 Spallation Neutrons and Pressure Diffractometer: SNAP

The diffractometer SNAP at the SNS Oak Ridge National Laboratory in the United States of America was used to collect neutron diffraction data of ND_4F. Like PEARL (discussed above in section 7.1.2) this instrument has been optimised for high pressure studies. However, the two instruments are very different in appearance: SNAP is designed with both Paris-Edinburgh presses and diamond anvil cells (DACs) in mind as sample environments.

SNAP faces onto a poisoned decoupled hydrogen moderator. This beam is shaped using choppers to give a broad spectrum of wavelengths resulting in a so-called "white beam" incident on the sample. The two wavelength ranges available for the incident neutrons on SNAP are 0.5 - 3.5 Å and 3.7 - 6.7 Å [45]. In this experiment the shorter wavelength range was used. The incident neutrons are focussed using a parabolic mirror guide, which reduces the size of the beam at the sample position and increases the flux incident on the sample. This is key for high pressure experiments, which typically have smaller sample sizes.

There are two main detector banks on SNAP, each comprised of nine square cameras. These are mounted upon circular rails, which allow for the centre of these detectors to be positioned at any 2θ angle between 50° and 115° in the horizontal plane on each side of the sample, with the 0° angle defined as the straight-through beam [45]. Additionally, a small detector is positioned directly behind the sample in order to measure the beam transmitted through the sample.

The ND_4F experiment carried out on SNAP differs from that on PEARL because a DAC was used to pressurise the sample, rather than a Paris-Edinburgh Press. This gives a much higher maximum pressure accessible by the experiment but a smaller sample size. The cells for this experiment were prepared and the sample loaded in a glovebox with a microscope. The diamonds used had 2 mm culets, with a sample diameter of 664 µm. This experiment was carried out entirely at room temperature so no heaters or coolants were necessary. Despite having a much reduced sample size compared to the Paris-Edinburgh press, the increased

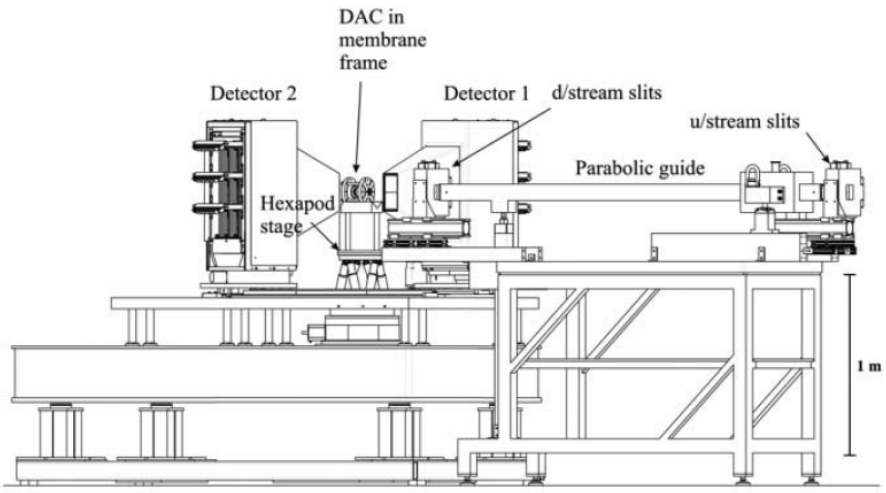

Figure 7.2 *A schematic of the instrument SNAP at SNS Oak Ridge National Laboratory. Here the neutrons arrive from the moderator from the right of the image. Diagram provided by the authors of reference [45].*

flux on SNAP compared to PEARL means that it is not necessary to count for a longer period of time.

The arrangement of SNAP for a DAC comprises of positioning the DAC such that the axis through the centre of the two diamonds is along the direction of the beam. The two main detector banks are positioned at $2\theta = 90°$ and are aligned so that they detect neutrons scattered from the sample that are not scattered into the diamonds. This allows for a total 2θ range of 40° to 127° to be measured. Figure 7.2 illustrates this setup, though does not show the transmission monitor.

The choice of a DAC as the sample environment does change the data processing procedure from that used for a Paris-Edinburgh press. This setup means that that the beam must pass through one diamond before reaching the sample, and as such has been attenuated by scattering from the diamond [75]. This attenuation is dependent on wavelength and 2θ, so manifests differently for each of the detectors. To correct for the attenuation, the beam transmitted through the entire system (two diamonds and a sample) is measured with the transmission detector, and the UB matrices for the two diamonds are determined by observed Bragg peaks in the diffraction detectors. The UB matrix describes the orientation of a single crystal on the instrument. As the two diamonds are differently oriented, knowing the UB matrices allows the Bragg peaks of the first and second diamond to be distinguished. The transmission of the first diamond is then calculated, and this information is used to correct the final spectrum observed for the sample. Only

the transmission of the first diamond is required to correct the data due to the position of the detectors perpendicular to the beam. The data is also normalised to a vanadium spectrum. All of this procedure was carried out using a pre-written script in Mantid [6], though the masking of diamond Bragg peaks in the final spectrum was done by hand. In the analysis for this experiment no explicit background subtraction was carried out, and instead the background was fit to a polynomial in GSAS II [178].

Multiple methods were used to calibrate the pressure in this experiment. A ruby sphere was placed in the DAC and fluorescence measurements carried out. Additionally, the equations of state of both the rhenium gasket and the ND_4F sample were used. These three diagnostic methods each gave slightly differing pressure results. The ruby fluorescence was found to give a very broad signal, from which the pressure could not be accurately ascertained. The rhenium gasket is not expected to be at the same pressure as the sample, as it is closer to the edges of the diamond. Thus the equation of state for ND_4F was used to diagnose the pressures. It should be noted that this ND_4F equation of state returned lower values for the pressure than the rhenium and ruby measurements at pressures above 10 GPa.

The experiment on SNAP was conducted by Bernhard Massani, Dr. John Loveday, Dr. Malcolm Guthrie, Dr. Bianca Haberl and Dr. Reinhard Böhler. The sample was grown by Dr. Luke Damian.

7.2 Results

This section presents the results of the studies carried out on ammonium fluoride. First, Raman experiments are presented comparing the modes in ND_4F and NH_4F. Then, a neutron diffraction experiment on PEARL aiming to investigate the phase transitions suggested by Raman spectroscopy. After this, the results from DFT simulations are discussed. Finally, a second neutron diffraction experiment on SNAP is presented, and the deviatoric strain in the system is characterised.

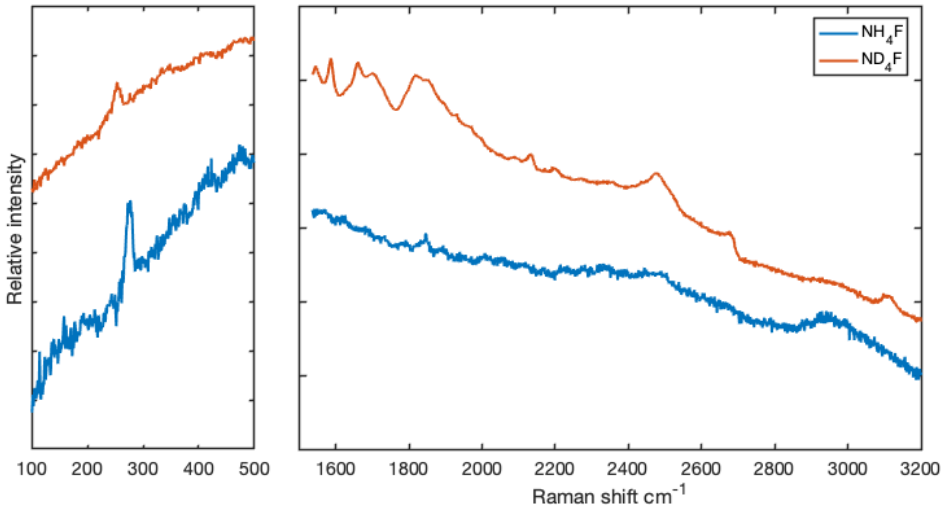

Figure 7.3 *A comparison of the Raman spectra measured in NH_4F (collected at 4.42 GPa) and ND_4F (4.38 GPa).*

7.2.1 Raman Results

Raman spectra were collected for NH_4F and ND_4F samples to confirm that the transitions observed by Bellin *et al* [17] in NH_4F are also present in ND_4F. Figure 7.3 shows the spectra collected for both compounds at ∼4.4 GPa. In the NH_4F data the transverse optic (TO) mode at ∼260 cm^{-1} and NH_4^+ bending ν_2 mode at ∼1840 cm^{-1} are clearly visible. The NH_4^+ stretching modes ν_1 and ν_3 at ∼3000 cm^{-1} are also observed, but are very broad. The NH_4^+ bending ν_4 mode and other combination modes observed by Bellin *et al* are not seen in this experiment. The NH_4F data is of lower quality than the ND_4F data, likely due to the different loading techniques used for the two compounds.

From literature measurements on other systems containing ND_4^+, the modes in ND_4F are expected to be observed at lower Raman shift than those in the NH_4^+ compound [34, 35]. Indeed, for the TO mode this is seen to be true. The peak at ∼3100 cm^{-1} is therefore likely a combination mode, and not a hardened ν_1 or ν_3 mode. As there are several other modes present in the region of 1500 cm^{-1} to 2000 cm^{-1}, the location of the ν_2 mode in ND_4F is not immediately apparent. The aim of this project is not to characterise the Raman modes in ND_4F, so this is left for further studies.

The position of the TO optic mode in NH_4F was observed by Bellin *et al* to have two regions of differing pressure dependence, with the transition occurring at 10 GPa [17]. Figure 7.4 shows the data from Bellin *et al* overlaid with the

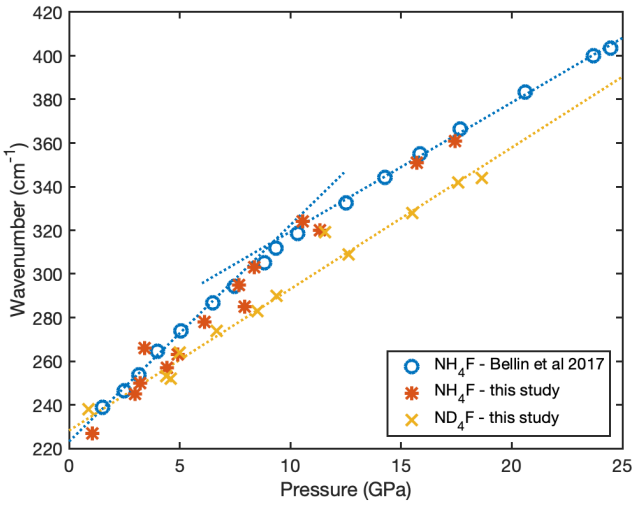

Figure 7.4 *The pressure dependence of the transverse optic mode in NH_4F and ND_4F, including data taken from this study and data from Bellin et al [17]. Dashed lines act as a guide for the eye.*

data collected in this study. The plotted dashed lines act as a guide to the eye for the trends. This study observes greater variance in the position of the NH_4F modes than is observed by Bellin *et al* but the two are broadly in agreement. The frequency of the ND_4F TO mode is less than for NH_4F at all pressures excepting the lowest, which is interpreted as the ND_4F not being in phase III. The ND_4F point at 11.5 GPa is identified as an outlier, likely as a result of the ruby fluorescence not being a true representation of the pressure due to not being measured at the centre of the cell.

Overall, the trend in the ND_4F data appears not to match that observed in the NH_4F data, with the data being well represented by a single trend, rather than requiring a transition between two regions of behaviour. It is possible that a very shallow transition between two regions of behaviour exists, however there is insufficient data to establish this. Therefore it is unclear to what extent conclusions for NH_4F can be generalised to ND_4F and vice versa.

7.2.2 Diffraction Results from PEARL Experiment

The diffraction experiment on PEARL first measured the room temperature structures of ND_4F up to 12 GPa. Figure 7.5 shows the observed diffraction patterns as pressure is increased. Below 5.5 GPa a coexistence of phases II and III of ND_4F was observed. Above this pressure only phase III is observed and no

phase transitions are seen.

Some additional peaks not linked to any ND_4F phase or diamond peaks are observed. In particular below 5.5 GPa a peak is observed at 2.9 Å, and above this pressure a small hump is observed at 2.4 Å which decreases in d-spacing with pressure. These are attributed to contamination from other members of the ND_3-DF binary, which are expected to appear in this sample as they can form as part of the deuteration method used.

Upon cooling at 12 GPa to 100 K no new peaks appeared, though a thermal contraction was observed, indicating that no phase transition had occurred. As such, these results are not plotted. These pressure and temperature conditions are only on the edge of Bellin *et al*'s predicted tetragonal region [17], so it could be the case that this experiment was simply not able to reach the suggested phase transition.

However, close examination of the room temperature diffraction patterns does yield an interesting result. The widths of the (100), (110) and (111) peaks appear to broaden differently with pressure, whereas one would expect any pressure effects of broadening to manifest equally for all peaks. Figure 7.6 plots the relative full width at half maximum of these three peaks. Onset at approximately 5 GPa, the (100) peak is broadening twice as much as the (110) peak up to 12 GPa, and the (111) is not broadening significantly at all.

This broadening of peaks can be understood as a peak splitting that is smaller than the resolution of the instrument. The full width at half maximum of the peaks observed would be equivalent to a peak splitting due to a tetragonal distortion of the system. This distortion would be of the order of a 1% expansion or contraction along the c axis. Thus a tetragonal phase transition is suggested at different temperature and pressure conditions than those predicted by Bellin *et al*.

7.2.3 Results from CASTEP Simulations

In order to validate the existence of the tetragonal phase transition as seen in the PEARL neutron diffraction data, DFT calculations were carried out in CASTEP. The enthalpy and volume of the known phases of NH_4F were first calculated in a series of constant-pressure calculations up to 35 GPa, then multiple candidate

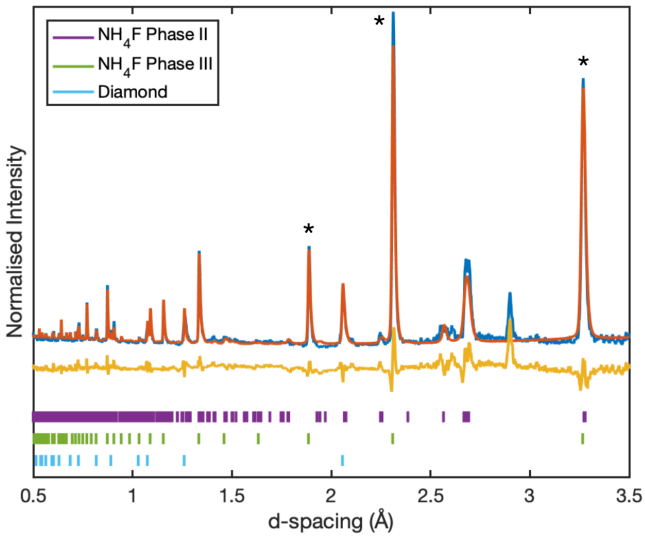

(a) *ND_4F sample at 3.04 GPa, showing both phases II and III.*

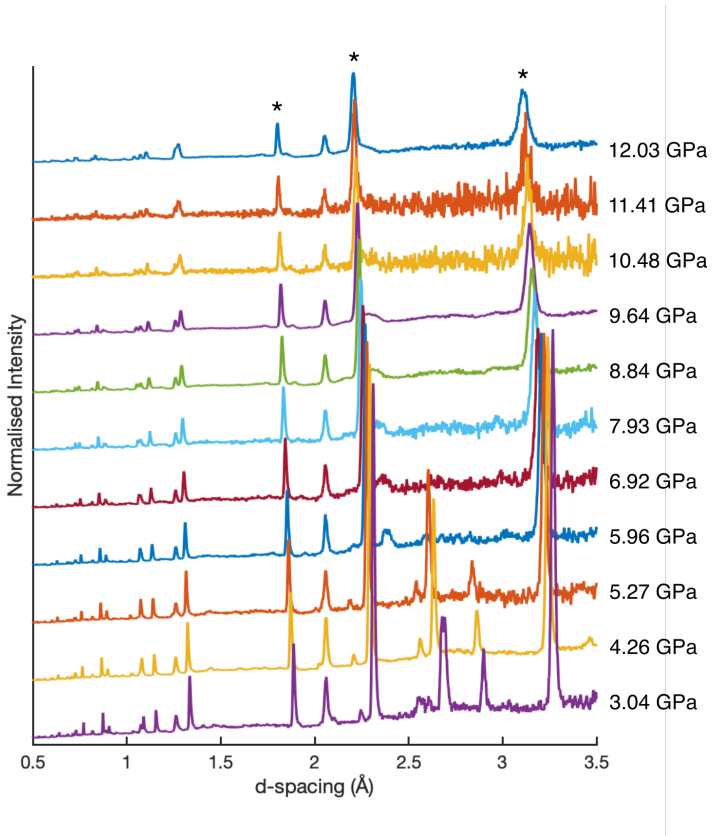

(b) *Waterfall plot of all room temperature diffraction patterns.*

Figure 7.5 *Diffraction patterns of ND_4F at room temperature obtained during experiment on PEARL. The phase III (100), (110) and (111) peaks are marked with asterisks.*

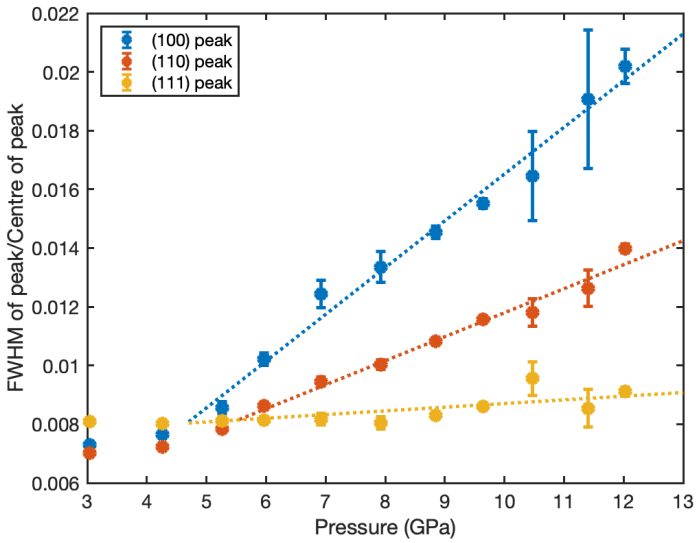

Figure 7.6 *Relative width of the (100), (110) and (111) peaks from the PEARL data with pressure.*

structures were developed to compare with the known phases. These candidate structures are intended to investigate the reported phase transition at 25 GPa [17] which was not reached by the neutron diffraction measurements in this thesis. Note that here we are considering the hydrogenous, not deuterated, structures of NH_4F. Candidate NH_4F structures can be constructed by manually building NH_4F equivalents of known water ice structures. The requirement for bonding between NH_4^+ and F^- ions restricts candidate structures to ice structures which do not posses odd numbered rings. The known phases of NH_4F are all ice analogues which fulfil these requirements. The only other allowed ice analogue phases are of ice II and ice VI.

The results of the simulated known and candidate NH_4F phases are shown in figure 7.7. The low pressure phase transitions of the system are correctly replicated in the enthalpy calculations. As well as the ice II and ice VI analogue phases, also tested was a $P2_1/m$ structure, reported in NH_4Br above 58 GPa [82]. The results show that the cubic phase III is the preferred crystal structure at all pressures, though the $P2_1/m$ structure has the same volume per formula unit at pressures above 30 GPa. It should be noted that the ice VI analogue structure collapses into the $P2_1/m$ structure above 25 GPa.

The pressure dependence of the phase III structure of NH_4F may be extracted from these calculations. Bellin *et al* found that the equation of state for NH_4F is best fitted by a Murnaghan third order model. Using this same model we

find fit parameters as follows: $V_0 = 36.43 \pm 0.03\,\text{Å}^3$, $K_0 = 46.2 \pm 0.5\,\text{GPa}$ and $K' = 4.30 \pm 0.04\,\text{GPa}$.

In their paper, Bellin *et al* proposed that an observed change in the Raman modes at 20 GPa which had no associated change in the x-ray diffraction pattern was due to a change in hydrogen ordering [17]. To test the response of the cubic phase III to different hydrogen ordering, two (1 x 2 x 2) supercells were constructed: one with alternating NH_4 molecules, and the other with the molecules in alignment. The starting structure for the case of the alternating molecular alignement is shown in figure 7.8a, with differently oriented atoms marked in different colours. The fluoride ions at [x, 0.5, 0] and [x, 0, 0.5] are restricted to their positions, and all parameters are allowed to vary. By testing small variations in x around the zero displacement, the stability of the different hydrogen ordered structures is tested. An example of a corrugated unit cell for the case of alternating NH_4F molecules is shown in figure 7.8c.

For the case of the aligned NH_4 molecules, an enthalpy minima at the zero fluoride displacement was found for all pressures tested. This gave a c/a axis ratio as would be expected from the cubic phase, and the supercell reduced to the observed phase III structure. As such, the cubic phase III is stable for the case of aligned NH_4 molecules.

Upon testing the cubic supercell containing alternating NH_4 molecules, non-zero values of x were found to be preferable, with the value of x being pressure dependant. Alongside this, the c/a axis ratio was observed to increase with pressure. The variation in optimal corrugation with pressure is shown in figure 7.8b, with a diffraction pattern for the optimum structure at 10 GPa in figure 7.8d. A comparison of the diffraction patterns of the optimally corrugated structure and the $P2_1/m$ structure show that these two structures are very similar, and indeed are found to have the same enthalpy. It is thus concluded that for the case of alternating NH_4 molecules, the stable structure is not cubic phase III, but is rather $P2_1/m$ structure as observed for NH_4Br in Ref. [82]. The $P2_1/m$ structure, which approaches the phase III structure in enthalpy (as seen in figure 7.7a), does not provide a good fit to the neutron scattering data.

The conclusion from this DFT investigation is that, at base temperature, the cubic hydrogen ordered phase III is the most stable NH_4F phase between 3 GPa and at least 35 GPa. This implies that the tetragonal distortion observed in the PEARL neutron scattering data is not a real phase transition and is as a

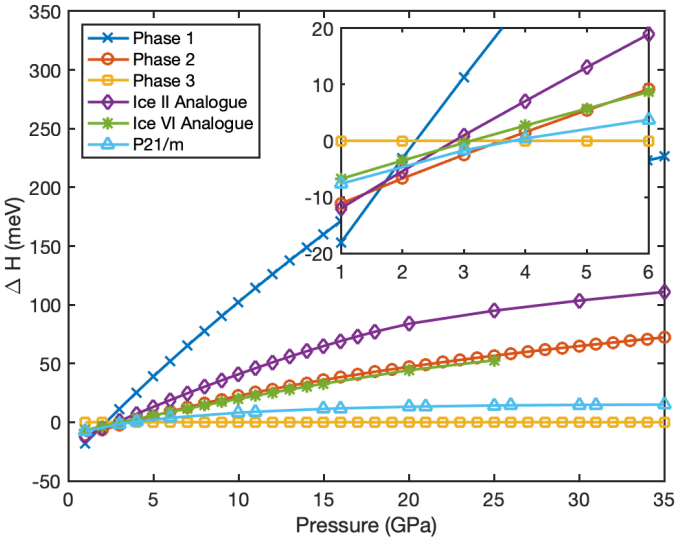

(a) *Enthalpies of NH_4F known and candidate phases. Inset: zoomed-in enthalpies for the region between 1 to* 6 GPa.

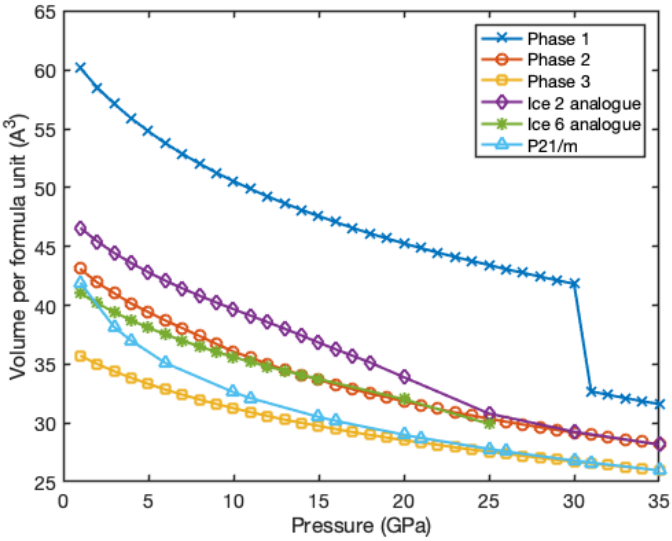

(b) *Volumes of NH_4F known and candidate phases.*

Figure 7.7 *Comparison of stability of known and candidate NH_4F phases from CASTEP calculations.*

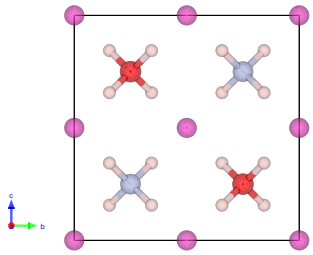

(a) *The starting structure for the refinements on the corrugated structure looking along the a axis. The NH_4^+ ions marked in red have alternate alignments to those marked in blue.*

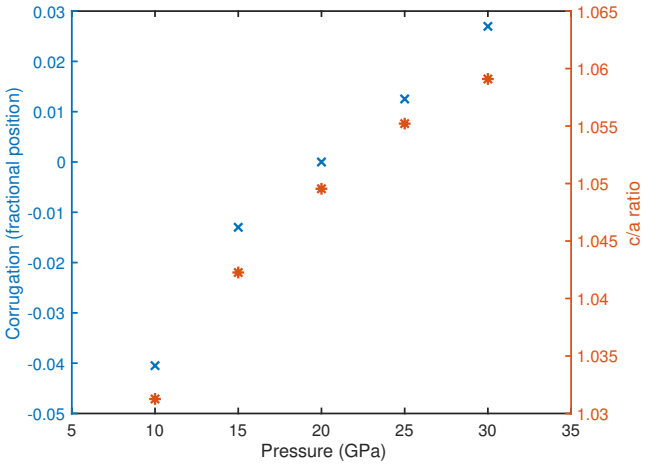

(b) *Optimal value of corrugation and the c/a axis ratio per formula unit for the corrugated structure.*

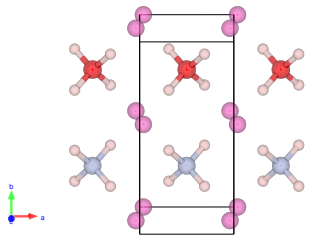

(c) *Example of the optimal corrugated structure at* 10 GPa *looking along the c axis.*

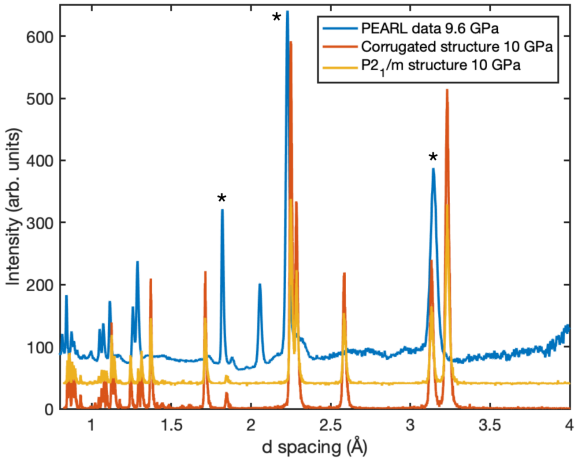

(d) *A comparison of the corrugated structure, the $P2_1/m$ structure, and neutron scattering data at* 10 GPa. *As before, the three principle peaks of NH_4F are marked with asterisks*

Figure 7.8 *DFT results for the corrugated structure for a cubic supercell containing alternating NH_4 molecules.*

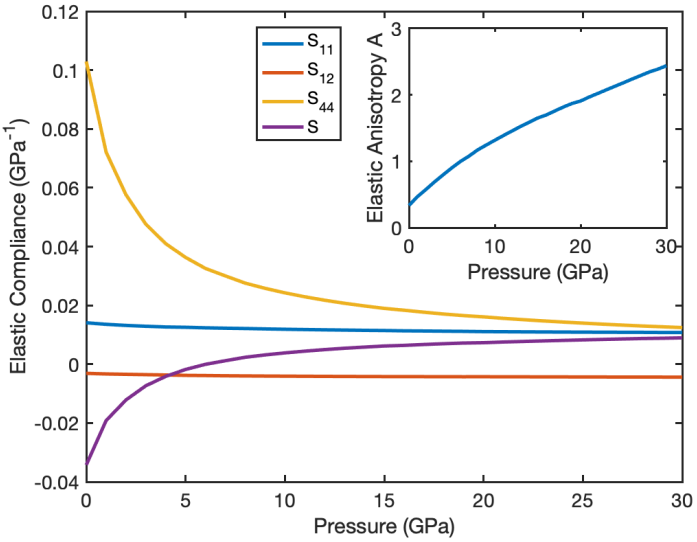

(a) *The calculated components of the elastic compliance matrix S_{ij}. Inset: the pressure dependence of the elastic anisotropy.*

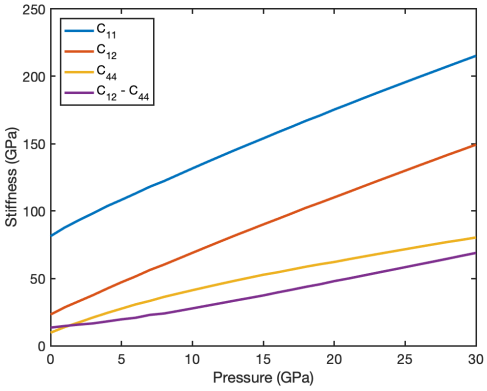

(b) *The calculated components of the stiffness matrix C_{ij}.*

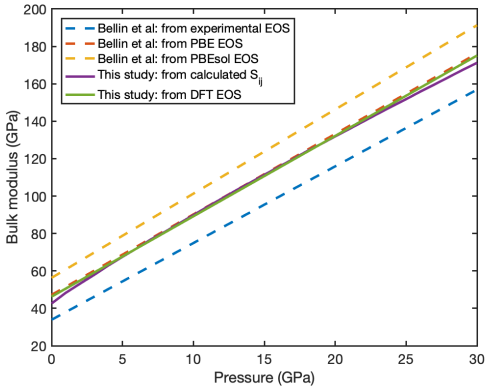

(c) *The bulk modulus of NH_4F calculated from simulations compared with literature values from simulation and experiment.*

Figure 7.9 *The elastic properties of NH_4F extracted from the DFT simulation results.*

result of another effect. There is a temperature difference between the DFT and PEARL results, however Bellin et al suggested that the tetragonal distortion would be enhanced by low temperatures so we would expect to see this in the DFT results [17].

The CASTEP code includes a command allowing for the stiffness matrix C_{ij} to be calculated from the unit cells produced in geometry refinements. This is done by applying small deformations to the unit cell and observing how the structure changes in response to this. A set of linear equations can then be formed and Hooke's law solved for the system. The results for the pressure dependence of the three unique components of C_{ij} (C_{11}, C_{12} and C_{44}) are shown in figure 7.9b. Also plotted in figure 7.9b is a value for $C_{12}-C_{44}$, which will be compared to literature values in section 7.3. This parameter is useful as it describes the deviation from Cauchy's relation $C_{12} = C_{44}$ which holds for a perfect ionic system where the forces act through the ionic centres. Here it can be seen that NH_4F deviates from Cauchy's relation at all pressures, with this deviation increasing with pressure.

The elastic compliance matrix S_{ij}, the inverse of C_{ij}, is of more use in analysing strain effects in neutron diffraction data. The pressure dependence of the three unique components of S_{ij} are plotted in figure 7.9a, with $S = S_{11} - S_{12} - S_{44}/2$. This parameter S is observed to change sign at 6 GPa.

In cubic compounds such as NH_4F, the difference between the group velocity of the two TA modes along the $\langle 110 \rangle$ direction is described by the elastic anisotropy $A = (v_{TA_1}/v_{TA_2})^2 = 2C_{44}/(C_{11} - C_{12})$. Elastically isotropic systems are defined as having $A = 1$, and values less than or greater than this are anisotropic. A plot of the pressure dependence of A is shown in the inset to figure 7.9a. From this, it can be seen that $A = 1$ at 6 GPa: the same pressure at which S becomes positive. Above and below this pressure the system is anisotropic.

To compare the calculated values of the elastic compliance to the literature, the bulk moduli can be compared. The bulk modulus K for a cubic system depends on the elastic compliance as $K = 1/(3S_{11} + 6S_{12})$. Bellin *et al* identified the equation of state for NH_4F to be Murnaghan third-order [17], which means the bulk modulus is expected to increase linearly with pressure. Figure 7.9c compares our bulk modulus as calculated from the elastic compliance to that from the equation of state for our computational data and those found by Bellin *et al.* The two routes to calculate the bulk modulus used in this study are in good agreement, however the bulk modulus as calculated from S_{ij} is not linear, implying that the

choice of a Murnaghan third order equation of state does not fully characterise the behaviour of the system. The computational results in all studies produce a larger bulk modulus than is observed in experiment. Our computational results agree well with the PBE equation of state as found by Bellin *et al.*

7.2.4 Strain Results from SNAP Experiment

Measurements of the angular dependence of the diffraction pattern are possible on SNAP due to the large angular banks, whereas PEARL has much lower angular coverage. An angular dependence to the measured peak positions would be indicative of deviatoric strain causing distortions to the unit cell. The detector banks on SNAP cover a 2θ angle from 40° to 127°. However, the parameter of interest for measuring strain as described in section 4.1.1 is ψ, which is defined by the relative arrangement of the load axis to the incoming beam. For the geometry of this experiment $\psi = 90° - \theta$, so we are able to probe $\psi = 30°$ to 70°. For analysis, the detectors were split into 10° sections in 2θ, meaning that the diffraction patterns can be probed in increments of 5° in ψ. Values of $\psi < 45°$ did not have large enough d-space coverage to observe the (100) peak, however the positions of the (110) and (111) peaks can be compared for all diffraction patterns.

Figure 7.10a shows the diffraction pattern collected at 16.7 GPa for two different values of ψ. Here, the positions of the (110) and (111) peaks can be seen to have moved, though it is more evident for the narrower (111) peak. This suggests that deviatoric strain may indeed be present in the sample. To characterise this the (100), (110) and (111) peaks are fitted with Gaussians and their peak centres extracted.

In the experiment presented in section 7.2.2 a tetragonal transition was posited based upon the different broadenings of the (100), (110) and (111) peaks. Figure 7.10b shows the broadening of these three peaks for the data collected in the $\psi = 60°$ angle bank. The requirement for a tetragonal distortion is that the (100) should broaden by twice as much as the (110) peak. This is not seen here, rather the (100) and (110) peaks are broadening equally, though still more than the (111) peak. Therefore a tetragonal distortion occurring simultaneous to deviatoric strain is ruled out, and this peak broadening is instead attributed to microstrain effects, which manifest due to the differing strain environments within the individual crystallites within the sample [159]. The peak broadening seen in

this experiment is slightly larger than that seen in section 7.2.2. This is likely due to the higher pressure gradient in the DAC compared to the Paris-Edinburgh press.

The position of the ND_4F peaks with ψ for two pressures is shown in figure 7.11. For the lowest pressure point at 8.7 GPa no obvious angular dependence in peak position is seen. Here the position of the (100) peak is only characterisable at one value of ψ due to insufficient counts in these detectors at the high d-spacing values. At the highest pressure, 21.5 GPa, there is a far more obvious angular dependence of peak position, but slightly reduced angular coverage. Note that for intermediate pressures the angular coverage is improved, especially for the (100) peak. For deviatoric stress there is expected to be a linear relationship between peak centre and $1-3\cos^2\psi$. While the measurements here show a slight discontinuity around $1-3\cos^2\psi = -0.2$, the data is well fitted by a linear trend. The expected larger variation in peak position for lower values of $\Gamma(hkl)$ is also clearly observed in this data.

The lowest pressure point was measured on the diamond anvil cell as-prepared, and did not have any additional applied load. This is likely the reason why no angular dependence in peak position is observed in the data at 8.7 GPa.

Fitting the dependence in peak position to a linear relation reveals the 'true' d-spacing (the value for which $1-3\cos^2\psi = 0$), which has then been combined with Bellin *et al*'s experimental equation of state to extract the pressure of the sample [17]. For the data at 8.7 GPa the peak position was simply fitted to a constant as there is no linear relation at this pressure. Indeed, the extracted pressure at 8.7 GPa agrees well with the pressure found from ruby fluorescence. However at all other pressures where ruby and rhenium equation of state measurements were used they overestimated the pressure compared to the ND_4F equation of state. This overestimation by the ruby and rhenium pressure gauges is also present if the equation of state as obtained from our simulations in section 7.2.3 is used to find the pressure of ND_4F.

Also extracted from the plots of peak position against $1-3\cos^2\psi$ is the gradient $Q(hkl)$. As detailed in section 4.1.1, $Q(hkl)$ is dependent on the peak $\Gamma(hkl)$, the elastic compliances S_{ij} and the uniaxial stress component t. Thus by fitting a linear relation between $Q(hkl)$ and $\Gamma(hkl)$ according to equation 4.9 a value for $m_1 = tS$ is extracted from the gradient and the y-intersect $m_0 = \frac{t}{3}(S_{11} - S_{12})$. Such a fit to the 21.5 GPa data is shown in figure 7.12. As the data for the (100)

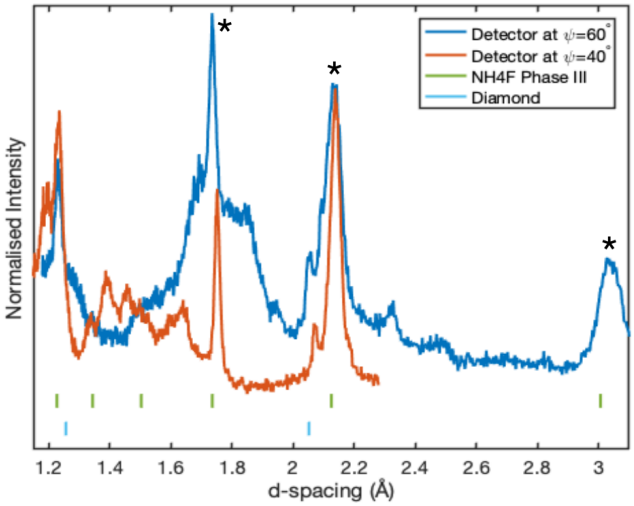

(a) *The raw diffraction data collected at* 16.7 GPa *for two different angle banks* $\psi = 60°$ *and* $40°$*. The (100), (110) and (111)* ND_4F *peaks are marked with asterisks.*

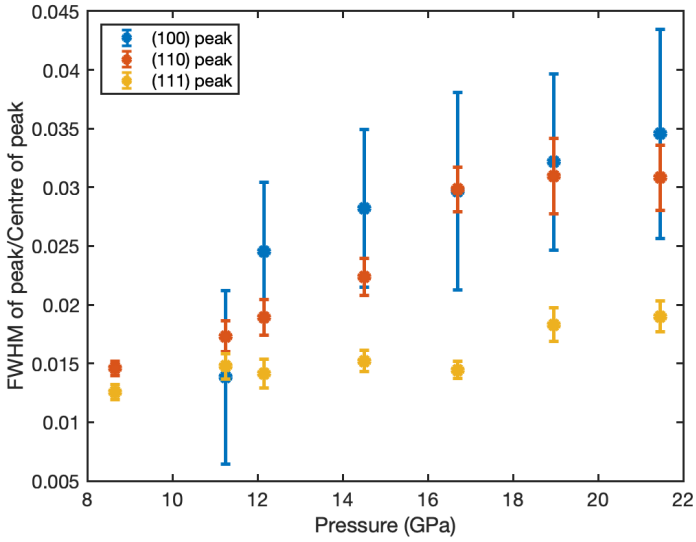

(b) *The width of the (100), (110) and (111) peaks for the* $\psi = 60°$ *angle bank.*

Figure 7.10 *Identification of peaks in diffraction data collected at* 16.7 GPa *for two different angle banks and graph of peak width with pressure for the three principle peaks.*

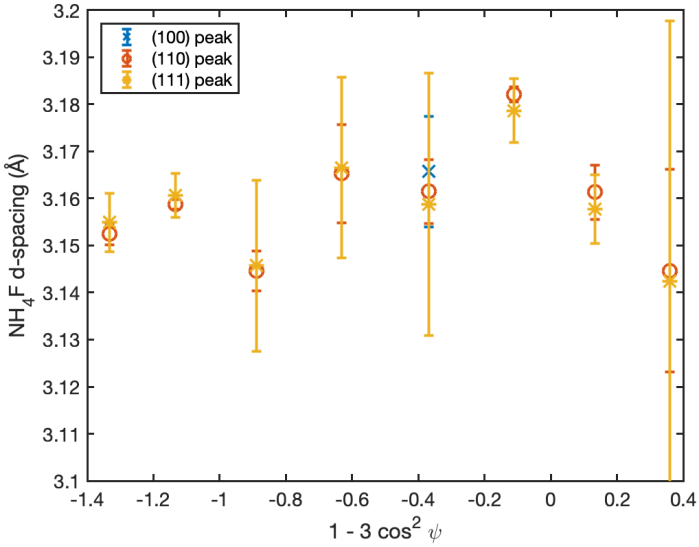

(a) 8.7 GPa

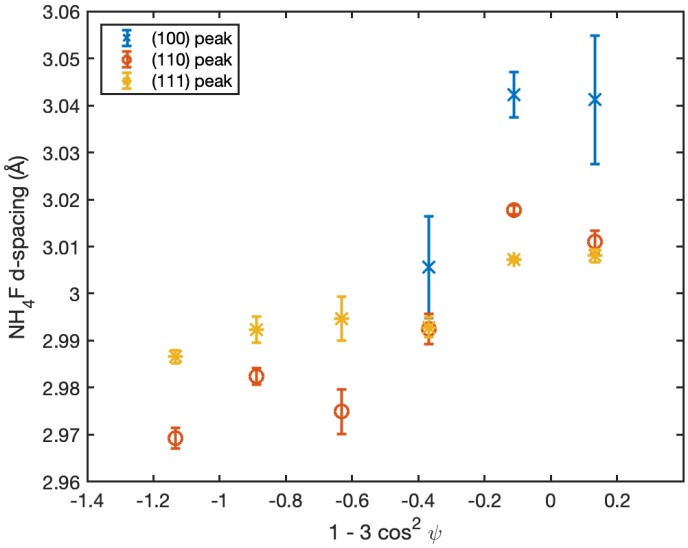

(b) 21.5 GPa

Figure 7.11 *The angular dependence on the size of the unit cell as extracted from the (100), (110) and (111) peaks in the diffraction pattern of ND_4F at two pressures. Some error bars have been cut off by the chosen limits of the plot.*

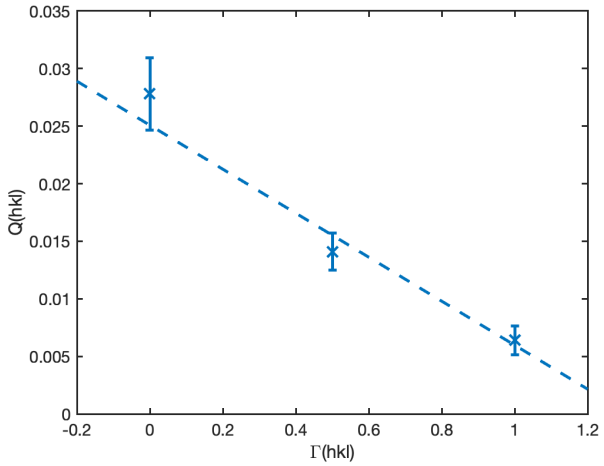

Figure 7.12 *A fit to $Q(hkl)$ versus $\Gamma(hkl)$ as extracted from the peak positions at* 21.5 GPa.

peak covers a smaller range of ψ, the error on $Q(hkl)$ for this peak is an order of magnitude larger than that on the (110) and (111) peaks.

The elastic compliances have previously been calculated from DFT simulations in section 7.2.3. By combining the fitted gradient and y-intersect of $Q(hkl)$ against $\Gamma(hkl)$ as follows, one can isolate only elastic compliance terms:

$$1 - \frac{m_1}{3m_0} = 1 - \frac{S}{S_{11} - S_{12}} = \frac{S_{44}}{2(S_{11} - S_{12})}. \tag{7.1}$$

Thus the values for the elastic compliance matrix from calculations and experiment may be directly compared. Figure 7.13a shows the pressure dependence of this value extracted from the elastic compliance. At all pressures the result from experiment is larger than from the calculations, though below 15 GPa the calculated value is within error of the experiments. Therefore the calculated values for S_{ij} increasingly disagree with experiment as pressure is increased, though it is unclear whether this disagreement is as a result of a single component or multiple components of S_{ij}. This discrepancy may be as a result of the fact that the computational simulations considered hydrogenous NH_4F, while the measurements presented here are of the deuterated compound. Similarly, the DFT results are carried out at base temperature, whereas this data is collected at room temperature. However, a difference of up to 15% between experimental and computational S_{ij} can be expected [98].

The value for the uniaxial stress component t can now be isolated from the fitted values of the gradient of $Q(hkl)$, $m_1 = tS$, and the y-intercept of $Q(hkl)$,

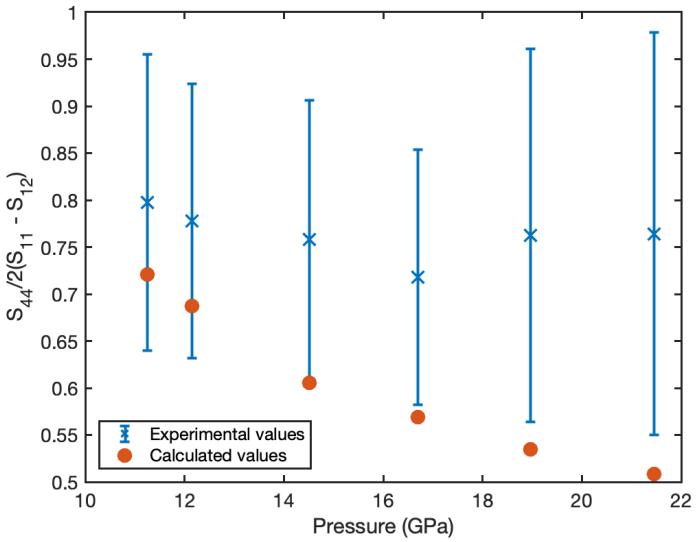

(a) *$S_{44}/2(S_{11} - S_{12})$ as extracted from experiment and calculated from DFT simulation.*

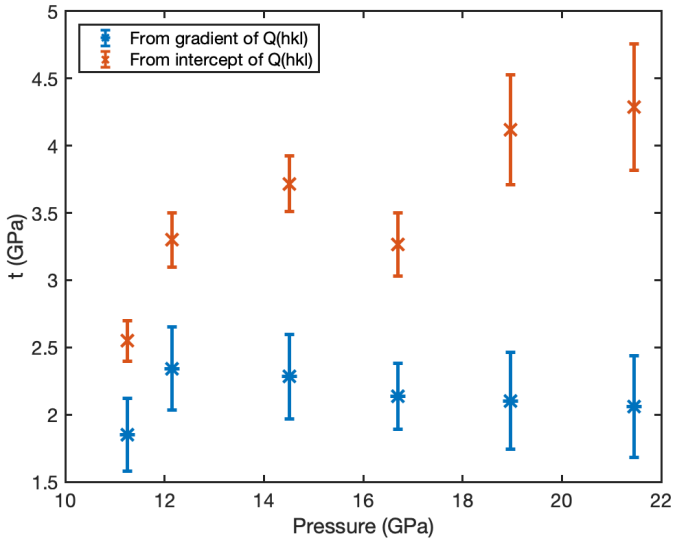

(b) *The uniaxial stress component t from experiment. This value is calculated from two different fitted values: from the gradient and from the y-intercept.*

Figure 7.13 *The pressure dependence of $S_{44}/2(S_{11}-S_{12})$ and the uniaxial stress component t.*

$m_0 = \frac{t}{3}(S_{11} - S_{12})$. The pressure dependence of the two is shown in figure 7.13b. These values are not in good agreement, with the value extracted from m_0 being larger at all pressures. This discrepancy is as a result of the known disagreement between the calculated and experimental S_{ij}, with this error manifesting as the two values for t have different dependence on S_{ij}. However, from the mean of the two extracted values for t, it can be observed that the uniaxial stress component is approximately constant at high pressures. In both results t appears to increase at low pressures, then levels out, though the pressure at which this change occurs is unclear: by inspection it appears to be somewhere between 12 and 14 GPa.

7.3 Discussion

This chapter has presented a study of NH_4F which was initiated in order to resolve some contradictions between literature sources as to the phase diagram of this material. Firstly, Raman spectroscopy was used to compare the deuterated ND_4F samples to be used in the neutron diffraction measurements to the hydrogenated samples discussed in the literature. These results did not detect the observed change in Raman modes reported by Bellin *et al* in NH_4F in the ND_4F compound. This Raman data is therefore inconclusive in establishing whether any transitions suggested by NH_4F Raman data would also be present in ND_4F.

Secondly, a diffraction study using the instrument PEARL was presented. From these results we are able to identify phase III of ND_4F as being hydrogen ordered, in agreement with Glazkov *et al* [71]. This experiment found no evidence of a tetragonal phase transition at 12 GPa and 100 K, as had been reported in this region by Bellin *et al* [17]. However a tetragonal distortion onset at 5 GPa was inferred from peak broadening effects, which increased with pressure. This tetragonal distortion was not observed in the DFT calculations carried out. Instead these simulations found that the known cubic phase III was the most stable form up to pressures of at least 35 GPa. The elastic compliance matrix was extracted from these simulations. Finally, a study of the deviatoric stress present in the sample was carried out using the instrument SNAP. This found deviatoric stress to be present at all pressures measured for which load was applied to the cell. The uniaxial stress component t was found to be constant in the range above $\sim$12 GPa.

The uniaxial stress component being constant at high pressures implies that the

sample is in the region of plastic deformation. As there is only one data point below 12 GPa in the SNAP data it cannot be said for certain whether this pressure is outside the plastic deformation region or is simply an outlier. As the peak broadening with pressure observed in the PEARL experiment cannot be explained by a tetragonal distortion, it must instead be due to strain effects. The linear nature of this peak broadening implies an elastic deformation, however further studies would be required to validate this. The onset of peak broadening observed at 6 GPa matches up with the pressure at which $S = 0$ and the elastic anisotropy $A = 1$. This is to be expected as the gradient of $Q(hkl)$ is zero for all cases when $S = 0$. An elastic anisotropy parameter of 1 means that the system is isotropic. Above 6 GPa the elastic anisotropy increases with pressure, in agreement with the observation that the structural distortions are onset at 6 GPa. Though ND_4F phase III is also anisotropic below 6 GPa no distortion of the peak shapes is observed in the PEARL diffraction data below this pressure. In the low-pressure region the uniaxial stress component is expected to be small and thus any peak broadening effects would be small. However this anisotropy could explain the region of coexistence of phases II and III observed below 5.5 GPa.

In the Raman experiments carried out by Bellin *et al*, changes were observed at approximately 6 GPa, 10 GPa and 25 GPa [17]. The experiments reported by Bellin *et al* do differ in method from ours by the inclusion of a helium pressure transmitting medium, however the elastic compliance is a material property independent of experimental setup. The change in Raman signal at 6 GPa can be associated with the onset of structural distortions, which in diffraction data manifests in peak broadening. A change in Raman signal at 10 GPa is at a lower pressure than the posited shift between elastic and plastic deformation in this study. However, the Raman results presented in this thesis suggest that a higher transition pressure was to be expected in the deuterated sample. Therefore it is posited that this change in Raman modes aligns with the transition between regions of elastic and plastic deformation. Lastly, while the experiments carried in this thesis out did not reach 25 GPa, the DFT simulation results presented do not observe a further phase transition at this pressure. The Raman peaks observed by Bellin *et al* are reported to have a pressure dependence to their broadness which is enhanced by low temperatures. This suggests that there may be a temperature dependence to the uniaxial stress component.

Raman results conducted on hydrogenous NH_4F by Zou *et al*, in which they did not use a pressure transmitting medium, also suggested a phase transition at

14 GPa [194]. This does not align with the transitions identified in this study or by Bellin *et al*. However, as uniaxial stress is not an intrinsic material property, this could be dependent on on the sample and experimental setup. As such, one must be careful making generalisations between studies.

The x-ray diffraction results collected by Bellin *et al* appear to show peak broadening with pressure, but it is not quantified [17]. As Bellin *et al* are only able to clearly discern two peaks at all pressures and their sample is a poor powder, their results would not permit deviatoric strain analysis to be carried out upon them. However, x-ray measurements such as these could be used to validate the results presented in this chapter. The equation of state calculated by Bellin *et al* was compared to the simulations presented in this chapter by extracting the bulk moduli from the two. The bulk modulus from both our simulations and those carried out by Bellin *et al* was larger than that observed in experiment at all pressures. This could be as a result of deviatoric strain effects in the experiment, and implies that the experimental equation of state found by Bellin *et al* is not a reliable diagnostic of pressure. Additionally, the bulk modulus as calculated from the elastic compliance matrix S_{ij} is not linear with pressure, suggesting that the Murnaghan third order equation of state does not fully describe the behaviour of the system. In this chapter Bellin *et al*'s experimental equation of state is used to diagnose the pressure in order to facilitate easy comparison between the two studies, however further experiments to characterise the equation of state for NH_4F are necessary.

While neutron diffraction experiments have previously been carried out by Glazkov *et al* the pressures probed in their study did not exceed 3 GPa [71], and thus none of the peak broadening effects reported here would be expected. Despite this, their study did identify ND_4F as being significantly less compressible than the other ammonium halides. This would explain why such strong deviatoric stress effects as observed in this study of ND_4F have not been reported in other members of this family. Glazkov *et al* found that the N−D distance in ND_4F is shorter than that in ND_4I, with both being independent of pressure in the region investigated. The radius of the halide ions is identified as being the key influence on the compressibility, with smaller more electronegative ions being less compressible. In agreement with this, X-ray measurements of the high temperature NaCl-like phase VI of NH_4F show that this phase is more plastic than the analogous phase in the other ammonium halides [31].

Ice VII is the proton-disordered structural analogue phase to NH_4F phase III.

The pressure dependence of the stiffness matrix, C_{ij}, for ice VII has been studied numerous times, both experimentally and theoretically. These studies reveal that ice VII is an elastically anisotropic phase like ND_4F phase III. In ice VII the elastic anisotropy increases with pressure, with anomalies in this trend linked to dipole ordering and changes to the hydrogen bond structure [98, 108, 156]. A measurement of the uniaxial stress component t of ice VII using the same method in this thesis found a large peak in t at the same pressure where anomalies were observed in the elastic anisotropy, but otherwise follows a linear trend with pressure [164]. This behaviour in t is identified as being indicative of a ferroelastic transition. An interesting contradiction between the studies of ice VII is the Cauchy relation, which states that if $C_{12} = C_{44}$ the forces act as in a perfect ionic system with no charge screening. Both Shimizu *et al* [156] and Li *et al* [108] find that the Cauchy relation holds and thus the forces act through the symmetry centres of the oxygen atoms. However, Kuriakose *et al* [98] finds a large and negative value for $C_{12} - C_{44}$, implying decentralised forces and a high brittleness.

Purely ionic CsCl-like compounds may also break the Cauchy relation. For example, the SrX (X = O, S, Se and Te) compounds are all found to exhibit a positive and increasing value for $C_{12} - C_{44}$ [181]. In these compounds this effect is linked to strengthening anharmonic effects and decentralisation of forces due to screening of charges. These SrX compounds have a constant elastic anisotropy with pressure, so differ to ice VII in that regard. Conversely, YAg also breaks the Cauchy relation but is observed to have pressure dependent elastic anisotropy. This elastic anisotropy increases in the region of mechanical stability, then becomes negative when the compound becomes unstable [142]. A study of transition metal CsCl-like compounds TiX, ZrX and HfX (X = Fe, Ru and Os) found that the Fe compounds always have greater elastic anisotropy than that of the larger radius transition metals [11]. This is in agreement with the assertion that smaller halide ions are less compressible.

Plastic phases have previously been observed in molecular materials such as NH_3, H_2S and CH_4 [96, 108, 155]. The pressure dependence of the elastic anisotropy in these molecular materials varies greatly: in NH_3 it is constant with pressure; in H_2S it appears to decrease with pressure; and in CH_4 it increases with pressure. The pressure dependence of elastic anisotropy in CH_4 is explained as due to a coupling between the rotational and translational modes in the molecules [155]. On the contrary, the decrease in elastic anisotropy observed in H_2S is linked to a strengthening in hydrogen bonding due to the decreasing intermolecular

distance [96].

The elastic properties of ND_4F observed in this thesis is unsurprising considering the low compressibility of the F^- ion and the known behaviour of analogue systems. In the study presented here, ND_4F is found to have an increasing elastic anisotropy with temperature. This is also observed in ice VII, some CsCl ionic compounds, and plastic CH_4. However, ND_4F is unique in that it passes though a point of elastic anisotropy within its stable pressure range. Unlike in ice VII, this is not an anomaly that can be linked to a change in the proton ordering or dipole moment. Rather, it is likely as a result of the coupling of the translational and rotational modes of the molecule acting in competition with the hydrogen bonding: effects that are linked to the behaviour of other plastic molecular systems CH_4 and H_2S. It should be noted that the elastic anisotropy in ND_4F at 30 GPa is comparable in magnitude to that of ice VII below 8 GPa [156]. Furthermore, in NH_4F the large value for $C_{12} - C_{44}$, the magnitude of which increases at a faster rate than that observed in ice VII [98], implies strong anharmonic effects and decentralised forces. Anharmonic molecular motion is known to exist in hydrogen bonded systems, with intermolecular motion particularly affected [176]. The behaviour of the uniaxial stress component in ice VII is related to a ferroelastic transition. Such a transition cannot be identified in ND_4F from the range of the data collected. Therefore the conclusion drawn is that the competition between molecular motion and hydrogen bonding is the strongest influence on the plastic properties of ND_4F.

7.4 Summary

This chapter has presented results on the structure of NH_4F with pressure. Firstly, Raman results were used to compare NH_4F and ND_4F. This found comparable Raman spectra between the two compounds, however the pressure dependence of the these modes did not exhibit the exact same behaviour. These results were therefore inconclusive in establishing whether any transitions suggested by NH_4F Raman data would also be present in ND_4F.

The initial diffraction results collected on PEARL implied the existence of a tetragonal distortion onset at 5 GPa, suggesting that the tetragonal phase observed by Bellin *et al* appeared at much lower pressures than previously thought. However, the following results from DFT calculations found no existence

of a tetragonal phase, and that the cubic phase III was energetically favourable up to at least 35 GPa. A second diffraction study was then conducted using SNAP, this time with the aim of establishing whether deviatoric stress was present in the system. An angular dependence in peak position was observed at all pressures above 10 GPa, with the extracted uniaxial stress component found to be constant above approximately 12 GPa.

From this it is concluded that the cause of the apparent tetragonal distortions in the system was from deviatoric stress. At pressures above ∼12 GPa the system is in the region of plastic distortion, though it is unclear exactly at which pressure this is onset. Above 6 GPa the increasing elastic anisotropy of the system with pressure is linked to a strengthening in the coupling between the rotational and translational modes of the molecule.

The influence of hydrogen bonding upon the structure and phases of NH_4F was already known prior to this work. Here, it has been proved that the molecular motions and hydrogen bonding have a strong influence on the plasticity of the compound. This plasticity can explain the features observed in Raman and diffraction data which had previously been interpreted as a tetragonal phase transition.

The experimental and theoretical values for the elastic compliances found in this work do show a discrepancy. Therefore future work should include experiments to resolve these differences. In addition, these experiments did not reach 25 GPa where a further change in Raman modes has been observed. Further diffraction studies should be carried out to investigate this higher pressure region. Finally, the equation of state for NH_4F should be re-characterised in light of these observations of deviatoric stress.

Chapter 8

The Mixing Behaviour of CH_4 in H_2O

In this chapter, experiments are carried out with the aim of understanding why the liquid mixing behaviour of methane and water is non-linear with pressure, as was introduced in chapter 3. Quasielastic neutron scattering results on the liquid mixture are presented, with selective deuteration used to isolate the dynamic properties of the water molecules. The diffusional properties of the water are characterised and compared to the reported literature values for pure water. From here, inferences about the dynamical behaviour of the mixing species are made.

8.1 Experimental Setup

In this section the experimental setup used for the neutron scattering experiment is described, and the procedure used to grow the solid CD_4–H_2O clathrate is detailed. Additionally, an explanation is given of the method used to calculate the multiple scattering from the CD_4–H_2O mixture, the results from which are used in the analysis of the data in section 8.2.

8.1.1 Cold Neutron Time-of-Flight Spectrometer: IN6-SHARP

The IN6-SHARP (Spectromètre Hybride Alpes Région Parisienne) time-of-flight spectrometer is located at the Institut Laue Langevin (ILL) in Grenoble, France. This instrument was used to collect QENS spectra of the methane and water mixtures at high pressure. It should be noted that the experiments detailed in this chapter were carried out before the upgrades to the secondary spectrometer that are part of the SHARP project, so the below discussion will be of the instrument at time of usage.

IN6-SHARP differs from the instruments at the ISIS and Oak Ridge facilities which have been detailed in previous chapters (see sections 6.1.1, 6.1.2, 6.1.3, 7.1.2 and 7.1.4), as it is situated at the ILL which is a steady state neutron reactor source, rather than a pulsed source. It is situated on the H15 beamline, a source of cold neutrons, from which a pyrolitic graphite monochromator selects the incident wavelength. There are four possible wavelengths available; 4.1, 4.6, 5.1 and 5.9 Å. For this study the 5.9 Å wavelength was selected as it gives high energy resolution (70 µeV) while still providing sufficient flux such that the high pressure equipment does not render the time requirements of the experiment unreasonable.

In order to achieve the time-of-flight properties of this instrument, a Fermi chopper is used to create a time-focussed beam of neutrons. By measuring both the time-of-flight of the neutrons and their angular positions, the momentum and energy transfer between the scattered neutrons and the sample can be measured. IN6 has 337 He^3 detectors, which give a horizontal angular coverage of 10° to 115° and ± 15° in the vertical plane. The layout of these is shown in the schematic fig. 8.1. The secondary spectrometer is very similar in layout to the instrument MAPS detailed in chapter 6 except that this instrument is able to move about the monochromator in order to change wavelengths.

To reach the pressures desired for this experiment a Paris-Edinburgh press was used. The setup featured a spherical sample geometry in single toroidal anvils. As in chapter 7, sintered diamond anvils were chosen, and so this experiment shared the same maximum pressure. In this case, sintered diamond was not chosen for their pressure performance, but rather because temperatures of 400 K were desired throughout the experiment. This temperature was chosen to allow for

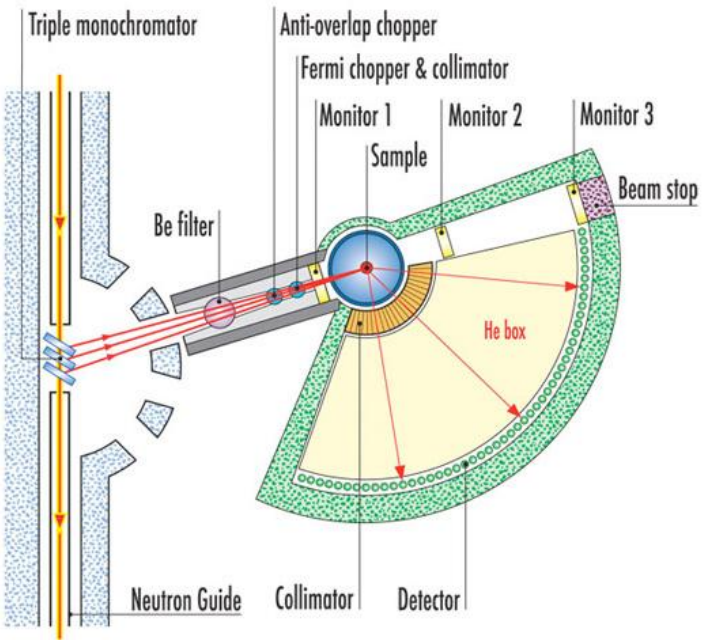

Figure 8.1 *A labelled schematic of the instrument IN6-SHARP at ILL.*

easier comparison of results with the literature: in particular the mixing pressure between CH_4 and H_2O has been best characterised at this temperature. The sample heating was achieved by using resistive heating inserts to directly heat the tops of the anvils where the gasket containing the sample is situated, as was also done for the low temperature measurements presented in chapter 7 (for details, see section 7.1.2).

The Paris-Edinburgh press does not give any quasielastic signal and so does not interfere with the data of interest, but does require a small sample volume of 1 mm^3. This means that, despite the large incoherent cross section of hydrogen, long count times of order 12 hours are necessary in order to collect high quality data. The Paris-Edinburgh press contributes to the elastic line, however a measurement was taken of a Paris-Edinburgh press containing a polystyrene ball to act as a background. During data processing, this background was subtracted from the elastic line, and a vanadium calibration was used.

In this experiment no pressure marker was used by which to infer the pressure. As the sample to be measured is a fluid, no Bragg peaks from this could be used to identify the pressure. Instead, the pressure loading curve of the Paris-Edinburgh press was used - for more information on this see chapter 5. This pressure identification is made possible by the choice of a simple sample geometry. The loading curve assumes a perfectly compacted sample: while this is true for

the fluid sample upon compression, we cannot be certain that the initial loaded solid sample was perfectly compacted. As a result of this reduced precision, there is a $\pm$ 0.1 GPa error on all of the pressure points.

The experiment presented out in this chapter was carried out by the author, Dr. Ciprian Pruteanu, Dr. Jean-Marc Zanotti, Dr. Stefan Klotz and Dr. John Loveday. The initial data processing for this experiment was carried out in QENSH, a software written by Dr. Jean-Marc Zanotti. The analysis for this experiment was carried out in MATLAB, using the same scripts as in chapter 6.

8.1.2 Sample Growth

If one were to load gaseous CH_4 and liquid H_2O into the Paris-Edinburgh Press, finding the ratio of the two in the sample chamber would be very difficult. Instead, a solid methane hydrate with structure sI was loaded, which is 16.2% CD_4 and 83.8% H_2O by weight. This was then melted after loading, to provide a fluid mixture of known component ratios. For the experiment described in this chapter a CD_4-H_2O clathrate sample was used. This selective deuteration allows the behaviour of the water molecules to be studied in isolation. This CD_4-H_2O clathrate was grown at Edinburgh, and in this section the growth method used will be described.

To grow a methane clathrate, first a fine powder of ice is created by spraying water through a fine nozzle into a bath of liquid nitrogen. This results in very small particulates of hexagonal ice Ih, which are then transferred into a SwageLok® sample bottle, which has a maximum pressure limit of 120 bar. This sample bottle was then left open inside a freezer set to $-5.5\,^{\circ}$C such that the ice particulates remain frozen but any liquid nitrogen transferred alongside the ice may slowly evaporate away.

The SwageLok® sample bottle was then attached to a pressurised bottle of methane. In the case of the CD_4 gas used in this sample growth, the bottle was at a pressure of 50 bar and was small enough to be stored in the freezer in which the sample bottle is kept, so the two could remain attached throughout the growth.

The exact rate of clathrate formation, i.e. the diffusion of the methane into the ice, is dependant on the pressure and temperature conditions of the sample, as

described in Kuhs *et al* [95]. There are two stages to this growth: the formation of a clathrate on the ice particle surface, and then the growth of this shell to then convert the whole ice particle into a clathrate. The second of these stages is the longer process, and is dominated by the diffusion of the methane molecules through the ice structure. Hence, the optimal thermodynamic conditions are such that the methane may permeate though the ice lattice with greatest ease.

The optimum temperature for growth is $-5\,^{\circ}\mathrm{C}$, however as the freezer temperature control used causes the temperature to fluctuate approximately $\pm\ 2\,^{\circ}\mathrm{C}$ around the set temperature, a set temperature of $-5.5\,^{\circ}\mathrm{C}$ was used to prevent temperatures of above $-3\,^{\circ}\mathrm{C}$ being reached. As well as potentially causing the ice to melt, a high temperature on the sample bottle could result in outgassing of any gas in the ice structure, and an associated sudden increase in pressure, which could reduce the integrity of the sample bottle. Low temperatures impede the diffusion of the methane and thus slow clathrate formation. A higher gas pressure results in faster formation of clathrate. In this case we are limited by the gas pressure in the pure methane bottle, and the pressure limits of the SwageLok® setup. A high quality growth thus depends on leaving the ice powder under methane gas pressure for an extended amount of time (on the order of months). The sample bottle was regularly topped up with methane (at 50 bar) to maintain this gas pressure.

The growth of CD_4-H_2O carried out used 5.6 g of H_2O, so would be expected to net 6.68 g of CD_4-H_2O sI clathrate. However, as some of the clathrate adheres to the sides of the growth container the final amount recovered was less than this. The recovered sample was stored at liquid nitrogen temperatures until it was loaded into the Paris-Edinburgh press for the experiment. As the resulting sample is highly hydrogenous, no neutron diffraction pattern could be taken to verify its purity.

The CD_4-H_2O clathrate growth was carried out by the author, Bernhard Massani and Dr. John Loveday.

8.1.3 Simulating the Multiple Scattering Contribution

A spherical hydrogenous sample such as the CD_4-H_2O sI clathrate used in this experiment will result in multiple scattering events. This phenomena is explained in more detail in chapter 4. Multiple scattering events should be accounted for

in fits to the QENS data, as they have Q and E dependence which can cause misleading results.

The software McStas is commonly used for the simulation of neutron instruments. It uses Monte Carlo calculations to simulate the paths of neutrons through components and produces an expected signal [186]. The package includes multiple types of editable components and a model of the setup on IN6-SHARP, dated 2005. It is this model of IN6-SHARP that will be used in the calculation of the CD_4-H_2O multiple scattering.

The component `Isotropic_Sqw` describes the sample in the IN6-SHARP McStas model. This was edited to reflect the properties of the sample. The sample geometry was set to be a sphere of 5 mm radius. The cross section of CD_4-H_2O is simply a sum of the components. It is also important to know the density of the mixture as pressure is increased, as this will cause the multiple scattering contribution to change. From diffraction studies, the density of the CD_4-H_2O mixture is again found to be the sum of the components. Values of the densities of H_2O and CD_4 were taken from results from Abramson *et al* [1] and Li *et al* [107] respectively. Note that the Paris-Edinburgh press is not considered in these calculations and, as such, there is likely to be additional absorption unaccounted for.

In order to isolate the multiple scattering contribution, two simulations were run for each pressure. Both of these simulations considered only incoherent scattering, which was modelled by recreating the QENS signal as found in by Bove *et al* [22]. Ideally these simulations would also consider the elastic scattering, and therefore give a comparison of the multiple scattering contribution to the total scattering. However, partially deuterated mixtures are not desirable for elastic scattering studies so no data is available. Of these simulations, one included only single scattering events, whereas the other allowed for all scattering events. McStas returns the total number of multiple and single scattering events, and this was used to normalise the two simulations to have the same number of single scattering events. These were then subtracted to show only multiple scattering events. An example of the 0.5 GPa data is shown in figure 8.2.

The resulting multiple scattering contribution is strongly E dependent at low Q, whereas at high Q it becomes a more constant background. As such, it is expected that this simulation will have a larger impact on analysis for the low Q results.

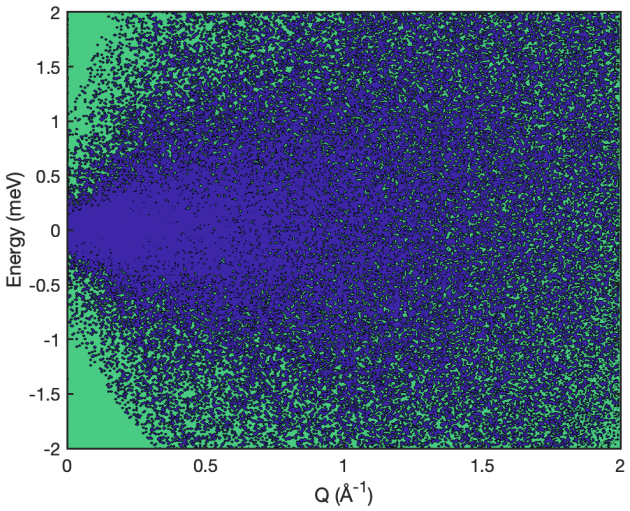

Figure 8.2 *Normalised results from simulation in McStas at* 0.5 GPa *showing only the multiple scattering contributions. Dark blue shows measured multiple scattering events, and light green shows the areas with no multiple scattering.*

Table 8.1 *The contribution of multiple scattering to the incoherent signal of* $CD_4 - H_2O$*, as found from the McStas simulation.*

Pressure (GPa)	Multiple Scattering Contribution to Incoherent Signal
0.6	67.47%
1.5	67.51%
1.7	66.58%
1.9	68.55%
2.3	72.69%

The overall contribution to the signal from incoherent scattering is shown in Table 8.1. This shows an overall large ratio between the expected quasielastic signal and the signal from multiple scattering. However, due to the large fluctuations in this simulation, the errors on the results shown in Table 8.1 are comparable in magnitude to the extracted values. Therefore these numbers should be interpreted as a guideline as to the magnitude of the multiple scattering contribution that is expected.

8.2 Quasielastic Neutron Scattering Results

Water has been heavily studied through quasielastic neutron scattering over the years, so the choice of model to fit this data should be based upon the literature. Foremost, the study by Bove *et al* [22] studied the QENS response of water at pressures in the same range as this thesis and 400 K, using the same instrument as was used here. As such, the results collected in this experiment should be directly comparable to this study.

Bove *et al* considered two excitations when fitting the data, a rotational and a translational diffusion. The form of the fit they used is as follows:

$$S(Q,E) = I_{el}(Q)\delta(E) + A(Q)\frac{\Gamma_T(Q)}{E^2 + \Gamma_T(Q)^2} + B(Q)\frac{\Gamma_T(Q) + D_R}{E^2 + (\Gamma_T(Q) + D_R)^2}, \quad (8.1)$$

where $\Gamma_T(Q)$ describes a function of the translational diffusion coefficient D_T and D_R is the rotational diffusion coefficient.

In order to apply this fit to the data collected in this study, the multiple scattering contribution must first be subtracted from the data. This was done by considering the energetic region above 0.5 meV and below −0.5 meV, in order to exclude the contribution from the elastic line. The simulated multiple scattering signal was then scaled according to the values in table 8.1, in order to contribute the correct proportion of the total signal in this region. The scaled multiple scattering contribution was then subtracted from the data. Excluding the region around the elastic line where both the quasielastic and multiple scattering signal vary more strongly does mean that the multiple scattering does not exactly contribute the proportion listed in table 8.1 to the signal. However, it was found that increasing the multiple scattering contribution above the scaling chosen resulted in the multiple scattering signal exceeding the raw signal at large energy transfers. Therefore the subtraction used is appropriate for this purpose.

In addition to the multiple scattering contribution, there is a contribution to the quasielastic signal from the vibrational modes. This is a flat signal at all $|Q|$ and E in liquids as there are no discrete phonon modes. In their study of pure water at this pressure and temperature Bove *et al* reported the contribution to the signal from vibrational modes was negligible relative to the signal from translational and rotational motion [22]. Therefore, as vibrational modes are a much smaller contribution than the multiple scattering no correction will be carried out for

this.

Figure 8.3 shows fits to the multiple scattering data using equation 8.1, with all of the parameters allowed to vary freely. These fits show in all cases that the broader quasielastic contribution is set to zero, with the value for D_R being set to an unphysically large value. Limiting D_R to a smaller range resulted in mis-fits to the low $|Q|$ data at all pressures. For high $|Q|$ data where it was possible to well describe the signal with two quasielastic contributions by limiting D_R, the resulting form of the two contributions compared poorly to those found by Bove *et al*: Bove *et al* found a larger contribution from the translational diffusion, but the fits forcing two quasielastic components at high $|Q|$ for this data found a larger contribution from the rotational diffusion. It was therefore concluded that any attempts to control the form of the fit by limiting the values for $\Gamma_T(Q)$ and D_R would not be of any benefit to obtaining a true reflection of the dynamical behaviour of the system.

These fits imply that the data is best described by a single diffusional contribution, however this is in direct contradiction with the results from literature. At high temperatures such as that measured here, all previous studies have found both a translational and a rotational diffusional contribution [4]. The only studies that have found a single diffusional contribution have been conducted at low temperature (such as for supercooled water [145]), or upon water confined within cavities [109]. This therefore implies an issue with the fitting method used here. The obvious origin of this discrepancy is the multiple scattering subtraction used: the simulated multiple scattering data contains large fluctuations and therefore has large errors associated with it even when smoothed. This multiple scattering subtraction may therefore be masking the broad rotational contribution to the data. However, no alternative method is available to calculate the multiple scattering contribution, and so this issue cannot be resolved.

It is still of interest to analyse the extracted value for $\Gamma_T(Q)$ from this multiple-scattering subtracted data, though it is understood to not be an exact reflection of the true translational diffusion due to the fitting issues discussed above. Figure 8.4 shows fits to the extracted $\Gamma_T(Q)$ using three different models as detailed in chapter 4. This shows a better fit to the data at 0.6 GPa than at 2.3 GPa, suggesting that the multiple scattering subtraction and approximation of the signal as a single diffusional contribution is a better representation of the data at low pressures. All three models trialled well-describe the data across the reciprocal space range probed. The Chudley-Elliott model is excluded from

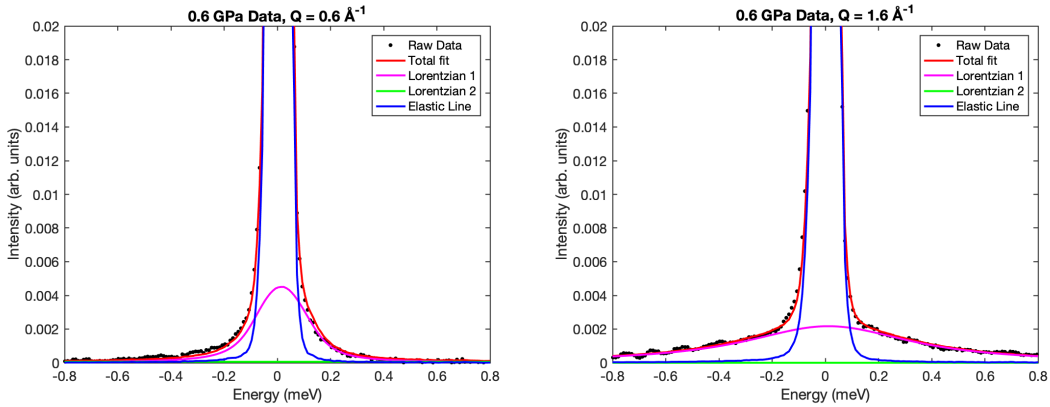

(a) 0.6 GPa*:* 0.6 Å^{-1} **(b)** 0.6 GPa*:* 1.6 Å^{-1}

(c) 2.3 GPa*:* 0.6 Å^{-1} **(d)** 2.3 GPa*:* 1.6 Å^{-1}

Figure 8.3 *Fits to the linewidth of the multiple scattering-subtracted data at* 0.6 GPa *and* 2.3 GPa, 0.6 Å^{-1} *and* 1.6 Å^{-1}*, using the model used by Bove et al [22].*

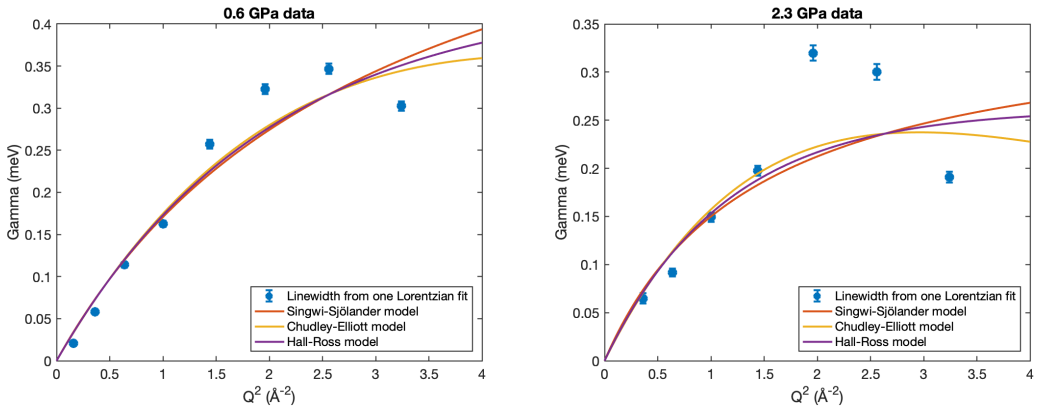

(a) 0.6 GPa **(b)** 2.3 GPa

Figure 8.4 *A comparison of models to fit the Q dependence of the linewidth of the translational water diffusion for fits to the multiple-scattering subtracted data at* 0.6 GPa *and* 2.3 GPa.

further analysis, as it describes motions on a lattice, which is not what would be expected in this fluid mixture. Bove *et al* employ the Singwi-Sjölander model to describe their data, and as such that model is selected preferentially to the Hall-Ross model.

The values for D_T extracted from fits to $\Gamma_T(Q)$ for the multiple scattering subtracted data are shown in figure 8.5. There is a ± 0.1 GPa error on all pressures as was discussed in section 8.1.1. This shows very poor agreement between the D_T found in this study from the multiple-scattering subtracted data with the results found by Bove *et al* at all pressures except 1.5 GPa. Results above 1.7 GPa, that is above the mixing pressure, show much larger errors associated with the extracted values for D_T. The result at 2.3 GPa is unphysical for the conditions of the sample in this experiment and must therefore be excluded from any discussion.

However, the result for the data at 0.6 GPa is of interest. This data set was well fitted by the Singwi-Sjölander model, as shown by the small errorbars on the result. The result for D_T at 0.6 GPa is lower than that found by Bove *et al*, implying some arrested motion of the water molecules at pressures below mixing.

In order to improve upon the results extracted for D_T at high pressures, it is necessary to reconsider the approach used in analysis. As it is the multiple scattering contribution that is identified as corrupting the final results, a fit to the raw data is expected to reveal further information. However, the question then comes as to how to approximate the multiple scattering contribution without using the results found from simulation. The multiple scattering contribution,

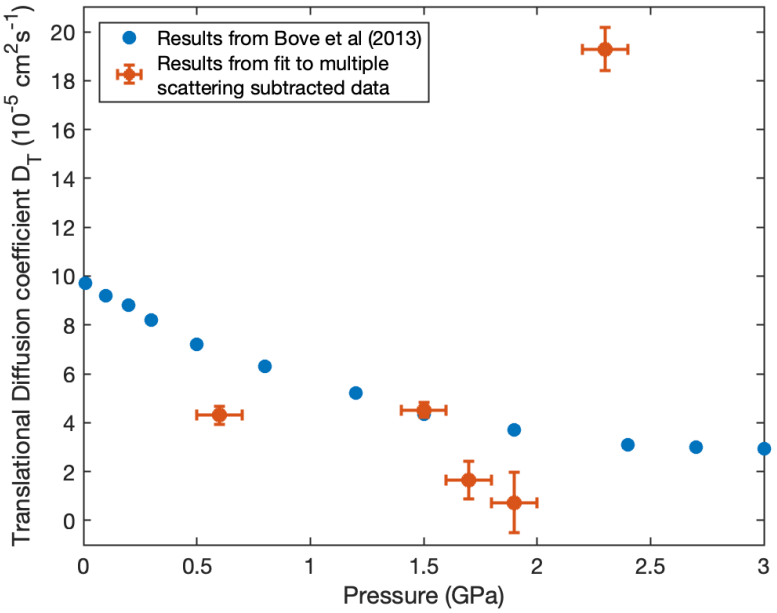

Figure 8.5 *Comparison of D_T values extracted from a fits to the multiple-scattering subtracted data and the results found in Bove et al [22].*

the contribution from vibrational modes, and the contribution from rotational diffusion are all broad signals. Therefore, these three contributions shall be fitted to a single "background" contribution, leaving the translational contribution to be fitted separately. The vibrational modes are a flat contribution to the signal, and at high $|Q|$ the multiple scattering contribution is a constant in the energy transfer range of this experiment. Therefore the "background" shall be approximated as an energy independent constant. As this is a rough approximation, it is expected to give larger errors on the translational component extracted from the fit. It should be emphasised that this is not well in line with the expected form of the fits from the literature, where the two diffusional contributions are fitted separately. This method should however give a picture of the behaviour of the translational diffusion to compare with the results from the multiple scattering subtracted data.

It should be noted that it is possible to fit the raw data to a two Lorentzian model with an additional constant background term, where the background term only describes the multiple scattering and vibrational mode contributions. However, as the contribution from rotational dynamics is more sensitive to problems in the multiple scattering subtraction, this fitting method would not be expected to give a true picture of the the rotational quasielastic contribution. By taking the simplest approach and considering only a single quasielastic contribution, this

reduces the number of degrees of freedom in the fit. As this model is only intended as an approximation it is desirable to make the fitting model less sensitive to the background contributions. It is hoped that this method will provide a foundation for future studies on this system by giving an initial picture of the translational behaviour of the water molecules.

The fit used to describe the raw data is then characterised by a single Lorentzian and the flat background component $B(Q)$ as follows:

$$S(Q,E) = I_{el}(Q)\delta(E) + A(Q)\frac{\Gamma_T(Q)}{E^2 + \Gamma_T(Q)^2} + B(Q) \tag{8.2}$$

Again, it must be emphasised that this is an approximation of the true form of the "background" contributions, in particular the rotational diffusional contribution, as they all also have an energy dependence. In particular, at low $|Q|$ where the multiple scattering is strongly energy dependent (see figure 8.2), this is expected to not describe the data well.

Figure 8.6 shows fits to the raw data using equation 8.2, with all parameters allowed to value freely. Reassuringly, this does not show a mis-fit at low $|Q|$ where the background contribution is expected to be more energy dependent. Instead, an acceptable fit is found at all pressures and $|Q|$.

Fits to the value for $\Gamma_T(Q)$ extracted from the one Lorentzian fits to the raw data are shown in figure 8.7. A comparison between these results and those shown in figure 8.4 shows that the $\Gamma_T(Q)$ from the one Lorentzian fit is better described by the three models trialled. In particular, the high pressure 2.3 GPa data shows good agreement at all $|Q|^2$. Again, the Singwi-Sjölander model shall be selected to describe this data in order to allow for direct comparison with the results found by Bove *et al.*

Figure 8.8 shows the extracted values for D_T for the data fitted by one Lorentzian. As expected, these show a larger errorbar on D_T than the results shown in figure 8.5. However, all of the results for D_T shown here are comparable with those found by Bove *et al.* In particular, above 1.7 GPa these results show good agreement with those found for pure water. This implies that above the mixing pressure the water in the mixture is uninhibited as if it were pure water.

Comparing the results for 0.6 GPa and 1.5 GPa from the one Lorentzian fitted data (figure 8.8) and the multiple scattering subtracted data (figure 8.5) yields some interesting observations. In figure 8.5 the result at 1.5 GPa agreed exactly

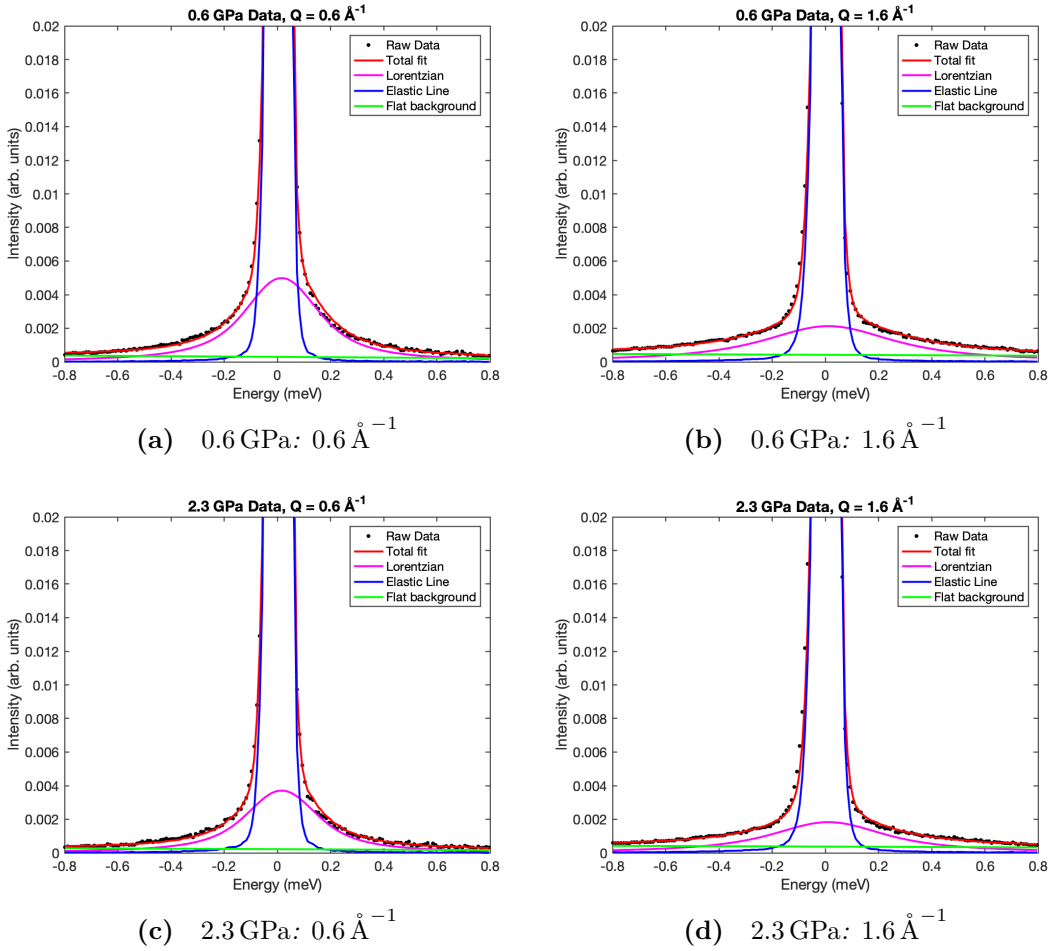

(a) 0.6 GPa*:* 0.6 Å^{-1} **(b)** 0.6 GPa*:* 1.6 Å^{-1}

(c) 2.3 GPa*:* 0.6 Å^{-1} **(d)** 2.3 GPa*:* 1.6 Å^{-1}

Figure 8.6 *Fits to the linewidth of the raw data at* 0.6 GPa *and* 2.3 GPa*,* 0.6 Å^{-1} *and* 1.6 Å^{-1}*, using single Lorentzian and approximated background contribution.*

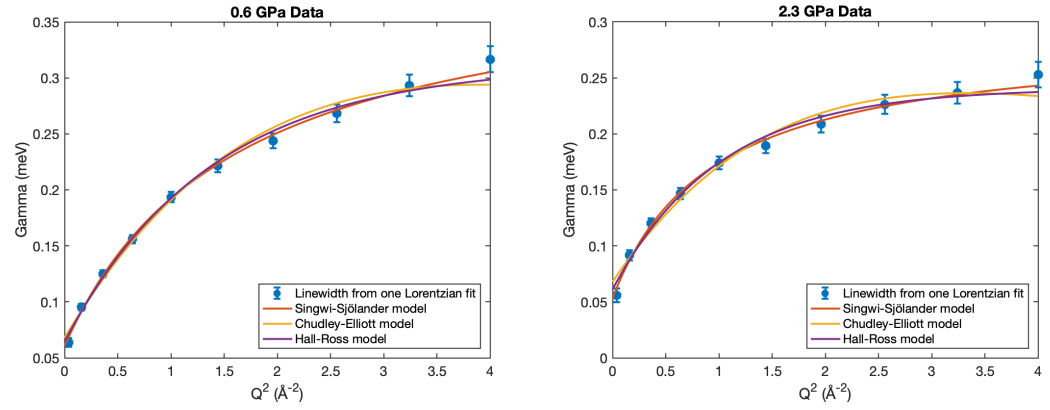

(a) 0.6 GPa **(b)** 2.3 GPa

Figure 8.7 *A comparison of models to fit the Q dependence of the linewidth of the translational water diffusion for a one Lorentzian fit at* 0.6 GPa *and* 2.3 GPa*.*

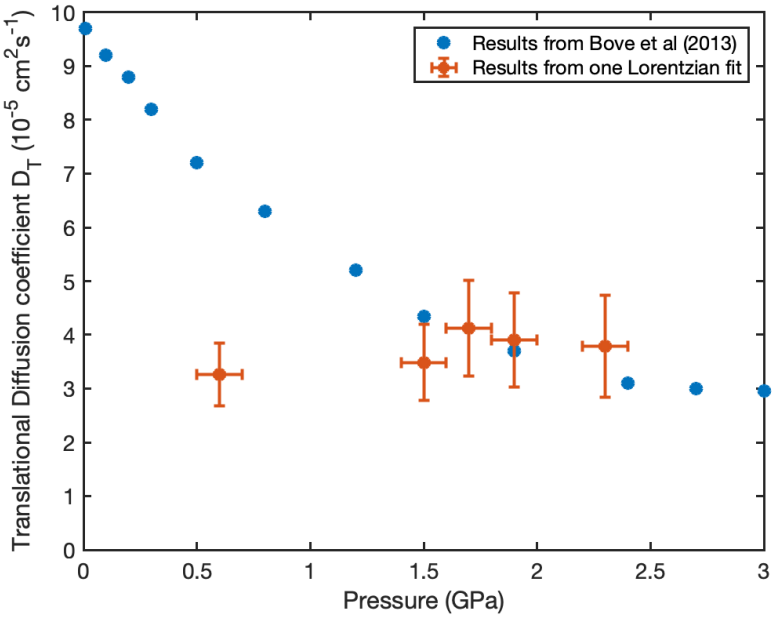

Figure 8.8 *Comparison of D_T values extracted from a one Lorentzian fit and those found in Bove et al [22].*

with that found by Bove *et al*, whereas in figure 8.8 the value for D_T is slightly reduced. At 1.5 GPa the sample is just below the mixing pressure, and thus it is expected that it is approaching the pure water behaviour as inferred for the higher pressure results. The 0.6 GPa result for D_T is lower than that found by Bove *et al* for both fitting procedures. This means it can be concluded that the translational motion of the water molecules is affected by the presence of methane bubbles in the unmixed state.

8.3 Discussion

In this chapter the diffusion of water in a mixture of CD_4 and H_2O was measured using quasielastic neutron scattering. Two methods were used to fit the results. The first method used the same approach as Bove *et al*, which considered two dynamical contributions to multiple scattering subtracted data [22]. However, this approach was not successful in this study, as only one dynamical contribution could be extracted, which is in contradiction with the literature for this temperature and pressure range. Additionally, the results extracted for the dynamical contribution that could be extracted showed large disagreement with literature above 1.7 GPa, with the 2.3 GPa result returning an

unphysical value for D_T. The problem with this approach was identified to be due to the large errors on the multiple scattering simulation, resulting in a masking of the broader dynamical contribution in the multiple scattering subtracted data. The second method used considered the multiple scattering contribution, the contribution from the broader dynamical contribution, and other contributions such as the vibrational modes as a single "background" contribution. The translational dynamical component was then fitted to the data not described by this "background". As with the previous approach, this method is in contradiction with the expected two dynamical contributions. However, it did allow for higher quality results for D_T to be extracted above 1.7 GPa. By comparing these two fitting procedures, a picture of the behaviour of the translational diffusion of water in the mixing process of methane and water may be formed.

Studies have been conducted where the quasielastic signal of water was best fitted by a single component. In these cases the translational and rotational dynamics of the molecule are highly coupled, for instance for supercooled water [145] or under confinement [109]. The proportion of CH_4 in this mixture is not sufficient to confine the water molecules. The rotational and translational modes of the water molecules will however couple to those of the methane, with the greatest impact for the molecular dynamics of H_2O molecules that neighbour CH_4 molecules [10]. This would be expected to give the most visible impact at pressures above the mixing transition. Due to the poor quality of the multiple scattering results, it cannot be established whether the coupling of CH_4 and H_2O motions causes a change in the relationship between the rotational and translational dynamics in the mixed water molecules compared to pure water.

The $|Q|$ dependence of the quasielastic linewidth extracted from the two fitting methods used in this study yielded the behaviour of the translational diffusional coefficient against pressure. In the fit to the multiple scattering subtracted data the translational diffusional coefficient could only be extracted for pressures below the mixing transition. However, results were recovered for all pressures in the second fitting procedure. In comparison to the literature values, the values for the diffusion coefficient D_T are markedly lower at 0.6 GPa, whereas above 1.7 GPa they are in agreement. This suggests that the water molecules are far more arrested than in pure water at 0.6 GPa. The Stokes-Einstein Law (shown in equation 2.8) links the temperature dependence of the diffusion coefficient to the viscosity, temperature, and radius of the larger species. As the experiment in this chapter was carried out at a constant temperature we can thus conclude

that a decrease in D_T implies an increase in either the radius of the methane bubble or the viscosity. It is unknown whether there is a time dependence of the methane bubble size on the scale of the experiment presented in this chapter (approximately 12 h per pressure). However, the radius extracted from D_T will be an average of any radius variation across the total measurement time.

An increase in viscosity would result from the presence of unmixed methane bubbles impeding the motion of the water according to Batchelor's equation (shown in equation 2.9). Upon mixing, this impediment is no longer present as the methane has dissolved into the water. We can use equation 2.9 to calculate the effective change in viscosity due to the presence of the bubbles. As the sI clathrate used for this experiment is 16.2% CD_4 by weight and methane is half the density of water at this pressure [1, 107] we can approximate the methane bubble volume fraction as 27.9%. From Pruteanu *et al*, the solubility of methane is expected to be less than 1 mol% at this pressure [140], so assuming 100% of the methane is in bubbles is an acceptable approximation. This leads to a predicted 1.76 times increase in viscosity. At 0.6 GPa in the results shown in figure 8.8 we observe a value for D_T which is approximately half that of pure water, meaning that there has been a doubling in viscosity. In this case Batchelor's equation slightly underestimates the viscosity change observed here due to the presence of the methane bubbles. For the 0.6 GPa result shown in figure 8.5 the value from Batchelor's equation better describes this viscosity change.

A change in viscosity of water has been observed to occur without an associated structural change [94], so this disparity cannot be explained by a change in the hydrogen-bonded water network. Rather, the disparity can be explained by considering the change in bubble size. Batchelor's equation assumes the bubbles to be the same radius at each pressure point, and that only the volume fraction is changing. Therefore two pressure points with different bubble radii cannot be compared by considering only Batchelor's equation. The use of a larger bubble radius in the Stokes-Einstein equation is expected to reduce the diffusion coefficient below that predicted by Batchelor's equation alone.

Batchelor's equation does not consider interactions between the species, only the contributions from Brownian motion. Thus any influence on the viscosity due to changes in the interactions are not accounted for in our above discussion. Computational simulations have suggested that the dipole moment of the methane increases during mixing [141]. Before mixing occurs, the dipole moment is almost zero. Additionally, Pruteanu *et al* established that there is an

increase in hydrogen bonds per H_2O molecule with pressure during mixing with methane [141]. Any viscosity change due to bubbles that persisted during and above the mixing pressure would not be well described by Batchelor's equation, but after mixing the volume fraction of bubbles is expected to be small enough as to not influence the viscosity. Therefore any differences between the viscosities observed and those expected from Batchelor's equation at low pressures must be due to hydrophobic or hydrogen bonding interactions between the methane and water molecules.

At 1.5 GPa the fluids are expected to be fully or almost-fully mixed. In the results presented here, the observed difference in D_T between pure water and the methane-water mixture is small. This suggests either a small volume fraction of bubbles or bubbles with small radii persist at this pressure. A useful further study would be to measure the value of D_T at other pressures below the mixing pressure. Carrying this experiment out in a DAC rather than a PE press would allow for visual confirmation of the volume fraction and size of the bubbles. This would provide useful information as to the macroscopic structure of the sample, and shed light on whether it is the volume fraction or bubble size of methane which influences the near-mixing behaviour of the diffusion coefficient.

From these observations, we comment that the behaviour of the water described here does not strongly deviate from the viscosity predictions for this mixture. As such, we conclude that the water dynamics do not influence the mixing properties of the methane, and rather are simply reacting to the change in volume fraction of the bubbles. Thus the change in solubility of the methane must come from a change in properties of the methane molecule.

8.4 Summary

This chapter has presented quasielastic neutron scattering results on the mixing behaviour of liquid water with gaseous methane as pressure is increased. Two fitting methods were employed, with the final extracted translational diffusional coefficients from each then compared to give a picture of how this changed in the mixing process. It was necessary to use two fitting methods to describe these results, as the simulated multiple scattering results were found to have too large an associated error to compare accurately with the raw data. In both fitting methods it was not possible to extract the rotational diffusional coefficients.

These results showed a lower diffusion coefficient compared to pure water at pressures below mixing, which then reached that of pure water once mixing was achieved. This is linked to a higher viscosity of the water before mixing with the methane. From Batchelor's equation we would expect the viscosity to increase by a factor of 1.76. The observed viscosity increase at 0.6 GPa is well approximated by this value. Batchelor's equation does not consider interaction changes and so we must also note the hydrophobic interaction and hydrogen bonding between methane and water molecules, which could contribute to this lower viscosity in the unmixed state.

Overall, the water dynamics react as predicted to the change in volume fraction of methane bubbles in the mixture. There are no anomalous changes in water dynamics that imply they are coupled with the solubility of the methane.

This study represents a first investigation into the dynamical changes during this mixing behaviour. The results that could be extracted were limited by the quality of multiple scattering simulations that could be carried out. Therefore a more robust method for carrying out these calculations, particularly in the case where total scattering data is unavailable, must be developed before future experiments can be carried out. Further experimentation should build upon the observed diffusivity of water: collecting additional data points in the pressure range below the mixing pressure would reveal more information about the rate of change of viscosity leading up to mixing. The dynamic properties of the methane molecules also warrant investigating, to examine whether the suggested change to dipole moment has any effect on this.

Chapter 9

Conclusion

This thesis has presented results on three different systems, all with different scientific questions. The common thread linking these studies has been the use of neutron scattering techniques, necessitated by the importance of hydrogen and hydrogen bonding to the problems being probed.

First, the rotation of the molecule in the methylammonium lead halide ($MAPbX_3$) compounds was examined using inelastic neutron scattering, Raman spectroscopy and quasielastic neutron scattering. Both the $MAPbCl_3$ and $MAPbBr_3$ compounds exhibit a series of transitions: going from a room temperature cubic phase; which in $MAPbBr_3$ is followed by a tetragonal phase not seen in $MAPbCl_3$; then transitioning through a short-lived tetragonal phase; and ending as a low temperature orthorhombic structure. It is found that rotational dynamics and molecular disorder decrease as temperature is reduced, with the short-lived tetragonal phase acting as a region of transitional dynamics. This change in dynamics is associated with the cage surrounding the molecule decreasing in size and the hydrogen bonds between the molecule and cage becoming stronger.

Second, the high pressure phase diagram of ammonium fluoride (NH_4F) was studied using neutron diffraction, Raman spectroscopy and density functional theory (DFT) calculations. These results revealed that the signals previously interpreted as a tetragonal phase transition were in fact due to deviatoric stress. The pressure dependence of the elastic anisotropy observed implies that the rotational and translational modes of the molecule are coupled, and the strength of this coupling is larger than that of the hydrogen bonding in the system.

Finally, the dynamics of the mixing behaviour of methane and water (CD_4-H_2O) with pressure was measured using quasielastic neutron scattering. The viscosity of water was found to be larger than that of pure water before mixing, while in the presence of methane bubbles. After mixing the viscosity returned to the value expected for pure water at this pressure. The observed viscosity change was well approximated by Batchelor's equation, which neglects changes to bubble size and any intermolecular interactions. However, it is expected that a full description of the influences upon the molecular motion will require the inclusion of hydrogen bonding and hydrophobic interactions.

In the $MAPbX_3$ and NH_4F chapters, the contribution of hydrogen bonding to the properties of the material is evident. It was known prior to this thesis that the tumbling of the molecule in $MAPbX_3$ had some influence upon the photovoltaic properties. Here we have observed that decreasing molecular motion due to increased hydrogen bonding between the molecule and inorganic framework in $MAPbBr_3$ occurs at the same temperature at which the photovoltaic properties decrease. The results presented in this thesis show that this same competition between molecular dynamics and hydrogen bond strength is an influence upon the elastic anisotropy of ND_4F. This results in the plastic properties and deviatoric stress effects observed in phase III of this compound. The influence of hydrogen bonding upon the dynamics of the mixing of CH_4 and H_2O is more unclear. It is expected that hydrogen bonding should be considered in giving a full explanation of the changes in water dynamics. However it is possible that the hydrogen bond strength is weak in comparison to the kinetic energy due to Brownian motion.

Overall, the results contained in this thesis serve to illustrate the importance of understanding the bonding properties and dynamics in molecular materials. These phenomena compete, and by changing the pressure or temperature it is possible to switch the dominant effect. This can allow for the tuning of material properties relevant to many different fields of science.

Future work to build off that done in this thesis could take many directions. In the case of the $MAPbX_3$ compounds, the results found in the QENS studies presented here suggested a larger variety of molecular dynamics with differing energy scales than had previously been suggested. This warrants further investigation of these materials with a wider variety of probes, and the review of previous literature with this result in mind. The study of NH_4F found that the equation of state presented in the literature for this compound does not consider the strong anisotropic strain effects, and therefore future research should re-characterise this. In addition,

efforts to describe the phase diagram of NH_4F at higher pressures should continue, utilising a variety of experimental and computational techniques. Finally, the work on CD_4-H_2O mixing in this thesis is intended as a preliminary investigation, and therefore has much scope for further studies. The primary direction to be taken from this work is the improvement of multiple scattering simulations for hydrogenous materials in high pressure experiments. Further to this, additional experiments should be carried to verify the dynamical behaviour of the H_2O above and below the mixing transition. The dynamics of the CH_4 molecules should also be studied to assess how this contributes or responds to the mixing of the two species.

Bibliography

[1] Abramson, E. H., and J. M. Brown. "Equation of state of water based on speeds of sound measured in the diamond-anvil cell." *Geochimica et Cosmochimica Acta* 68, 8: (2004) 1827–1835.

[2] Adams, M. A., K. Refson, and B. J. Gabrys. "The high resolution inelastic neutron scattering spectrum of ammonium fluoride." *Physical Chemistry Chemical Physics* 7, 21: (2005) 3685–3692.

[3] Adrian, H. W. W., and D. Feil. "The structure of NH_4F as determined by neutron and X-ray diffraction." *Acta Crystallographica Section A* 25, 3: (1969) 438–444.

[4] Amann-Winkel, K., M.-C. Bellissent-Funel, L. E. Bove, T. Loerting, A. Nilsson, A. Paciaroni, D. Schlesinger, and L. Skinner. "X-ray and Neutron Scattering of Water." *Chemical Reviews* 116, 13: (2016) 7570–7589.

[5] Andreani, L. C., A. Bozzola, P. Kowalczewski, M. Liscidini, and L. Redorici. "Silicon solar cells: Toward the efficiency limits." *Advances in Physics: X* 4, 1.

[6] Arnold, O., J. C. Bilheux, J. M. Borreguero, A. Buts, S. I. Campbell, L. Chapon, M. Doucet, N. Draper, R. Ferraz Leal, M. A. Gigg, V. E. Lynch, A. Markvardsen, D. J. Mikkelson, R. L. Mikkelson, R. Miller, K. Palmen, P. Parker, G. Passos, T. G. Perring, P. F. Peterson, S. Ren, M. A. Reuter, A. T. Savici, J. W. Taylor, R. J. Taylor, R. Tolchenov, W. Zhou, and J. Zikovsky. "Mantid - Data analysis and visualization package for neutron scattering and μ SR experiments." *Nuclear Instruments and Methods in Physics Research, Section A: Accelerators, Spectrometers, Detectors and Associated Equipment* 764: (2014) 156–166.

[7] Ashcroft, N. W. "Hydrogen dominant metallic alloys: High temperature superconductors?" *Physical Review Letters* 92, 18: (2004) 1–4.

[8] Baikie, T., N. S. Barrow, Y. Fang, P. J. Keenan, P. R. Slater, R. O. Piltz, M. Gutmann, S. G. Mhaisalkar, and T. J. White. "A combined single crystal neutron/X-ray diffraction and solid-state nuclear magnetic resonance study

of the hybrid perovskites $CH_3NH_3PbX_3$ (X = I, Br and Cl)." *Journal of Materials Chemistry A* 3, 17: (2015) 1–5.

[9] Bakulin, A. A., M. S. Pshenichnikov, H. J. Bakker, and C. Petersen. "Hydrophobic molecules slow down the hydrogen-bond dynamics of water." *Journal of Physical Chemistry A* 115, 10: (2011) 1821–1829.

[10] Banerjee, P., and B. Bagchi. "Ions' motion in water." *Journal of Chemical Physics* 150, 19. `http://dx.doi.org/10.1063/1.5090765`.

[11] Bao, W., D. Liu, Y. Duan, and M. Peng. "First-principles predictions of anisotropies in elasticity and sound velocities of CsCl-type refractory intermetallics: TiTM, ZrTM and HfTM (TM = Fe, Ru, Os)." *Philosophical Magazine* 99, 21: (2019) 2681–2702.

[12] Barbiellini, B., C. Bellin, G. Loupias, T. Buslaps, and A. Shukla. "How the hydrogen bond in NH_4F is revealed with Compton scattering." *Physical Review B* 79, 15: (2009) 2–5.

[13] Bartlett, G., and I. Langmuir. "The crystal structures of the ammonium halides above and below the transition temperatures." *Journal of the American Chemical Society* 43, 1: (1921) 84–91.

[14] Batchelor, G. K. "The effect of Brownian motion on the bulk stress in a suspension of spherical particles." *Journal of Fluid Mechanics* 83, 1: (1977) 97–117.

[15] Bée, M. *Quasielastic Neutron Scattering Principles and Application in Solid State Chemistry, Biology and Materials Science.* Adam Hilger, 1988.

[16] Bell, P. M., J. A. Xu, and H. K. Mao. "High-Pressure Ruby and Diamond Fluorescence: Observations at 0.21 to 0.55 Terapascal." *Science* 232, 4756: (1986) 1404–1406.

[17] Bellin, C., A. Mafety, C. Narayana, P. Giura, G. Rousse, J. P. Itié, A. Polian, A. M. Saitta, and A. Shukla. "Disorder-order phase transition at high pressure in ammonium fluoride." *Physical Review B* 96, 9: (2017) 3–9.

[18] Bewley, R. I., J. W. Taylor, and S. M. Bennington. "LET, a cold neutron multi-disk chopper spectrometer at ISIS." *Nuclear Instruments and Methods in Physics Research Section A* 637: (2011) 128–134.

[19] Bezacier, L., E. Le Menn, O. Grasset, O. Bollengier, A. Oancea, M. Mezouar, and G. Tobie. "Experimental investigation of methane hydrates dissociation up to 5GPa: Implications for Titan's interior." *Physics of the Earth and Planetary Interiors* 229: (2014) 144–152.

[20] Böer, K. W., and U. W. Pohl. *Elasticity and Phonons.* 1. 2020.

[21] Bove, L. E., S. Klotz, A. Paciaroni, and F. Sacchetti. "Anomalous proton dynamics in ice at low temperatures." *Physical Review Letters* 103, 16: (2009) 1–4.

[22] Bove, L. E., S. Klotz, T. Strässle, M. M. Koza, J. Teixeira, and A. M. Saitta. "Translational and rotational diffusion in water in the gigapascal range." *Physical Review Letters* 111, 18: (2013) 185,901.

[23] Boyle, R. *A defence of the doctrine touching the spring and weight of the air, propos'd by Mr. R. Boyle in his New Physico-Mechanical Experiment... by the author of those experiments.* London : Printed by F. G. for Thomas Robinson, 1662.

[24] Bragg, W. H., and W. L. Bragg. *X-rays and crystal structure.* London: G. Bell, 1924, fourth edition.

[25] Bridgman, P. W. "Polymorphism at High Pressures." *Proceedings of the American Academy of Arts and Sciences* 52, 3: (1916) 91.

[26] Brivio, F., J. M. Frost, J. M. Skelton, A. J. Jackson, O. J. Weber, M. T. Weller, A. R. Goñi, A. M. A. Leguy, P. R. F. Barnes, and A. Walsh. "Lattice dynamics and vibrational spectra of the orthorhombic, tetragonal, and cubic phases of methylammonium lead iodide." *Physical Review B* 92: (2015) 144,308.

[27] Brown, K. L., S. F. Parker, I. R. García, S. Mukhopadhyay, V. G. Sakai, and C. Stock. "Molecular orientational melting within a lead-halide octahedron framework: The order-disorder transition in $CH_3NH_3PbBr_3$." *Physical Review B* 96: (2017) 174,111.

[28] Brunetti, B., C. Cavallo, A. Ciccioli, G. Gigli, and A. Latini. "On the Thermal and Thermodynamic (In)Stability of Methylammonium Lead Halide Perovskites." *Scientific Reports* 6, August: (2016) 1–10.

[29] Buffett, B. A. "Clathrate Hydrates." *Annual Review of Earth and Planetary Sciences* 28, 1: (2000) 477–507.

[30] Bull, C. L., N. P. Funnell, M. G. Tucker, S. Hull, D. J. Francis, and W. G. Marshall. "PEARL: the high pressure neutron powder diffractometer at ISIS." *High Pressure Research* 36, 4: (2016) 493–511.

[31] Calvert, L. D., and E. Whalley. "Structure of ammonium fluoride IV." *The Journal of Chemical Physics* 53, 6: (1970) 2151–2155.

[32] Campbell, S., M. Telling, and C. Carlile. "The optimisation of analyser geometry in near-backscattering spectrometers – IRIS on the ISIS-pulsed source." *Physica B* 276: (2000) 206 – 207.

[33] Carlile, C., and M. Adams. "The design of the IRIS inelastic neutron spectrometer and improvements to its analysers." *Physica B* 182, 4: (1992) 431 – 440. Quasielastic Neutron Scattering.

[34] Carter, R. L. "Raman spectra of $(NH_4)3ZnCl_4NO_3$ and $(ND_4)3ZnCl_4NO_3$ between 295 and 60 K." *Spectrochimica Acta Part A: Molecular and Biomolecular Spectroscopy* 58, 14: (2002) 3185–3195.

[35] Carter, R. L., and L. K. O'Hare. "Raman spectra of solid $(NH_4)2CrO_4$ and $(ND_4)2CrO_4$ obtained by a rotating cell technique." *Applied Spectroscopy* 30, 2: (1976) 187–190.

[36] Chaikin, P. M., T. C. Lubensky, and T. A. Witten. *Principles of condensed matter physics*, volume 1. Cambridge university press Cambridge, 1995.

[37] Chandler, D. "Interfaces and the driving force of hydrophobic assembly." *Nature* 437, 7059: (2005) 640–647.

[38] Chen, C., X. Hu, W. Lu, S. Chang, L. Shi, L. Li, H. Zhong, and J. B. Han. "Elucidating the phase transitions and temperature-dependent photoluminescence of $MAPbBr_3$ single crystal." *Journal of Physics D: Applied Physics* 51, 4.

[39] Chen, J., Z.-H. Mo, X. Yang, H.-L. Zhou, and Q. Gao. "Exploration of organic-inorganic hybrid perovskites for surface-enhanced infrared spectroscopy of small molecules." *Chemical Communications* 53: (2017) 6949–6952.

[40] Chen, T., B. J. Foley, B. Ipek, M. Tyagi, J. R. D. Copley, C. M. Brown, J. J. Choi, and S.-H. Lee. "Rotational dynamics of organic cations in the $CH_3NH_3PbI_3$ perovskite." *Physical Chemistry Chemical Physics* 17: (2015) 31,278–31,286.

[41] Chi, L., I. P. Swainson, L. Cranswick, J. H. Her, P. Stephens, and O. Knop. "The ordered phase of methylammonium lead chloride $CH_3ND_3PbCl_3$." *Journal of Solid State Chemistry* 178, 5: (2005) 1376–1385.

[42] Cho, C. H., J. Urquidi, S. Singh, S. C. Park, and G. W. Robinson. "Pressure effect on the density of water." *Journal of Physical Chemistry A* 106, 33: (2002) 7557–7561.

[43] Choukroun, M., O. Grasset, G. Tobie, and C. Sotin. "Stability of methane clathrate hydrates under pressure: Influence on outgassing processes of methane on Titan." *Icarus* 205, 2: (2010) 581–593.

[44] Chung, I., B. Lee, J. He, R. P. Chang, and M. G. Kanatzidis. "All-solid-state dye-sensitized solar cells with high efficiency." *Nature* 485, 7399: (2012) 486–489.

[45] Coates, L., H. B. Cao, B. C. Chakoumakos, M. D. Frontzek, C. Hoffmann, A. Y. Kovalevsky, Y. Liu, F. Meilleur, A. M. Dos Santos, D. A. Myles, X. P. Wang, and F. Ye. "A suite-level review of the neutron single-crystal diffraction instruments at Oak Ridge National Laboratory." *Review of Scientific Instruments* 89, 9.

[46] Comin, R., M. K. Crawford, A. H. Said, N. Herron, W. E. Guise, X. Wang, P. S. Whitfield, A. Jain, X. Gong, A. J. H. McGaughey, and E. H. Sargent. "Lattice dynamics and the nature of structural transitions in organolead halide perovskites." *Physical Review B* 94: (2016) 094,301.

[47] Cruickhank Miller, C. "The Stokes-Einstein Law Diffusion." *Proc. Royal Soc. Lond. A* 17, 5: (1924) 724–748.

[48] Cui, X., S. Yuan, H. Zhang, X. Zhang, P. Wang, L. Tu, Z. Sun, J. Wang, and L. Zheng. "Temperature-dependent electronic properties of inorganic-organic hybrid halide perovskite ($CH_3NH_3PbBr_3$) single crystal." *Applied Physics Letters* 233302: (2017) 1–6.

[49] Dasannacharya, B. A., and G. Venkataraman. "Dynamics of Liquid CH_4 from Cold-Neutron Scattering." *Physical Review* 156, 1: (1967) 196–203.

[50] Dill, K. A. "The meaning of hydrophobicity." *Science* 250, 4978: (1990) 297–298.

[51] Dove, M. T. "An introduction to the use of neutron scattering methods in mineral sciences." *European Journal of Mineralogy* 14: (2002) 203–224.

[52] Drain, L. E. "Nuclear magnetic resonance in ammonium fluoride." *Discussions of the Faraday Society* 19, 200: (1955) 200–207.

[53] Drużbicki, K., R. S. Pinna, S. Rudić, M. Jura, G. Gorini, and F. Fernandez-Alonso. "Unexpected Cation Dynamics in the Low-Temperature Phase of Methylammonium Lead Iodide: The Need for Improved Models." *The Journal of Physical Chemistry Letters* 7, 22: (2016) 4701–4709.

[54] Duan, Z., and S. Mao. "A thermodynamic model for calculating methane solubility, density and gas phase composition of methane-bearing aqueous fluids from 273 to 523 K and from 1 to 2000 bar." *Geochimica et Cosmochimica Acta* 70, 13: (2006) 3369–3386.

[55] Dubrovinskaia, N., L. Dubrovinsky, N. A. Solopova, A. Abakumov, S. Turner, M. Hanfland, E. Bykova, M. Bykov, C. Prescher, V. B. Prakapenka, S. Petitgirard, I. Chuvashova, B. Gasharova, Y.-L. Mathis, P. Ershov, I. Snigireva, and A. Snigirev. "Terapascal static pressure generation with ultrahigh yield strength nanodiamond." *Science Advances* 2, 7. `https://advances.sciencemag.org/content/2/7/e1600341`.

[56] Duffy, T. S. "Synchrotron facilities and the study of the Earth's deep interior." *Reports on Progress in Physics* 68, 8: (2005) 1811–1859.

[57] Duffy, T. S., and R. F. Smith. "Ultra-high pressure dynamic compression of geological materials." *Frontiers in Earth Science* 7, February: (2019) 1–20.

[58] Egelstaff, P. A. *An introduction to the liquid state*. Oxford series on neutron scattering in condensed matter. Clarendon Press, 1992. `https://books.google.co.uk/books?id=iCLwAAAAMAAJ`.

[59] Endres, J., D. A. Egger, M. Kulbak, R. A. Kerner, L. Zhao, S. H. Silver, G. Hodes, B. P. Rand, D. Cahen, L. Kronik, and A. Kahn. "Valence and Conduction Band Densities of States of Metal Halide Perovskites: A Combined Experimental–Theoretical Study." *Journal of Physical Chemistry Letters* 7, 14: (2016) 2722–2729.

[60] Even, J., M. Carignano, and C. Katan. "Molecular disorder and translation/rotation coupling in the plastic crystal phase of hybrid perovskites." *Nanoscale* 8: (2016) 6222–6236.

[61] Even, J., S. Paofai, P. Bourges, A. Letoublon, S. Cordier, O. Durand, and C. Katan. "Carrier scattering processes and low energy phonon spectroscopy in hybrid perovskites crystals." *Proceedings of SPIE* 9743: (2016) 97,430M–97,430M–8.

[62] Even, J., L. Pedesseau, J.-M. Jancu, and C. Katan. "Importance of Spin–Orbit Coupling in Hybrid Organic/Inorganic Perovskites for Photovoltaic Applications." *The Journal of Physical Chemistry Letters* 4, 17: (2013) 2999–3005.

[63] Fabini, D. H., T. Hogan, H. A. Evans, C. C. Stoumpos, M. G. Kanatzidis, and R. Seshadri. "Dielectric and Thermodynamic Signatures of Low-Temperature Glassy Dynamics in the Hybrid Perovskites $CH_3NH_3PbI_3$ and $HC(NH_2)_2PbI_3$." *Journal of Physical Chemistry Letters* 7, 3: (2016) 376–381.

[64] Fanetti, S., M. Citroni, K. Dziubek, M. M. Nobrega, and R. Bini. "The role of H-bond in the high-pressure chemistry of model molecules." *Journal of Physics Condensed Matter* 30, 9.

[65] Gallop, N. P., O. Selig, G. Giubertoni, H. J. Bakker, Y. L. A. Rezus, J. M. Frost, T. L. C. Jansen, R. Lovrinčić, and A. A. Bakulin. "Rotational Cation Dynamics in Metal Halide Perovskites: Effect on Phonons and Material Properties." *The Journal of Physical Chemistry Letters* 9, 20: (2018) 5987–5997. `http://pubs.acs.org/doi/10.1021/acs.jpclett.8b02227`.

[66] Gao, W., X. Gao, T. A. Abtew, Y.-Y. Sun, S. Zhang, and P. Zhang. "Quasiparticle band gap of organic-inorganic hybrid perovskites: Crystal structure, spin-orbit coupling, and self-energy effects." *Physical Review B* 93: (2016) 085,202.

[67] García Sakai, V., E. Mamontov, J. W. Lynn, L. Viciu, and R. J. Cava. "Dynamics of water in the $Na_{0.3}CoO_2 \cdot 1.4H_2O$ superconductor." *Physical Review B* 75: (2007) 014,505.

[68] Gay-Lussac, J. L. "Recherches sur la dilatation des gaz et des vapeurs." In *Annales de chimie*. 1802, volume 43, 137–175.

[69] Giguère, P. A. "Bifurcated hydrogen bonds in water." *Journal of Raman Spectroscopy* 15, 5: (1984) 354–359.

[70] Glazkov, V. P., D. P. Kozlenko, B. N. Savenko, and V. A. Somenkov. "Vibrational spectra of the ammonia halides NH_4I and NH_4F at high pressures." *Journal of Experimental and Theoretical Physics* 90, 2: (2000) 319–323.

[71] Glazkov, V., V. Somenkov, S. Shil'shtein, D. Kozlenko, and B. Savenko. "Neutron diffraction study of structural variations in ND_4I and ND_4F ammonium halides under high pressures." *Crystallography Reports* 44, 1: (1999) 50–55.

[72] Guillot, T. "The Interiors of Giant Planets: Models and Outstanding Questions." *Annual Review of Earth and Planetary Sciences* 33, 1: (2005) 493–530.

[73] Guo, Y., O. Yaffe, D. W. Paley, A. N. Beecher, T. D. Hull, G. Szpak, J. S. Owen, L. E. Brus, and M. A. Pimenta. "Interplay between organic cations and inorganic framework and incommensurability in hybrid lead-halide perovskite $CH_3NH_3PbBr_3$." *Physical Review Materials* 1–9.

[74] Guthrie, M. "Future directions in high-pressure neutron diffraction." *Journal of Physics: Condensed Matter* 27, 15.

[75] Guthrie, M., C. G. Pruteanu, M. E. Donnelly, J. J. Molaison, A. M. Dos Santos, J. S. Loveday, R. Boehler, and C. A. Tulk. "Radiation attenuation by single-crystal diamond windows." *Journal of Applied Crystallography* 50, 1: (2017) 76–86.

[76] Gutt, C., B. Asmussen, W. Press, C. Merkl, H. Casalta, J. Greinert, G. Bohrmann, J. S. Tse, and A. Hüller. "Quantum rotations in natural methane-clathrates from the Pacific sea-floor." *Europhysics Letters* 48, 3: (1999) 269–275.

[77] Hempelmann, R. *Quasielastic Neutron Scattering and Solid State Diffusion.* Oxford University Press, 2000.

[78] Henry, W. "Experiments on the quantity of gases absorbed by water, at different temperatures, and under different pressures." *Philosophical Transactions of the Royal Society* 93, January: (1803) 29–274.

[79] Herz, L. M. "Charge-Carrier Dynamics in Organic-Inorganic Metal Halide Perovskites." *Annual Review of Physical Chemistry* 67, 1: (2016) 65–89.

[80] Hohenberg, P., and W. Kohn. "Inhomogeneous Electron Gas." *Physical Review* 136, 3B: (1964) B864–B871.

[81] Huang, Y., X. Huang, L. Wang, G. Wu, D. Duan, K. Bao, Q. Zhou, B. Liu, and T. Cui. "Structural properties of ammonium iodide under high pressure." *RSC Advances* 5, 50: (2015) 40,336–40,340.

[82] Huang, Y., X. Huang, W. Li, L. Wang, G. Wu, Z. Zhao, D. Duan, K. Bao, Q. Zhou, B. Liu, and T. Cui. "Pressure-induced structural changes in NH_4Br." *Journal of Chemical Physics* 143, 6.

[83] Inganäs, O., and V. Sundström. "Solar energy for electricity and fuels." *Ambio* 45: (2016) 15–23.

[84] Jaffe, A., Y. Lin, C. M. Beavers, J. Voss, W. L. Mao, and H. I. Karunadasa. "High-pressure single-crystal structures of 3D lead-halide hybrid perovskites and pressure effects on their electronic and optical properties." *ACS Central Science* 2, 4: (2016) 201–209.

[85] Jayaraman, A. "Diamond anvil cell and high-pressure physical investigations." *Reviews of Modern Physics* 55, 1: (1983) 65–108.

[86] Kawamura, Y., and H. Mashiyama. "Modulated Structure in Phase II of $CH_3NH_3PbCl_3$." *Journal of the Korean Physical Society* 35: (1999) S1437–S1440.

[87] Kawamura, Y., H. Mashiyama, and K. Hasebe. "Structural Study on Cubic-Tetragonal Transition of $CH_3NH_3PbI_3$." *Journal of the Physical Society of Japan* 71, 7: (2002) 1694–1697.

[88] Kieslich, G., J. M. Skelton, J. Armstrong, Y. Wu, F. Wei, K. L. Svane, A. Walsh, and K. T. Butler. "Hydrogen Bonding versus Entropy: Revealing the Underlying Thermodynamics of the Hybrid Organic-Inorganic Perovskite $[CH_3NH_3]PbBr_3$." *Chemistry of Materials* .

[89] Kittel, C. *Introduction to Solid State Physics, 8th edition.* 2004.

[90] Klotz, S., J. M. Besson, G. Hamel, R. J. Nelmes, J. S. Loveday, W. G. Marshall, and R. M. Wilson. "Neutron powder diffraction at pressures beyond 25 GPa." *Applied Physics Letters* 66, 1995: (1995) 1735.

[91] Klotz, S., J. C. Chervin, P. Munsch, and G. Le Marchand. "Hydrostatic limits of 11 pressure transmitting media." *Journal of Physics D: Applied Physics* 42, 7.

[92] Klotz, S., T. Strässle, G. Rousse, G. Hamel, and V. Pomjakushin. "Angle-dispersive neutron diffraction under high pressure to 10 GPa." *Applied Physics Letters* 86, 3: (2005) 1–3.

[93] Kohn, W., and L. J. Sham. "Self-Consistent Equations Including Exchange and Correlation Effects." *Physical Review* 140, 4A: (1965) A1133–A1138.

[94] Krynicki, K., C. D. Green, and D. W. Sawyer. "Pressure and temperature dependence of self-diffusion in water." *Faraday Discussions of the Chemical Society* 66: (1978) 199–208.

[95] Kuhs, W. F., D. K. Staykova, and A. N. Salamatin. "Formation of methane hydrate from polydisperse ice powders." *Journal of Physical Chemistry B* 110, 26: (2006) 13,283–13,295.

[96] Kume, T., M. Daimon, S. Sasaki, and H. Shimizu. "High-pressure elastic properties of liquid and solid ammonia." *Physical Review B - Condensed Matter and Materials Physics* 57, 21: (1998) 13,347–13,350.

[97] Kuriakose, A. K., and E. Whalley. "Phase Diagram of Ammonium Fluoride to 20 kbar." *The Journal of Chemical Physics* 48, 5: (1968) 2025–2031.

[98] Kuriakose, M., S. Raetz, Q. M. Hu, S. M. Nikitin, N. Chigarev, V. Tournat, A. Bulou, A. Lomonosov, P. Djemia, V. E. Gusev, and A. Zerr. "Longitudinal sound velocities, elastic anisotropy, and phase transition of high-pressure cubic H_2O ice to 82 GPa." *Physical Review B* 96, 13: (2017) 1–13.

[99] Laamari, M. E., A. Cheknane, A. Benghia, and H. S. Hilal. "Optimized opto-electronic and mechanical properties of orthorhombic methylamunium lead halides ($MAPbX_3$) (X = I, Br and Cl) for photovoltaic applications." *Solar Energy* 182, December 2018: (2019) 9–15.

[100] Lawson, A. C., R. B. Roof, J. D. Jorgensen, B. Morosin, and J. E. Schirber. "Structure of ND_4F-II." *Acta Crystallographica Section B* 45, 3: (1989) 212–218.

[101] Lee, J.-H., N. C. Bristowe, P. D. Bristowe, and A. K. Cheetham. "Role of hydrogen-bonding and its interplay with octahedral tilting in $CH_3NH_3PbI_3$." *Chemical Communications* 51: (2015) 6434–6437.

[102] Lee, J.-H., N. C. Bristowe, J. H. Lee, S.-H. Lee, P. D. Bristowe, A. K. Cheetham, and H. M. Jang. "Resolving the Physical Origin of Octahedral Tilting in Halide Perovskites." *Chemistry of Materials* 28, 12: (2016) 4259–4266.

[103] Leguy, A. M. A., J. M. Frost, A. P. McMahon, V. G. Sakai, W. Kockelmann, C. Law, X. Li, F. Foglia, A. Walsh, B. C. O'Regan, J. Nelson, J. T. Cabral, and P. R. F. Barnes. "The dynamics of methylammonium ions in hybrid organic-inorganic perovskite solar cells." *Nature Communications* 6: (2015) 7124 EP –.

[104] Leguy, A. M. A., A. R. Goni, J. M. Frost, J. Skelton, F. Brivio, X. Rodriguez-Martinez, O. J. Weber, A. Pallipurath, M. I. Alonso, M. Campoy-Quiles, M. T. Weller, J. Nelson, A. Walsh, and P. R. F. Barnes. "Dynamic disorder, phonon lifetimes, and the assignment of modes to the vibrational spectra of methylammonium lead halide perovskites." *Physical Chemistry Chemical Physics* 18: (2016) 27,051–27,066.

[105] Levy, H. A., and S. W. Peterson. "Neutron Diffraction Determination of the Crystal Structure of Ammonium Bromide in Four Phases." *Journal of the American Chemical Society* 75, 7: (1953) 1536–1542.

[106] Li, B., Y. Kawakita, Y. Liu, M. Wang, M. Matsuura, K. Shibata, S. Ohira-Kawamura, T. Yamada, S. Lin, K. Nakajima, and S. F. Liu. "Polar rotor scattering as atomic-level origin of low mobility and thermal conductivity of perovskite $CH_3NH_3PbI_3$." *Nature Communications* 8, May: (2017) 16,086.

[107] Li, M., F. Li, W. Gao, C. Ma, L. Huang, Q. Zhou, and Q. Cui. "Brillouin scattering study of liquid methane under high pressures and high temperatures." *Journal of Chemical Physics* 133, 4: (2010) 0–7.

[108] Li, X., W. Shi, X. Liu, and Z. Mao. "High-pressure phase stability and elasticity of ammonia hydrate." *American Mineralogist* 104, 9: (2019) 1307–1314.

[109] Line, C. M. B., B. Winkler, and M. T. Dove. "Quasielastic incoherent neutron scattering study of the rotational dynamics of the water molecules in analcime." *Physics and Chemistry of Minerals* 21, 7: (1994) 451–459.

[110] Loerting, T., C. Salzmann, I. Kohl, E. Mayer, and A. Hallbrucker. "A second distinct structural 'state' of high-density amorphous ice at 77 K and 1 bar." *Physical Chemistry Chemical Physics* 3, 24: (2001) 5355–5357.

[111] López, C. A., M. V. Martínez-Huerta, M. C. Álvarez-Galván, P. Kayser, P. Gant, A. Castellanos-Gomez, M. T. Fernández-Díaz, F. Fauth, and J. A. Alonso. "Elucidating the Methylammonium (MA) Conformation in $MAPbBr_3$ Perovskite with Application in Solar Cells." *Inorganic Chemistry* 56, 22: (2017) 14,214–14,219.

[112] Loveday, J. *High-Pressure Physics*. Scottish Graduate Series. Taylor & Francis, 2012.

[113] Loveday, J. S., and R. J. Nelmes. "High-pressure gas hydrates." *Physical Chemistry Chemical Physics* 10, 7: (2008) 937–950.

[114] Maaej, A., M. Bahri, Y. Abid, N. Jaidane, Z. B. Lakhdar, and A. Lautié. "Raman study of low temperature phase transitions in the cubic perovskite $CH_3NH_3PbCl_3$." *Phase Transitions* 64, 4: (1998) 179–190.

[115] Mackay, D., W.-Y. Shiu, K.-C. Ma, and S. C. Lee. "Handbook of physical-chemical properties and environmental fate for organic chemicals." *Choice Reviews Online* 45, 07: (2013) 45–3795–45–3795.

[116] Mao, H. K., J. Xu, and P. M. Bell. "Calibration of the ruby pressure gauge to 800 kbar under quasi-hydrostatic conditions." *Journal of Geophysical Research* 91, B5: (1986) 4673.

[117] Mao, H. K., X. J. Chen, Y. Ding, B. Li, and L. Wang. "Solids, liquids, and gases under high pressure." *Reviews of Modern Physics* 90, 1: (2018) 15,007.

[118] Mashiyama, H., Y. Kawamura, H. Kasano, T. Asahi, Y. Noda, and H. Kimura. "Disordered configuration of methylammonium of $CH_3NH_3PbBr_3$ determined by single crystal neutron diffractometry." *Ferroelectrics* 348, January: (2007) 182–186.

[119] Mashiyama, H., Y. Kawamura, and Y. Kubota. "The Anti-Polar Structure of $CH_3NH_3PbBr_3$." *Journal of the Korean Physical Society* 51: (2007) 850.

[120] Mason, T. E., T. J. Gawne, S. E. Nagler, M. B. Nestor, and J. M. Carpenter. "The early development of neutron diffraction: Science in the wings of the Manhattan Project." *Acta Crystallographica Section A: Foundations of Crystallography* 69, 1: (2013) 37–44.

[121] Mayers, J., N. I. Gidopoulos, M. A. Adams, G. Reiter, C. Andreani, and R. Senesi. "Comment on "High-energy neutron scattering from hydrogen using a direct geometry spectrometer"." *Physical Review B* 84: (2011) 056,301.

[122] McCrone, A., U. Moslener, F. D'Estais, C. Grüning, T. Ajadi, R. Boyle, D. Strahan, M. Kimmel, B. Collins, A. Cheung, and L. Becker. "Global Trends in Renewable Energy." *Proceedings of Scientific Works of Cherkasy State Technological University. Series: Economic Sciences* 1, 40.

[123] McCusker, L. B., R. B. Von Dreele, D. E. Cox, D. Louër, and P. Scardi. "Rietveld refinement guidelines." *Journal of Applied Crystallography* 32, 1: (1999) 36–50. https://doi.org/10.1107/S0021889898009856.

[124] Motta, C., F. El-Mellouhi, S. Kais, N. Tabet, F. Alharbi, and S. Sanvito. "Revealing the role of organic cations in hybrid halide perovskite $CH_3NH_3PbI_3$." *Nature Communications* 6: (2015) 7026 EP –.

[125] Murai, Y., and H. Oiwa. "Increase of effective viscosity in bubbly liquids from transient bubble deformation." *Fluid Dynamics Research* 40, 7-8: (2008) 565–575.

[126] Nabar, M. A., L. D. Calvert, and E. Whalley. "X-ray and thermal analysis of quenched ammonium fluoride II and III: Three new phases." *The Journal of Chemical Physics* 51, 4: (1969) 1353–1356.

[127] Niemann, R. G., A. G. Kontos, D. Palles, E. I. Kamitsos, A. Kaltzoglou, F. Brivio, P. Falaras, and P. J. Cameron. "Halogen Effects on Ordering and Bonding of $CH_3NH_3^+$ in $CH_3NH_3PbX_3$ (X = Cl, Br, I) Hybrid Perovskites: A Vibrational Spectroscopic Study." *The Journal of Physical Chemistry C* 120, 5: (2016) 2509–2519.

[128] Niesner, D., M. Wilhelm, I. Levchuk, A. Osvet, S. Shrestha, M. Batentschuk, C. Brabec, and T. Fauster. "Giant Rashba Splitting in $CH_3NH_3PbBr_3$ Organic-Inorganic Perovskite." *Physical Review Letters* 117: (2016) 126,401.

[129] Nilsson, A., and L. G. M. Pettersson. "The structural origin of anomalous properties of liquid water." *Nature Communications* 6, 1: (2015) 8998.

[130] Noh, J. H., S. H. Im, J. H. Heo, T. N. Mandal, and S. I. Seok. "Chemical Management for Colorful, Efficient, and Stable Inorganic–Organic Hybrid Nanostructured Solar Cells." *Nano Letters* 13, 4: (2013) 1764–1769.

[131] Omta, A. W., M. F. Kropman, S. Woutersen, and H. J. Bakker. "Negligible Effect of Ions on the Hydrogen-Bond Structure in Liquid Water." *Science* 301, 5631: (2003) 347–349.

[132] Page, K., J. E. Siewenie, P. Quadrelli, and L. Malavasi. "Short-Range Order of Methylammonium and Persistence of Distortion at the Local Scale in $MAPbBr_3$ Hybrid Perovskite." *Angewandte Chemie International Edition in English* 55, 46: (2016) 14,320–14,324.

[133] Perring, T. G., A. D. Taylor, D. M. Paul, A. T. Boothroyd, and G. Aeppli. "MAPS: A Chopper Spectrometer to Measure High Energy Magnetic Excitations in Single Crystals." *ICANS XII* I–60.

[134] Pistor, P., A. Ruiz, A. Cabot, and V. Izquierdo-Roca. "Advanced Raman Spectroscopy of Methylammonium Lead Iodide: Development of a Non-destructive Characterisation Methodology." *Scientific Reports* 6: (2016) 35,973.

[135] Pistorius, C. W. F. T. "Melting Curves and Phase Transitions of the Ammonium Halides to 40 kbar." *The Journal of Chemical Physics* 50, 3: (1969) 1436–1442.

[136] ———. "Phase relations and structures of solids at high pressures." *Progress in Solid State Chemistry* 11, 1: (1976) 1–151.

[137] Plumb, R. C., and D. F. Hornig. "Infrared spectrum, x-ray diffraction pattern, and structure of ammonium fluoride." *The Journal of Chemical Physics* 23, 5: (1955) 947–953.

[138] Poglitsch, A., and D. Weber. "Dynamic disorder in methylammoniumtrihalogenoplumbates (II) observed by millimeter-wave spectroscopy." *The Journal of Chemical Physics* 87, 11: (1987) 6373–6378.

[139] Price, L. C. "Aqueous solubility of methane at elevated pressures and temperatures." *AAPG Bulletin* 63, 9: (1979) 1527–1533.

[140] Pruteanu, C. G., G. J. Ackland, W. C. K. Poon, and J. S. Loveday. "When immiscible becomes miscible - Methane in water at high pressures." *Science Advances* 3, 8: (2017) 1–6.

[141] Pruteanu, C. G., V. Naden Robinson, N. Ansari, A. Hassanali, S. Scandolo, and J. S. Loveday. "Squeezing Oil into Water under Pressure: Inverting the Hydrophobic Effect." *Journal of Physical Chemistry Letters* 11, 12: (2020) 4826–4833.

[142] Pu, C., D. Zhou, Y. Song, Z. Wang, F. Zhang, and Z. Lu. "Phase transition and thermodynamic properties of YAg alloy from first-principles calculations." *Computational Materials Science* 102: (2015) 21–26.

[143] Quan, L. N., M. Yuan, R. Comin, O. Voznyy, E. M. Beauregard, S. Hoogland, A. Buin, A. R. Kirmani, K. Zhao, A. Amassian, D. H. Kim, and E. H. Sargent. "Ligand-Stabilized Reduced-Dimensionality Perovskites." *Journal of the American Chemical Society* 138, 8: (2016) 2649–2655.

[144] Quarti, C., E. Mosconi, J. M. Ball, V. D'Innocenzo, C. Tao, S. Pathak, H. J. Snaith, A. Petrozza, and F. De Angelis. "Structural and optical properties of methylammonium lead iodide across the tetragonal to cubic phase transition: Implications for perovskite solar cells." *Energy and Environmental Science* 9, 1: (2016) 155–163.

[145] Qvist, J., H. Schober, and B. Halle. "Structural dynamics of supercooled water from quasielastic neutron scattering and molecular simulations." *Journal of Chemical Physics* 134, 14.

[146] Raghurama, G., and R. Narayan. "The structures of the ammonium halides." *Journal of Physics and Chemistry of Solids* 44, 7: (1983) 633–638.

[147] Rakita, Y., E. Meirzadeh, T. Bendikov, V. Kalchenko, I. Lubomirsky, G. Hodes, D. Ehre, and D. Cahen. "$CH_3NH_3PbBr_3$ is not pyroelectric, excluding ferroelectric-enhanced photovoltaic performance." *APL Materials* 4, 5.

[148] Ranieri, U., M. M. Koza, W. F. Kuhs, S. Klotz, A. Falenty, P. Gillet, and L. E. Bove. "Fast methane diffusion at the interface of two clathrate structures." *Nature Communications* 8, 1: (2017) 1–7.

[149] Ren, Y., I. W. H. Oswald, X. Wang, G. T. McCandless, and J. Y. Chan. "Orientation of Organic Cations in Hybrid Inorganic–Organic Perovskite $CH_3NH_3PbI_3$ from Subatomic Resolution Single Crystal Neutron Diffraction Structural Studies." *Crystal Growth and Design* 16, 5: (2016) 2945–2951.

[150] REN21 Members. *Renewables 2019 Global Status Report.* 2019.

[151] Salihoğlu, S., H. Yurtseven, and Y. Enginer. "P–T phase diagram for NH_4F." *Solid State Sciences* 4, 4: (2002) 529–534.

[152] Salzmann, C. G. "Advances in the experimental exploration of water's phase diagram." *The Journal of Chemical Physics* 150, 6: (2019) 060,901.

[153] Schaack, S., U. Ranieri, P. Depondt, R. Gaal, W. F. Kuhs, A. Falenty, P. Gillet, F. Finocchi, and L. E. Bove. "Orientational Ordering, Locking-in, and Distortion of CH_4 Molecules in Methane Hydrate III under High Pressure." *Journal of Physical Chemistry C* 122, 20: (2018) 11,159–11,166.

[154] Sharma, S., K. K. Jain, and A. Sharma. "Solar Cells: In Research and Applications—A Review." *Materials Sciences and Applications* 06, 12: (2015) 1145–1155.

[155] Shimizu, H., N. Nakashima, and S. Sasaki. "High-pressure Brillouin scattering and elastic properties of liquid and solid methane." *Physical Review B - Condensed Matter and Materials Physics* 53, 1: (1996) 111–115.

[156] Shimizu, H., M. Ohnishi, S. Sasaki, and Y. Ishibashi. "Cauchy relation in dense H_2O ice VII." *Physical Review Letters* 74, 14: (1995) 2820–2823.

[157] Shirane, G., S. M. Shapiro, and J. M. Tranquanda. *Neutron Scattering with a Triple-Axis Spectrometer*. Cambridge University Press, 2002.

[158] Silverstein, K. A. T., A. D. J. Haymet, and K. A. Dill. "A simple model of water and the hydrophobic effect." *Journal of the American Chemical Society* 120, 13: (1998) 3166–3175.

[159] Singh, A. K. "X-ray diffraction from solids under nonhydrostatic compression - Some recent studies." *Journal of Physics and Chemistry of Solids* 65, 8-9: (2004) 1589–1596.

[160] Sivia, D. *Elementary Scattering Theory For X-ray and Neutron Users*. Oxford University Press, 2011.

[161] Smart, L. E., and E. A. Moore. *Solid State Chemistry: An Introduction*. CRC press, 2016.

[162] Smith, J. D., C. D. Cappa, K. R. Wilson, B. M. Messer, R. C. Cohen, and R. J. Saykally. "Energetics of Hydrogen Bond Network Rearrangements in Liquid Water." *Science* 306, 5697: (2004) 851–853.

[163] Sokolova, T. S., P. I. Dorogokupets, and K. D. Litasov. "Self-consistent pressure scales based on the equations of state for ruby, diamond, MgO, B2-NaCl, as well as Au, Pt, and other metals to 4 Mbar and 3000 K." *Russian Geology and Geophysics* 54, 2: (2013) 181–199.

[164] Somayazulu, M., J. Shu, C. S. Zha, A. F. Goncharov, O. Tschauner, H. K. Mao, and R. J. Hemley. "In situ high-pressure x-ray diffraction study of H2 O ice VII." *Journal of Chemical Physics* 128, 6.

[165] Songvilay, M., M. Bari, Z.-G. Ye, G. Xu, P. M. Gehring, W. D. Ratcliff, K. Schmalzl, F. Bourdarot, B. Roessli, and C. Stock. "Lifetime-shortened acoustic phonons and static order at the Brillouin zone boundary in the

organic-inorganic perovskite $CH_3NH_3PbCl_3$." *Physical Review Materials* 2, 12: (2018) 123,601.

[166] Songvilay, M., Z. Wang, V. G. Sakai, T. Guidi, M. Bari, Z. G. Ye, G. Xu, K. L. Brown, P. M. Gehring, and C. Stock. "Decoupled molecular and inorganic framework dynamics in $CH_3NH_3PbCl_3$." *Physical Review Materials* 3, 12: (2019) 1–9.

[167] Stevenson, R. "Phase Transitions in the Ammonium Halides." *The Journal of Chemical Physics* 34, 5: (1961) 1757–1762.

[168] Stofan, E. R., C. Elachi, J. I. Lunine, R. D. Lorenz, B. Stiles, K. L. Mitchell, S. Ostro, L. Soderblom, C. Wood, H. Zebker, S. Wall, M. Janssen, R. Kirk, R. Lopes, F. Paganelli, J. Radebaugh, L. Wye, Y. Anderson, M. Allison, R. Boehmer, P. Callahan, P. Encrenaz, E. Flamini, G. Francescetti, Y. Gim, G. Hamilton, S. Hensley, W. T. K. Johnson, K. Kelleher, D. Muhleman, P. Paillou, G. Picardi, F. Posa, L. Roth, R. Seu, S. Shaffer, S. Vetrella, and R. West. "The lakes of Titan." *Nature* 445, 7123: (2007) 61–64.

[169] Strässle, T., S. Klotz, K. Kunc, V. Pomjakushin, and J. S. White. "Equation of state of lead from high-pressure neutron diffraction up to 8.9 GPa and its implication for the NaCl pressure scale." *Physical Review B* 90, 1: (2014) 1–8.

[170] Strässle, T., A. M. Saitta, Y. L. Godec, G. Hamel, S. Klotz, J. S. Loveday, and R. J. Nelmes. "Structure of dense liquid water by neutron scattering to 6.5 GPa and 670 K." *Physical Review Letters* 96, 6: (2006) 1–4.

[171] Strauβ, G., A. Bassen, H. Zweier, H. Bertagnolli, K. Tödheide, A. K. Soper, and J. Turner. "High-pressure neutron diffraction on fluid methane." *Physical Review E* 53, 4: (1996) 3505–3517.

[172] Svane, K. L., A. C. Forse, C. P. Grey, G. Kieslich, A. K. Cheetham, A. Walsh, and K. T. Butler. "How Strong Is the Hydrogen Bond in Hybrid Perovskites?" *Journal of Physical Chemistry Letters* 8, 24: (2017) 6154–6159.

[173] Swainson, I. P., C. Stock, S. F. Parker, L. Van Eijck, M. Russina, and J. W. Taylor. "From soft harmonic phonons to fast relaxational dynamics in $CH_3NH_3PbBr_3$." *Physical Review B* 92: (2015) 100,303.

[174] Swainson, I., R. Hammond, C. Soullière, O. Knop, and W. Massa. "Phase transitions in the perovskite methylammonium lead bromide, $CH_3ND_3PbBr_3$." *Journal of Solid State Chemistry* 176, 1: (2003) 97 – 104.

[175] Teixeira, J., M.-C. Bellissent-Funel, S.-H. Chen, and A. J. Dianoux. "Dynamics of supercooled water studied by neutron scattering." *Le Journal de Physique Colloques* 45, C7: (1984) C7–65–C7–71.

[176] Temelso, B., and G. C. Shields. "The role of anharmonicity in hydrogen-bonded systems: The case of water clusters." *Journal of Chemical Theory and Computation* 7, 9: (2011) 2804–2817.

[177] Titantah, J. T., and M. Karttunen. "Water dynamics: Relation between hydrogen bond bifurcations, molecular jumps, local density & hydrophobicity." *Scientific Reports* 3: (2013) 1–9.

[178] Toby, B. H., and R. B. Von Dreele. "GSAS-II: The genesis of a modern open-source all purpose crystallography software package." *Journal of Applied Crystallography* 46, 2: (2013) 544–549.

[179] Turner, M. S. "Origin of the Universe." *Scientific American* 301, 3: (2009) 36–43.

[180] Van Beek, C. G., J. Overeem, J. R. Ruble, and B. M. Craven. "Electrostatic properties of ammonium fluoride and deuterated ice-Ih." *Canadian Journal of Chemistry* 74, 6: (1996) 943–950.

[181] Varshney, D., S. Jain, S. Shriya, and R. Khenata. "High-pressure and temperature-induced structural, elastic, and thermodynamical properties of strontium chalcogenides." *Journal of Theoretical and Applied Physics* 10, 3: (2016) 163–193.

[182] Walsh, A. "Principles of chemical bonding and band gap engineering in hybrid organic-inorganic halide perovskites." *Journal of Physical Chemistry C* 119, 11: (2015) 5755–5760.

[183] Weller, M. T., O. J. Weber, P. F. Henry, A. M. Di Pumpo, and T. C. Hansen. "Complete structure and cation orientation in the perovskite photovoltaic methylammonium lead iodide between 100 and 352 K." *Chemical Communications* 51: (2015) 4180–4183.

[184] Whitfield, P. S., N. Herron, W. E. Guise, K. Page, Y. Q. Cheng, I. Milas, and M. K. Crawford. "Structures, Phase Transitions and Tricritical Behavior of the Hybrid Perovskite Methyl Ammonium Lead Iodide." *Scientific Reports* 6: (2016) 35,685.

[185] Wilfried, B., and J. B. F. N. Engberts. "Hydrophobic Effects. Opinions and Facts." *Angewandte Chemie International Edition in English* 32, 11: (2018) 1545–1579.

[186] Willendrup, P. K., and K. Lefmann. "McStas (i): Introduction, use, and basic principles for ray-tracing simulations." *Journal of Neutron Research* 22: (2019) 1–16.

[187] Wilson, C. C. *Single crystal neutron diffraction from molecular materials*, volume 2. World Scientific, 2000.

[188] Wright, A. D., C. Verdi, R. L. Milot, G. E. Eperon, M. A. Pérez-Osorio, H. J. Snaith, F. Giustino, M. B. Johnston, and L. M. Herz. "Electron-phonon coupling in hybrid lead halide perovskites." *Nature Communications* 7, May.

[189] Yaffe, O., Y. Guo, L. Z. Tan, D. A. Egger, T. D. Hull, C. C. Stoumpos, F. Zheng, T. F. Heinz, L. Kronik, M. G. Kanatzidis, J. S. Owen, A. M. Rappe, M. A. Pimenta, and L. E. Brus. "Local Polar Fluctuations in Lead Halide Perovskite Crystals." *Physical Review Letters* 118, 13: (2017) 1–7.

[190] Yin, T., Y. Fang, X. Fan, B. Zhang, J.-L. Kuo, T. J. White, G. M. Chow, J. Yan, and Z. X. Shen. "Hydrogen-Bonding Evolution during the Polymorphic Transformations in $CH_3NH_3PbBr_3$: Experiment and Theory." *Chemistry of Materials* 29, 14: (2017) 5974–5981.

[191] Yurtseven, H., S. T. Ozkarsligil, and O. Tari. "Variation of the Raman frequency of a soft mode with the pressure (20°C) for the phase transitions in NH_4F." *Anadolu University Journal of Science and Technology A* 17, AFG5 SPECIAL ISSUE: (2016) 747–747.

[192] Zaleski-Ejgierd, P., R. Hoffmann, and N. W. Ashcroft. "High pressure stabilization and emergent forms of PbH_4." *Physical Review Letters* 107, 3: (2011) 2–5.

[193] Zhu, H., K. Miyata, Y. Fu, J. Wang, P. P. Joshi, D. Niesner, K. W. Williams, S. Jin, and X.-Y. Zhu. "Screening in crystalline liquids protects energetic carriers in hybrid perovskites." *Science* 353, 6306: (2016) 1409–1413.

[194] Zou, G., Y. Zhao, Q. Cui, and Z. Jin. "Raman Spectra and Phase Transitions of NH_4F at High Pressure." *Solid State Physics Under Pressure* 191–196.

Molecular orientational melting within a lead-halide octahedron framework: The order-disorder transition in $CH_3NH_3PbBr_3$

K. L. Brown,[1] S. F. Parker,[2] I. Robles García,[1] S. Mukhopadhyay,[2,3] V. García Sakai,[2] and C. Stock[1]
[1]*School of Physics and Astronomy, University of Edinburgh, Edinburgh EH9 3JZ, United Kingdom*
[2]*ISIS Facility, Rutherford Appleton Laboratory, Chilton, Didcot OX11 0QX, United Kingdom*
[3]*Department of Materials, Imperial College London, Exhibition Road, London SW7 2AZ, United Kingdom*
(Received 27 August 2017; published 22 November 2017)

Lead-halide organic-inorganic perovskites consist of an inorganic host framework with an organic molecule occupying the interstitial space. The structure and dynamics of these materials have been heavily studied recently due to interest in their exceptional photovoltaic properties. We combine inelastic neutron scattering, Raman spectroscopy, and quasielastic neutron scattering to study the temperature dependent dynamics of the molecular cation in $CH_3NH_3PbBr_3$. By applying high resolution quasielastic neutron scattering, we confirm the $[CH_3NH_3]^+$ ions are static in the low temperature orthorhombic phase yet become dynamic above 150 K where a series of structural transitions occur. This molecular melting is accompanied by a temporal broadening in the intramolecular modes probed through high energy inelastic spectroscopy. Simultaneous Raman measurements, a strictly $|Q| = 0$ probe, are suggestive that this broadening is due to local variations in the crystal field environment around the hydrogen atoms. These results confirm the strong role of hydrogen bonding and also a coupling between molecular and framework dynamics.

DOI: 10.1103/PhysRevB.96.174111

I. INTRODUCTION

Organic-inorganic perovskites have recently received a lot of attention due to their potential applications in optoelectronics [1]. These compounds are of the perovskite structure ABX_3, where in this case A is an organic cation [typically methylammonium (MA: $[CH_3NH_3]^+$) or formamidinum (FA: $[HC(NH_2)_2]^+$), though others have been investigated], B is a metal (Pb or Sn), and X is a halogen (Cl, Br, or I). In particular, $MAPbI_3$ has been investigated in depth after it was found to have desirable photovoltaic properties, with thin-film solar panels made of this material or $MAPb(I_{1-x}Br_x)_3$ achieving efficiencies of above 20% [2–6]. The key differences between the three different halide ions in $MAPbX_3$ (X = I, Br, Cl) is their nuclear radii. This radius affects the size of the inorganic cages in which the MA cation sits, and thus the exact radius of rotation accessible for the molecule. In the case of Cl, the decreased size of the halide ion has been linked to the presence of two potential orientational states of the cation in the low temperature phase, as opposed to the single orientation found when I or Br is present instead [7–11]. The choice of halide anion also has an impact on the exact optical properties of the system, and a mixture of anions can be used to tune the band gap of the system [2–5].

The behavior of the organic cation in these hybrid organic-inorganic compounds is recognized to be key to understanding their overall properties, including the photovoltaic properties and how this material can be implemented in solar panel devices [5,12,13]. Importantly, the molecule is able to rotate in the perovskite cage, and the exact nature of this rotation and how it depends on the structural phase of the system is still yet to be understood. As the temperature is lowered, $MAPbBr_3$ experiences multiple structural phase transitions, driven by the perovskite rotational modes [14–21]. At room temperature $MAPbBr_3$ is cubic (phase I) undergoing a transition to a tetragonal unit cell (phase II) at 225 K. At 155 K a second structural transition occurs into an unknown phase (phase III) which is fitted by a tetragonal space group, but believed by some to be incommensurate, with a final structural transition occurring at 150 K to an orthorhombic unit cell (phase IV). The structure of these phases was first solved by Poglitsch and Weber, who identified phase I as being $Pm3m$, $a = 5.90$ Å; phase II as being $I4/mcm$, $a = 8.32$ Å, $c = 11.83$ Å; phase III as being tetragonal $P4/mmm$, $a = 5.89$ Å, $c = 5.86$ Å; and phase IV as $Pna2_1$, $a = 7.97$ Å, $b = 8.58$ Å, $c = 11.85$ Å [7]. It has been suggested that the motion of the perovskite cages is strongly coupled with the behavior of the organic cation [17,18,22]. It should be noted that $MAPbBr_3$ is structurally identical to $MAPbI_3$ in the cubic phase, however $MAPbBr_3$ is found to have different space groups in the tetragonal and orthorhombic phases (phases II and IV in $MAPbBr_3$), and displays an additional intermediate phase, which we refer to as phase III [7,21,23–25].

The organic-inorganic perovskites consist of a MA ion occupying the interstitial sites of a lead-halide framework. The molecules' center of mass gives positional order, however the orientational order depends on the local bonding and thermal fluctuations. It is tempting to draw parallels between this and liquid crystals, specifically the melting of the smectic phase to the nematic phase, though in reality the two systems are not very similar [26]. In the nematic phase of liquid crystals there is an orientational order, but no positional order [27,28], whereas in the smectic phase both positional and orientational order is obtained [8–11]. The situation in $MAPbBr_3$ is somewhat analogous to the molecular ionic crystals calcite and sodium nitrate where molecular positions are fixed by the crystalline lattice, however transitions from orientational order to disorder occurs with increasing temperatures [29,30]. Such a transition has been termed an order-disorder transition and in calcite is characterized by a soft vertical "column" of scattering at the zone boundary [29,30]; this contrasts with the soft mode which drives displacive transitions [31]. Analogous cases have also been reported to exist in molecular plastic phases [32].

Previous phonon work on $MAPbBr_3$ has identified a soft zone boundary acoustic phonon which softens at ~150 K and

is accompanied by a temporally broad relaxational response at high temperatures [20]. Similar studies have been performed on $MAPbI_3$ [33,34]. In this paper we study the response of the molecular vibrations in $MAPbBr_3$ through high resolution quasielastic scattering and simultaneous Raman and inelastic neutron scattering measurements. We will show that the transition from the low temperature orthorhombic phase to higher temperature structures at 150 K is accompanied by an increase in the number of active, and freely rotating, molecular ions. This is accompanied by an increase in the linewidth of the internal molecular motions. This strong coupling between molecular motions and the $PbBr_3$ framework lattice indicates the importance of hydrogen bonding.

II. EXPERIMENT

A powder sample of $MAPbBr_3$ was prepared by the reaction of stoichiometric amounts of lead acetate and methylamine hydrobromide in hydrobromic acid, then evaporating away the excess acid to leave an orange colored precipitate. This precipitate was washed with diethyl ether to remove any residual acid in the sample. For all measurements discussed below, the sample was wrapped in niobium foil to protect from reaction of any residual acid with the outer aluminum sample holders. Care was taken to always store the sample in a dry atmosphere to prevent water absorption or possible degradation. As discussed below, multiple experiments were performed on different samples with differing thermal histories providing the same results.

High resolution quasielastic measurements probing the low energy molecular fluctuations were carried out on IRIS [35] at ISIS (Rutherford Appleton Labs, UK), using PG002 analyzers with a fixed final energy of 1.843 meV providing a dynamic range of ± 0.5 meV. An empty can background subtraction was carried out from a measurement performed at room temperature. The resolution was measured from the base temperature response of the $MAPbBr_3$ sample, and was found to be 23.8 μeV from a Gaussian fit (full-width at half-maximum). The IRIS spectrometer also features a diffraction detector bank at $2\theta \sim 170^\circ$, allowing for simultaneous diffraction data to be taken for a small range of **Q** set by the time channel settings for the quasielastic measurements. This afforded a measurement of the structural transitions simultaneously while measuring excitations.

High energy inelastic neutron scattering measurements to study the internal molecular motions were carried out on the MAPS spectrometer at ISIS (Rutherford Appleton Labs, UK), using the high resolution Fermi A chopper in parallel with a t_0 chopper spun at the proton source repetition rate of 50 Hz to eliminate high energy neutrons. Three incident energies were used for these measurements, with different associated Fermi chopper frequency: 60 meV with 100 Hz chopper, 250 meV with 400 Hz, and 650 meV with 600 Hz. The full-width half-maximum energy resolutions, at the elastic position, for these measurements were 2, 6, and 16 meV, respectively. Simultaneous to these spectroscopy measurements, Raman spectra were collected using a modified Renishaw InVia spectrometer [36] with a wavelength of 785 nm. Two gratings of 1200 and 1800 lines per mm were used, which provided measurements of different spectral ranges, giving a total range of 20 to 3200 cm^{-1} (2.5 to 396.8 meV).

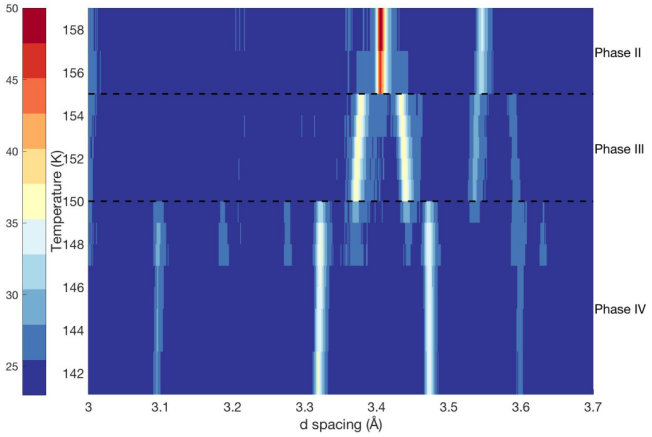

FIG. 1. The diffraction data obtained on IRIS for $MAPbBr_3$, showing the phase transitions II to III at 155 K and III to IV at 150 K. The data were obtained simultaneously while performing quasielastic measurements probing the molecular motions. The limited range in d spacing is due to the constraints in time imposed by the inelastic measurements.

A. Quasielastic neutron scattering using IRIS-molecular motions

We first investigate the static structural properties of our sample using the diffraction detectors on IRIS. $MAPbBr_3$ experiences four structural phase transitions between the cubic room temperature phase (phase I) and the tetragonal phase at base temperature (phase IV), with phase II being orthorhombic and phase III being previously identified as both incommensurate and tetragonal [7,23–25]. The diffraction data obtained on IRIS, shown in Fig. 1, can be used to confirm the presence of two phase transitions: the first at 150 K (IV to III), the second at 155 K (III to II). Some coexistence can be seen between the phases, most noticeably just below 150 K around 3.4 and 3.5 Å. It should be noted that the extra lines seen only between 147 and 150 K not associated with phase II are present at lower temperatures, but counting times were not long enough to discern them clearly in the false color image. The range of **Q** space available on IRIS is not large enough to substantiate a structural refinement to allow a comparison to the space groups found by Poglitsch and Weber [7]. These measurements confirm the structural transitions and the presence of an intermediate phase between the orthorhombic and tetragonal phases in our solution-synthesized samples.

Having confirmed the structural transitions, we now discuss the molecular dynamics. Because the neutron incoherent cross section of H is over an order of magnitude larger than those of the non-H atoms, the neutron cross section measured is dominated by H dynamics [37]. Underlying this assumption is the fact that the incoherent cross section for H is 80.3 barns with the next largest incoherent scatter in $MAPbBr_3$ being N with a cross section of 0.5 barns. We now use this and discuss the low energy quasielastic data sensitive to molecular motions based on data taken on the IRIS backscattering spectrometer.

Two example spectra from IRIS are shown in Fig. 2 taken at 100 and 200 K. The solid red curve is a fit to the sum of an

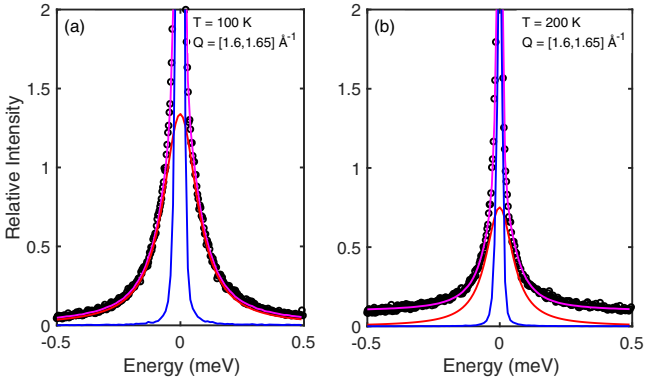

FIG. 2. Examples of the spectra obtained on IRIS at (a) 100 K and (b) 200 K. The black circles show the data points, the pink line shows the total fit, the blue shows the resolution delta function, and the red shows the dynamical contribution. The additional increased baseline due to dynamical contributions outside the dynamic range is not explicitly plotted.

elastic and dynamic component

$$S(E) = [I_{\mathrm{el}} + I_{\mathrm{qe}}] = I_{\mathrm{el}}\delta(E) + \frac{I_{\mathrm{dyn}}}{[1 + (E/\gamma)^2]},$$

where 2γ is the full-width at half-maximum of the dynamic component, convolved with the measured resolution function $\delta(E)$. The linewidth 2γ was found not to vary with momentum indicating no measurable diffusion. This conclusion, and our analysis of the energy linewidth, is decoupled from the momentum dependence and therefore is independent of the model applied to the molecular motion and corresponding Q dependence discussed below. A plot of how this quasielastic full-width (2γ) averaged across the entire measured $|Q|$ range changes with temperature is shown in Fig. 3(a), showing an initial increase, indicative of shortened lifetimes, with increasing temperature followed by a distinct drop at the 150 K phase transition, which only begins to increase again after ∼160 K. Two separate experiments are plotted in different colors as the exact temperature of the phase transition is expected to be dependent on the thermal history [11]; here we find the results from our separate experiments agree within error.

It should be noted that, in the fits from which a full-width 2γ was obtained (examples of which are shown in Fig. 2), for temperatures above 150 K a second faster component existed which was too broad to reliably fit over the ±0.5 meV dynamic range, and was instead fitted as a constant increased baseline [see Fig. 2(b) for an example]. This means that a second rotation of shorter time scale, which is not possible to measure with this instrument, is becoming activated at this point and has an energy scale outside the resolution of the IRIS spectrometer. Indeed, work reported in Ref. [20] suggests the presence of faster fluctuations above the 150 K transition with an energy scale on the order meV. This is further corroborated by real-time vibrational spectroscopy [38] which identifies a fast motion around a particular axis and a slow "jumplike" motion associated with a molecular dipole reorientation with similar time scales to that measured at high temperatures by NMR [39]. Based on this comparison we conclude that

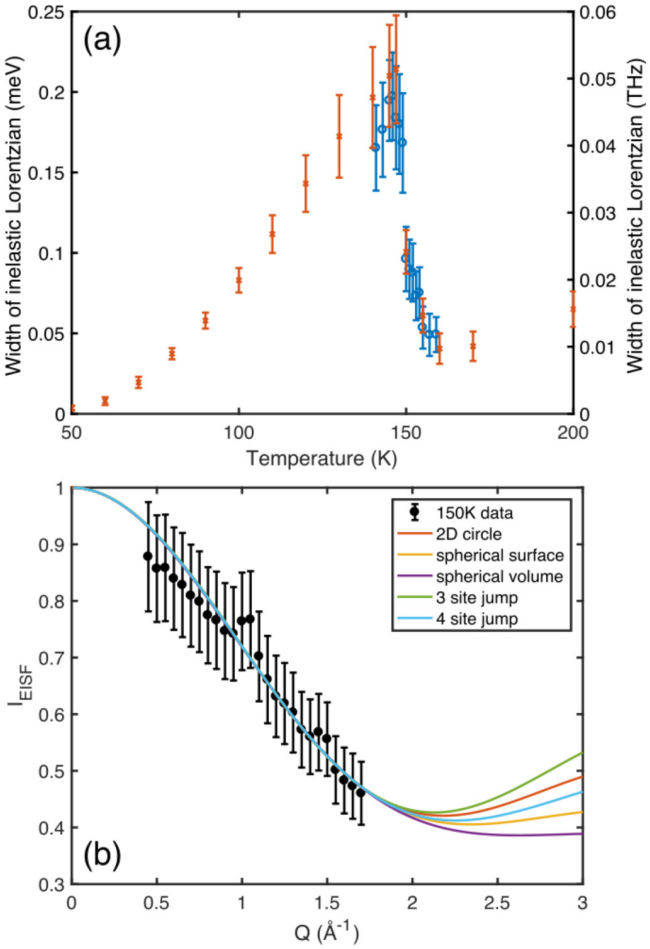

FIG. 3. (a) The variation in width of the $|Q|$ averaged fitted quasielastic component with temperature. Blue and red data points are from two separate experiments. (b) Trial fits to the $I_{\mathrm{EISF}}(Q)$ at 150 K. A systematic error for multiple scattering has been included in $I_{\mathrm{EISF}}(Q)$.

the molecular motions are crossing over from "wobbling" around a particular axis to full body motions as temperature is increased. The assignment of the lower temperature response to a wobbling of the molecular around a particular axis is also consistent with quasielastic neutron scattering data taken on the iodine variant [40].

We now examine the elastic incoherent structure factor (EISF):

$$I_{\mathrm{EISF}}(Q) = \frac{S_{\mathrm{el}}(Q)}{S_{\mathrm{el}}(Q) + S_{\mathrm{qe}}(Q)},$$

where $S_{\mathrm{el}}(Q)$ and $S_{\mathrm{qe}}(Q)$ are integrated over all energies. The momentum dependence of the EISF is sensitive to the real space nature of the equilibrium molecular motions. In our calculations of the EISF, the intensity of the elastic peak $S_{\mathrm{el}}(Q)$ is taken as the area underneath the resolution convolved delta function component of the fit, and the sum $S_{\mathrm{el}}(Q) + S_{\mathrm{qe}}(Q)$ is taken as the area underneath the total fit. This means that despite the fact that the second, broader Lorentzian seen at higher temperatures is fitted as an increased baseline, it is still included in the calculations of the EISF. The measured

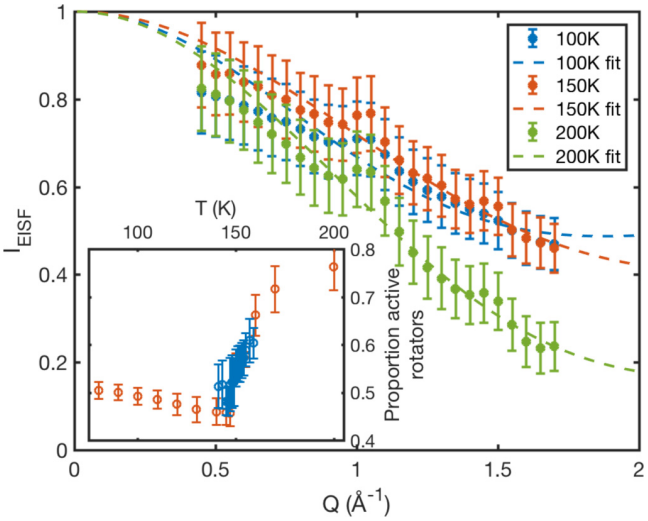

FIG. 4. The fits to the $I_{EISF}(Q)$ at 100, 150, and 200 K, using the model of rotation on a spherical surface. The peak at ∼1 Å^{-1} is due to contamination from a $PbBr_3$ framework Bragg peak. Inset: The number of active rotators in the system with temperature. Blue and red data points are from two separate experiments. In the fit the radius of rotation was allowed to vary, and was found to be between 1.5 and 1.9 Å, however, as this value is model dependent and sensitive to multiple phonon scattering, the temperature dependence of the radius of rotation is not plotted. A systematic error for multiple scattering has been included in I_{EISF}.

$I_{EISF}(Q)$ was fitted to a function $A(Q)$ dependent on the proportion of rotators p and radius of rotation r as follows:

$$A(Q) = p + (1 - p)f(Qr),$$

where $f(Qr)$ is a model chosen for the nature of the molecular rotation.

A plot of the $I_{EISF}(Q)$ extracted from the data at 150 K is shown in Fig. 3(b), with the fits from multiple models shown. The expected models to be appropriate based upon previous studies are the three, four, and eight site jump models [9,33,41,42]. However, from the results obtained in our experiment, we conclude that the Q range constrained by kinematics of the experiment is not sufficient to justify the choice of one model above another. Instead, the simplest model of a rotation on a spherical volume was used for our analysis, $f(Qr) = [j_0(Qr)]^2$, plotted in yellow in Fig. 3(b).

A summary of the temperature dependence, based on this analysis, is plotted in Fig. 4. In the main panel the fits for three temperatures are plotted showing that the model chosen is appropriate for all measurements across the temperature range. The inset to Fig. 4 shows how the proportion of rotators changes across the phases, and once again a clear increase can be seen at the 150 K phase transition. No increase is seen at the second phase transition, and the proportion of rotators begins to level out once more after 160 K. The radius of rotation was allowed to vary freely and was found to be between 1.5 and 1.9 Å, suggesting that the motions seen here are of the C-N bond tumbling within the cage. From these results it is suggested that phase III has more in common dynamically with phase II than phase IV.

B. High energy inelastic scattering data and Raman studies

Previous studies have already characterized the Raman spectra for members of the $MAPbX_3$ family, and the neutron spectra for $MAPbI_3$ [33,34,43–46]. While previous inelastic neutron scattering measurements on $MAPbBr_3$ focused at low energies below ∼75 meV to characterize the soft modes [20], here we apply simultaneous neutron and Raman spectroscopy between 5 and 550 meV (40 to 4400 cm^{-1}) to investigate the internal molecular vibrations and their response to the structural transitions noted above.

Typical momentum and energy data sets for $E_i = 650$ meV obtained from MAPS are displayed in Fig. 5 at 5, 151, and 240 K. At small momentum transfers, well-defined, underdamped in energy modes are observed. This is particularly prominent in Fig. 5(a) (5 K) where a series of sharp excitations are observed below ∼8 Å^{-1} and the intensity grows with increasing momentum transfer as expected for phonon modes or lattice excitations. At higher momentum transfers, these excitations broaden in energy and even appear to disperse up in energy. Given the large momentum transfers, in particular in comparison to Raman spectroscopy which is a strictly $|Q| = 0$ probe, we speculate that this region is crossing over to the deep inelastic region where the impulse approximation applies and hydrogen recoil effects become important.

Hydrogen recoil is particularly prominent in neutron scattering due to the fact that the neutron mass is of the same order as that of the hydrogen nucleus, meaning that when the H nucleus is struck at high energies, it behaves as if it is free. In the extreme limit of large energy and momentum transfers (as shown in Ref. [47] for polyethylene) the energy position of the hydrogen recoil scales as Q^2 with the maximum energy transfer occurring when $2\theta = 90°$. In our data, hydrogen recoil effects appear as a broadening of the signal in the energy at larger momentum transfers, and scattering angle 2θ and this is illustrated in Figs. 5 (plotted as a function of $|Q|$) and 6 (plotted as a function of 2θ) with an incident energy of $E_i = 650$ meV.

In analyzing our neutron data and comparing it with Raman spectroscopy, a balance between minimizing contamination from recoil effects and obtaining enough statistics for a meaningful spectra had to be established. We therefore chose to integrate the data in 2θ in the range of 0° to 20° which was found not to result in broadening of the inelastic response, while providing enough statistics. The region of integration is shown in Fig. 6. Having discussed how we obtained the neutron spectra, we now discuss the results and compare with Raman spectroscopy.

Figure 7 shows the data collected at base temperature (5 K in the orthorhombic phase) for both Raman and also neutron spectroscopy discussed above. The peak positions from the Raman data agree well with that found in previous studies, particularly that of Leguy *et al.*, at base temperature, and as such we shall use their assignments of the Raman modes [33,43–46]. The peak positions in energy from Raman and neutron spectroscopy at high energies ($E_i = 250$ and 650 meV) show good agreement, with the neutron spectroscopy data being broader in comparison as a result of instrumental resolution. However, there is a clear difference between the neutron spectroscopy and Raman spectra in the low energy area, a regime dominated by modes linked to the rotation of

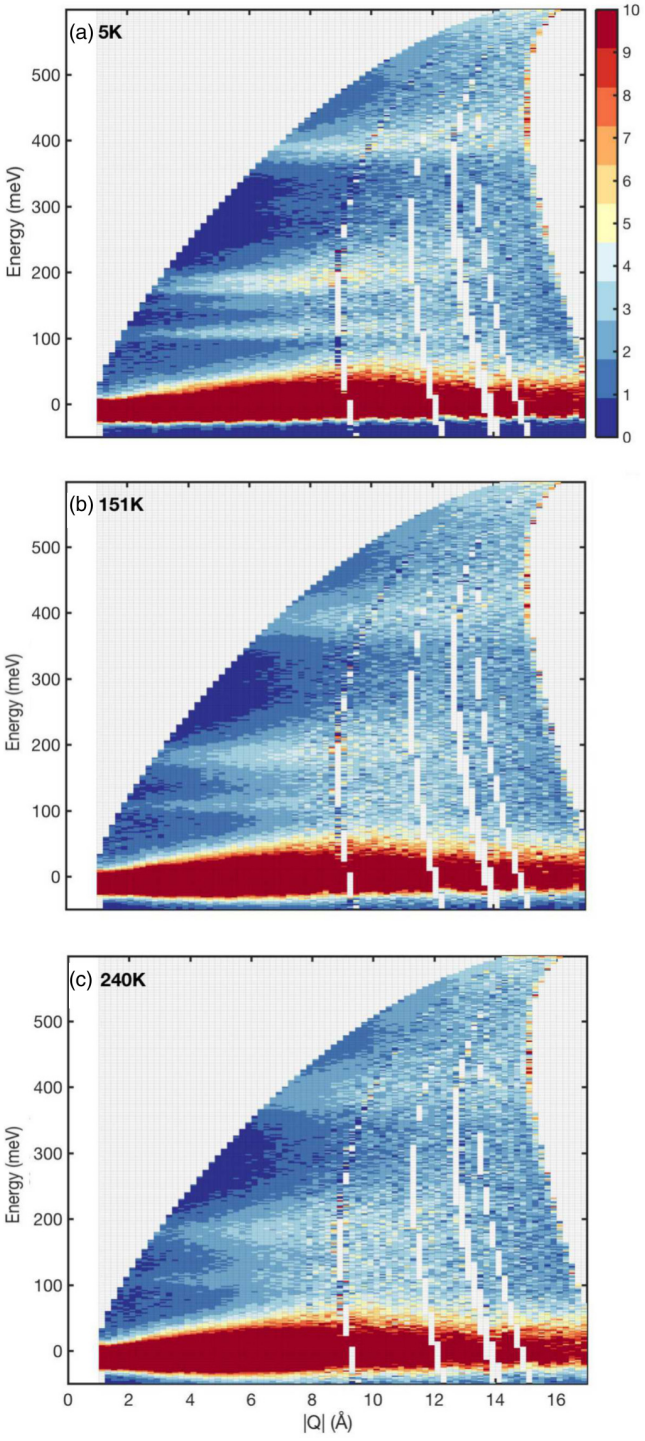

FIG. 5. Slices taken from the 650 meV data at the three temperatures discussed in this paper, showing the $|Q|$ dependence of the intensities measured.

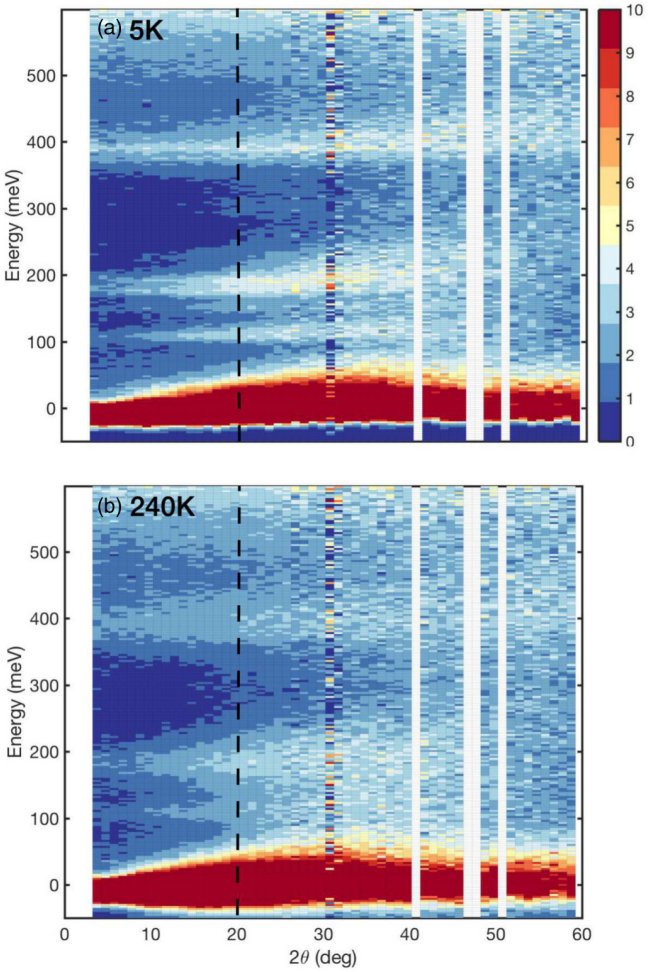

FIG. 6. Slices taken from the 650 meV data at base and high temperature, showing the 2θ dependence of the intensities measured. The dashed black lines show the cutoff at 20° which was used to remove hydrogen recoil effects.

the $PbBr_3$ octahedra, and the lurching of the MA molecule [48]. Such low energy modes are highly dispersive throughout the Brillouin zone and, while Raman probes the modes at $|Q| = 0$, the neutron spectra performs a momentum averaging $\tilde{S}(Q,E) = \frac{1}{4\pi}\int d\Omega S(\vec{Q},E)$ due to the powder nature of the sample. With lattice vibrations that vary considerably with momentum, a larger difference is therefore expected between Raman and neutron spectroscopy.

The higher energy modes in Fig. 7 are linked to intramolecular motions, such as the stretching and breathing of intramolecular bonds, and the bending of the C-N bond. Such motions are internal to the molecule and therefore do not disperse strongly with momentum. All of the bending and stretching modes, as well as the mode for the breathing of the C-N bond, occur between 120 and 200 meV, whereas the C-H and N-H breathing modes are higher energy, occurring between 350 and 400 meV [33]. These modes show good agreement between neutron and Raman techniques.

Results at temperatures above the transition from an orthorhombic phase are shown in Figs. 8 and 9 for 151 and 240 K, respectively. When comparing this to the data taken at base temperature, a large broadening in energy of all excitations is observed in the neutron response indicative of a shortened lifetime. Both Raman and neutron spectra show a large temporal broadening at low energies (below 50 meV) in agreement with previous neutron and Raman spectra [33,34]. This broadening was previously linked to the onset of fast

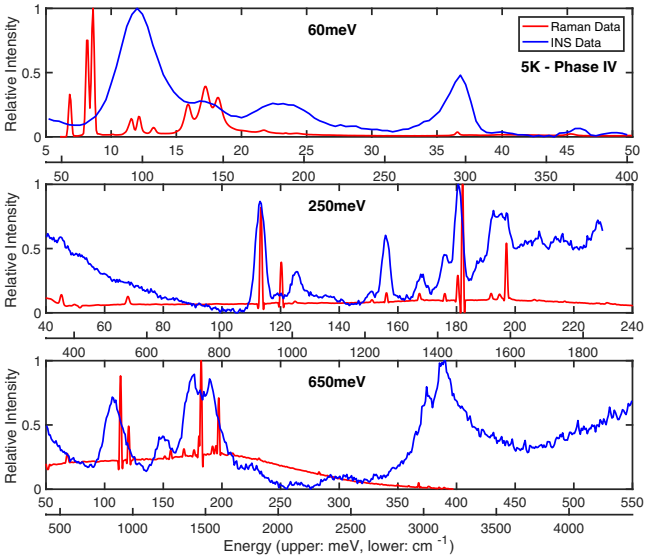

FIG. 7. The results from MAPS at 60, 250, and 650 meV in the orthorhombic phase at base temperature (5.3 K). Raman data are shown in red; inelastic neutron scattering data in blue.

molecular relaxational dynamics [20]. These results, particularly those at energies below 60 meV, also confirm the faster relaxational time scale present at high temperatures postulated above based on high resolution quasielastic scattering, which lead to an increased flat background in the quasielastic scattering at temperatures greater than approximately 150 K. We note that the fast molecular motions dominate the neutron cross section over modes associated with the inorganic cage [48] at these temperatures owing to the dominant neutron cross section discussed above [37].

For the higher energy modes, while the peak positions are in general agreement between neutron and Raman data, the temperature dependence of the linewidths is different.

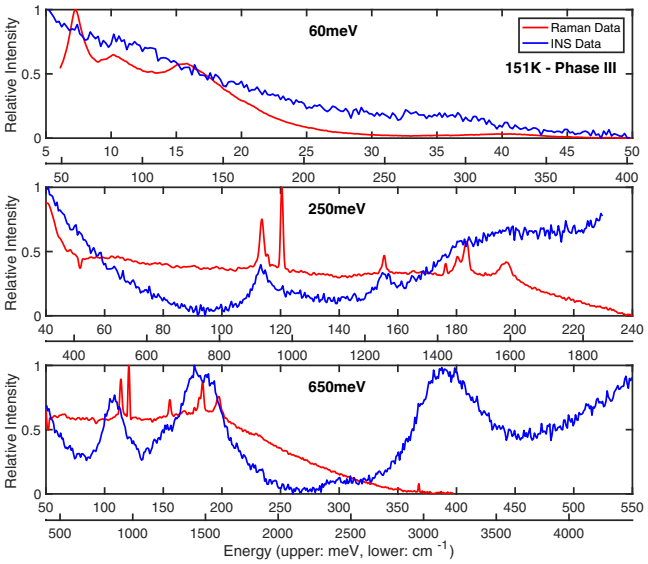

FIG. 8. The results from MAPS at 60, 250, and 650 meV in the incommensurate/tetragonal phase (151 K).

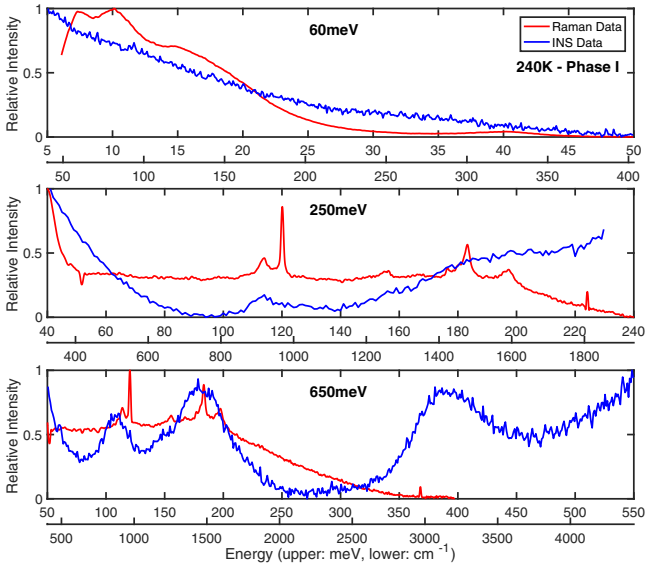

FIG. 9. The results from MAPS at 60, 250 and 650 meV in the cubic phase (240 K).

The neutron and Raman results show a difference with the neutron response displaying a broadening with increased temperature and also a broadening over Raman spectra taken over a comparable energy range. This is illustrated in Table I which displays the temperature variation of the full-width at half-maximum for the peak at 113 meV (915 cm^{-1}). This peak was chosen due to its clear separation from other peaks at all temperatures, and has been identified to be linked to the rocking motions of the MA cation [48]. Both neutron and Raman peaks at low temperature are resolution limited. The peak measured with neutrons broadens to ∼10 meV while the Raman peak broadens only to ∼3 meV.

One reason for this increased broadening in the neutron response could be due to the possibility of multiple phonon scattering which effectively folds in scattering from larger scattering angles resulting from the large neutron cross section of hydrogen. We investigate the possibility of such an effect in Fig. 10 where we plot the momentum dependence of the neutron response over the range of 175–200 meV as a function of Q^2. This energy range has been chosen for presentation purposes due to the presence of a well defined peak in the 650 meV data at all temperatures probed. An increase in multiple phonon scattering would manifest as differing y intercepts at each temperature. The data are in good agreement at low momentum transfers indicating no observable enhancement or change of multiple phonon

TABLE I. The full width at half maximum of the peak at 113 meV (915 cm^{-1}) for three temperatures.

	FWHM of 113 meV peak (meV)		
Temperature	5.3 K	151 K	240 K
Neutron	5.122 ± 0.151	8.253 ± 0.968	10.176 ± 2.872
Raman	1.057 ± 0.019	2.474 ± 0.040	3.710 ± 0.090

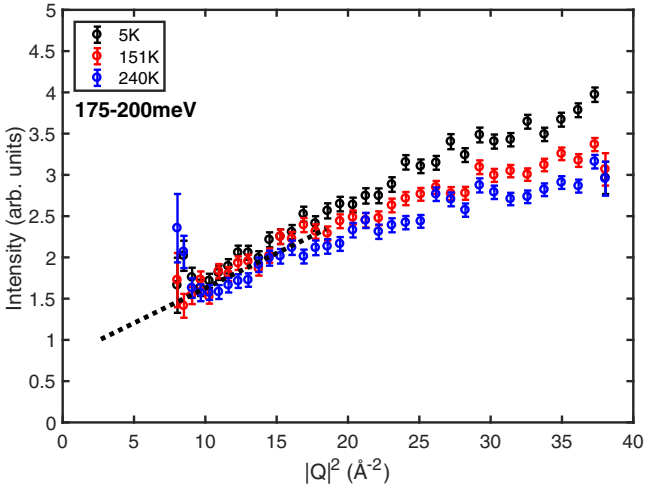

FIG. 10. Data collected at 650 meV, integrated over an energy range of 175–200 meV and plotted against $|Q|^2$. A dotted line is plotted as a guide to the eye.

scattering with increased temperature. Normally one would expect the y intercept in all cases to be zero, however here no explicit background subtraction has been carried out, leading to the nonzero value extrapolated here. The plot in Fig. 10 is selected for a particular and representative energy range. However, all other peaks were observed to show a lack of a temperature dependence in the $\lim_{Q\to 0}$ as shown here.

There are several possible reasons why this difference between neutron and Raman techniques might be observed. First, Raman spectra are strictly at $|Q| = 0$, whereas inelastic neutron scattering integrates and averages over all $|Q|$ as discussed above owing to kinematics and powder averaging. This means that an effect at other positions in momentum, for example the zone boundary, could cause the momentum averaged energy width to be increased more than what is measured at a single wave vector like with Raman spectroscopy at $\vec{Q} = 0$. Second, the inelastic neutron spectra are dominated by hydrogen, whereas Raman is more sensitive to heavier elements, meaning that neutron scattering disproportionately samples the motions on the hydrogen sites. This is further confirmed by the sensitivity of these high energy excitations to recoil effects at large momentum transfers and scattering angles as discussed above. We discuss these two possibilities in more detail below in the discussion section.

There is the possibility Raman techniques preferentially measure molecules close to the surface (see for example surface enhanced spectroscopy discussed in Ref. [49]), whereas inelastic neutron scattering considers the bulk system. However, while surface over bulk differences have been suggested in the organic-inorganic perovskites (for example the effect of dimensionality discussed in Ref. [50]), this latter possibility is unlikely in this case given that surface-enhanced Raman spectroscopy in molecular systems and liquids has typically resulted in a broadening of linewidths or intensity enhancement at the surface. We observe the reverse case with the Raman measurements being more well defined in energy than the bulk neutron scattering technique. The agreement between neutron and Raman at lower energies also does not suggest a near surface versus bulk difference for neutron and Raman spectra noted here.

III. DISCUSSION

We have presented results from both a neutron low energy and high resolution quasielastic scattering study and high energy neutron spectroscopy measurements. The low energy neutron experiments performed on IRIS probes the single atom motions with a range of energy scales, whereas the higher energy inelastic data, obtained on MAPS and compared with Raman spectroscopy, measures harmonic modes of the molecules. We have focused on the internal molecular motions at energies above ∼100 meV.

The quasielastic neutron scattering from IRIS is unable to provide any conclusive information on the exact molecular jump model given the limited range in momentum forced by kinematics of neutron scattering. However, by applying arguably the simplest model of free motion on a sphere we observed changes in the quasielastic linewidth at the 150 K phase transition, and the appearance of the second, broader in energy contribution at higher temperatures. This indicates a rotational mode active in the low temperature phase and a second faster energy scale that becomes active at the phase transition to the tetragonal phase [33,42]. We also observe a precipitous increase in the number of active molecules at ∼150 K indicative of an increase in local molecular disorder as temperature is increased. This is corroborated by diffraction studies [9–11], NMR studies [51], and computational investigations [17,52].

A similar result is obtained from our spectroscopic study of the internal molecular motions obtained using a combination of the inelastic neutron scattering and Raman spectroscopy on MAPS. The energy locations and the temperature dependence of the Raman data presented are generally in agreement with previous studies [33,34,43–46]. At low energies below ∼50 meV, Raman and neutron spectroscopy are in agreement with both showing a significant temporal broadening of the excitations upon heating from the orthorhombic phase, indicative of faster fluctuations with shortened lifetimes. This is corroborated by the quasielastic neutron data probing molecular motions discussed above. However, Raman and neutron spectroscopy show differences at higher energies with neutron spectroscopy measuring broadened linewidths of internal molecular motions. This broadening is indicative of an increased distribution of energy scales for these motions.

As discussed above, this difference can be explained by either noting that neutron spectroscopy is preferentially sensitive to hydrogen motions given the large cross section over other heavier atoms or the averaging over all momentum in contrast to the fact that Raman only probes $|Q| = 0$. Given that electronic band structure may indicate a preferential coupling between lattice and electronic degrees of freedom at nonzero $|Q|$ [15,53], it maybe expected that there might be a coupling of these internal modes at regions away from the zone center. However, these high energy internal molecular excitations are associated with excitations which are highly localized in real space and therefore are expected to show no

momentum dependence. We therefore associate the difference between Raman and neutron results at high temperatures due to the dominance of the hydrogen cross section in neutron spectroscopy. This would indicate a distribution of crystalline electric fields for the hydrogen resulting in a corresponding spread in energy scales for the molecular motions involving them. Theoretically, such a scenario has been predicted as outlined in Ref. [54], and the importance of hydrogen bonding within this system has been previously discussed in Ref. [17], in line with our findings.

The suggestion that the molecular cation in the system is experiencing a range of different local environments is supported in other experimental studies: ARPES studies of $MAPbBr_3$ find both centrosymmetric and noncentrosymmetric domains in the crystal, which persist throughout the low temperature phase [55]. This effect has also been reported for other phases of $MAPbBr_3$ and $MAPbI_3$, which reports that symmetry breaking domains survive past the phase transition between the cubic and tetragonal phases both when heated and cooled [16,56]. Additionally, significant disorder on the halide site has also been reported in diffraction results for $MAPbI_3$ [57]; such disorder may influence local hydrogen crystalline electric field environments.

It is clear that the onset of molecular dynamics at 150 K results in a large scale dynamic molecular disorder of the entire crystal. This is evidenced from both the onset of dynamic sites found with low energy quasielastic neutron scattering and also the presence of a distribution of environments for the hydrogen site. This has been previously discussed theoretically, with the system being compared to plastic crystals [54], and the term "glassy disorder" was coined to describe the molecular motions in the low temperature phase [58]. However, the present results imply that the change in dynamics between the orthorhombic and tetragonal phases is more akin to a orientational melting analogous to that in the smectic to nematic transition in liquid crystals and, more precisely, the order-disorder transitions reported in minerals such as calcite [59].

We shall now discuss the implications of these findings on the electronic properties of these materials. For $MAPbI_3$, the key contributions to the edges of the band structure come from the hybridization of the $5p$ orbitals of iodine and $6s$ orbitals of lead for the valence band, and the empty $6p$ orbitals of lead for the conduction band [5,60]. While the MA cation does not contribute directly to the band structure, the coupling between the motion of the molecule and the structure of the inorganic components makes it a key influence upon the electronic response, and hence upon the photovoltaic properties.

Therefore, the observed difference in the dynamics of the system between low and high temperature structural phases implies that there will be a linked change in the electronic and photovoltaic properties. Photoluminescence spectra results show that there is a change in the energy of the maximum photoluminescence intensity at the 150 K transition [61], in agreement with the observation made here that the key change in whole body molecular dynamics is at this temperature. This suggests that it is the whole body rotations of the MA cation and their interactions with the surrounding inorganic framework [12] that is key to understanding the photovoltaic properties. However, it is important to note that the change in photoluminescence observed at 150 K is not large.

Further to these observations of the photovoltaic properties, studies have also identified a coupling between the cation rotation to the quasiparticle band gap of the system, through hydrogen bonding between the cation and inorganic cages. The hydrogen bonding has been identified as strongly linked with the octahedral tilts of the system, and the phase transitions within the system, with the hydrogen bonding stronger in the low-T phase where the molecular motion is lower [17,18,22,62]. Due to the fact that the structure is so heavily dependent on the cation dynamics, this then influences the band gap of the system, with the states near the top of the valence band stabilized by the octahedral tilting in the low temperature phase with fewer cation dynamics [12,17,18].

Additional evidence showing that the coupling between molecular motions and electronic properties is relevant for the photovoltaic properties, it has also been found that the cation dynamics provides screening which protects the energetic carriers [13]. This implies that, from the results presented here, the assumption can be made that the low temperature phase has least carrier protection and thus the carriers are less long lived. Also, a large Rashba splitting [55] resulting from a breaking of inversion symmetry and strong spin orbit coupling [56] has been reported. Our results suggest that it is not only the lead halide framework coupled to electronic properties [61], but also the molecular motions.

IV. CONCLUSION

In conclusion, we have reported two neutron scattering studies which show that there is a significant change in the molecular dynamics of the MA cation in $MAPbBr_3$ as temperature is increased from the orthorhombic phase to the higher temperature structural phases. We have used quasielastic neutron scattering data to establish that whole body molecular dynamics are activated at 150 K. From a comparison of Raman and high energy inelastic neutron scattering and Raman, the significance of the local environment around the hydrogen sites is implicated pointing to the importance of hydrogen bonding to the properties of the system. It is known that the motion of the MA cation is able to strongly influence the photovoltaic properties through interactions with the surrounding $PbBr_3$ octahedra [5,12,13]. The onset of rotational motion agrees with an observed feature in the photoluminescence data [61], supporting the observation that the behavior of the organic cation is key to understanding the photovoltaic and optic properties of this compound.

ACKNOWLEDGMENTS

Support is gratefully acknowledged from the Engineering and Physical Sciences Research Council (EPSRC), the Science and Technologies Facilities Council (STFC), the Royal Society, and the Carnegie Trust for the Universities of Scotland. We thank P. M. Gehring, I. P. Swainson, J. P. Attfield, and M. Songvilay for helpful discussions.

[1] B. Saparov and D. B. Mitzi, Chem. Rev. **116**, 4558 (2016).
[2] J.-S. Park, S. Choi, Y. Yan, Y. Yang, J. M. Luther, S.-H. Wei, P. Parilla, and K. Zhu, J. Phys. Chem. Lett. **6**, 4304 (2015).
[3] J. H. Noh, S. H. Im, J. H. Heo, T. N. Mandal, and S. I. Seok, Nano Lett. **13**, 1764 (2013).
[4] H. Zhou, Q. Chen, G. Li, S. Luo, T.-b. Song, H.-S. Duan, Z. Hong, J. You, Y. Liu, and Y. Yang, Science **345**, 542 (2014).
[5] L. M. Herz, Annu. Rev. Phys. Chem. **67**, 65 (2016).
[6] T. D. Bennett, A. K. Cheetham, A. H. Fuchs, and F.-X. Coudert, Nat. Chem. **9**, 11 (2016).
[7] A. Poglitsch and D. Weber, J. Chem. Phys. **87**, 6373 (1987).
[8] J. D. Brock, D. Y. Noh, B. R. McClain, J. D. Litster, R. J. Birgeneau, A. Aharony, P. M. Horn, and J. C. Liang, Z. Phys. B Condens. Matter **74**, 197 (1989).
[9] Y. Ren, I. W. H. Oswald, X. Wang, G. T. McCandless, and J. Y. Chan, Cryst. Growth Design **16**, 2945 (2016).
[10] H. Mashiyama, Y. Kawamura, H. Kasano, T. Asahi, Y. Noda, and H. Kimura, Ferroelectrics **348**, 182 (2007).
[11] P. S. Whitfield, N. Herron, W. E. Guise, K. Page, Y. Q. Cheng, I. Milas, and M. K. Crawford, Sci. Rep. **6**, 35685 (2016).
[12] W. Gao, X. Gao, T. A. Abtew, Y.-Y. Sun, S. Zhang, and P. Zhang, Phys. Rev. B **93**, 085202 (2016).
[13] H. Zhu, K. Miyata, Y. Fu, J. Wang, P. P. Joshi, D. Niesner, K. W. Williams, S. Jin, and X.-Y. Zhu, Science **353**, 1409 (2016).
[14] Y. Fujii, S. Hoshino, Y. Yamada, and G. Shirane, Phys. Rev. B **9**, 4549 (1974).
[15] F. Brivio, J. M. Frost, J. M. Skelton, A. J. Jackson, O. J. Weber, M. T. Weller, A. R. Goñi, A. M. A. Leguy, P. R. F. Barnes, and A. Walsh, Phys. Rev. B **92**, 144308 (2015).
[16] R. Comin, M. K. Crawford, A. H. Said, N. Herron, W. E. Guise, X. Wang, P. S. Whitfield, A. Jain, X. Gong, A. J. H. McGaughey, and E. H. Sargent, Phys. Rev. B **94**, 094301 (2016).
[17] J.-H. Lee, N. C. Bristowe, P. D. Bristowe, and A. K. Cheetham, Chem. Commun. **51**, 6434 (2015).
[18] J.-H. Lee, N. C. Bristowe, J. H. Lee, S.-H. Lee, P. D. Bristowe, A. K. Cheetham, and H. M. Jang, Chem. Mater. **28**, 4259 (2016).
[19] A. Létoublon, S. Paofai, B. Rufflé, P. Bourges, B. Hehlen, T. Michel, C. Ecolivet, O. Durand, S. Cordier, C. Katan, and J. Even, J. Phys. Chem. Lett. **7**, 3776 (2016).
[20] I. P. Swainson, C. Stock, S. F. Parker, L. Van Eijck, M. Russina, and J. W. Taylor, Phys. Rev. B **92**, 100303 (2015).
[21] Y. Kawamura and H. Mashiyama, J. Korean Phys. Soc. **35**, S1437 (1999).
[22] K. P. Ong, T. W. Goh, Q. Xu, and A. Huan, J. Phys. Chem. Lett. **6**, 681 (2015).
[23] H. Mashiyama, Y. Kawamura, and Y. Kubota, J. Korean Phys. Soc. **51**, 850 (2007).
[24] K. Page, J. E. Siewenie, P. Quadrelli, and L. Malavasi, Angew. Chem. Int. Ed. **55**, 14320 (2016).
[25] I. Swainson, R. Hammond, C. Soullière, O. Knop, and W. Massa, J. Solid State Chem. **176**, 97 (2003).
[26] J. D. Brock, R. J. Birgeneau, D. Litster, and A. Aharony, Contemp. Phys. **30**, 321 (1989).
[27] J. Als-Nielsen, J. D. Litster, R. J. Birgeneau, M. Kaplan, C. R. Safinya, A. Lindegaard-Andersen, and S. Mathiesen, Phys. Rev. B **22**, 312 (1980).
[28] R. Pindak, C. Y. Young, R. B. Meyer, and N. A. Clark, Phys. Rev. Lett. **45**, 1193 (1980).
[29] M. Hagen, M. Dove, M. Harris, U. Steigenberger, and B. Powell, Physica B **180**, 276 (1992).
[30] M. J. Harris, M. T. Dove, I. P. Swainson, and M. E. Hagen, J. Phys. Condens. Matter **10**, L423 (1998).
[31] G. Shirane, J. D. Axe, J. Harada, and J. P. Remeika, Phys. Rev. B **2**, 155 (1970).
[32] A. Vispa, D. Monserrat, G. J. Cuello, F. Fernandex-Alonso, S. Mukhopadhyay, F. Demmel, J. Ll. Tamarit, and L. C. Pardo, Phys. Chem. Chem. Phys. **19**, 20259 (2017).
[33] A. M. A. Leguy, A. R. Goni, J. M. Frost, J. Skelton, F. Brivio, X. Rodriguez-Martinez, O. J. Weber, A. Pallipurath, M. I. Alonso, M. Campoy-Quiles, M. T. Weller, J. Nelson, A. Walsh, and P. R. F. Barnes, Phys. Chem. Chem. Phys. **18**, 27051 (2016).
[34] K. Drużbicki, R. S. Pinna, S. Rudić, M. Jura, G. Gorini, and F. Fernandez-Alonso, J. Phys. Chem. Lett. **7**, 4701 (2016).
[35] S. Campbell, M. Telling, and C. Carlile, Physica B **276**, 206 (2000).
[36] M. A. Adams, S. F. Parker, F. Fernandez-Alonso, D. J. Cutler, C. Hodges, and A. King, Appl. Spectrosc. **63**, 727 (2009).
[37] V. F. Sears, Neutron News **3**, 26 (1992).
[38] A. A. Bakulin, O. Selig, H. J. Bakker, Y. L. Rezus, C. Müller, T. Glaser, R. Lovrincic, Z. Sun, Z. Chen, A. Walsh, J. M. Frost, and T. L. C. Jansen, J. Phys. Chem. Lett. **6**, 3663 (2015).
[39] O. Knop, R. E. Wasylishen, M. A. White, T. S. Cameron, and M. J. M. V. Oort, Can. J. Chem. **68**, 412 (1990).
[40] A. M. A. Leguy, J. M. Frost, A. P. McMahon, V. G. Sakai, W. Kockelmann, C. Law, X. Li, F. Foglia, A. Walsh, B. C. O'Regan, J. Nelson, J. T. Cabral, and P. R. F. Barnes, Nat. Commun. **6**, 7124 (2015).
[41] M. T. Weller, O. J. Weber, P. F. Henry, A. M. Di Pumpo, and T. C. Hansen, Chem. Commun. **51**, 4180 (2015).
[42] T. Chen, B. J. Foley, B. Ipek, M. Tyagi, J. R. D. Copley, C. M. Brown, J. J. Choi, and S.-H. Lee, Phys. Chem. Chem. Phys. **17**, 31278 (2015).
[43] A. Maaej, M. Bahri, Y. Abid, N. Jaidane, Z. B. Lakhdar, and A. Lautié, Phase Transit. **64**, 179 (1998).
[44] P. Pistor, A. Ruiz, A. Cabot, and V. Izquierdo-Roca, Sci. Rep. **6**, 35973 (2016).
[45] O. Yaffe, Y. Guo, L. Z. Tan, D. A. Egger, T. Hull, C. C. Stoumpos, F. Zheng, T. F. Heinz, L. Kronik, M. G. Kanatzidis, J. S. Owen, A. M. Rappe, M. A. Pimenta, and L. E. Brus, Phys. Rev. Lett. **118**, 136001 (2017).
[46] Y. Guo, O. Yaffe, D. W. Paley, A. N. Beecher, T. D. Hull, G. Szpak, J. S. Owen, L. E. Brus, and M. A. Pimenta, Phys. Rev. Mater. **1**, 042401(R) (2017).
[47] C. Stock, R. A. Cowley, J. W. Taylor, and S. M. Bennington, Phys. Rev. B **81**, 024303 (2010).
[48] R. G. Niemann, A. G. Kontos, D. Palles, E. I. Kamitsos, A. Kaltzoglou, F. Brivio, P. Falaras, and P. J. Cameron, J. Phys. Chem. C **120**, 2509 (2016).
[49] J. Chen, Z.-H. Mo, X. Yang, H.-L. Zhou, and Q. Gao, Chem. Commun. **53**, 6949 (2017).
[50] L. N. Quan, M. Yuan, R. Comin, O. Voznyy, E. M. Beauregard, S. Hoogland, A. Buin, A. R. Kirmani, K. Zhao, A. Amassian, D. H. Kim, and E. H. Sargent, J. Am. Chem. Soc. **138**, 2649 (2016).
[51] C. Roiland, G. Trippe-Allard, K. Jemli, B. Alonso, J.-C. Ameline, R. Gautier, T. Bataille, L. Le Polles, E. Deleporte, J. Even, and C. Katan, Phys. Chem. Chem. Phys. **18**, 27133 (2016).

[52] A. Mattoni, A. Filippetti, M. I. Saba, and P. Delugas, J. Phys. Chem. C **119**, 17421 (2015).
[53] C. Motta, F. El-Mellouhi, S. Kais, N. Tabet, F. Alharbi, and S. Sanvito, Nat. Commun. **6**, 7026 (2015).
[54] J. Even, M. Carignano, and C. Katan, Nanoscale **8**, 6222 (2016).
[55] D. Niesner, M. Wilhelm, I. Levchuk, A. Osvet, S. Shrestha, M. Batentschuk, C. Brabec, and T. Fauster, Phys. Rev. Lett. **117**, 126401 (2016).
[56] J. Even, S. Paofai, P. Bourges, A. Letoublon, S. Cordier, O. Durand, and C. Katan, Proc. SPIE **9743**, 97430M (2016).
[57] J. L. Minns, P. Zajdel, D. Chernyshov, W. van Beek, and M. A. Green, Nat. Commun. **8**, 15152 (2017).
[58] D. H. Fabini, T. Hogan, H. A. Evans, C. C. Stoumpos, M. G. Kanatzidis, and R. Seshadri, J. Phys. Chem. Lett. **7**, 376 (2016).
[59] R. M. Lynden-Bell and K. H. Michel, Rev. Mod. Phys. **66**, 721 (1994).
[60] J. Endres, D. A. Egger, M. Kulbak, R. A. Kerner, L. Zhao, S. H. Silver, G. Hodes, B. P. Rand, D. Cahen, L. Kronik, and A. Kahn, J. Phys. Chem. Lett. **7**, 2722 (2016).
[61] A. D. Wright, C. Verdi, R. L. Milot, G. E. Eperon, M. A. Pérez-Osorio, H. J. Snaith, F. Giustino, M. B. Johnston, and L. M. Herz, Nat. Commun. **7**, 11755 (2016).
[62] K. T. Butler, K. Svane, G. Kieslich, A. K. Cheetham, and A. Walsh, Phys. Rev. B **94**, 180103 (2016).

Journal of Physics: Condensed Matter

PAPER

Depth dependant element analysis of $PbMg_{1/3}Nb_{2/3}O_3$ using muonic x-rays

To cite this article: K L Brown *et al* 2018 *J. Phys.: Condens. Matter* **30** 125703

IOP Publishing Journal of Physics: Condensed Matter
J. Phys.: Condens. Matter **30** (2018) 125703 (5pp) https://doi.org/10.1088/1361-648X/aaade3

Depth dependant element analysis of $PbMg_{1/3}Nb_{2/3}O_3$ using muonic x-rays

K L Brown[1], C P J Stockdale[1], H Luo[2], X Zhao[3], J-F Li[4], D Viehland[4], G Xu[5], P M Gehring[5], K Ishida[6], A D Hillier[7] and C Stock[1,8]

[1] School of Physics and Astronomy, University of Edinburgh, Edinburgh EH9 3JZ, United Kingdom
[2] Shanghai Institute of Ceramics, Chinese Academy of Sciences, Shanghai 201800, People's Republic of China
[3] Shanghai Normal University, Shanghai 200234, People's Republic of China
[4] Department of Materials Science and Engineering, Virginia Tech., Blacksburg, VA 24061, United States of America
[5] National Institute of Standards and Technology, Gaithersburg, MD 90899, United States of America
[6] RIKEN Nishina Center, RIKEN, Wako, Saitama, Japan
[7] ISIS Pulsed Neutron and Muon Facility, STFC Rutherford Appleton Laboratory, Didcot OX11 0QX, United Kingdom

E-mail: cstock@ed.ac.uk

Received 5 January 2018, revised 6 February 2018
Accepted for publication 8 February 2018
Published 28 February 2018

Abstract

The relaxor $PbMg_{1/3}Nb_{2/3}O_3$ (PMN) has received attention due to its potential applications as a piezoelectric when doped with $PbTiO_3$ (PT). Previous results have found that there are two phases existing in the system, one linked to the near-surface regions of the sample, the other in the bulk. However, the exact origin of these two phases is unclear. In this paper, depth dependant analysis results from negative muon implantation experiments are presented. It is shown that the Pb content is constant throughout all depths probed in the sample, but the Mg and Nb content changes in the near-surface region below 100 μm. At an implantation depth of 60 μm, it is found that there is a 25% increase in Mg content, with a simultaneous 5% decrease in Nb content in order to maintain charge neutrality. These results show that the previously observed skin effects in PMN are due to a change in concentration and unit cell.

Keywords: ferroelectricity, domains, composition, muonic x-rays, structural order parameter

(Some figures may appear in colour only in the online journal)

In the conventional theorem of phase transitions, a single temperature-dependant length scale is required to describe the critical fluctuations as the phase transition is approached [1]. However, a number of systems have been found experimentally which exhibit two length scales at phase transitions, with the second length scale appearing at temperatures just above the critical temperature [1–7]. The first material for which this was observed was $SrTiO_3$, which was found to exhibit an anisotropic dispersion in the critical scattering at the R point [2]. Similar results have been found in pure Ho and Tb crystals, as well as other compounds [6–8]. The magnetic analogue to this structural effect has also been observed in spin systems described by the random-field Ising model [9, 10].

Neutron scattering results on these systems have revealed that, of the two phase transitions observed experimentally, one is only present in the bulk, and the other is in the surface of the sample [4–6, 8]. The question remains about whether or not these surface effects are intrinsic properties of the system.

X-ray and neutron scattering studies of relaxors; ferroelectric materials that exhibit large electrostriction; have suggested the presence of an effect similar to the two length scale problem, known as the 'skin effect', which has a different temperature dependance, appearing far above the critical temperature, and persisting below it [11]. A number of

[8] Author to whom any correspondence should be addressed.

1361-648X/18/125703+5$33.00

relaxors are found to have a perovskite structure A(B',B'') O_3, where there are two different elements sharing the B site, not necessarily with equal proportions of each. Examples of these include $PbZn_{1/3}Nb_{2/3}O_3$ (PZN) and $PbMg_{1/3}Nb_{2/3}O_3$ (PMN), which is the focus of this paper. The key property of a relaxor is their broad frequency dependant dielectric response, which differs from that seen in regular ferroelectrics, as the peak of this dielectric response is not associated with a ferroelectric phase transition [12, 13]. These materials have been highly researched due to their promising properties as piezoelectric devices when they are doped with $PbTiO_3$ (PT), so two competing phases could have a large impact on these properties.

Initially, the phase diagrams of PZN and PMN were studied. PZN systems exhibit a diffuse structural transition between cubic and rhombohedral phases in a temperature range of 325–385 K [14, 15]. Conversely, PMN does not exhibit a structural phase transition and retains a cubic unit cell down to 5 K, however a strain is observed that is correlated with a phase transition temperature that is predicted from studies of PMN doped with $PbTiO_3$ [11, 15]. Further experimentation found that the Bragg peaks observed in the high temperature cubic phase begin to split at the temperature where this strain manifests, meaning that a cubic and rhombohedral phase are coexisting [16–18]. There is disagreement as to exactly where these two phases are originating from. Some results suggest that the structure is in fact rhombohedral, and the observed effects are as a result of domain size and population gradient within the crystal [19]. On the other hand, several studies suggest a near-surface rhombohedral region which creates the skin effect, around the cubic bulk, with the surface region found to have a depth of approximately 100 μm [17, 20]. The most profound evidence for this skin effect is the conflict between bulk measurements, such as neutron diffraction, which report a cubic structure, and the rhombohedral structure found from surface-sensitive probes, such as x-ray diffraction [21, 22]. This near-surface region has also been reported in PZN, with a depth of 10–50 μm, where it is suggested that the structural phase transition observed in this system does not necessarily affect the whole bulk [23, 24]. Similarly to the two length scale effect, there is not yet any evidence as to the origin of the skin effect, and whether it is intrinsic or not.

In this paper, negative muons are used to provide a depth-dependant compositional analysis of PMN, with the aims of establishing whether there is a difference in composition in the near-surface and bulk regions. This will then establish whether the occurrence of the proposed skin effects is due to sample-specific phenomena, or whether these observations are due to more fundamental properties. The use of negative muons as a technique is currently uncommon, despite its effectiveness in characterising samples both in the bulk and near-surface regions. The key advantage of the use of negative muons, as opposed to extended x-ray absorption fine structure (EXAFS), is that EXAFS is a destructive technique (depending on the surface), making negative muons a preferred method for samples of importance.

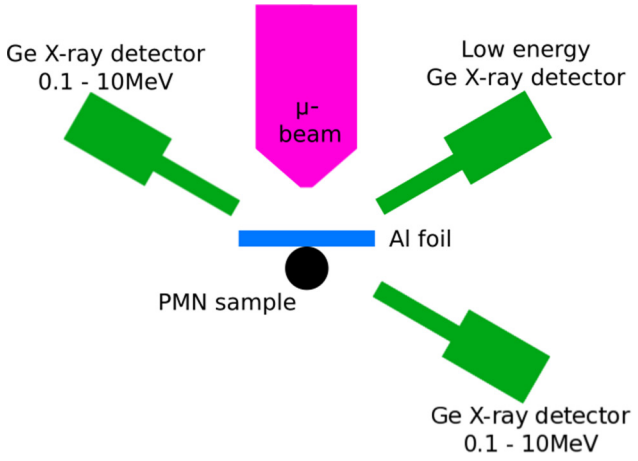

Figure 1. A diagram to show the basic setup of this experiment, showing approximate positions and angles of the equipment used. The sample was centred in the muon beam to achieve maximum bombardment.

When a muon is implanted in the sample, it can be captured by one of the atoms in the sample and comes to rest on one of the electronic energy levels. By then measuring the energy of the x-rays emitted when the muon decays, the exact atom and electronic state the muon came to rest upon can be identified [25, 26]. This allows for simple calibration and comparison of the data collected. For this experiment, two relevant energy regions were identified: 200–500 keV, where Mg and Pb peaks are measurable; and 2000–3000 keV, where Nb and Pb peaks may be measured. These shall henceforth be referred to as the low and high energy regions.

Negative muon experiments were carried out at ISIS using the experimental area CHRONUS on the RIKEN beamline. For these experiments a constant incident momenta of negative muons of 30 MeV c^{-1} was used, with a 4% momentum bite (calculated as $\Delta p/p$). A 12 mm Pb collimator was used to direct the beam. Three detectors were available for use: low energy and 0.1–10 MeV Ge x-ray detectors directed at the front of the sample (next to the μ^- beam), and a second 0.1–10 MeV Ge detector directed at the back of the sample. The detector employed in these measurements was the 0.1–10 MeV Ge x-ray detector in front of the sample, as the sample was too large for an appropriate intensity of x-rays to reach the detector behind the sample. For a full diagram of the equipment setup see figure 1.

In the results presented here, a large 9.3 cm^3 single crystal of PMN grown using the modified Bridgemann technique described in [27] was used. This sample has also been used in previous studies of this system, and as a result has been previously heated and cooled, with the maximum temperature it has been exposed to being 600 K ([18, 20]). A large [1 0 0] cut surface was oriented to face the muon beam.

The implantation depth of the muons was controlled using 0.1 mm layers of Al foil, in direct contact with the sample, as opposed to varying the energy of the muons as in [28]. The foil acts to impede the momentum of the incident muons, thus reducing the depth at which they are implanted. By varying the thickness of the foil from 6 μm to no foil, multiple depths in the sample were probed [37, 38]. The implantation depth and the

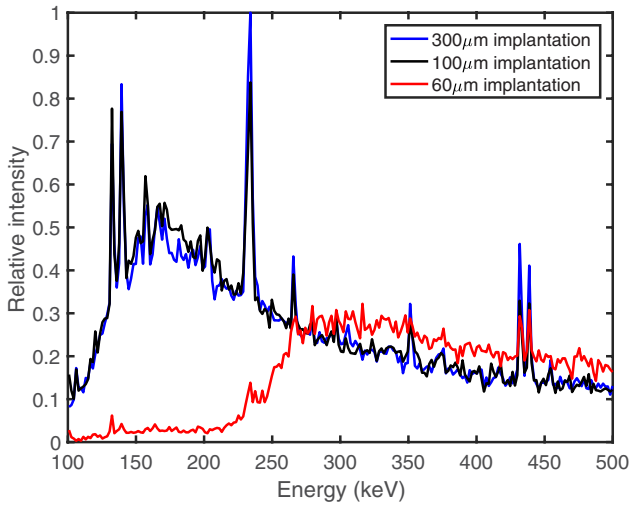

Figure 2. Graph showing the raw data between 100 and 500 keV for the 300 μm, 100 μm and 60 μm data.

Table 1. The energies of the peaks examined in this study and their origin.

Element	Excitation	Energy (keV)
Pb	$3d_{3/2} \rightarrow 2p_{1/2}$	2642
	$3d_{5/2} \rightarrow 2p_{3/2}$	2500
	$5g_{7/2} \rightarrow 4f_{5/2}$	438
	$5g_{9/2} \rightarrow 4f_{7/2}$	431
Mg	$4p \rightarrow 1s$	372
	$3p \rightarrow 1s$	353
Nb	$2p_{3/2} \rightarrow 1s_{1/2}$	2626
	$2p_{1/2} \rightarrow 1s_{1/2}$	2603

errors on this value were calculated using the SRIM and TRIM software to find the stopping profile of Al [29], however these implantation depths are not exact as the calculations assume a perfectly monochromatic beam.

Five different implantation depths were measured, and figure 2 shows the raw data at low energies for three of these measurements, including the largest and smallest penetrations. The peaks examined for the other elements are shown in table 1, with multiple excitations examined for each. The peak positions have been calibrated to the position of the Pb peaks, which were found to be present in all measurements regardless of depth. We do not believe that there is any low-energy attenuation of the x-rays due to the presence of Pb, because no peak position changes are observed with depth of muon implantation, and all of the measurements are taken very close to the surface so there is only a very small amount of Pb in the path of the x-rays. The measurement closest to the surface shows both the largest background and a cutoff in energy at approximately 250 keV. It is for this reason that no results concerning the O concentration is presented, as the peaks for O occur below this energy at 133 keV. The results for O at all other depths are found to be constant, so no change in the concentration is observed.

In order to compare the relative concentrations of each element, the integrated intensities of each peak are normalised such that, at the deepest depth probed, which we assume to be the bulk, the relative intensity is 1. For each of the peaks studied the integration range was chosen by hand in order to ensure that there is minimal contribution from background or other peaks. In these experiments no explicit background subtraction was possible, however, estimates of the backgrounds for all depths are found to be comparable, so this is not expected to influence the final results substantially. The resulting plots showing the changes in relative peak intensity for Pb, Mg and Nb are shown in figure 3. These changes in intensity are directly linked to the relative abundances of each element. From these results it is then easy to track any changes in concentration with depth. The errors in relative intensity shown in figure 3 are the errors extracted from the raw data and then scaled.

The changes in concentration for Pb are shown in panel (a) of figure 3, and here no clear changes in intensity are seen with depth. This result for Pb is expected to be influenced by the presence of Pb further up in the beam, but we believe that this is not a problem as it is the relative change in peak size being studied here. It is noted that the measurement for an implantation depth of 100 μm appears to be lower than the rest, however this trend appears to be repeated for Nb, so we suggest that this is a result of the total number of muons implanted in the sample being slightly reduced compared to the larger depths due to stopping in the air and aluminium foil. Panel (b) shows the changes in Mg concentration, which shows a clear increase of approximately 25% at a depth of 60 μm, though the exact depth at which this increase begins is unclear if the 100 μm peak is assumed to be anomalous. The Nb peak height variations in panel (c) are the most difficult to analyse due to the large errors associated with these results.

When charge neutrality in the system is considered, if there is a 25% increase in Mg^{2+} ions, there must be an associated 5% decrease in Nb^{5+} ions. This is within the errors of the measurement carried out here. For the case of a 25% increase in Mg, the unit cell formula of the system will become $PbMg_{0.42}Nb_{0.63}O_3$. This is no longer an ideal perovskite structure, as there is more than one atom on the B site, which may explain the transformation from the cubic to rhombohedral phase. In order to maintain the ideal perovskite structure, the unit cell formula must be $PbMg_{0.42}Nb_{0.58}O_3$, which is within the errors on the data presented here. This formula gives a net charge of $-0.26e$, meaning that the region is polar. A change in the number of O^{2-} ions could not compensate for this change in Mg content alone, but could if there was a coupled change in Nb, which is a possibility. Similarly, a decrease in Pb^{2+} ions could compensate for this, but as the mass of Pb is significantly larger than that of the elements it can be assumed that this element has least mobility and can be considered constant across the sample.

Previous studies have suggested regions of $Nb : Mg = 1 : 1$ concentration to explain anomalous results in diffuse neutron scattering, Raman, and TEM data. These areas are often referred to as polar nano-regions (PNRs), due to the lack of charge balance, and are expected to have rhombohedral symmetry and very small correlation lengths due to their small size [13, 22]. A diffraction peak in neutron data was identified as linked to 1:1 concentration regions, and was found to

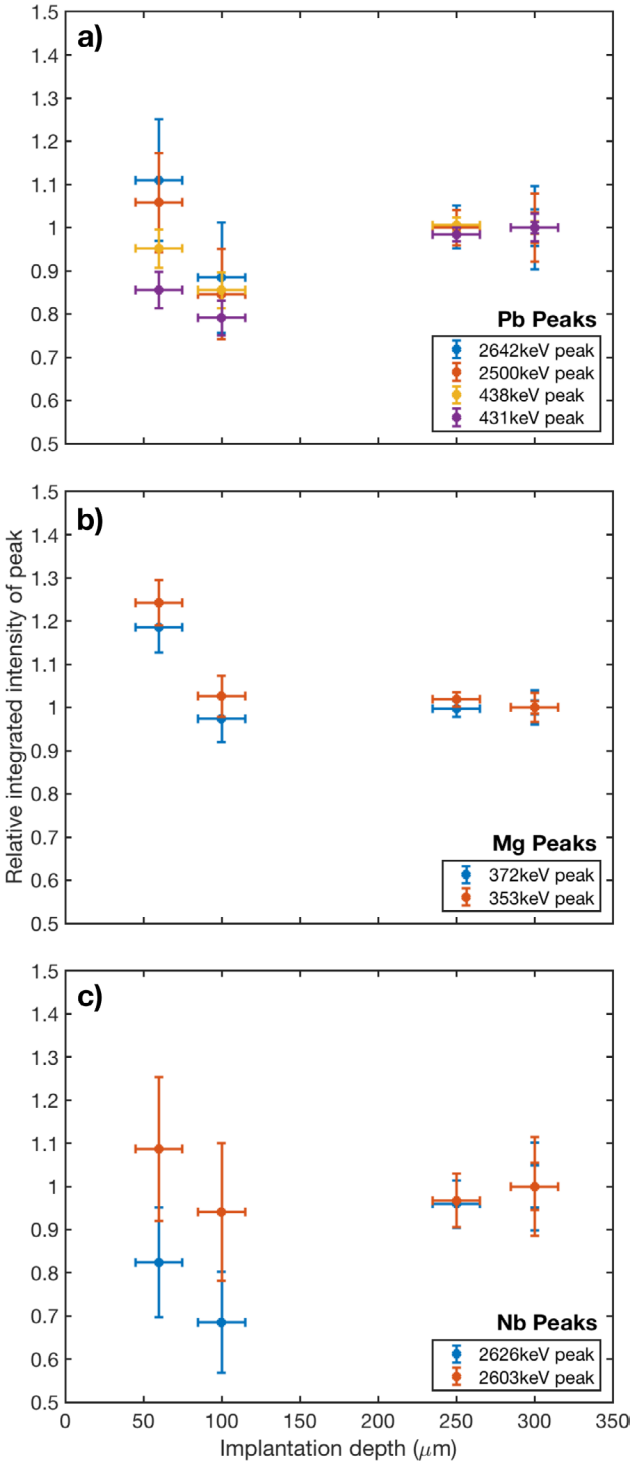

Figure 3. The change in relative peak size as the implantation depth is varied for: (a) four Pb peaks; (b) two Mg peaks; (c) two Nb peaks. It should be noted that the errors in implantation depth are systematic.

have strong temperature dependance below the phase transition temperature [30], and other diffraction studies have identified the presence of PNRs from the increase of line tails for temperatures below 600 K [31]. In Raman studies, a peak was seen at approximately 4 meV and linked to such a 1:1 concentration region, but has not been seen in equivalent neutron studies [32–34]. PNRs are expected to also have a large influence upon the ferroelectric soft mode, which has been used to explain some of the unexpected phenomena in the phonon spectra, though it is unclear if this model completely satisfies all of the observations [18, 34, 35]. Therefore, it is suggested that a clustering of PNRs near to the surface could be the cause of the observed change in concentration here, as well as the other 'skin' effects that have been noted in other studies.

It should also be noted that chemically ordered regions (CNRs) have also been observed in relaxor systems through TEM measurements, which may also be linked to changes in concentration to maintain charge neutrality, but they have been identified to require excess Nb [13]. This suggests that, assuming the sample has overall 2:1 Nb:Mg concentration, then CNRs must form in order to compensate for the existence of PNRs. TEM studies have also shown that PNRs inhibit domain growth due to their negative charge, which raises questions as to at what point these regions appeared in the sample [36]. No previous studies have reported a gradient in O concentration, so the assumption made here that this remains constant is reflected in the literature.

The results presented here are unable to give evidence for the mechanism behind this change in concentration with depth. However, due to the long length scale for the concentration variation, it is suggested that the cause of the concentration gradient must be driven by diffusion. As these measurements were carried out on a cut and polished surface, the statement that this change in concentration is an artefact of the sample growth cannot be made. Rather, it is possible that the cutting and heating of the sample to create this surface may have influenced this diffusion. The fact that this concentration change is observed suggests that the composition may be close to being unstable, in which case this separation of phases may serve to stabilize the bulk phase. Evidence from other studies have found that surface effects can be much shorter range, with a depth of 10–50 μm reported in $PbZn_{1/3}Nb_{2/3}O_3$ [24].

To conclude, the results collected here using negative muon techniques show that there is a clear increase in the concentration of Mg in $PbMg_{1/3}Nb_{2/3}O_3$ (PMN) less than 100 μm below the surface, which we also link to a reduction in the Nb concentration. Three possible structures are suggested for the surface region: the rhombohedral $PbMg_{0.42}Nb_{0.63}O_3$; the polar $PbMg_{0.42}Nb_{0.58}O_3$; or a combination of PMN and polar nano-regions with 1:1 Nb:Mg concentration. The presence of polar nano-regions has been previously reported in other studies, and we thus conclude that our results show a clustering of 1:1 Mg:Nb regions near the surface of the crystal. This suggests that the skin effects observed in this compound are linked to the changes in unit cell and the associated strains.

Acknowledgment

Support is gratefully acknowledged from the EPSRC, the STFC, the Royal Society, and the Carnegie Trust for the Universities of Scotland.

ORCID iDs

K L Brown https://orcid.org/0000-0002-5977-7370
D Viehland https://orcid.org/0000-0002-2736-0677
G Xu https://orcid.org/0000-0003-1441-8275
P M Gehring https://orcid.org/0000-0002-9236-2046
A D Hillier https://orcid.org/0000-0002-2391-8581
C Stock https://orcid.org/0000-0003-4265-8241

References

[1] Cowley R A 1996 *Phys. Scr.* **1996** 24
[2] Andrews S R 1986 *J. Phys. C: Solid State Phys.* **19** 3721
[3] Shapiro S M, Axe J D, Shirane G and Riste T 1972 *Phys. Rev.* B **6** 4332
[4] Hlinka J, Currat R, de Boissieu M, Livet F and Vysochanskii Y M 2005 *Phys. Rev.* B **71** 052102
[5] Wang Y J, Kim Y-J, Christianson R J, LaMarra S C, Chou F C and Birgeneau R J 2001 *Phys. Rev.* B **63** 052502
[6] Gehring P M, Hirota K, Majkrzak C F and Shirane G 1995 *Phys. Rev.* B **51** 3234
[7] Thurston T R, Helgesen G, Gibbs D, Hill J P, Gaulin B D and Shirane G 1993 *Phys. Rev. Lett.* **70** 3151
[8] Hirota K, Shirane G, Gehring P M and Majkrzak C F 1994 *Phys. Rev.* B **49** 11967
[9] Hill J P, Feng Q, Harris Q J, Birgeneau R J, Ramirez A P and Cassanho A 1997 *Phys. Rev.* B **55** 356
[10] Hill J P, Thurston T R, Erwin R W, Ramstad M J and Birgeneau R J 1991 *Phys. Rev. Lett.* **66** 3281
[11] Xu G, Gehring P M, Stock C and Conlon K 2006 *Phase Transit.* **79** 135
[12] Colla E V, Koroleva E Y, Okuneva N M and Vakhrushev S B 1992 *J. Phys.: Condens. Matter* **4** 3671
[13] Fu D, Taniguchi H, Itoh M and Mori S 2012 $Pb(Mg_{1/3}Nb_{2/3})O_3$ (PMN) relaxor: dipole glass or nano-domain ferroelectric? *Advances in Ferroelectrics* ed A Peláiz-Barranco (Rijeka: InTech) (https://doi.org/10.5772/52139)
[14] Iwase T, Tazawa H, Fujishiro K, Uesu Y and Yamada Y 1999 *J. Phys. Chem. Solids* **60** 1419
[15] Lebon A, Dammak H, Calvarin G and Ahmedou I O 2002 *J. Phys.: Condens. Matter* **14** 7035
[16] de Mathan N, Husson E, Calvarn G, Gavarri J R, Hewat A W and Morell A 1991 *J. Phys.: Condens. Matter* **3** 8159
[17] Gehring P M, Chen W, Ye Z-G and Shirane G 2004 *J. Phys.: Condens. Matter* **16** 7113
[18] Stock C, Luo H, Viehland D, Li J F, Swainson I P, Birgeneau R J and Shirane G 2005 *J. Phys. Soc. Japan* **74** 3002
[19] Kisi E H and Forrester J S 2005 *J. Phys.: Condens. Matter* **17** L381
[20] Conlon K H, Luo H, Viehland D, Li J F, Whan T, Fox J H, Stock C and Shirane G 2004 *Phys. Rev.* B **70** 172204
[21] Stock C, Gehring P M, Hiraka H, Swainson I, Xu G, Ye Z-G, Luo H, Li J-F and Viehland D 2012 *Phys. Rev.* B **86** 104108
[22] Dkhil B, Kiat J M, Calvarin G, Baldinozzi G, Vakhrushev S B and Suard E 2001 *Phys. Rev.* B **65** 024104
[23] Xu G, Zhong Z, Bing Y, Ye Z-G, Stock C and Shirane G 2003 *Phys. Rev.* B **67** 104102
[24] Xu G, Zhong Z, Bing Y, Ye Z-G, Stock C and Shirane G 2004 *Phys. Rev.* B **70** 064107
[25] Engfer R, Schneuwly H, Vuilleumier J L, Walter H K and Zehnder A 1974 *At. Data Nucl. Data Tables* **14** 509
Engfer R, Schneuwly H, Vuilleumier J L, Walter H K and Zehnder A 1975 *At. Data Nucl. Data Tables* **16** 580 (erratum)
[26] Measday D 2001 *Phys. Rep.* **354** 243
[27] Luo H, Xu G, Xu H, Wang P and Yin Z 2000 *Japan. J. Appl. Phys.* **39** 5581
[28] Hillier A, Paul D and Ishida K 2016 *Microchem. J.* **125** 203
[29] Ziegler J F, Ziegler M and Biersack J 2010 *Nucl. Instrum. Methods Phys. Res.* B **268** 1818 (*19th Int. Conf. on Ion Beam Analysis*)
[30] Gosula V, Tkachuk A, Chung K and Chen H 2000 *J. Phys. Chem. Solids* **61** 221
[31] Bonneau P, Garnier P, Calvarin G, Husson E, Gavarri J R, Hewat A W and Morell A 1991 *J. Solid State Chem. France* **91** 350
[32] Taniguchi H, Itoh M and Fu D 2011 *J. Raman Spectrosc.* **42** 706
[33] Naberezhnov A, Vakhrushev S, Dorner B, Strauch D and Moudden H 1999 *Eur. Phys. J.* B **11** 13
[34] Gehring P M, Wakimoto S, Ye Z-G and Shirane G 2001 *Phys. Rev. Lett.* **87** 277601
[35] Bosak A, Chernyshov D, Vakhrushev S and Krisch M 2012 *Acta Crystallogr.* A **68** 117
[36] Chen J, Chan H M and Harmer M P 1989 *J. Am. Ceram. Soc.* **72** 593
[37] Stock C, Brown K L, Stockdale C P J and Hillier A D 2017 RB1710367 dataset (STFC ISIS Facility) (https://doi.org/10.5286/ISIS.E.86391844)
[38] Stock C, Stockdale C P J, Gehring P M and Hillier A D 2016 RB1620326 dataset (STFC ISIS Facility) (https://doi.org/10.5286/ISIS.E.82431336)

Decoupled molecular and inorganic framework dynamics in $CH_3NH_3PbCl_3$

M. Songvilay,[1] Zitian Wang,[1] V. Garcia Sakai,[2] T. Guidi,[2] M. Bari,[3] Z.-G. Ye,[3] Guangyong Xu,[4] K. L. Brown,[1] P. M. Gehring,[4] and C. Stock[1]

[1]*School of Physics and Astronomy, University of Edinburgh, Edinburgh EH9 3FD, United Kingdom*

[2]*ISIS Facility, Rutherford Appleton Laboratory, Chilton, Didcot OX11 0QX, United Kingdom*

[3]*Department of Chemistry and 4D LABS, Simon Fraser University, Burnaby, British Columbia V5A1S6, Canada*

[4]*NIST Center for Neutron Research, National Institute of Standards and Technology, 100 Bureau Drive, Gaithersburg, Maryland 20899, USA*

(Received 22 October 2019; published 30 December 2019)

The organic-inorganic lead-halide perovskites are composed of organic molecules imbedded in an inorganic framework. The compounds with general formula $CH_3NH_3PbX_3$ ($MAPbX_3$) display large photovoltaic efficiencies for halogens X = Cl, Br, and I in a wide variety of sample geometries and preparation methods. The organic cation and inorganic framework are bound by hydrogen bonds that tether the molecules to the halide anions, and this has been suggested to be important to the optoelectronic properties. We have studied the effects of this bonding using time-of-flight neutron spectroscopy to measure the molecular dynamics in $CH_3NH_3PbCl_3$ ($MAPbCl_3$). Low-energy/high-resolution neutron backscattering reveals thermally activated molecular dynamics with a characteristic temperature of ∼95 K. At this same temperature, higher-energy neutron spectroscopy indicates the presence of an anomalous broadening in energy (reduced lifetime) associated with the molecular vibrations. By contrast, neutron powder diffraction shows that a spatially long-range structural phase transitions occurs at 178 K (cubic → tetragonal) and 173 K (tetragonal → orthorhombic). The large difference between these two temperature scales suggests that the molecular and inorganic lattice dynamics in $MAPbCl_3$ are actually decoupled. With the assumption that underlying physical mechanisms do not change with differing halogens in the organic-inorganic perovskites, we speculate that the energy scale most relevant to the photovoltaic properties of the lead-halogen perovskites is set by the lead-halide bond, not by the hydrogen bond.

DOI: 10.1103/PhysRevMaterials.3.125406

I. INTRODUCTION

The lead-halide perovskites have generated considerable interest within the condensed matter physics community because they exhibit outstanding photovoltaic and optoelectronic properties that have already been exploited in the design of new solar cell devices [1–7]. These materials can be grouped into two categories: the hybrid organic-inorganic perovskites and the all-inorganic perovskites. The first group comprises materials based on an inorganic framework of PbX_6 octahedra (X = I, Br, Cl) and an organic molecular cation [commonly methylammonium (MA) or formamidinium (FA)] [8]. Although the molecular cation does not directly contribute to the optoelectronic properties, its asymmetric shape and its ability to rotate and vibrate within the interstices of the inorganic framework affects the crystal structure and, thus, the electronic band gap [4,9–11]. Furthermore, quasielastic neutron scattering studies of $MAPb(Br, I)_3$ [12–14] demonstrate that the molecular cation participates in an order-disorder transition that is also associated with a dielectric anomaly and may therefore be connected with changes in the photoluminescence spectra as a function of temperature [15]. However, while $MAPbI_3$ shows the highest photovoltaic power conversion efficiency to date (over 25%) [16,17] among the lead-halide perovskites [4,18,19], recent experimental studies have shown that all-inorganic perovskite materials actually display comparable efficiencies (15% for $CsPbI_3$) [20]. Consequently, the role and importance of the organic cation to the photovoltaic properties remain unclear [21,22].

In order to understand the interplay between the organic cation and the inorganic framework, as well as the effect of the molecule on the thermal conductivity and optoelectronic properties, numerous studies have been devoted to characterizing the molecular dynamics in the lead halides using optical spectroscopy techniques (Raman, infrared), x-ray and neutron scattering methods, and NMR [9,23–28]. Some of these works also address the coupling between the relaxational dynamics arising from the organic cation and the phonons associated with the inorganic framework in both powder and single-crystal samples [12–14,29]. All these studies observe an onset of fast and overdamped (i.e., short-lived) relaxational molecular dynamics on heating that coincides with a distortion in the inorganic unit cell and are indicative of a coupling between the inorganic lattice and molecular dynamics.

$MAPbCl_3$ [Fig. 1(a)] undergoes two structural transitions on cooling: a cubic-to-tetragonal transition at 178 K and a transition to an orthorhombic phase at 173 K. This sequence of transitions is reflected in the temperature dependence of the $\mathbf{Q} = (0\ 0\ 1)$ Bragg peak intensity shown in Fig. 1(b), measured on the IRIS neutron backscattering spectrometer, and is similar to that observed in the bromine and iodine analogues. These phases were first characterized by Poglitsch and Weber [30] who identified the respective space groups as cubic $Pm\bar{3}m$ ($a = 5.675$ Å), tetragonal $P4/mmm$ ($a = 5.656$ Å, $c = 5.630$ Å), and orthorhombic $P222_1$ ($a = 5.673$ Å, $b = 5.628$ Å, $c = 11.182$ Å). Chi *et al.* [31] later suggested that the orthorhombic space group was actually *Pnma*

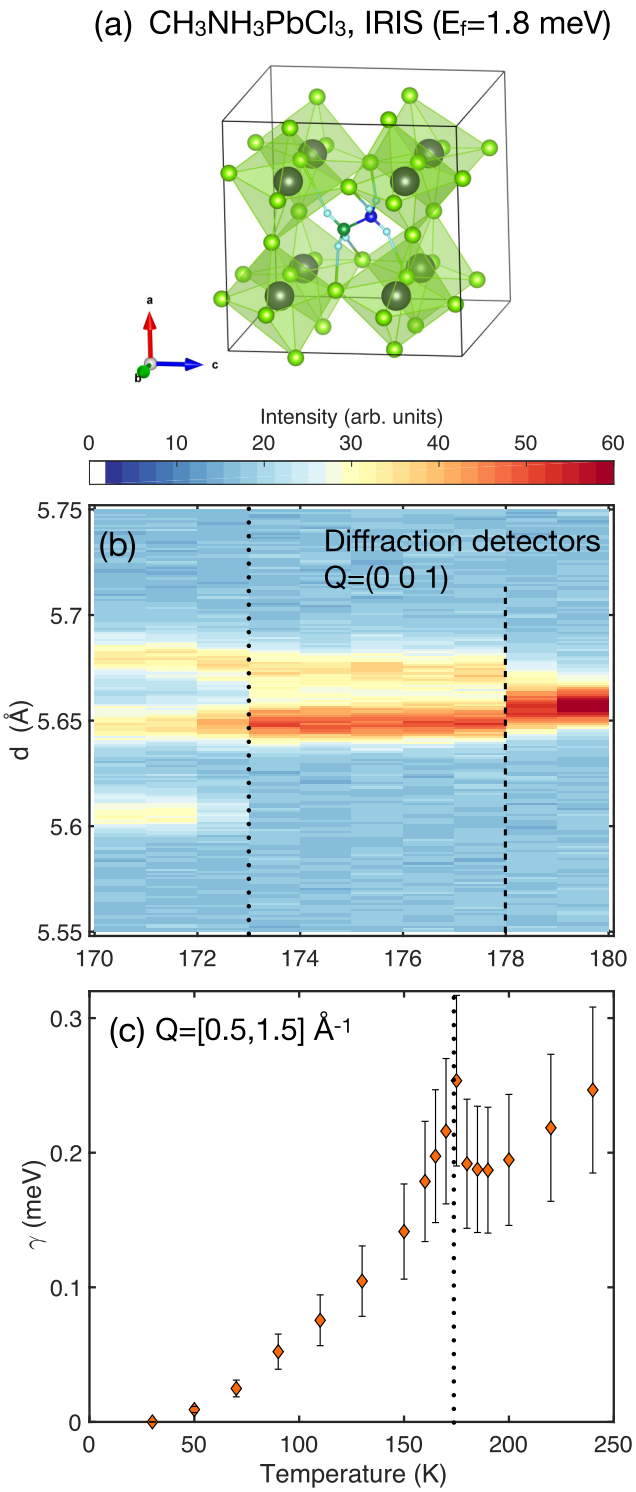

FIG. 1. (a) Crystallographic structure of $MAPbCl_3$ in the orthorhombic phase. The Pb cations are represented by gray spheres and the Cl anions by green spheres. In this ordered phase, the H, N, and C atoms forming methylammonium molecules are represented with light blue, dark blue, and dark green spheres, respectively. (b) Temperature dependence of the intensity of the (0 0 1) Bragg reflection, measured with the diffraction detectors of IRIS. The dashed lines denote transitions to the tetragonal (178 K) and orthorhombic phases (173 K). (c) Temperature dependence of the quasielastic linewidth. The dashed line indicates the order-disorder transition.

($a = 11.1747$ Å, $b = 11.3552$ Å, $c = 11.2820$ Å), based on powder diffraction measurements. In this low-temperature *Pnma* phase it was shown that the methylammonium cations order in an antiparallel arrangement, along with a strong distortion of the $PbCl_6$ octahedra, mediated by the hydrogen bonds between the methylammonium and the chlorine anions. That the octahedral distortion occurs upon ordering of the molecules is evidence that the molecular cation is the most rigid unit in this compound [31]. A single-crystal diffraction study of the intermediate tetragonal phase was also carried out by Kawamura and Mashiyama [32,33], who observed both superlattice and incommensurate reflections, which were also reported for $MAPbBr_3$ [34] and $MAPbI_3$ [35].

In this paper, we investigate the dynamics of MA molecular cations in $MAPbCl_3$ using neutron inelastic scattering and provide a comparison with previous results on other halide materials. As the halogen radius affects the inorganic framework size, the radius of the space available for the MA molecule to rotate is also expected to change depending on the halogen anion, thus affecting the dynamics and therefore potentially the optoelectronic properties. We will show that there is a decoupling between molecular and framework dynamics and discuss the role of the molecule in the electronic and low-energy framework dynamics.

II. EXPERIMENTAL DETAILS

Powder samples were prepared out of solution following the procedure outlined in Ref. [31]. Methylamine hydrochloride and lead acetate were dissolved in hydrochloric acid. An excess of an approximately 8–10 molar ratio of methylamine hydrochloride was required to obtain phase pure samples. The resulting powder was washed multiple times with diethyl ether to remove residual acid. For all neutron measurements the powder was wrapped in niobium foil as a precaution to prevent reaction of the aluminum sample holder with any residual acid on the powder.

High-resolution measurements of the quasielastic scattering were performed on the IRIS spectrometer (ISIS, UK). IRIS is an indirect geometry, time-of-flight spectrometer that uses PG002 crystal analyzers to produce a fixed final neutron energy $E_f = 1.84$ meV. The energy transfer is given by $E = E_i - E_f$, with a default dynamic range of ± 0.5 meV, and the spectrometer energy resolution, given by the full width at half maximum (FWHM) of a Gaussian fit at low temperatures, was $\delta E = 23$ μeV. An empty-can measurement for background subtraction was carried out at room temperature. The IRIS spectrometer provides a diffraction bank of detectors at $2\theta \sim 170^\circ$ that allowed us to measure the structural transitions and unit cell parameters simultaneously while also measuring the excitations.

The high-energy molecular dynamics was studied using the MARI direct geometry spectrometer (ISIS, UK). The incident neutron energy was fixed at $E_i = 100$, 50, and 25 meV using a Gd Fermi chopper spinning at a frequency of 600 Hz, 400 Hz, and 400 Hz, respectively. This configuration gave energy resolutions at the elastic position ($E = 0$) of 2.25, 1.15, and 0.48 meV, respectively. The incident energies were small enough that hydrogen recoil scattering is not relevant for the discussion here [36]. A thick disk chopper was used and spun

at 50 Hz to remove high-energy neutrons before the Fermi chopper. Neutrons with very high energy (∼eV) were filtered with a $t0$ chopper spun at 50 Hz. For all measurements on MARI and IRIS, a closed-cycle helium refrigerator was used to control the temperature of the sample.

III. NEUTRON SPECTROSCOPY

Our goal in performing neutron spectroscopic measurements on the powders of $MAPbCl_3$ was to track the temperature dependence of the molecular dynamics so that we could correlate the response to distortions of the inorganic framework and crystal structure and compare our findings to previous studies of the bromine variant. To this end we conducted experiments on two spectrometers, each designed to cover a substantially different energy range and therefore probing different timescales. The IRIS backscattering spectrometer, which provides extremely sharp energy resolution, was used to characterize the quasielastic scattering, which is observed in systems that display diffusive behavior. Quasielastic scattering is low-energy inelastic scattering that peaks at zero energy transfer ($E = 0$) and has a nonzero intrinsic energy width. In the case of $MAPbCl_3$, quasielastic scattering is sensitive to the reorientational motions or jumps of the MA molecule within the interstices of the inorganic framework. We emphasize here that such reorientational dynamics are not harmonic modes which would instead appear as peaks at nonzero energy transfer. The time-of-flight chopper instrument MARI, which provides access to dynamics at much higher energy transfers, was then used to study the higher-energy harmonic molecular modes and their temperature dependence.

A. Quasielastic neutron scattering

We first discuss the quasielastic scattering, and in this context it is important to note that the neutron incoherent cross section of hydrogen is roughly one order of magnitude larger than the cross sections (coherent or incoherent) of the other atoms in $MAPbCl_3$. Specifically, the neutron incoherent cross section for hydrogen is 80.3 barns whereas the next largest coherent/incoherent scatterer is chlorine, which has a cross section of only 11.5 barns/5.3 barns [37]. For this reason, the quasielastic scattering we observed is effectively a measure of the low-energy molecular dynamics associated with single-particle motions of the hydrogen atoms.

In order to motivate an appropriate choice of scattering cross section $\tilde{I}(Q, E)$ with which to model the neutron quasielastic scattering from $MAPbCl_3$, we begin by examining two spectra measured at low (50 K) and high (240 K) temperatures, shown in Figs. 2(a) and 2(b), respectively, that were obtained by integrating the scattered intensity over Q from 1.5 Å to 2.0 Å. The 50 K spectrum is well described by a Gaussian function of energy with a width equal to the instrumental elastic resolution, which means that no dynamics are visible at 50 K on the timescale sampled by IRIS. This spectrum changes on heating to 240 K, as shown in Fig. 2(b), where it evolves into a two-component energy profile. The first component exhibits a resolution-limited energy width like that at 50 K, but it is noticeably weaker; by contrast, the

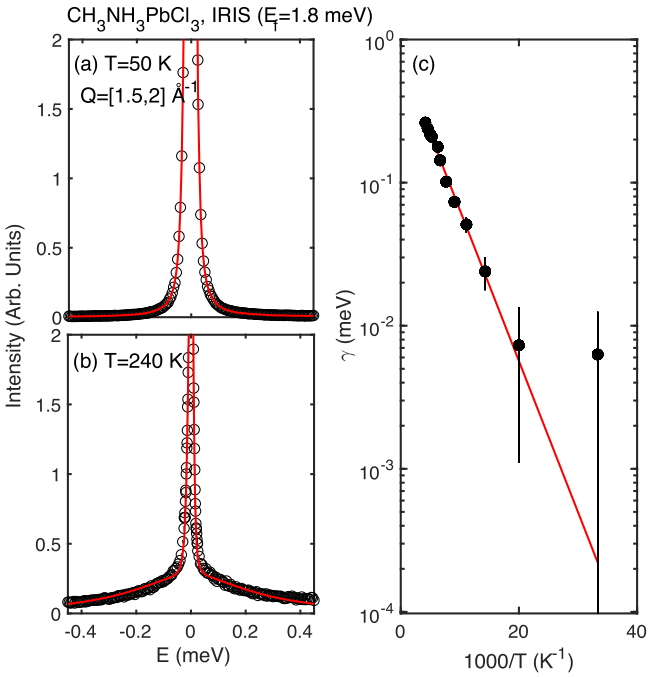

FIG. 2. (a), (b) Quasielastic scans measured on the IRIS backscattering spectrometer at 50 K and 240 K. The scan at 50 K is dominated by a strong resolution-limited peak at $E = 0$, which indicates that the molecular dynamics are static on the timescale set by the instrumental resolution. The scan at 240 K exhibits an energy profile with two distinct components, both centered at $E = 0$: one with a resolution-limited energy width (like that at 50 K but weaker), and another that is much broader in energy, which reflects the molecular dynamics. The solid curves are fits to the model discussed in the text. (c) Plot of Arrhenius fits to the quasistatic energy linewidths as a function of temperature.

second component is much broader and extends out to at least ±0.5 meV. The presence of two components suggests that the molecular dynamics of $MAPbCl_3$ can be characterized by two timescales, one of which is static compared to the dynamic range accessible by IRIS, and the other of which is dynamic and inversely proportional to the energy width of the broad component. Thus, to parametrize the quasielastic scattering in terms of the momentum transfer Q, energy transfer E, and temperature T our data were fitted to the following model scattering cross section that contains both a static and a dynamic component:

$$\tilde{I}(Q, E) = I_{el}(Q) + I_{\mathrm{dyn}}(Q) = I_{el}(Q)\delta(E) + \frac{I_{\mathrm{dyn}}(Q)}{1 + (E/\gamma(T))^2}. \quad (1)$$

Here, I_{el} and I_{dyn} are the static and dynamic components, respectively, γ is the energy linewidth, which is inversely proportional to the lifetime of the molecular fluctuations $\tau \sim 1/\gamma$, and $\delta(E)$ is a Dirac delta function in energy. This cross section was convolved with the spectrometer resolution function given by the 50 K spectrum as mentioned above, and representative fits to the data are shown as solid red curves in Figs. 2(a) and 2(b). For a given temperature, we find that the energy linewidth γ is independent of momentum

transfer Q, which indicates that no measurable diffusion of molecules occurs in the sample. We also note that the single Lorentzian used to describe the dynamic component in Fig. 2(b) shows small, systematic deviations from the data at small energy transfers. This may indicate the presence of multiple timescales and a need for a more complicated model cross section. The values for γ that we obtain from our fits should therefore be interpreted as an average or a range of timescales rather than that for a single damped harmonic oscillator. Regardless, our use of a single Lorentzian function and a single dynamical timescale describes the data quite well over a broad range of temperatures and wave vector Q and thus captures the most important physical features of the low-energy molecular dynamics.

The temperature dependence of the quasielastic linewidth γ is shown in Fig. 1(c), and a substantial increase is observed in the vicinity of the two structural transitions. We note that due to the small temperature difference between the two structural transitions, we were not able to definitively observe these separate transitions in the molecular dynamics. This behavior demonstrates the presence of some coupling between the inorganic framework and molecular dynamics, which then gives rise to critical scattering near the transitions. The strength of this coupling can be quantified by fitting the temperature dependence of γ to an Arrhenius law as shown in Fig. 2(c), where γ is plotted on a log scale as a function of $1000/T$. The data within ± 10 K of the structural transitions have been removed because they are dominated by the critical scattering. The red solid line in Fig. 2(c) is a fit of the remaining data to the expression $\gamma(T) = \gamma_0 \exp(-E_a/k_B T)$, where $\gamma_0 = 8.5 \pm 0.8$ K and $E_a = 243 \pm 15$ K. These parameters are smaller than those obtained for the bromine variant (see Ref. [13]), where $\gamma_0(\mathrm{Br}) = 27 \pm 2$ K and $E_a(\mathrm{Br}) = 323 \pm 20$ K, and indicates that the molecular dynamics in $MAPbCl_3$ are softer than that in $MAPbBr_3$. Recent neutron studies of the iodine variant report an even larger activation energy $E_a(I) \sim 600$ K [14,38], although a more complex rotational jump model was used to analyze the data. Nevertheless, the results on $MAPbX_3$ establish a clear trend in which the molecular dynamics hardens as the halide changes from Cl to Br and to I. It is tempting to attribute this trend to a halogen-dependent variation in the strength of the N-H-X hydrogen bonding between the inorganic framework and the molecular cation and this is corroborated by calculations for hydrogen bonding with halogens [39] and consistent with the idea that the framework structure is strongly correlated with the molecule [40]. But first-principles calculations of the hydrogen-bonding strength in $MAPbX_3$ yield a value of 0.09 eV/cation that is identical for $X =$ Cl, Br, and I [41] and indeed the necessity of the molecule for the exceptional semiconducting properties has been questioned [42]. If this is correct, then there must be some other bonds that set the energy scale of the molecular dynamics in the organic lead-halide perovskites.

Our discussion so far has dealt primarily with the energy dependence of the quasielastic scattering. We now move on to examine the momentum dependence, which provides information about the real-space symmetry of the molecular dynamics in which the hydrogen atoms participate through the elastic incoherent structure factor (EISF), which is defined as

$$I_{\mathrm{EISF}}(Q) = \frac{I_{el}(Q)}{I_{el}(Q) + I_{\mathrm{dyn}}(Q)}. \tag{2}$$

Different model cross sections have been used successfully to describe a wide variety of molecular dynamics, including isotropic rotational dynamics and rotational jump dynamics, each of which exhibits a different dependence on momentum transfer. But the data must span a sufficiently large Q range in order to distinguish between these models and determine the symmetry of the dynamics in $MAPbCl_3$ uniquely. This is because the EISF for these models is nearly identical for Q less than ~ 2 Å^{-1}, a point that is illustrated in Fig. 3 of Ref. [12]. Neutron scattering kinematics limits the maximum Q accessible on the IRIS backscattering spectrometer to less than ~ 2 Å^{-1}. For this reason we have chosen the simplest model, which describes the molecular dynamics in terms of two components, one static, corresponding to bound molecules, and the other dynamic. This later component corresponds to unbound molecules which contribute to the inelastic signal fitted to a Lorentzian line shape described above. Thus the total neutron scattering cross section has the form

$$\begin{aligned} I_{\mathrm{total}}(Q) &= (1-\alpha) I_{\mathrm{bound}} + \alpha \tilde{I} \\ &\equiv (1-\alpha) I_{\mathrm{bound}} + \alpha [I_{el}(Q) + I_{\mathrm{dyn}}(Q)], \end{aligned} \tag{3}$$

where $(1-\alpha)$ is the fraction of bound molecules that do not contribute to the dynamics. A similar model was applied in Ref. [43] to characterize the dynamics of water molecules in minerals, and that study motivated the use of the same formalism to study the molecular dynamics in $MAPbBr_3$ [12,13]. Given the similarities between $MAPbCl_3$ and $MAPbBr_3$, we have opted to pursue the same approach here by dividing the EISF into two components, one representing the fraction of molecules that are constrained, therefore contributing no Q dependence, and a second representing the fraction of molecules that are dynamic. For the dynamic component, we have again assumed the simplest case where the motions are spherically symmetric. In this case, the EISF takes the form

$$I_{\mathrm{EISF}}^{\mathrm{total}}(Q) = \alpha \frac{\tilde{A} \sin(Qr)}{Qr} + (1-\alpha), \tag{4}$$

where $\tilde{A}$ is a factor that takes into account the effects of multiple scattering, which reduces the cross section in the limit $Q \to 0$. This parameter varied from 0.9 to 1 for all temperatures. It is thus indicative of the overall uncertainty associated with the EISF and was used to set the error bars in Figs. 3(c)–3(e). The parameter r is the radius associated with the molecular fluctuations; it was fixed to the ammonia hydrogen-hydrogen distance of 1.8 Å because a universal fit to all temperatures and momentum transfers found this value gives the best description of the data. Representative fits are shown in Fig. 3, where panel (a) illustrates how the quasielastic cross section varies with Q. Panels (c)–(e) show representative fits to Eq. (4) for a series of three temperatures that indicate a good fit to the data. At $T = 30$ K [Fig. 3(c)], the static or bound component of the quasielastic cross section dominates, and the scattering is independent of momentum transfer. At higher temperatures [Figs. 3(d)–3(e)] the bound

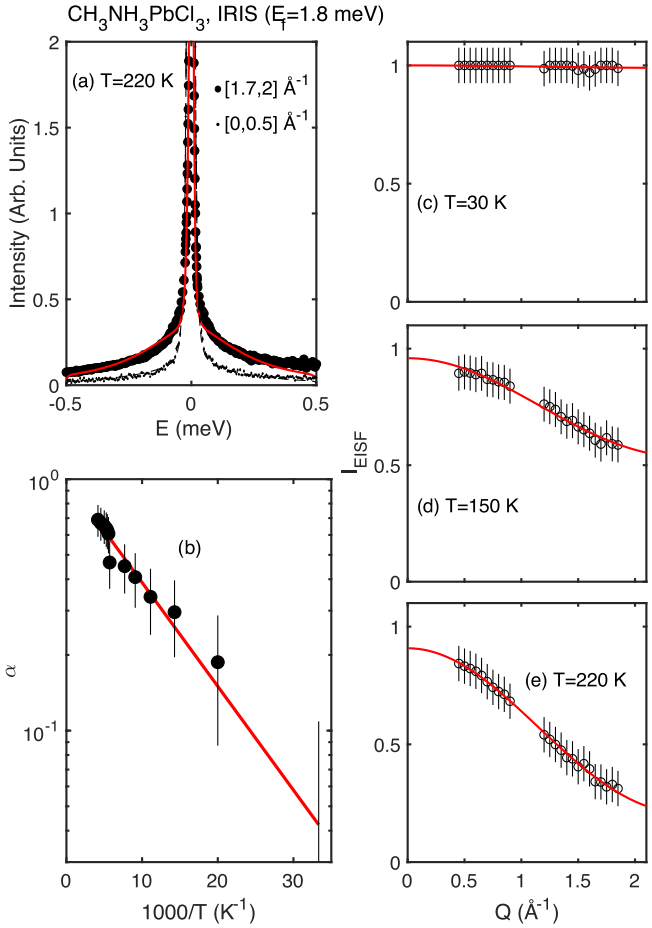

FIG. 3. (a) Energy dependence of the quasielastic scattering at 220 K for two different Q ranges. (b) Arrhenius plot of the dynamic molecular fraction determined by the EISF discussed in the text. (c)–(e) Plots of the EISF at 30 K, 150 K, and 220 K, respectively. The solid curve is a fit to a two-component model consisting of static/bound and dynamic molecules.

component of the cross section accounts for less of the total scattering, and a decay with momentum is observed.

Figure 3(b) shows a plot of the dynamic fraction of the EISF as a function of $1000/T$. In order to extract an activation energy for the molecules that are free to vibrate, these data were fitted to an Arrhenius curve represented by the solid line and given by $\alpha = \alpha_0 \exp[E_\alpha/k_B T]$, where $\alpha_0 = 1.0 \pm 0.15$ and $E_\alpha = 95 \pm 5$ K. These values may be compared to those determined for $MAPbBr_3$ [13], where a similar analysis yielded $E_\alpha(\mathrm{Br}) = 51 \pm 10$ K. Physically, the parameter α_0 should be equal to 1 because all molecules should become activated and contribute to the dynamics in the high-temperature limit. We found that fixing α_0 for both the chlorine and bromine variants does not change the parameter E_α within our uncertainties. Consequently, we conclude that the activation energy E_α decreases with increasing halogen atomic number. This is consistent with the fact that the interstitial spaces in the heavier halide perovskites are larger, and thus one should expect the energy barrier to molecular activation to be correspondingly lower. This was quantified in Ref. [8] by estimating an effective radius for the molecule with the goal of being able to calculate tolerance factors finding an estimated radius of 1.81, 1.96, and 2.20 Å [4] for the chlorine, bromine, and iodine compounds, respectively. The radius for the chlorine compound agrees well with the value we have obtained from our analysis outlined in Eq. (4) and also with previous analysis of the bromine compound [12].

B. Molecular dynamics spectra at high energy

The harmonic modes associated with the molecular cation are located at energies significantly higher than can be accessed by the dynamic range of ±0.5 meV provided by the backscattering spectrometer IRIS. To characterize these modes, neutron inelastic spectra spanning a much larger energy range were measured on the chopper instrument MARI using neutron incident energies of 100 meV, 50 meV, and 25 meV, each of which covers a different dynamic range due to kinematic constraints. Figures 4(a)–4(c) display neutron spectra for $E_i = 100$, 50, and 25 meV, respectively, measured at $T = 5$ K. These low-temperature data (Fig. 4) show five modes below 20 meV, two modes around 40 meV, one mode at 60 meV, and another mode around 90 meV, all of which agree with those identified by previous Raman and infrared studies of $MAPbCl_3$ [25,44]. Using the assignments of the Raman data reported in Ref. [25], which were also compared to DFT calculations, we are able to identify the peaks measured on MARI with specific octahedral and molecular vibrations.

The phonon modes below 10 meV correspond to transverse acoustic and optic phonons that are primarily associated with displacements of the $PbCl_6$ octahedra involving both twists (or rigid-body motions) and distortions. The peak near 11 meV, termed the "nodding donkey" mode, corresponds to a rotational vibration of the cation around either the carbon or nitrogen atoms. These molecular motions are presumably affected by the octahedra tilting and distortions because of the hydrogen bonding with the halogen, and thus they provide some measure of the coupling between the molecule and the inorganic framework. This is discussed in Refs. [12,13] for the bromine compound and in Refs. [24,28] for $MAPbI_3$. This coupling was also implicated in single-crystal neutron scattering studies of the chlorine [29] and iodine [45] compounds where it was suggested that the molecular motions also affect the low-energy transverse acoustic phonons.

Above 12 meV, the observed phonon modes correspond to lurching motions of the MA cations, and the mode at 60 meV has been previously assigned to the torsions of the carbon-nitrogen (C-N) axis. Finally, a weak mode can be observed around 90 meV that may arise from C-N bond stretching. These high-energy modes are associated with internal modes of the MA molecule and are consistent with previous Raman and infrared studies of the iodine and bromine compounds [24,25].

Figures 5(a)–5(c) show color maps of the neutron inelastic scattering cross section that summarize the temperature dependence from 5 K to 200 K. Figures 5(d)–5(f) display energy cuts of the Q-integrated spectra at different temperatures. These energy cuts reveal the surprising finding that while the inelastic spectra exhibit sharp modes at 5 K, the molecular vibrations become strongly overdamped (shorter lifetime) on heating ~100 K, which is far below either of the structural

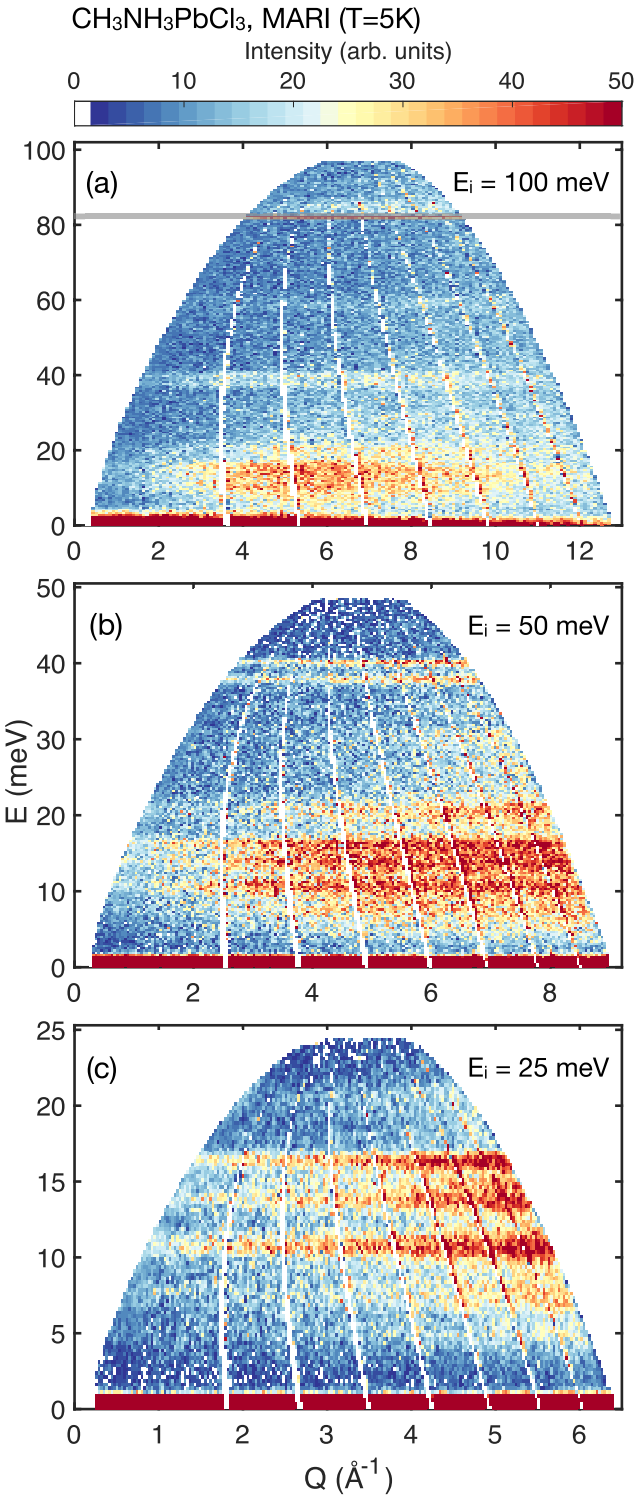

FIG. 4. (a)–(c) Phonon spectra measured by neutron inelastic scattering on MARI at $T = 5$ K for incident energies $E_i = 100$, 50, and 25 meV, respectively. The data have been corrected for a background corresponding to the high-temperature data. The gray line in (a) corresponds to a spurion generated by the back side of the Gd Fermi chopper spinning at 600 Hz. This spurious feature is often referred to as the "π pulse."

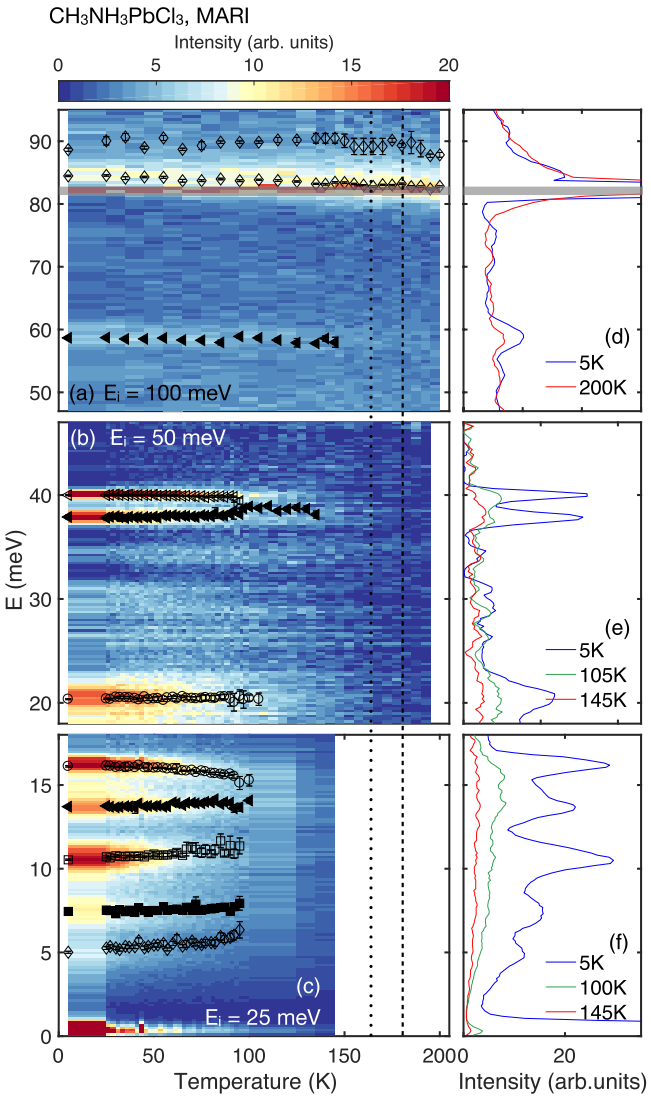

FIG. 5. (a)–(c) Temperature dependence of the molecular modes in $MAPbCl_3$ measured at incident energies $E_i = 100$, 50, and 25 meV, respectively. At each temperature, the data were integrated over the entire Q range, corrected for a background derived from the featureless high-temperature data and corrected for the thermal factor. (e), (f) Energy cuts at different temperatures extracted from the $E_i = 100$, 50, and 25 meV data, respectively. The gray line in (a) corresponds to a "π pulse" spurion from the back side of the Gd Fermi chopper spinning at 600 Hz.

transitions associated with the inorganic framework (indicated by the vertical dashed lines). This temperature dependence differs from that observed in the bromine compound, where a broad relaxational behavior is observed at temperatures that coincide with the structural transitions [13] (see also Refs. [24,28] for a discussion of $MAPbI_3$). Internal motions, such as C-N distortions at high energies (Fig. 1), persist above this temperature; however we note that these are internal molecular modes and hence not expected to couple to the

inorganic framework surrounding the molecule. These spectroscopic results therefore show that the molecular motions coupled to the framework become strongly damped at temperatures much lower than the structural transitions where the overall lattice distorts.

We finally note that the energy cuts in Figs. 5(d)–5(f) show that several modes around 15 and 40 meV collapse into a single broad mode at 100 K. This may be due to a change in the interactions between the hydrogen and chlorine atoms when the molecules start to reorient. These results imply that the hydrogen bond tethering the molecules to the inorganic framework lattice is not a dominant energy scale and contrasts to the case of the bromine variant where the damping of molecular vibrations occurs at a much higher temperature that coincides with the structural distortion of the lattice.

IV. DISCUSSION AND CONCLUSION

We observe a strong damping (reduction in lifetime) and weakening of the molecular modes in $MAPbCl_3$ on heating to ~100 K, a temperature that is much lower than that associated with the structural transitions of the inorganic framework near ~170 K. By contrast, the molecular modes in the bromine compound become overdamped, and can be characterized by a relaxational line shape, at temperatures that coincide with that where the overall structure distorts [13]. We observe that these two effects occur on very different temperature scales in $MAPbCl_3$, which suggests that the molecular and inorganic framework dynamics are actually relatively decoupled. It is tempting to explain this result in terms of a halide-dependent hydrogen bond that is weaker for chlorine than for bromine. However, recent first-principles calculations show that the hydrogen bond energies in $MAPbX_3$ are relatively weak (~0.09 eV/cation) and independent of halide for $X = $ Cl, Br, and I [41]. Our result is even more notable given the fact that the interstices of the framework cage surrounding the molecule in $MAPbCl_3$ are significantly smaller than those in $MAPbBr_3$ and $MAPbI_3$.

The softer molecular dynamics in $MAPbCl_3$, which are more sensitive to temperature than those in the other halide compounds, is reflected in our quasielastic measurements, which yield smaller activation energies from Arrhenius fits to the energy linewidths. This is further consistent with calculations reported in Ref. [25], which find a general softening of the lattice dynamics on going from iodine to chlorine organic-inorganic perovskites.

It is interesting to discuss this decoupling in terms of the electronic and thermal properties. In the context of the importance of phonons, it has been proposed that high photovoltaic efficiency in the organic-inorganic perovskites is the result of "hot carriers" [46] where photoexcited charges can spatially propagate allowing time for them to be collected. Normally, these charge carriers are highly damped by low-energy phonons, thereby reducing charge mobility. However, in the organic-inorganic perovskites these phonons have such short lifetimes that they cannot affect the charge carriers, thus allowing highly efficient collection of the charge.

$MAPbCl_3$ generally shows a significantly lower mobility compared to $MAPbI_3$ for a broad range of sample geometries likely due to the larger band gap [47]. On adding chlorine to $MAPbI_3$, the diffusion lengths increase [48,49] through improving film quality. It is difficult to understand the role of the molecular and framework lattice dynamics in improving the electronic properties. The lead-halide perovskites $MAPbI_3$ [45], $MAPbBr_3$ [50], $MAPbCl_3$ [29], and even fully inorganic $CsPb(Br, Cl)_3$ [51,52] all display quantitatively similar acoustic phonon lifetimes as a function of wave vector and temperature that results in poor thermal conductivity [53]. This alone illustrates that the low-energy acoustic phonon damping is not the origin of the change in photovoltaic efficiencies with the change in halogen. Another model is that the molecule increases the dielectric constant, thereby reducing the exciton binding energies. However, electro-optics has reported very small binding energies of ~2 meV [54], which is well below the thermal energy of k_BT (=300 K) ~ 25 meV, making this mechanism unlikely.

We propose an alternative idea where the molecule does not participate in damping the low-energy acoustic phonons but instead provides a means of coupling the high-energy charge sector to the much lower energy phonon sector. A coupling between the A site and the framework has been established through a comparison of $CsPbBr_3$ and $MAPBr_3$ [55] and calculations have shown that such coupling is required to stabilize an orthorhombic unit cell at low temperatures [56] as is present in the fully inorganic variants. While these two channels exist on very different energy scales, calculations have shown that molecular motions coupled with the underlying inorganic framework do influence the electronic structure [10]. We also note that internal molecular modes occur on much higher energy scales than do overall lattice fluctuations (like those observed in the perovskite $SrTiO_3$ [57]) and may provide a means of coupling the electronic sector in organic-inorganic perovskites to the already highly damped low-energy acoustic phonon response. This maybe consistent with the enhanced dissociation of charge transfer states with molecular loading of the framework lattice [58,59]. In this heuristic picture, the strength of this coupling between electronic degrees of freedom and the low-energy lattice dynamics would depend on the band gap which is set by the lead-halide bond and is expected (based on the unit cell volumes) to be smaller for the iodine and bromine variants [60,61]. This idea would imply that fully inorganic perovskites have the potential to be efficient photovoltaics, provided that a means of coupling the phonons on the meV scale with electronic excitations on the eV scale can be achieved. The speculation that framework-molecule coupling, set by the lead-halide bond and hence the band gap, is the important feature for attractive electronic properties requires further theoretical and experimental investigation.

We now discuss the origin of the damping of the molecular motions in the chlorine compound compared to the bromine variant. We have shown that damped, or lifetime shortened, molecular dynamics occur at a significantly lower temperature than in the bromine compound published previously. We have used this fact combined with the common acoustic phonon damping observed in both organic-inorganic and fully inorganic perovskites to question the role of the molecule in enhancing the electronic properties. As discussed above, the volume that is available for the molecule to rotate can be quantified by an effective radius and is noted to be

smaller in the chlorine variant than the bromine and iodine organic-inorganic perovskites. This decreased volume around the molecule may make it more sensitive to disorder that is present in the surrounding inorganic cage. The highly damped acoustic phonons for shorter wavelengths located away from the Brillouin zone center maybe indicative of disorder in the low-temperature inorganic framework structure. This is present for all halogens, but the molecular motions in the chlorine variant may be more susceptible to this disorder owing to the smaller volume for the molecular motions to occur. This is speculation at this point based on the dynamics, and future work comparing the structure through improved diffraction experiments will be required to corroborate this suggestion. However, we note that recent work on fully inorganic $CsPbBr_3$ did note significant disorder through enhanced thermal factors of the atomic positions [52].

In summary, we report a neutron inelastic scattering investigation of $MAPbCl_3$ that was motivated by recent studies on the photovoltaic properties of organic-inorganic perovskites and neutron studies performed on the bromine and iodine variants. We observe a decoupling of the molecular and framework dynamics based on the temperature dependence of the molecular vibrations which differ from the response of the distorted framework driven by acoustic phonons. We therefore speculate that the molecule may provide a means of connecting the disparate energy scales of the charge and low-energy phonon sectors, which in turn may contribute to the attractive electronic properties of these materials. In this picture, the important energy scale is set by the lead-halide bond, and not by hydrogen bonding.

ACKNOWLEDGMENTS

We acknowledge funding from the EPSRC and the STFC. We are thankful to M. A. Green, I. Swainson, and P. Bourges for fruitful discussions. This work was also supported by the Natural Sciences and Engineering Research Council of Canada (NSERC Grant No. 203773) and the US Office of Naval Research (ONR Grant No. N00014-16-1-3106).

[1] D. A. Egger, A. M. Rappe, and L. Kronik, Acc. Chem. Res. **49**, 573 (2016).
[2] D. A. Egger, A. Bera, D. Cohen, G. Hodes, T. Kirchartz, L. Kronik, R. Lovrincic, A. Rappe, D. R. Reichnman, and O. Yaffe, Adv. Mater. **30**, 1800691 (2018).
[3] T. M. Brenner, D. A. Egger, L. Kronik, G. Hodes, and D. Cahen, Nat. Rev. Mater. **1**, 15007 (2016).
[4] B. Saparov and D. B. Mitzi, Chem. Rev. **116**, 4558 (2016).
[5] N. J. Jeon, J. H. Noh, W. S. Yang, Y. C. Kim, S. Ryu, J. Seo, and S. Seok, Nature (London) **517**, 476 (2015).
[6] Z. Shi and A. H. Jayatissa, Materials **11**, 729 (2018).
[7] T. Zhu and E. Ertekin, Energy Environ. Sci. **12**, 216 (2019).
[8] G. Kieslich, S. Sun, and A. K. Cheetham, Chem. Sci. **5**, 4712 (2014).
[9] A. A. Bakulin, O. Selig, H. J. Bakker, Y. L. A. Rezus, C. Müller, T. Glaser, R. Lovrincic, Z. Sun, Z. Chen, A. Walsh, J. M. Frost, and T. L. C. Jansen, J. Phys. Chem. Lett. **6**, 3663 (2015).
[10] C. Motta, F. El-Mellouhi, S. Kais, N. Tabet, F. Alharbi, and S. Sanvito, Nat. Commun. **6**, 7026 (2015).
[11] A. R. Warwick, J. Iniguez, P. D. Haynes, and N. C. Bristowe, J. Phys. Chem. Lett. **10**, 1416 (2019).
[12] K. L. Brown, S. F. Parker, I. R. Garcia, S. Mukhopadhyay, V. G. Sakai, and C. Stock, Phys. Rev. B **96**, 174111 (2017).
[13] I. P. Swainson, C. Stock, S. F. Parker, L. Van Eijck, M. Russina, and J. W. Taylor, Phys. Rev. B **92**, 100303(R) (2015).
[14] A. M. Leguy, J. M. Frost, A. P. McMahon, V. G. Sakai, W. Kockelmann, C. Law, X. Li, F. Foglia, A. Walsh, B. C. O'Regan, J. Nelson, J. T. Cabral, and P. R. Barnes, Nat. Commun. **6**, 7124 (2015) .
[15] A. D. Wright, C. Verdi, R. L. Milot, G. E. Eperon, M. A. Pérez-Osorio, H. J. Snaith, F. Giustino, M. B. Johnston, and L. M. Herz, Nat. Commun. **7**, 11755 (2016).
[16] NREL, https://www.nrel.gov/pv/cell-efficiency.html.
[17] Z. Chen, B. Turedi, A. Y. Alsalloum, X. Z. C. Yang, I. Gereige, A. AlSaggaf, O. F. Mohammed, and O. M. Bakr, ACS Energy Lett. **6**, 1258 (2019).
[18] M. T. Weller, O. J. Weber, P. F. Henry, A. M. Pumpo, and T. C. Hansen, Chem. Commun. **51**, 4180 (2015).
[19] Y. Ren, I. W. Oswald, X. Wang, G. T. McCandless, and J. Y. Chan, Cryst. Growth Des. **16**, 2945 (2016).
[20] K. Wang, Z. Jin, L. Liang, H. Bian, D. Bai, H. Wang, J. Zhang, Q. Wang, and S. Liu, Nat. Commun. **9**, 4544 (2018).
[21] W. Lee, H. Li, A. B. Wong, D. Zhang, M. Lai, Y. Yu, Q. Kong, E. Lin, J. J. Urban, J. C. Grossman, and P. Yang, Proc. Natl. Acad. Sci. USA **114**, 8693 (2017).
[22] M. Kulbac, D. Cahen, and G. Hodes, J. Phys. Chem. Lett. **6**, 2452 (2015).
[23] A. Maalej, Y. Abid, A. Kallel, A. Daoud, A. Lautié, and F. Romain, Solid State Commun. **103**, 279 (1997).
[24] C. Quarti, G. Grancini, E. Mosconi, P. Bruno, J. M. Ball, M. M. Lee, H. J. Snaith, A. Petrozza, and F. De Angelis, J. Phys. Chem. Lett. **5**, 279 (2014).
[25] A. M. A. Leguy, A. R. Goñi, J. M. Frost, J. Skelton, F. Brivio, X. Rodrígue-Martinez, O. Weber, A. Pallipurath, M. I. Alonso, M. Campoy-Quiles, M. T. Weller, J. Nelson, A. Walsh, and P. R. F. Barnes, Phys. Chem. Chem. Phys. **18**, 27051 (2016).
[26] E. Mosconi, C. Quarti, T. Ivanovska, G. Ruani, and F. De Angelis, Phys. Chem. Chem. Phys. **16**, 16137 (2014).
[27] T. Baikie, N. S. Barrow, Y. Fang, P. J. Keenana, P. R. Slater, R. O. Piltz, M. Gutmann, S. G. Mhaisalkar, and T. J. White, J. Mater. Chem. A **3**, 9298 (2015).
[28] F. Brivio, J. M. Frost, J. M. Skelton, A. J. Jackson, O. J. Weber, M. T. Weller, A. R. Goñi, A. M. A. Leguy, P. R. F. Barnes, and A. Walsh, Phys. Rev. B **92**, 144308 (2015).
[29] M. Songvilay, M. Bari, Z.-G. Ye, G. Xu, P. M. Gehring, W. D. Ratcliff, K. Schmalzl, F. Bourdarot, B. Roessli, and C. Stock, Phys. Rev. Mater. **2**, 123601 (2018).
[30] A. Potglisch and D. Weber, J. Chem. Phys. **87**, 6373 (1987).
[31] L. Chi, I. Swainson, L. Cranswick, J. Her, P. Stephens, and O. Knop, J. Solid State Chem. **178**, 1376 (2005).
[32] Y. Kawamura and H. Mashiyama, J. Korean Phys. Soc. **35**, S1437 (1999).

190

[33] I. P. Swainson, Acta Cryst. **B61**, 616 (2005).
[34] Y. Guo, O. Yaffe, D. W. Paley, A. N. Beecher, T. D. Hull, G. Szpak, J. S. Owen, L. E. Brus, and M. A. Pimenta, Phys. Rev. Mater. **1**, 042401 (2017).
[35] V. L. R. Jacques, A. Gallo-Frantz, A. Tejeda, D. Le Bolloc'h, F. Lédée, G. Trippé-Allard, D. Garrot, P. Fertey, E. Deleporte, and O. Plantevin, J. Phys. D: Appl. Phys. **52**, 314001 (2019).
[36] C. Stock, R. A. Cowley, J. W. Taylor, and S. M. Bennington, Phys. Rev. B **81**, 024303 (2010).
[37] V. F. Sears, Neutron News **3**, 26 (1992).
[38] T. Chen, B. J. Foley, B. Ipek, M. Tyagi, J. R. D. Copley, C. M. Brown, J. J. Choi, and S. H. Lee, Phys. Chem. Chem. Phys. **17**, 31278 (2015).
[39] L. Brammer, E. A. Bruton, and P. Sherwood, Cryst. Growth Des. **1**, 277 (2001).
[40] M. Kulbac, D. Cahen, and G. Hodes, Chem. Mater. **28**, 4259 (2016).
[41] K. L. Svane, A. C. Forse, C. P. Grey, G. Kieslich, A. K. Cheetham, A. Walsh, and K. T. Butler, J. Phys. Chem. Lett. **8**, 6154 (2017).
[42] H. Zhu, M. T. Trinh, J. Wang, Y. Fu, P. P. Joshi, K. Miyata, S. Jin, and X. Y. Zhu, Adv. Mater. **29**, 1603072 (2017).
[43] C. M. B. Line, B. Winkler, and M. T. Dove, Phys. Chem. Miner. **21**, 451 (1994).
[44] T. Glaser, C. Müller, M. Sendner, C. Krekeler, O. E. Semonin, T. D. Hull, O. Yaffe, J. S. Owen, W. Kowamsky, A. Pucci, and R. Lovrincic, J. Phys. Chem. Lett. **6**, 2913 (2015).
[45] A. Gold-Parker, P. M. Gehring, J. M. Skelton, I. C. Smith, D. Parshall, J. M. Frost, H. I. Karundadasa, A. Walsh, and M. F. Toney, Proc. Natl. Acad. Sci. USA **115**, 11905 (2018).
[46] D. Konig, K. Casalenuovo, T. Takeda, G. Conibeer, J. F. Guillemoles, R. Patterson, L. M. Huang, and M. A. Green, Phys. E (Amsterdam) **42**, 2862 (2010).
[47] L. M. Herz, ACS Energy Lett. **2**, 1539 (2017).
[48] M. Kim, G. H. Kim, T. K. Lee, I. W. Choi, H. W. Choi, Y. Jo, Y. J. Yoon, J. W. Kim, J. Lee, D. Huh, H. Lee, S. K. Kwak, J. Y. Kim, and D. S. Kim, Joule **3**, 2179 (2019).
[49] S. D. Stranks, G. E. Eperon, G. Grancini, C. Menalaou, J. P. Alcocer, T. Leijtens, L. M. Herz, A. Petrozza, and H. J. Snaith, Science **342**, 341 (2013).
[50] A. C. Ferreira, A. Létoublon, S. Paofai, S. Raymond, C. Ecolivet, B. Rufflé, S. Cordier, C. Katan, M. I. Saidaminov, A. A. Zhumekenov, O. M. Bakr, J. Even, and P. Bourges, Phys. Rev. Lett. **121**, 085502 (2018).
[51] T. Fujii, S. Hoshino, Y. Yamada, and G. Shirane, Phys. Rev. B **9**, 4549 (1974).
[52] M. Songvilay, N. Giles-Donovan, M. Bari, Z. G. Ye, J. L. Minns, M. A. Green, G. Xu, P. M. Gehring, K. Schmalzl, W. D. Ratcliff, C. M. Brown, D. Chernyshov, W. van Beek, S. Cochran, and C. Stock, Phys. Rev. Mater. **3**, 093602 (2019).
[53] A. Kovalsky, L. Wang, G. T. Marek, C. Burda, and J. S. Dyck, J. Phys. Chem. C **121**, 3228 (2017).
[54] Q. Lin, A. Armin, R. C. R. Nagiri, P. L. Burn, and P. Meredith, Nat. Photon. **9**, 106 (2015).
[55] O. Yaffe, Y. Guo, L. Z. Tan, D. A. Egger, T. Hull, C. C. Stoumpos, F. Zheng, T. F. Heinz, L. Kronik, M. G. Kanatzidis, J. S. Owen, A. M. Rappe, M. A. Pimenta, and L. E. Brus, Phys. Rev. Lett. **118**, 136001 (2017).
[56] J. S. Bechtel and A. Van der Ven, Phys. Rev. Mater. **2**, 025401 (2018).
[57] R. A. Cowley, Phys. Rev. **134**, A981 (1964).
[58] B. Bernardo, D. Cheyns, B. Verreet, R. D. Schaller, B. P. Rand, and N. C. Giebink, Nat. Commun. **5**, 3245 (2014).
[59] Q. Leblebici, J. Lee, A. Weber-Bargioni, and B. Ma, J. Phys. Chem. C **121**, 3279 (2017).
[60] A. Walsh, J. Phys. Chem. C **119**, 5755 (2015).
[61] J. Bardeen and W. Shockley, Phys. Rev. **80**, 72 (1950).